Melt generation, storage and ascent below Tongariro Volcanic Complex, Southern Taupo Volcanic Zone

A thesis presented in partial fulfilment of the
requirements for the degree of

Doctor of Philosophy
in
Earth Science

at Massey University, Manawatu,
New Zealand

Maria Carmencita B. Arpa
2018

Abstract

The study of Tongariro Volcanic Complex in New Zealand gives an opportunity to view arc magmatism from a setting where the classic arc structure is overprinted by the regional tectonic setting. Instead of viewing the volcano (and associated magmatic processes) as a component of a volcanic arc to determine the origin of andesitic magmas, focus was given on magmatic processes within the volcanic complex. Processes within the plumbing system of the volcanic complex and their implications on andesitic magmatism and volcanic hazards were determined by tracking magma, of selected eruptive products, from their reservoirs to the surface. By focusing on processes that may determine the petrological characteristics of specific deposits (from known eruptions), the influence of local structures associated with eruptive centres within the complex and the diversity of resultant eruption styles may be interpreted as magmatic processes are evaluated.

The deposits for this study are from the last 16 ka history of Tongariro, majority are from the last 10 ka. These are from known eruptions and the deposits were mapped, dated and studied by previous researchers. Lava flow eruptions are from Te Maari and Red Crater, and Plinian to vulcanian eruptions are represented by the Mangamate Tephra and Ngauruhoe deposits. For each eruptive deposit, whole rock major, trace and isotope compositions were determined. Groundmass and mineral components were analysed for major elements. Major element and volatile (H_2O, CO_2, S, Cl) compositions of melt inclusions in component olivine and pyroxene crystals were also determined.

The deposits from the recent history of Tongariro Volcano can be related to a common source. The basalts can differentiate to more evolved andesitic to dacitic compositions by crystallization and/or melting. Magmatic differentiation takes place in different reservoirs, at different depths, within the complex. Differences were observed in the volatile contents of the

magmas and these may be related to magma storage and ascent processes. Magmatic processes for the deposits in this study, interpreted from compositions, considered and are consistent with eruption styles.

Acknowledgements

Whether there are regrets on my acceptance to the PhD program, I'm grateful for the opportunity to come to New Zealand and study a very interesting volcano. It is a good place to recover and heal. I'm thankful to my supervisors, Georg Zellmer, Bruce Christenson, Gert Lube and Shane Cronin, for providing support and advice for the completion of this project. Project funds from GNS Science covered analytical costs and enabled acquisition of crucial data. It was also very kind of Bruce Christenson to host me at NIC and I'm thankful for a mentor's guidance. I enjoyed the lab work at NIC and had help from many who I bothered from their everyday work. Thanks to all the VRS group at Massey, especially to Kate Arentsen, Karoly Nemeth and Jon Procter. In the labs at Massey, I learned from Bob Stewart, Clel Wallace, Anja Moebis, Paul Barrett, Ian Furkert and Glenys Wallace. For those who considered my experience in volcanology and had confidence in my work, I appreciate the kind regard.

The samples for this project were sent to different laboratories in New Zealand and all over the world. These are the big names who kindly accepted my samples for analysis: Gregory Shellnutt (National Taiwan Normal University), Ian Schipper (Victoria University), Maya Kamenetsky and Vadim Kamenetsky (University of Tasmania), Chris Harris (University of Cape Town), Julia Bryce and Flor Fahnestock (University of New Hampshire) and Samuel Mukasa (University of Minnesota). I'm grateful for the collaboration.

A challenging part of the project is the living aspect. Thanks to all the house owners who provided a room for me. Wonderful people from Ngaio flat and friends from Massey allowed for good times away from study.

Finally, good friends and family helped me continue through discouragements and enabled me to finish this work.

Tongariro Alpine Crossing trail from Ketetahi, a view of North Crater and Ketetahi fumaroles

LIST OF FIGURES

LIST OF TABLES

APPENDIX

1 Introduction

1.1 Statement of hypothesis

The volcano-tectonic setting of Tongariro Volcanic Complex can be regarded as both volcanic arc and back arc, and volcanism is influenced mainly by both flux melting and decompression melting. Large explosive eruptions from the volcano complex 10,000 years ago were attributed to major rifting events (Nakagawa *et al.*, 1998), and after 10,000 years, only smaller eruptions occurred. The most prominent stratocone (Ngauruhoe) in the complex, indicating strombolian and vulcanian activity, was built starting around 7,000 years ago (Moebis, 2010). The influence of subduction zone magmatism can here be regarded as constant where magma is being produced at the source from subduction zone processes, but punctuations in volcanic activity can be due to rifting. Geophysical models show an accumulation of basaltic (primary) melts in the lower crust (Harrison and White, 2006, Stern *et al.*, 2006), and rifting can bring these basaltic melts to the surface rapidly and/or induce batch melting of partially crystallized intrusions by decompression. If rifting is not accelerated, magma from the source ascends in stages through different levels within the crust as the magma evolves and compositions become less dense. Differentiation of basalts can start at the lower crust because the basaltic intrusions can crystallize and underplating of new intrusions can result to partial melting of previous intrusions. The resultant melts (residual, partial melts or mixed melts) are expected to have andesitic (intermediate) or more evolved compositions (**Figure 1-1**).

Magma stored at mid to upper crustal levels may interact with the hydrothermal system. The aspect of interaction examined here will be taken from the magma volatile contents. The source of magmatic volatiles may not only be primary sources (magma production at source), but volatiles may be gained and released by the magma during its rise to the surface or storage and

equilibration in shallower reservoirs. Isotope data for melt inclusions is not part of this study, but volatile sources may be tested by looking at relative abundances of volatiles from the different magma reservoirs in relation to depth of reservoirs, eruption style and type of magma. Magmatic volatiles can be regarded as a factor in magma genesis and eruption style and the overall picture of petrogenesis with respect to volcanism will be constructed using whole rock compositions, mineral chemistry, melt and volatiles compositions.

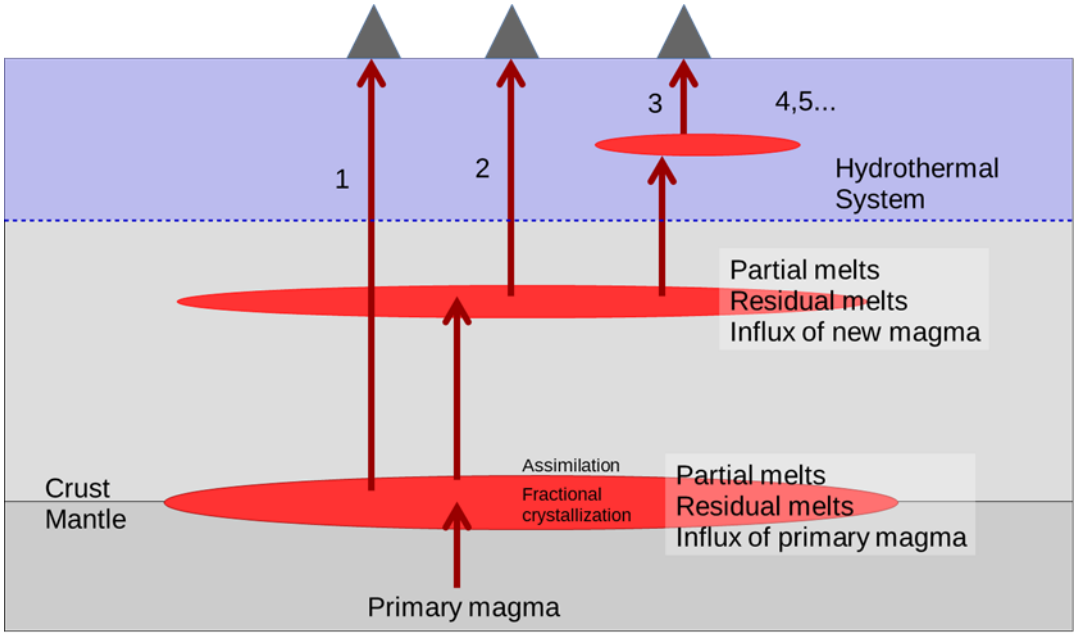

Figure 1-1. Abstract representation of magma storage and processes below Tongariro Volcano.

1.2 Importance of the project

Volcanism at Tongariro remains active to the present day. One of its craters, Upper Te Maari Crater, is the site of several historical eruptions including the most recent from Tongariro in August and November 2012. Two other vents, namely Ngauruhoe and Red Crater, produced significant eruptions in historical times. The latest eruption from Ngauruhoe was in 1975.

Historical eruptions from Tongariro were classified to have a Volcanic Explosivity Index (VEI) of 1 to 3, but prehistoric eruptions were much larger with VEI 5 (www.volcano.si.edu). The eruptions have produced volcanic hazards such as pyroclastic flows and surges, pyroclastic falls and ballistics, lahars and lava flows. Tongariro Volcanic Complex is being monitored for volcanic hazards by GNS Science, and a warning system is in place.

Volcano research is a significant part of pre-eruption hazard assessment. Information such as magma composition and volatile content has implications on eruption explosivity. The magmatic volatiles data from eruptive products determined from this study will have applications on the interpretation of quiescent period volcanic gas data. All information gathered on a volcano, from magma generation to eruption, contributes to monitoring methods and interpretation, and how to warn the public about volcanic hazards. The depth constraints on magma bodies, a major result of this project, will aid in the interpretation of seismic data and volcanic gas data. How the magma is stored and how it evolves in reservoirs beneath volcanoes will influence the magnitude of future eruptions. Interpretations of magma genesis with respect to the eruption style of past eruptions will contribute to assessment of future volcanic hazards. This project aims to make contributions to volcano research being done on Tongariro.

1.3 Objectives

This research looks at several eruptive deposits from the last ca. 10,000 years history of Tongariro, deposits erupted from several vents such as Te Maari, Ngauruhoe, Red Crater and North Crater. Members of the Mangamate formation considered to source from Tongariro are also included. The group of samples for this study, which represents different modes of eruption – fissure to central vent, will be used to test the generation, storage and ascent of magmas. The data will include bulk major and trace elements for rock samples and gas samples,

mineral chemistry, isotope data and melt inclusion chemistry (including H_2O, S, Cl, and CO_2). The objectives of this work will be: 1) To get the depths of magma crystallization and storage for the sample set, 2) Determine the volatiles content (magmatic H_2O, CO_2, S, Cl) from melt inclusions for the different eruptive deposits and set-up a possible degassing path for the magma of the 1500 AD Te Maari lava flow, and 3) Synthesis of petrological and volatiles data in terms of magma genesis to get an overall picture of the magmatic processes that resulted in the eruptions.

1.4 Background: review of arc magmatism

Convergent plate margins, where one tectonic plate subducts beneath another, are typically regions of active volcanism associated with the formation of volcanic arc systems. An arc system consists of, starting from the trench side: the inner slope of the trench, which overlies active subduction and accretion, a frontal arc or forearc, an active volcanic chain (volcanic arc) that occurs about 100km above the subducting plate, and an area of extension where magmatism also occurs (active marginal basin or back-arc) (Karig, 1974, Hamilton, 1988). The general model for subduction zone magmatism shows that magma/melt may be generated in the subducting slab, the mantle wedge, and by melting of the overriding crust (Mysen and Boettcher, 1975, Hildreth and Moorbath, 1988, Tatsumi, 1989, Peacock, 1990, Yogodzinski and Kelemen, 1998, Grove *et al.*, 2006).

1.4.1 Contributions from the subducting slab

Contributions from the subducting slab can come from the oceanic crust, upper mantle peridotite and unaccreted sediment cover. Partial melts can form from the subducted oceanic crust if the subduction zone is relatively warm and developed on young oceanic lithosphere as shown from models that show slab P-T-t paths that intersect the wet solidus at 10 to 28 kbar (Peacock, 1990). The slab can also melt in relatively old subduction system where heat is

provided by friction. Products of slab melts called Adakites that are found in the Aleutians for example, show high Sr and Nd/Yb ratios in high Mg# clinopyroxene phenocrysts among other typical slab melt signatures (Yogodzinski and Kelemen, 1998). There are cases however, that show a geochemical signature coming from melted subducted sediments that cover the slab and only dehydration without melting of the subducted oceanic lithosphere (Ryan *et al.*, 1995, Castillo and Newhall, 2004). Some geochemical variations between Taal and Mayon volcanoes can be attributed to the type and amount of sediments that were melted and dehydrated (Castillo and Newhall, 2004). Sediments can also detach from the subducted slab to form buoyant diapirs that melt at hotter temperatures within the mantle wedge to release the sediment chemical signature found in arc lavas (Behn *et al.*, 2011). Geochemical variation in the Kuril Islands arc shows decreasing hydrophilic elements such as B, Cs, As and Sb across arc correlated with decreasing dehydration of the slab, while K, Ba, ^{10}Be and LREE enrichment are regarded to be carried by slab sediment melts (Ryan *et al.*, 1995). In the Izu arc, Li isotope ratio decrease with increasing depth of the Wadati-Benioff zone suggesting a decrease in the input of subduction fluid component to the source of magmatism with increasing depth of slab (Moriguti and Nakamura, 1998). A model for recycling of subducted noble gases using their isotope compositions show that 98% of the noble gases and water return back to the surface through subduction volcanism (Staudacher and Allègre, 1988). The near constant Cl/K_2O ratios of uncontaminated OIB and MORB, imply that bulk of the Cl and K_2O are removed from the subducted crust by dehydration and dehydration melting and transferred to the shallow mantle sources of arc volcanism, leaving little to the deeper mantle sources of OIB (Lassiter *et al.*, 2002).

As the slab subducts, it undergoes metamorphism releasing fluids into the mantle wedge that can reach deeper depths through higher pressure hydrous minerals (Peacock, 1990, Ryan *et al.*, 1995, Moriguti and Nakamura, 1998, Rüpke *et al.*, 2002). The mantle directly above the slab

is hydrated, can be dragged down with the slab and itself also undergo dehydration and release fluids at depth according to the stability fields of the hydrous minerals (Tatsumi, 1989). Chlorite, for example, was shown to be an abundant phase on vapour-saturated peridotite solidus from 2 to up to 3.6 GPa and can provide sufficient H_2O upon breakdown at greater depths to enable hydrous mantle melting (Grove *et al.*, 2006, Till *et al.*, 2012). Phlogopite can form in the mantle wedge from the reaction of H_2O and K_2O rich fluids with peridotite, and can be stable at depths greater than 3 GPa (Peacock, 1990). When phlogopite bearing peridotite exceeds the hydrous solidus, the partial melts produced will be K_2O rich. Some chemical properties found in lavas can be explained to come from a breakdown of a particular hydrous mineral and this, in combination with other parameters, can be used to describe the source of melting. Along-arc chemical variation such as that between Nicaragua and Costa Rica may be explained by a difference in physical properties of the subducted slab (e.g. subduction angle and faulting) that determines whether there was predominantly dehydration of the amphibolite oceanic crust or dehydration of serpentinized lithosphere accessed through faults cutting across the slab (Rüpke *et al.*, 2002).

1.4.2 Contributions from the mantle

Addition of fluids to the mantle wedge lowers its solidus enabling melting at a shallower geotherm (Mysen and Boettcher, 1975, Grove *et al.*, 2006, Till *et al.*, 2012). The introduction of fluids from the slab to promote hydrous mantle melting produces the calc-alkaline geochemical signature typical of arc magmas (Grove *et al.*, 2003). A model for the hydration and melting of the mantle wedge shows maximum amount of hydration at the contact between the subducting slab and the mantle wedge and decreasing hydration towards the center (Grove *et al.*, 2006). Because temperature increases towards the center of the mantle wedge, maximum melting occurs in the hot core of the wedge at around 40-60 km depth (Grove *et al.*, 2006). There are cases however, where deeper sourced mantle melts mix with shallower hydrous

mantle melts. For example, whole rock, phenocrysts and melt inclusion chemical variations from basalts in the Lau Basin can be explained by decompression melting of asthenospheric mantle due to back-arc spreading and consequent melting of the overlying subduction hydrated shallower mantle by heat transfer from the rising melts (Kamenetsky *et al.*, 1997). In particular, evidence of hydrous mantle melting was inferred from estimates of liquidus temperature of olivines, based on melt inclusion homogenisation temperatures, that are lower than for a dry mantle crystallization of magnesian olivine (Kamenetsky *et al.*, 1997).

1.4.3 Contributions from the overriding crust

Melting of the overriding crust by latent heat of crystallization from stalled and crystallizing magma intrusions was shown to contribute to magmas produced in arc settings (Hildreth and Moorbath, 1988, Wolff *et al.*, 2000, Smith *et al.*, 2003, Annen *et al.*, 2006). Melts from the mantle stall at the base of the lower crust and melt/assimilate lower crustal materials producing geochemical signatures influenced by the character of the lower crust as evidenced from along arc variations in Central Chile (Hildreth and Moorbath, 1988). A range of felsic magma compositions produced along the Kermadec Arc was also attributed to lower crustal melting by underplated melts from the mantle (Smith *et al.*, 2003). Melting within an old crust can occur from partial melting of subduction magmatism derived ponded intrusions. For example, melting of ponded mantle derived moderate to K-rich calc-alkaline magmas that crystallized at mid-crust produced the K-rich silicic deposits found in southwestern Luzon, Philippines (Vogel *et al.*, 2006). A model for the andesitic system of Ruapehu shows that andesites were produced by interaction of mantle melts with the lower crust resulting in partial melting (Price et al., 2005). Subsequent shallower intrusions of more evolved melts transfer heat that could partially melt and assimilate surrounding crust resulting in a predicted evolution to more felsic compositions in time for Ruapehu (Price et al., 2005).

1.5 Background: magmatic degassing

Volatiles from the Earth's interior can reach the atmosphere through volcanism. A change (decrease) in pressure can cause fluids to exsolve, nucleate bubbles, form connections and separate from the magma in the conduit as it rises (Gonnermann and Manga, 2003, Mangan *et al.*, 2004), or during magma convection within the conduit (Kazahaya *et al.*, 1994, Stevenson and Blake, 1998, Kazahaya *et al.*, 2002), or convection within a deeper magma reservoir (Allard, 1997). Both volatiles sourcing from the Earth's formation and volatiles recycled from the subducting slab can reach the surface through volcanoes. This study is especially interested in gases released from arc volcanoes. Fischer (2008) provided and compiled gas flux estimates from arc volcanoes world-wide. The data were mostly from high temperature fumaroles where interactions with the shallow hydrothermal system are negligible (Fischer, 2008). The most dominant gas by mass from arc volcanoes is H_2O (up to 99%), followed by CO_2 and SO_2 and lesser amounts of H_2S, H_2, N_2, HCl, HF, NH_3, CH_4, CO, O_2, noble gases and additional trace elements (Taran *et al.*, 1995, Giggenbach, 1996, Fischer, 2008). Mass balance calculations using volcanic gas measurements, rate of subduction and water from the subducted lithosphere show that H_2O from the subducted oceanic lithosphere is recycled back to the atmosphere through volcanism (Fischer, 2008). Efficient recycling of volatiles in subduction zones is supported by a study by Staudacher and Allègre (1988) using noble gas isotopes. The water content of volcanic gas emitted from arc volcanoes are higher than for Mid-Ocean Ridge Basalt (MORB) and the high water content contributes to the explosive nature of arc volcanoes (Fischer, 2008).

Volatiles play an important role in eruption style. Constantly degassing magma at depth may not have enough drive to rise to the surface, such as for Satsuma-Iwojima Volcano (Kazahaya *et al.*, 2002) or erupt effusively as for the open-(conduit) system Mayon Volcano during the 2006 eruption. Gonnerman and Manga (2003) concluded that fragmentation near conduit walls

enables magma degassing and may reduce explosive behaviour. Closed-system volcanoes tend to erupt more explosively partly due to vapour-saturation of magma at depth. For example, an accumulated gas phase existed in the magma chamber of Pinatubo before its plinian eruption in 1991 (Gerlach *et al.*, 1996). In other cases, such as shown from modelling, where volatiles remain dissolved in the melt and bubble nucleation is delayed (maybe as for saturated conditions), the result is a higher pressure in the conduit as well as higher exit pressures (Mangan *et al.*, 2004).

Compositional variability shown by volcanic gas data can be due to different sources, magmatic and hydrothermal. Compositions can be affected by shallower processes such as interactions with the hydrothermal system (Giggenbach, 1987, Giggenbach, 1996). Moretti et al. (2013) for example identified mixed gas sources from the 30 year geochemical data from Campi Flegrei Caldera, which included hydrothermal and 2 magmatic sources at different depths. Analysis and modeling of gas geochemical data, including isotope compositions and data from condensates, to separate and identify contributions from magmatic and hydrothermal sources was done for the 1995-1996 eruption of Mt. Ruapehu (Christenson, 2000). Thermodynamic models support that surface gas compositions and fluxes can be explained by degassing of more than one magma source (Moretti *et al.*, 2013) and mixing of these sources (Edmonds *et al.*, 2010).

1.6 General geologic setting: Taupo Volcanic Zone

1.6.1 Tectonic setting for the Taupo Volcanic Zone

The Central Volcanic Region (CVR) in North Island (**Figure 1-2**), New Zealand is a wedge shaped area of Quaternary volcanism and tensional tectonics that covers Mt. Ruapehu at the apex in the south and opens towards the Bay of Plenty to the north (Stern, 1985). The CVR is regarded as the southward extension of the Havre Through and Lau Basin, a back-arc system

to the Tonga-Kermadec Arc (Karig, 1974, Stern, 1985, Rowland and Sibson, 2001, Smith and Price, 2006). The Tonga-Kermadec subduction system on oceanic lithosphere extends south to the continental crust of New Zealand through the continuation of the subduction zone system to the Hikurangi Trench (Karig, 1974, Stern, 1985, Hamilton, 1988). The convergence between the Australian plate and the Pacific plate goes from intra-oceanic in the north to continental-oceanic convergence in New Zealand, south of the Vening Meinesz Fracture Zone (Smith and Price, 2006). Clockwise rotation of the eastern North Island made the Hikurangi Trench continuous with the north-northeast trending Tonga-Kermadec Trench (Beanland and Haines, 1998, Reyners *et al.*, 2006, Stern *et al.*, 2006). Both the subduction and extension rates decrease southwards (Hamilton, 1988). Subduction rates are slower beneath the continental crust of New Zealand where oblique subduction takes place (Karig, 1974, Hamilton, 1988, Smith and Price, 2006) and where the Hikurangi Plateau was imaged to be subducting (Harrison and White, 2006). Extension along the back-arc systems becomes slower from north to south and was measured to be 8±2mm/year for the section just north of Lake Taupo (Darby *et al.*, 2000). The Taupo Volcanic Zone (TVZ), which includes Tongariro Volcanic Complex in the south, is on the eastern portion of the Central Volcanic Region and is regarded as the volcanic arc for the subduction along the Hikurangi segment (Beanland and Haines, 1998, Smith and Price, 2006, Stern *et al.*, 2010). The volcanic arc is about 80-100km above the subducted slab (Reyners *et al.*, 2006, Stratford and Stern, 2006). This means that the active magmatic arc is also in an area of rapid extension especially in the north (Hamilton, 1988). The general area where the Tongariro Volcanic Complex is located is therefore an area where melting of the mantle is both significantly influenced by flux/hydrous melting (as for the mantle below a volcanic arc) and decompression by extension (as for the mantle below a back-arc).

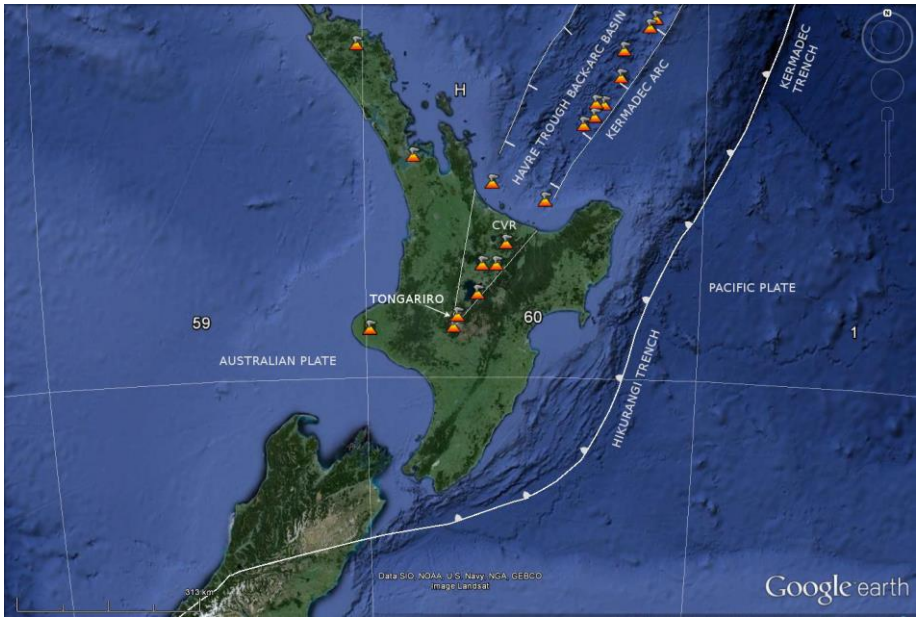

Figure 1-2. Regional tectonic setting for North Island, New Zealand.

Rhyolites, produced by melting of the overriding crust, make up the majority of the erupted material in the Taupo Volcanic Zone, while andesitic deposits presently predominates in the southern TVZ and the northeast end of the TVZ (Cole *et al.*, 2000, Price *et al.*, 2005). Intermediate and silicic magmas can be produced in areas of magmatism through accumulation of hydrous basalt intrusions in the lower crust, which can then differentiate, rise to shallower levels and partially melt surrounding crust (Hildreth and Moorbath, 1988, Annen *et al.*, 2006). This model of basalt underplating was applied in various interpretations using geophysical data for the identification of crust and mantle structures below the TVZ (**Figure 1-3A and B**). Magmatic intrusions at the base of the crust and shallower levels provide additional heat to account for the high heat flux within the TVZ (Bibby *et al.*, 1995). The crust in the central North Island was modelled to be thinner than the surrounding crust (Stern and Davey, 1987). The thickness of the crust in the CVR is around 15km (Stern *et al.*, 2006, Stratford and Stern, 2006, Stern *et al.*, 2010) with a 5km layer from 15 to 20km interpreted to be crustal underplating by basaltic intrusions (Stratford and Stern, 2006). Stern et al., 2010 extends the

ponded basaltic intrusions to a depth of 20 to 25km. An anomalous upper mantle was modelled to start from a depth of 20 to 25km, and the transition from crust to mantle does not appear to be distinct (Stern *et al.*, 2010). Another interpretation of the geophysical data puts the Moho beneath the TVZ at 30km depth (Harrison and White, 2006) and 35km (Reyners *et al.*, 2006). Harrison and White, 2006 agree that the TVZ crust is thinned by backarc extension, but it was thickened by numerous basaltic intrusions. The thicker zone (greater volume) in the lower crust for the underplated basalt and fractionation residue is consistent with an estimate from the volume of silicic material erupted (Harrison and White, 2006). The petrological definition of the crust-mantle boundary (Moho) is based on composition, identifying the crust as basaltic. In this case the thickness of the crust will include the thickness of the underplated basalts. For a petrological model, where the lower crust is melted by underplated basaltic melts that are stalled and crystallizing, the distinction between the crust and mantle can be indistinct (Hildreth and Moorbath, 1988). The geophysical models however, agree that the mantle below the crust in this area show low mantle velocities and is regarded as less dense than normal mantle (Harrison and White, 2006, Stern *et al.*, 2006, Stratford and Stern, 2006, Stern *et al.*, 2010). A 1-4% partial melt distribution in the mantle wedge below CVR was interpreted (Stern *et al.*, 2010) and a region of high partial melt of 6% was identified at 35±3km depth (Stratford and Stern, 2006). Note that the depth of 35km is the base of the crust according to Reyners et al., 2006. The presence of high percentage of melt in the mantle or a highly metasomatized mantle directly below the crust or near the crust can have implications on the petrological model for magmatism. Primary melts from basaltic to more evolved andesitic and dacitic compositions can be generated in a highly altered and metasomatised mantle (Straub *et al.*, 2011) and such melts may rapidly rise through the crust without ponding (Blatter and Carmichael, 1998). Reyners et al., 2006 imaged the slab at around 100km depth beneath the Tongariro area. They

suggested that magma appears to be ponding at the base of the crust in the andesite dominated southwestern region of the TVZ.

A.

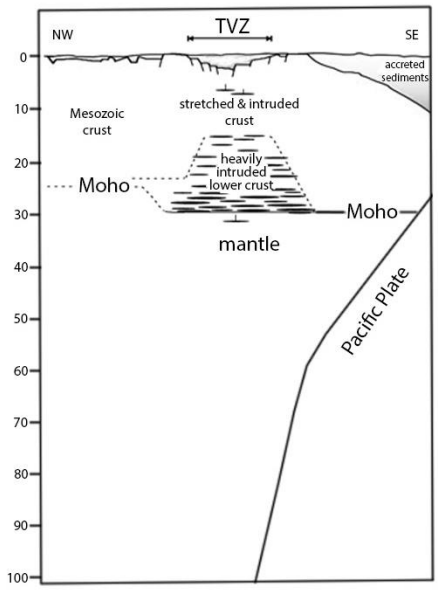

Modified Fig. 19 (Harrison and White, 2006)

B.

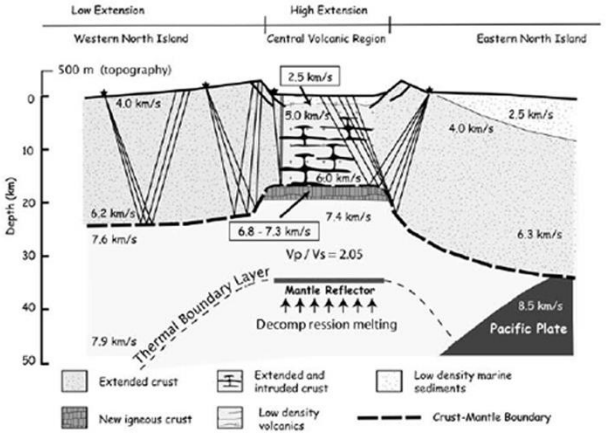

Figure 19 (Stern et al., 2006)

Figure 1-3. Two models for arc magmatism within the Central Volcanic Region, NZ based on geophysical data. (A) Modified from Figure 19 of Harrison and White (2006). The model shows a thick layer of mantle derived melts accumulated within the lower crust. (B) Figure 19 of Stern et al., 2006, which also shows an underplated crust and intruded lower and middle crust, but a different depth for the crust-mantle boundary.

1.6.2 Review of petrology of the Southern Taupo Volcanic Zone

The Taupo Volcanic Zone (TVZ) volcanics is composed mainly of rhyolite with a minor component of high-Al basalt, basalt and andesite (Cole, 1981, Graham *et al.*, 1995). The andesites are concentrated and exposed to the north (Bay of Plenty) and the southern TVZ (Graham *et al.*, 1995). The northern end of the TVZ is near the boundary where the subduction margin changes from continental plate – oceanic plate to oceanic-oceanic.

The Southern Taupo Volcanic Zone (STVZ), a region southwest of Lake Taupo, is predominated by andesitic volcanism. The four major andesite massifs of Kakaramea, Pihanga, Tongariro and Ruapehu comprise the Tongariro Volcanic Centre in the STVZ (Cole, 1978). Several studies have related the different volcanics in the STVZ in terms of their petrogenesis. Few andesites can be associated to high-Al basalts (Graham *et al.*, 1995), whereas andesites from Tongariro may be generated from low-Al basalts such as basalts from Red Crater (Graham *et al.*, 1995). High-Al basalts are concentrated on the central TVZ and they are regarded as near primary magma originating from a depleted mantle and erupted through an extensional crust by fissure eruptions (Cole, 1981, Graham *et al.*, 1995). High-Al basalt may also be produced from low pressure fractional crystallization of primary magma. At higher pressure, crystallization of pyroxene fractionates Al. The distribution of high-Al basalts shows that they are found within the more active extension and thinner crustal region of the central TVZ. Assuming a different depth of origin for the high-Al and low-Al basalts, it follows that the basalts have been modified by fractional crystallization with separate differentiation paths for the parental magma. However, Graham et al. (1995) have identified the high-Al basalt as the most primitive basalt in the TVZ and that low-Al basalt such as that from Red Crater of Tongariro can be related to the high-Al basalt by assimilation and fractional crystallization (AFC).

There are different models for how the andesites of the TVZ were generated. Gamble at el., (1990) relates the basalts and andesites to a common parental magma by fractional crystallization of olivine, plagioclase followed by clinopyroxene and then orthopyroxene as the magma cools. Assimilation plays an important role when the magmas rise through the crust (Gamble *et al.*, 1990, Graham *et al.*, 1995, Price *et al.*, 2005). Assimilation of Waipapa and Torlesse meta-greywackes with the basalts can result to andesite compositions in the TVZ as modelled using Pb isotopes (Graham *et al.*, 1995). Fractional crystallization also occurs, but it

will take a large percentage of crystallization to produce the isotopic trends from this process alone (Graham *et al.*, 1995). However, in considering the mush model and initial magma water content, fractional crystallization can explain the generation of andesites as well as rhyolites without a significant contribution from crustal assimilation (Deering *et al.*, 2011). Andesites resulted from residual melt of lower crustal mush (50 – 80% crystallinity) of dry basaltic magma and dacites were produced from wetter mush zones at shallower depth (Deering *et al.*, 2011). The geochemical trends shown by the TVZ andesites and dacites are consistent with the expected compositions of magmas derived from basalts of different water content (Deering *et al.*, 2011). Although not stated as extracted from a crystal mush, the 10 ka Pahoka Mangamate sequence resulted from melts rising rapidly to the surface and originating at different depths (Nakagawa *et al.*, 1998). From an eruption influenced by rifting, the first 2 sequences, which contained amphibole, originated from >8 km depth at water saturated conditions, and the last 3 sequences, without amphibole, originated at deeper (>20 km) depth (Nakagawa *et al.*, 1998).

1.7 Field area and samples: Tongariro Volcanic Complex

Tongariro is one of the four large andesitic volcanoes that belong to the Tongariro Volcanic Centre (Cole *et al.*, 1986). Tongariro is described as a large volcanic massif that is composed of at least 12 composite volcanic cones (Cole *et al.*, 1986) with the vents generally aligned to the north-northwest (Mathews, 1967). Named vents that comprise the Tongariro massif, from south to north, are as follows: Tama Lakes, Ngauruhoe, Pukekaikiore, Pukeonake Scoria Cone, Red Crater, Emerald Lakes, Central Crater, Blue Lake, North Crater, Ketetahi Springs, Upper Te Maari Crater, Lower Te Maari Crater (Topping, 1974) (**Figure 1-4**). Ngauruhoe (altitude 2,287 m), which lies at the southern part of Tongariro massif, is the youngest composite cone in Tongariro Volcano and the highest peak in the complex (Gregg, 1960, Topping, 1974, Cole *et al.*, 1986, Price *et al.*, 2013). The eruptive history of Tongariro volcano started 275 ka BP, developing, up to present, vents distributed over a 13 km long and 5 km wide corridor (Hobden

et al., 1999). The original Tongariro was believed to be an elongate volcano with several craters that after eruption and collapse, became the site where more recent vents developed (Gregg, 1960). More recent studies agree that the present Tongariro is a 60 km^3 composite structure built from at least 6 cones erupted between 275 – 65 ka BP of cone-building periods that were then overprinted by later eruptions from 25 ka BP to present (Hobden *et al.*, 1999, Price *et al.*, 2013).

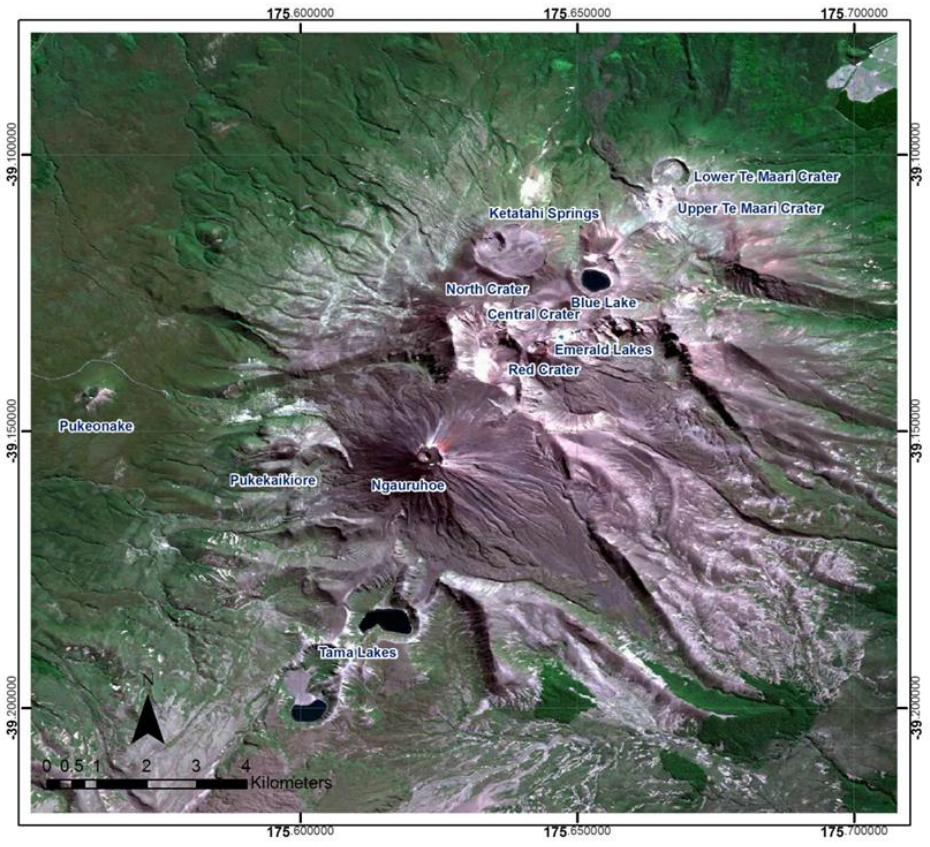

Figure 1-4. SPOT satellite imagery of Tongariro Volcanic Complex. The different eruptive centres are labelled.

1.7.1 Volcanic centres for this study

Tongariro Massif consist of 13 named volcanic centres (Topping, 1974), some of these vents are described below. Physical features and relevant deposits/events to this study were gathered from literature. **Figure 1-5** shows the field area.

Figure 1-5. The field area, view looking southeast.

1.7.1.1 Te Maari Craters: Lower Te Maari

Lower Te Maari Crater is located on the northern part of the alignment of vents that comprise the Tongariro Volcanic Complex. It is a circular flat floored crater 500 m wide and 60 m deep (Basher, 2005). The crater floor at times were seen partly occupied by a lake of brown water (Gregg, 1960). Fragmented volcanic rocks and 2 layers of lava can be seen exposed on the inner crater wall (Gregg, 1960). On the western wall is an area of hydrothermal activity with altered grounds and steam emissions (Basher, 2005). At present, the prominent fumaroles are found only within and around the Upper Te Maari Crater and along a lineament that passes near the southeast border of the Lower Te Maari Crater (**Figure 1-6**). Lower Te Maari has eruption accounts from the Maoris and it is considered older than the Upper Te Maari (Gregg, 1960, Topping, 1974). The Rotoaira Lapilli formation is regarded to have been sourced from Lower Te Maari (Topping, 1974). Charcoal directly below the Rotoaira Lapilli was dated to be 13,800 ± 800 years BP (Topping, 1974). Converting this radiocarbon age to calendar age gives a value of 16,100 ± 400 cal. yr BP (Fairbanks, 2005). Recent studies dated rhyolitic marker beds below (Rerewhakaaitu) and above (Waiohau) the Rotoaira to be 17.6 cal. yr BP and 13.6 cal. yr BP, respectively and giving an age of 16.6 cal. yr BP to the Rotoaira (Lowe *et al.*, 2008, Shane *et al.*, 2008) consistent with the original age from Topping (1974). The Rotoaira Lapilli

is an andesitic pyroclastic fall deposit consisting of ash to lapilli size clasts (Topping, 1974). The oldest lava flow from Lower Te Maari is around >14 ka (B.P.) (Lecointre *et al.*, 2004, Basher, 2005). There are other lava flows in the vicinity of the Te Maari Craters with possible ages of around 6-9.7 ka BP based on stratigraphic relationships (Topping, 1974). The sampled lavas have andesitic compositions (Hobden, 1997).

Figure 1-6. Sites of major fumarolic activity. Photos were taken last April 21-23, 2015.

1.7.1.2 Te Maari Craters: Upper Te Maari

The Upper Te Maari Crater is found on the southern upper slopes of Lower Te Maari at around 1500 m asl and about 100 m above Lower Te Maari. Some talus and one lava flow lobe from this crater spilled down into Lower Te Maari. It is a smaller crater and the site of several recent eruptions including the most recent one from Tongariro Volcanic Complex in 2012. Eruptions have been reported in 1869, 1886, 1892-1893, 1896-1897, and in 6 August 2012 and a smaller phreatic eruption in 21 November 2012 (www.gns.cri.nz, Christenson *et al.*, 2013). Very active fumaroles are found within and around the Upper Te Maari Crater. Lithologies within the crater consist of massive and bedded breccias (Basher, 2005) including hydrothermally-altered

blocky tuff breccias exposed in the eastern inner wall (Hobden, 1997). The Upper Te Maari lava flow is the youngest lava flow sourced from the Te Maari craters (Topping, 1974). It overlies the Taupo pumice and is estimated to be deposited close to 1528 AD based on analysis of tree-ring data (Topping, 1974). It was extruded before the recent explosive eruptions which formed the present configuration of the crater. The lava flow is aa to blocky type and has multiple overlapping lobes that flowed 4 km downslope to the northwest (Topping, 1974, Hobden, 1997, Basher, 2005). It is an andesite described as hypocrystalline and porphyritic-glomeroporphyritic consisting of plagioclase, orthopyroxene, clinopyroxene, opaques and olivine (Hobden, 1997, Basher, 2005). It is one of the olivine bearing lavas from Tongariro.

1.7.1.3 North Crater

North Crater, located at the north-western end of the Tongariro massif, has a distinctive flat-topped cone (Gregg, 1960, Topping, 1974). The crater rim measures about 1,100 m in diameter (Topping, 1974). Voluminous lava flows from North Crater flowed down towards Roto Aira, and the crater ponded with lava to form its flat summit (Gregg, 1960). A 300 m wide and 60 m deep explosion pit later formed in the north-western sector of the crater after the lava lake has cooled (Topping, 1974). Deposits of welded agglomerate, rheomorphic tuffs and lava define the crater rim (Topping, 1974, Hobden, 1997). The youngest lava flow from North crater deposited northwest of the crater and is considered to be older than the Pahoka-Mangamate eruption episodes (Nairn *et al.*, 1998). Nairn et al. (1998) found Te Rato lapilli, which have an age of 9,780 years BP (11,125 cal. yr BP) (Topping, 1974), overlying these lavas. Lava flows that are > 12,500 years BP found north of North crater are probably from this crater (Topping, 1974). Welded agglutinate sequences are found towards the north and northeast on the upper slopes near the crater (Shane *et al.*, 2008). Its age is not well constrained, but reworked Te Rato tephra was found to overlie the sequence (Shane *et al.*, 2008). A scoria flow 2-4 m thick exposed on the southwest slope is considered to be from North Crater (Hobden, 1997). There

are around 25 lava and pyroclastic units that can be attributed to North Crater and most of the major activities occurred at around 10-15 ka (Hobden, 1997). The composition of sampled deposits ranged from basaltic andesite to andesite (SiO_2 range of 56.3-60.1 wt. %), but mostly andesite (Hobden, 1997). Based on isopach data, Te Rato Lapilli, the oldest member of the Mangamate Formation, was erupted from North Crater (Topping, 1974). Te Rato Lapilli is distinguished from other members of the Mangamate Formation by the dominance of hornblende and scarcity (trace amounts) of olivine (Donoghue *et al.*, 1991).

1.7.1.4 Red Crater

Red Crater is approximately 350m in diameter on its longest side. It is elongated towards the northeast and has steep sided walls. Red Crater is a vent of a small scoria cone on the central part of the Tongariro Volcanic Complex (Topping, 1974). The cone is composed of beds of dark red and black variably welded basaltic andesite scoria intruded by feeder dikes for lava flows (Gregg, 1960, Topping, 1974, Hobden, 1997). The dike in the southeastern wall once fed lava flows towards Oturere and has since been partly emptied (Gregg, 1960). Red Crater is a recent vent with eruptions documented for the 1855 and 1859 events (Gregg, 1960). There are thermal areas on the northeast side of the crater elongated in the direction of 45˚N (Hochstein, 1985), following the alignment of the Emerald Lakes. The largest lava flow from Tongariro in the last approximately 14,000 years was erupted from Red Crater and flowed down Oturere Stream Valley (Stevens, 2002). Referred to as the Oturere lava flow, the volume is about 371-640 million m^3 (Stevens, 2002) and the composition is andesite (Hobden, 1997). Its age is constrained by stratigraphic relations. Mangamate Tephra, with the oldest unit at 9,780 years BP (11,125 cal. yr BP), does not cover it and sections overlying the flow gives it an upper limit of 2,500 years BP (Topping, 1974). Smaller lava flows that are younger than Oturere lava flow, a batch erupted after the Taupo pumice (1717 cal. yr BP (Lowe *et al.*, 2008)), are basaltic

andesite in composition (Hobden, 1997). The post Taupo lava flows deposited towards the South Crater, Central Crater and Oturere Valley (Hobden, 1997).

1.7.1.5 Ngauruhoe

Ngauruhoe is a basaltic andesite to andesite composite cone, located on the southern part of the Tongariro Volcanic Complex, rising 900 m from its base to 2,287 m above sea level (Topping, 1974, Hobden, 1997). It is the highest peak in the present Tongariro Volcanic Complex and its most active vent (Gregg, 1960, Topping, 1974). From 1839 to 1959 there has been 63 magmatic and/or ash producing documented eruptions (Gregg, 1960). The most recent eruption episode was from 1973 – 1975 (www.gns.cri.nz). Eruptions have been confined within the 400 m wide summit crater. Changes within the summit crater and formation of sub-craters/nested craters and minor cones during different eruption episodes since 1839 have been documented (Gregg, 1960).

Deposits from Ngauruhoe are consistently basaltic andesite to andesite, erupted in eruption styles ranging from strombolian, vulcanian to sub-plinian (Hobden *et al.*, 2002). There are many units of lava flows and pyroclastic deposits erupted from Ngauruhoe since its formation. Isopachs for the Mangatawai Tephra point to a Ngauruhoe source (Gregg, 1960). The age of the Mangatawai Tephra constrains the major episodes of cone growth for Ngauruhoe to have been around 2,500 years BP (Topping, 1974, Hobden, 1997). Possible smaller eruptions point to a much older eruptive history of about 7,000 cal. years BP (Moebis *et al.*, 2011). The ages of the oldest known lava flows from Ngauruhoe have not yet been determined by absolute dating. Hobden et al. (2002) identified 5 lava groups with the oldest group (Group 1) correlated to the Mangatawai Tephra. Group 1 and 2 are overlain by the Taupo pumice constraining its age to between 2,500 ka and 1,717 cal. yr B.P. (Hobden *et al.*, 2002). The youngest group, Group 5, includes historical eruptions from 1870 to 1975 (Hobden *et al.*, 2002). Moebis (2010)

divided Ngauruhoes's history into 4 stages based on the tephra record. Stage 1 is the oldest and range in age from around 7000 cal. yr BP to 3,694 ± 133 cal. yr BP, and the youngest (Stage 4) is post Taupo pumice (Moebis, 2010).

1.7.2 Deposits for this study

The rock samples for this study represent deposits from the last ca. 16,000 years and were erupted from different vents (**Figure 1-7**). Detailed source vents for the Mangamate Tephra Members are listed in **Table 1-1**. Only the Ohinepango member of the Mangamate Tephra was not sampled. The list of main rock samples is shown in **Table 1-2** and sample location for rocks and are shown in **Figure 1-8**.

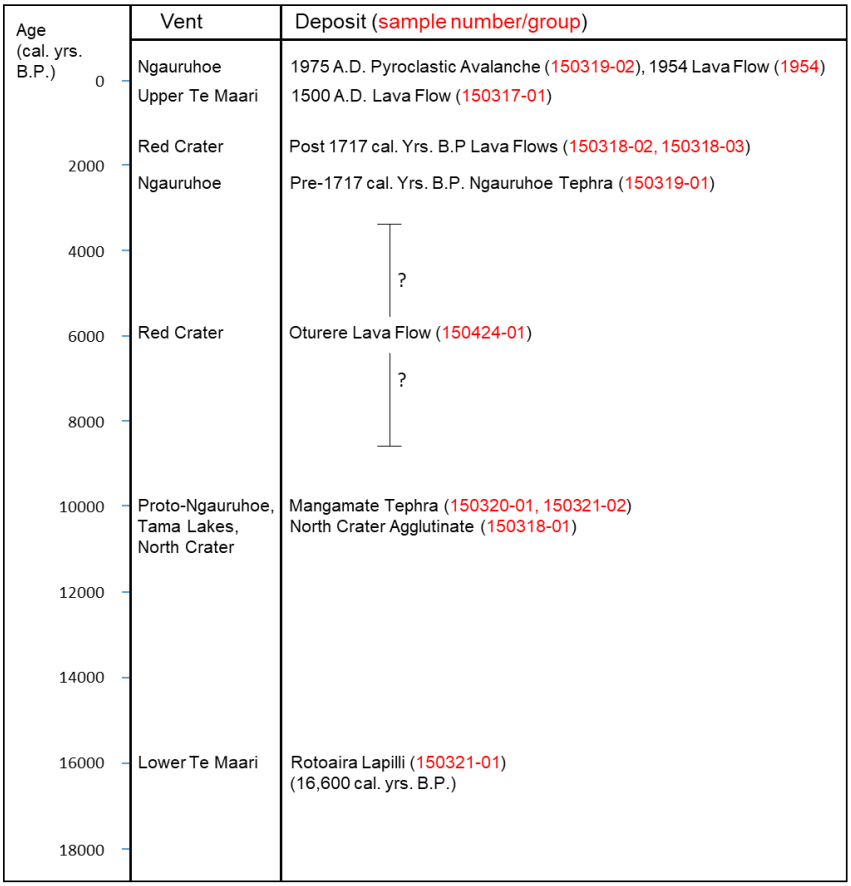

Figure 1-7. General stratigraphy of sampled units from Tongariro Volcanic Complex. Sources for the deposit ages are Lowe et al., 2008; Shane et al., 2008 (Rotoaira Lapilli, North Crater agglutinate); Topping, 1974 (Mangamate Formation, 1500 AD Upper Te Maari lava flow, Oturere lava flow); Hobden, 1997 (post-1717 cal. yrs. BP Red Crater lava flow).

Table 1-1. Mangamate Tephra Members dated 9,780 to 9,700 years BP or ~11,000 cal. years BP (Topping, 1974).

Mangamate Tephra Members (oldest:bottom to youngest)	Source Vent (Topping, 1973)	Source Vent (Nairn et al., 1998)
Poutu Lapilli/PM6	Blue Lake	Near Ngauruhoe (main vent); Tama Lakes, Te Maari Craters, Half Cone, Saddle Cone (minor vents)
Wharepu Tephra/PM5	Tama Lakes	Lower Tama Lake and adjacent craters (main vents)
Ohinepango Tephra/PM4b	Tama Lakes – Ngauruhoe area	Saddle Cone (main vent); Half Cone (minor vent)
Waihohonu Lapilli/PM4a	Tama Lakes – Ngauruhoe area	Saddle Cone (main vent); Half Cone (minor vent)
Oturere Lapilli/PM3	Tama Lakes – Ngauruhoe area	Saddle Cone, Half Cone (main vents); Tama Lakes (minor vents)
Te Rato Lapilli/PM2	North Crater	Proto North Crater (main vent); Te Maari Craters (minor vent)

Table 1-2. Description and location of rock samples. The complete list is in Appendix Table 1.

Sample main	Comment	Waypoints Station	Place	Longitude (Easting)	Latitude (Southing)	Comment
150116-01	Te Rato	WP1	Desert Road	175.73384	-39.22060	Tephra
150317-01	1500AD UTeMaari LF	WP3	Ketetahi trail	175.65614	-39.08202	Lava Flow
150318-01	agglutinate NC	WP7	Ketetahi trail	175.65448	-39.11628	Pyroclast (bomb)
150318-02	post 1.8ka RC LF (aa)	WP10	Alpine crossing near junction with Northern Circuit	175.65710	-39.13176	Lava Flow
150318-03	post 1.8ka RC LF (aa-blocky)	WP11	Northern Circuit	175.67152	-39.14234	Lava Flow
150319-01	pre 1.8ka tephra Ngauruhoe?	WP12	Mangatepopo Valley	175.61531	-39.14064	Tephra
150319-02	1st phase 1975 PF Ngauruhoe	WP13	Mangatepopo Valley	175.61752	-39.14286	Pyroclast (bomb)
150320-01A	Te Rato	WP1	Desert Road	175.73384	-39.22060	Tephra
150320-01B	Oturere	WP1	Desert Road	175.73384	-39.22060	Tephra
150320-01C	Waihohonu (above fine ash layer, middle coarse layer)	WP1	Desert Road	175.73384	-39.22060	Tephra
150320-01D	Wharepu (lower brown layer)	WP1	Desert Road	175.73384	-39.22060	Tephra
150320-01E	Wharepu (upper gray layer)	WP1	Desert Road	175.73384	-39.22060	Tephra
150320-01F	Poutu	WP1	Desert Road	175.73384	-39.22060	Tephra
150321-01A	RT3 lower orange brown lapilli layer	WP14	Rotoaira Road	175.75290	-39.07965	Tephra
150321-01B	RT3 gray layer	WP14	Rotoaira Road	175.75290	-39.07965	Tephra
150321-01C	RT3 orange brown lapilli layer	WP14	Rotoaira Road	175.75290	-39.07965	Tephra
150321-01D	RT3 gray coarse ash and lapilli, including the laminated gray layer	WP14	Rotoaira Road	175.75290	-39.07965	Tephra
150321-01E	RT3 orange brown lapilli layer	WP14	Rotoaira Road	175.75290	-39.07965	Tephra
150321-02	Te Rato	WP14	Rotoaira Road	175.75290	-39.07965	Tephra
150421-01	Lower Te Maari, top most lava layer	WP15	Lower Te Maari Crater	175.67345	-39.10789	Lava Flow
150421-02	altered outcrop, thermal area	WP18	Upper Te Maari Crater area	175.67125	-39.10898	Lava Flow
150424-01	Oturere lava flow	WP22	Oturere Valley	175.67155	-39.14675	Lava Flow
150829-01	Ngauruhoe lava flow, group 2, pre-Taupo	WP26	Mangatepopo Valley	175.61548	-39.14074	Lava Flow
150829-02	Ngauruhoe lava flow, group 5, post-Taupo	WP27	Mangatepopo Valley	175.61789	-39.14109	Lava Flow
150829-03	1st phase 1975 PF Ngauruhoe	WP28	Mangatepopo Valley	175.61765	-39.14295	Pyroclast (bomb)
1954	1954 Ngauruhoe lava flow					Lava Flow
160727-01	1500AD U Te Maari LF	WP29	near Ketetahi trail	175.65726	-39.08273	Lava Flow

Figure 1-8. Location of rock samples (circles) and fumaroles (balloons). Waypoints from Table 1-2 are shown.

2 Methods

2.1 Sample selection, collection and preparation

The samples are from deposits within the last 16 ka history of Tongariro Volcano, as also shown in Section 1.7.2. The selected period (16 ka, with detailed analysis on deposits from 10 ka) was constrained by a project goal to track a parental batch of magma in terms of ascent and chemical differentiation. A period of 16 ka is within a 30 ka time scale of magma differentiation in arcs, based on a study of Taal Volcano magmas using protactinium-radium isotopic data (Asmerom *et al.*, 2005). It is more likely that the samples for this study are within a single stage of magmatism for Tongariro. Older samples (>25 ka) may be from another differentiating system, as eruption rates and cone building episodes have maximum rates for different stages within the 275 ka history of Tongariro as shown in Hobden *et al.*, 1999.

The sampling of deposits within this period (16 ka) was limited by suitability of samples for the type of analysis used. Analysis for whole rock compositions by XRF and ICPMS, for example, requires at least 1.6 g of sample. Tephra that are too fine were not sampled, as individual clasts cannot be mixed for analysis. The duration of the study also limits the samples, as multiple analyses will be done on a single deposit. Only deposits with determined eruption age were sampled to put in eruptive history perspective the petrological interpretations.

It is necessary to sample both lava and pyroclastic deposits to determine if compositional differences influence the style of eruption. In the case where there are compositional differences due to differentiation originating from the manner of ascent or deposition, that is slow moving lava versus tephra from an explosive eruption, this can be evaluated from interpretation of data. For a closed system ascent from a single magma chamber, magma erupted as lava flow and magma explosively erupted as tephra should have similar

compositions. The 2000 eruption of Mayon Volcano, for example, produced tephra and lava flows with similar major element bulk composition (Arpa *et al.*, 2006).

The samples were selected to represent strombolian eruptions from Red Crater and Te Maari, vulcanian eruptions from Ngauruhoe, and Plinian eruptions that deposited the Mangamate tephra and Rotoaira Lapilli units. **Figure 2-1** shows photos of some of the sampled deposits and deposit label, and **Figure 2-2** shows a composite log of Mangamate Tephra Formation outcrops along Desert Road (WP1 in **Table 1-2)**. Sampling of coarse grained pyroclastic deposits requires collection of individual juvenile clasts within the unit; minimum of 10 if the pyroclasts are heterogenous, fewer if they appear to be compositionally similar. The samples from Ngauruhoe (with more detailed analysis) are cauliflower bombs from the 1st phase of the 1975 eruption, and lapilli to bomb size (1-3 cm, >6cm outsized clast) pre-1717 cal. yrs. BP tephra. Clasts from Mangamate Tephra units that are at least 1 g were analysed for bulk major element composition by XRF. The analysed clasts are about 1-3 cm in size, **Figure 2-3** shows selected clasts for analysis. Additional analyses were done for Te Rato (EPMA) and Wharepu (EPMA, FTIR) members. Lapilli size clasts from Te Rato are banded and vesiculated, and Wharepu clasts are finely vesiculated and containing lighter coloured more vesiculated bands. Rotoaira Lapilli (1-4.5 cm) are finely to coarsely vesiculated pumices. Most of the Rotoaira Lapilli clasts are too altered to give acceptable values for bulk analysis by XRF, but the stratigraphic log (**Figure 2-4**) is presented here to serve as reference to the archived samples and thin sections.

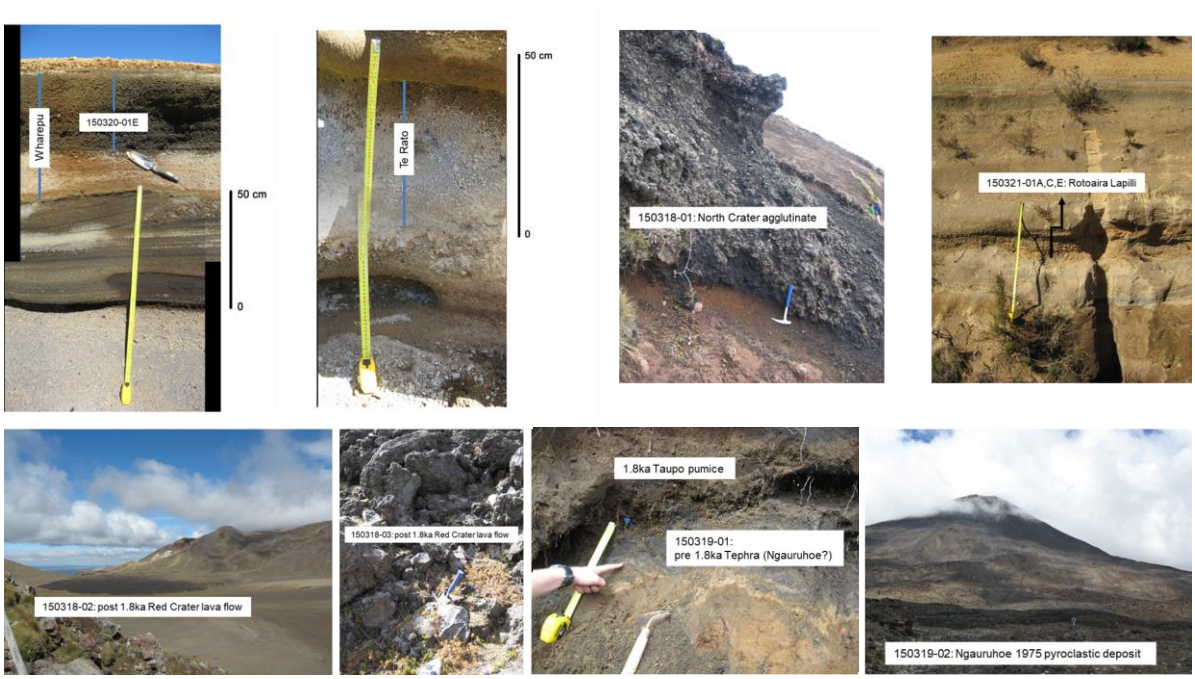

Figure 2-1. Photo documentation of some samples for this study.

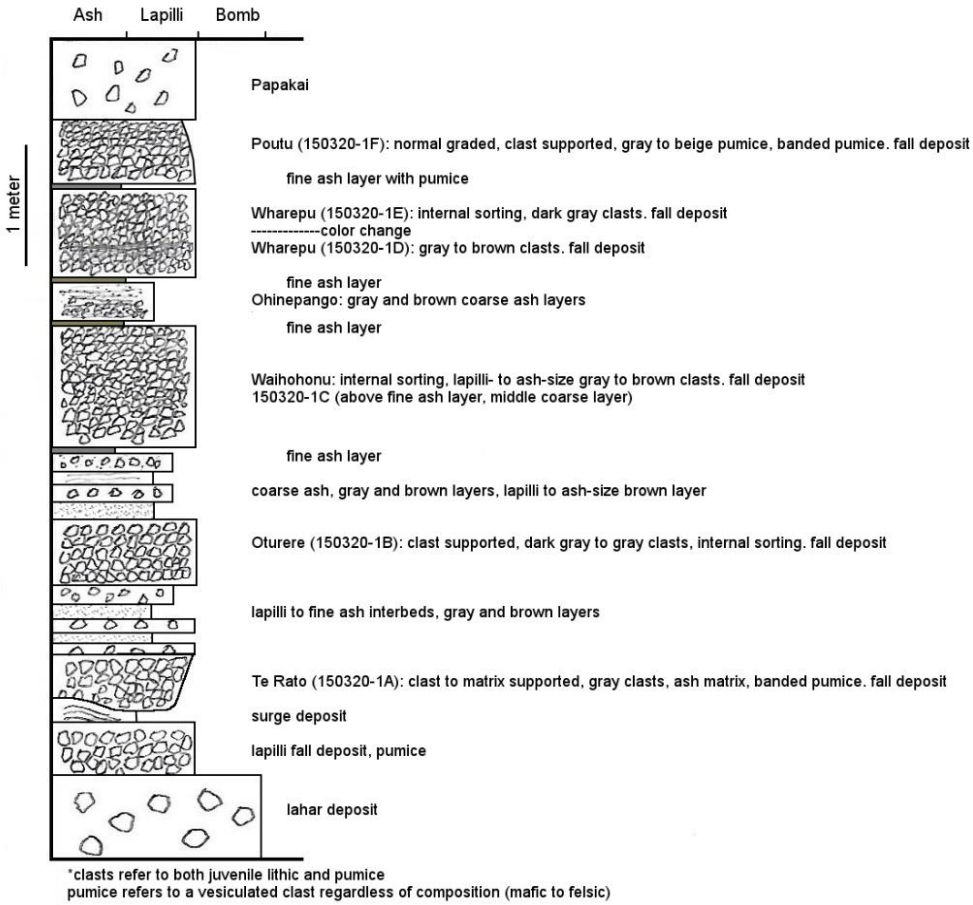

Figure 2-2. Composite log of Mangamate Tephra Formation outcrops along Desert Road (WP1 in Table 1-2). Sample numbers are shown.

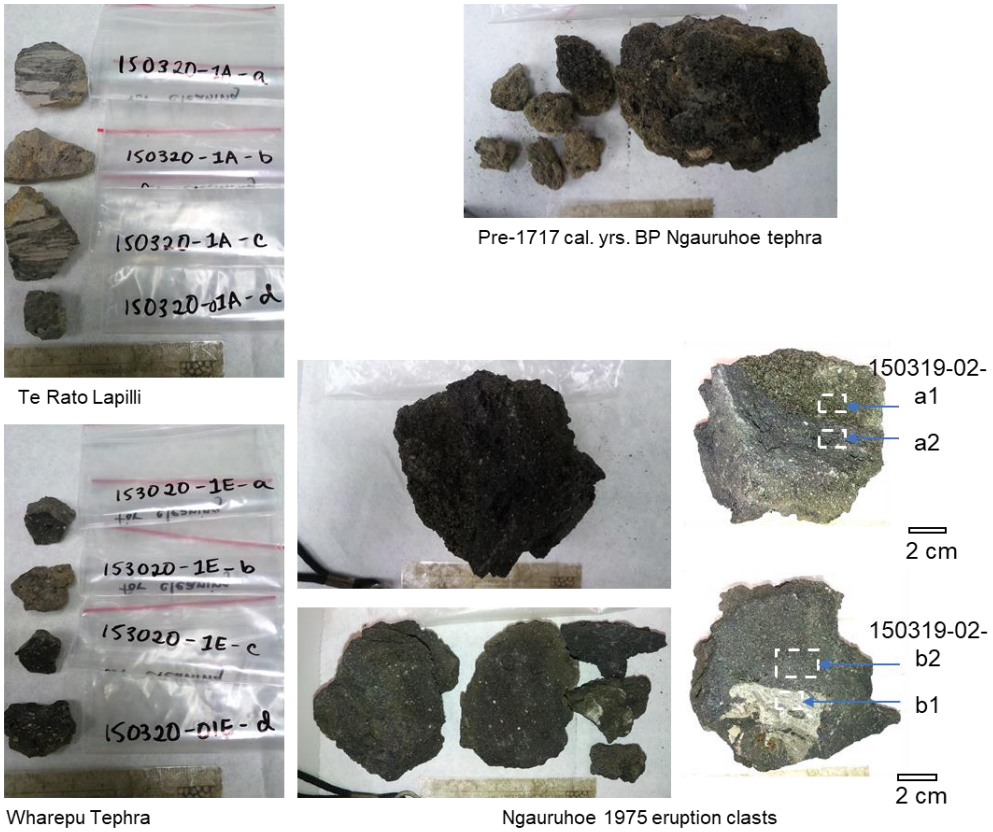

Figure 2-3. Photos of selected clasts before sample preparation (cutting and cleaning). Note, scale in each picture.

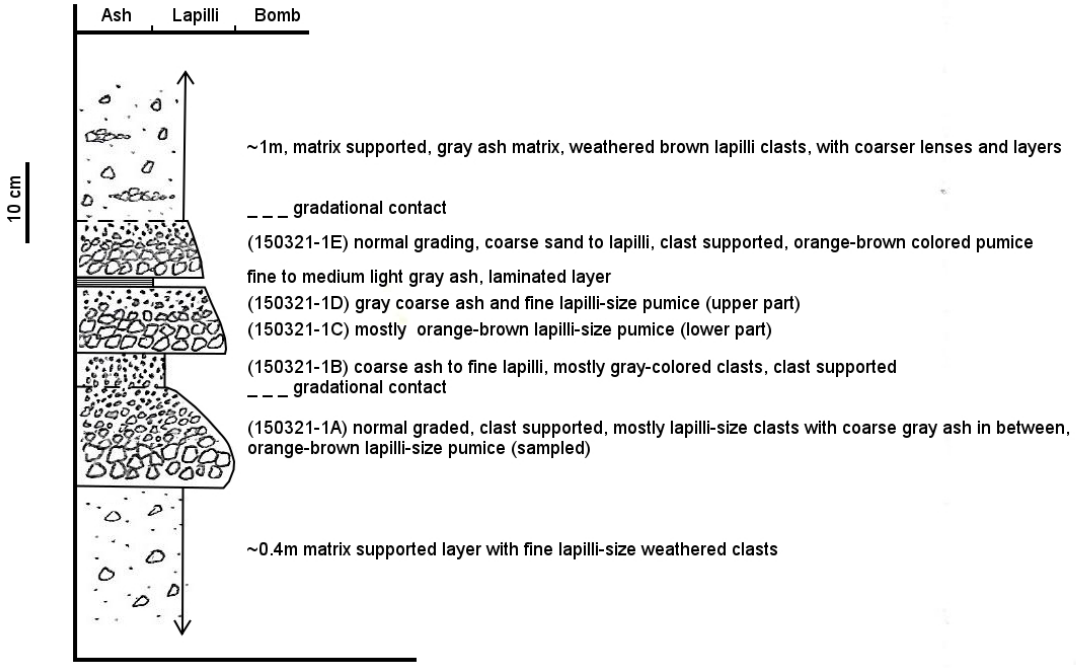

Figure 2-4. Stratigraphic log for samples from the Rotoaira Lapilli Formation outcrop along Rotoaira Road (WP14 in Table 1-2). Sample numbers are shown.

A complete list of samples collected for this study is found in **Appendix Table 1**. Each sample is subsampled for different types of sample preparation and analysis. The main sample would be labelled the date of collection and sample number (starting with 01). A single deposit sampled at different dates will have different labels. Subsamples of the same whole rock will have the same labels. Single pyroclast bomb or lapillus from the same deposit have an additional alphabet label. The main sample labels will be augmented with component label, mineral abbreviation and other descriptive terms for mineral, groundmass, glass and melt inclusion analyses. This form of labelling for the rock samples is used in all the text.

2.1.1 Sample preparation: rock

Rock samples had to be powdered for whole rock major and trace element analysis (fine powder) and whole rock oxygen and hydrogen isotope composition analysis (coarse powder). The sample powders were prepared at the Soil and Earth Sciences laboratory at Massey University. The lava samples were cut into smaller blocks and passed through a jaw crusher or stainless steel mortar and pestle to break into smaller pieces. For the lapilli-size tephra layers of the Mangamate Formation, single clasts from each juvenile population were picked for bulk analysis. Individual clasts were analysed for bulk compositions, combining small clasts for bulk composition analysis was not done. All samples, before final crushing, were cleaned by ultrasonic bath in tap water followed by reverse osmosis (RO) water. Samples that passed through the rock cutters were additionally cleaned by ultrasonic bath in ethanol to remove cutter lubricants. The samples were dried before crushing. Rock powders were made by hand crushing pumice and softer rock samples in agate mortar and pestle. Harder rock samples were powdered using a mechanical Tungsten Carbide ring grinder. The grinding containers were cleaned with water then wiped with ethanol after each sample. Standard powders were passed through the Tungsten Carbide mill after processing of a sample set to test for contamination.

2.1.2 Petrography

Thin (30 micron) and thick (100 micron) sections of rock slabs and lapilli-size pyroclasts for petrographic and microprobe analysis were done at the Mineral Services – Thin Sections Laboratory, National Isotope Centre, GNS Science, Lower Hutt. The thin sections were used for petrographic analysis. Textural and component characteristics have implications on petrogenesis. The thin sections were used to identify and describe component and groundmass characteristics and proportions for each sample. Initial observation of rock samples in thin section also aided in selecting ideal samples for melt inclusion studies. Both thin and thick sections were used for major element microprobe analysis.

2.2 Analytical methods and data presentation

2.2.1 Whole rock major and trace element chemistry

The sample powders were sent for major element whole rock analysis at the wavelength dispersive (WD) X-ray fluorescence spectrometer (XRF) PANalytical AXIOS^{max} laboratory at the Department of Earth Sciences, National Taiwan Normal University (NTNU). The samples were dried at 110˚C and were heated to 900˚C to determine loss on ignition (LOI). Fused glass beads were prepared from oxidized samples and Lithium Metaborate ($LiBO_2$) flux at a ratio of 1:10 for a 0.6 g sample using a Claisse M4 fluxer. Trace element compositions were determined by Inductively Coupled Plasma Mass Spectrometer (ICPMS) on dissolved samples at National Taiwan University (NTU). Additional major and trace element analysis was done at the X-Ray Centre at the University of Auckland using PANalytical Axios 1kW X-ray fluorescence spectrometer. The complete major and trace element data with standard reference values are shown in **Appendix Table 2 and 3**. Comparison of Ti values determined by XRF and ICPMS, and weathered samples excluded from interpretation are shown in **Figure 2-5**.

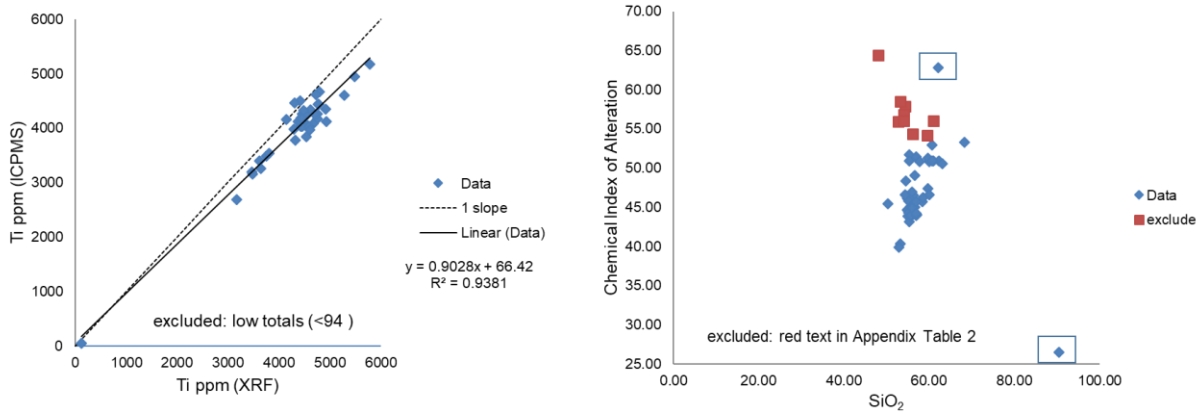

Figure 2-5. Agreement between Ti values determined by XRF and ICPMS. Exclusion of weathered samples is based on major element totals (<94) and high values for Chemical Index of Alteration, molar CIA=([Al_2O_3]/[CaO+K_2O+Na_2O])*100. Boxed points are xenoliths.

2.2.2 Whole rock FeO and Fe_2O_3 determination

FeO and Fe_2O_3 determination on bulk rock samples used a method modified from Maxwell (1968) as stated in the Laboratory Handbook of Petrographic Techniques (Hutchison, 1973). Four samples were analysed, 3 of them from the 1500 A.D. Te Maari lava flow (160727-01a-c) and one from the c. 1717 cal. yrs. B.P. Ngauruhoe tephra (150319-01-e). Sample 160727-01-a was ground to between 80-60 mesh in agate mortar and pestle while the rest of the samples were ground to finer powder by both agate and ceramic mortar and pestle. The method determines the wt. % FeO by titration provided total Fe in the sample is known. Total Fe is from whole rock XRF analysis.

A measured amount of powdered sample (0.5 g) was placed in a Pt crucible with water and H_2SO_4 to decompose the carbonates. The sample was then dissolved by a mixture of concentrated H_2SO_4 and HF heated over a low flame Bunsen. A second Bunsen was used to brush the sides and cover of the Pt crucible with a flame until the solution gently boils for about 10 minutes. The crucible and cover and its contents were then quickly submerged in a solution of boric acid, H_2SO_4 and H_3PO_4. The solutions were mixed carefully. The boric acid is for

neutralizing the unreacted HF and the H_3PO_4 is to react with Fe_2O_3 in the sample before titaration. This solution, with 0.2% barium diphenylamine sulfonate as indicator, was then immediately titrated with 0.1 N $K_2Cr_2O_7$ to the first appearance of permanent blue-violet color. The K_2Cr2O_7 reacts with FeO and H_2SO_4 to oxidize Fe. This experiment was done at the National Isotope Centre, GNS Science, Lower Hutt. The results of the experiment are shown in **Figure 2-6** and **Appendix Table 4**.

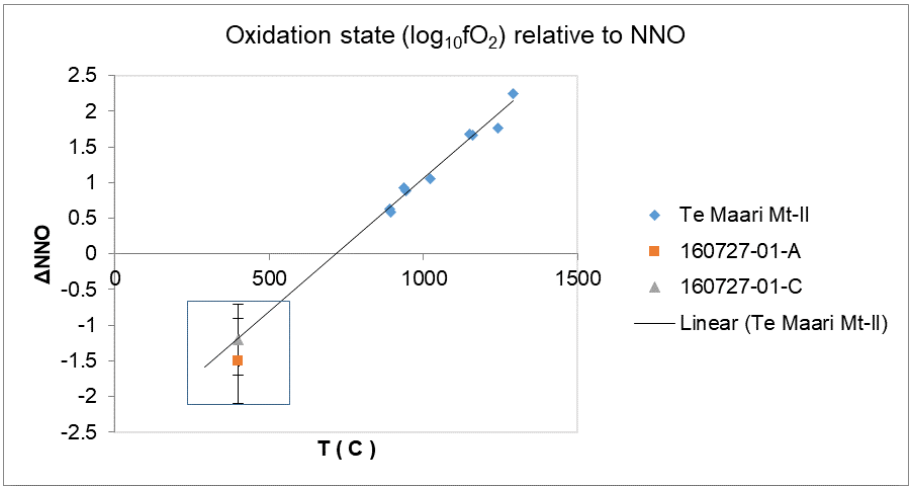

Figure 2-6. Results of whole rock FeO and Fe_2O_3 determination presented as redox buffer relative to NNO (Carmichael and Ghiorso, 1986, Kress and Carmichael, 1991), a temperature of 400°C was assigned to the whole rock samples. Magnetite-Ilmenite (Mt-Il) thermometer is from Ghiorso and Evans, 2008.

2.2.3 Whole rock isotope chemistry

Coarse powders of whole rock for Oxygen and hydrogen isotopic compositions analyses were sent to the Stable Isotope laboratory, Department of Geological Sciences, University of Cape Town. Analyses were done by conventional vacuum extraction line using ClF_3 as the reagent (Harris and Erlank, 1992). The samples were dried in vacuum at 200°C and melted using a propane torch to turn all the H in the sample into H_2O (C. Harris personal communications).

The standards Serina Kao, pure kaolinite from Serina mine near Cape Town with δD value of -57 (Harris et al., 1999) and 2 water standards (CTMP2010 and RMW) were used for the δD analysis. Corrections were done on raw data relative to the standard values. Raw and corrected data were provided by the laboratory (**Appendix Table 5**).

Fine powders of whole rock for analysis of Sr ($^{87}Sr/^{86}Sr$), Nd ($^{143}Nd/^{144}Nd$) and Pb ($^{208}Pb/^{204}Pb$, $^{207}Pb/^{204}Pb$, $^{206}Pb/^{204}Pb$) isotopes were sent to the College of Engineering and Physical Sciences, University of New Hampshire. Sample preparations were done in UNH clean lab with class 10,000 general spaces and class 1,000 workstations. Isotopes of Sr, Nd and Pb were analysed by Nu plasma II-ES multicollector inductively coupled plasma mass spectrometer. The data were bracket-corrected using standards: NIST SRM 987 and JNdi. Additional correction for within-instrument fractionation was done on Pb isotopic data using a Tl solution. Data and standard analysis are listed in **Appendix Table 6**.

2.2.4 Mineral and groundmass chemistry

Mineral, microlitic groundmass and glass groundmass were analysed on thick and thin sections quantitatively by electron microprobe and qualitatively by scanning electron microscope. Electron microprobe analysis for major element compositions were done using a JEOL JXA-8230 Electron Probe Micro-Analyzer (EPMA) equipped with 5 wavelength dispersive X-ray spectrometers (WDS) at the School of Geography, Environment and Earth Sciences, Victoria University of Wellington. Details of the analysis are also stated in Section 3.

Major element oxides analysed in the essential mineral phases (plagioclase, pyroxene, olivine, and Fe-Ti oxides) and groundmass are SiO_2, TiO_2, Al_2O_3, FeO, MnO and MgO. CaO and Na_2O were additionally analysed in the silicate minerals and groundmass and K_2O was also analysed in plagioclase, clinopyroxene and groundmass. The mafic silicates, Fe-Ti oxides and groundmass had an additional analysis for Cr_2O_3. NiO_2 was analysed in the pyroxene and

olivine crystals. SrO was analysed in some plagioclase crystals. Cl, SO_3 and in some cases P_2O_5 and F were analysed in the microlitic and aphyric groundmass. The complete microprobe data is listed in **Appendix Table 7**. Mineral and glass standards were analysed before and after each sample analysis. A list of the standard analysis for all the different sample sets are in **Appendix Table 8**. The table shows average values, standard deviations and reference values for the standards. Microprobe analytical conditions for each analysed phase are listed in **Appendix Table 9**. Minerals were analysed using a focused beam of 1 micron spot size at an accelerating potential of 15 kV and a beam current of 12 nA. Groundmass was analysed using a defocused beam with a spot size that varied from 5 to 25 μm and beam current of 8 nA. A spot size of 5 to10 μm were used for aphyric groundmass and 10 to 25 μm were used for microlitic groundmass. Majority of groundmass analysis were done using 10 μm spot size. Peak counting time was 30 to 15 seconds for all oxides.

Sample and area selection on the microprobe were aided by backscattered electron images. Images were taken for photo reference. Backscattered electron images were also taken at the Manawatu Microscopy and Imaging Centre, Massey University using a FEI Quanta 200 Environmental Scanning Electron Microscope (SEM) with EDAX module.

2.2.5 Melt inclusion chemistry from microprobe and FTIR

Melt inclusions were selected from olivine and pyroxene host crystals. The samples were ground using stainless steel mortar and pestle and sieved through 35, 45 and 60 mesh. Olivine and pyroxene crystals were then picked from the grains retained in the 45 mesh (<500 μm, >355 μm size). Melt inclusions were observed from crystals in immersion oil (n=1.6570). The unexposed melt inclusions were photographed and described. The oil was then cleaned from the crystals using acetone.

Olivine crystals from 3 samples (150320-01e-a, 150319-02-a2, 160727-01-c) containing partially crystallized melt inclusions and uncrystallised melt inclusions with bubble were sent to the School of Earth Sciences, University of Tasmania for melt inclusion homogenization. Melt inclusions in these grains contained boundary crystals and possible shrinkage bubble. The olivine grains were mixed with a carbon-alumina powder and placed inside a small platinum cylinder. The powder mixture prevents grain accretion and oxidation of olivine. The capsule was then placed in a custom made vertical heating stage. All samples were heated for 2 minutes at 1140 ± 3 °C for sample 150320-01e-a, 1145 ± 3 °C for sample 150319-02-a2, and 1270 ± 3 °C for sample 160727-01-c. The homogenization temperatures were based on olivine-liquid thermometer (Putirka, 2008).

Melt inclusion exposure procedure was done after the FTIR analysis manual at Massey University. The mineral grains were held by crystal bond and double polished on glass slides. The final polish was done on a 1 μm polishing film. Observation of interference colors on petrographic microscope provided initial estimation of wafer thickness before quantitative thickness measurement.

Determination of water content and CO_2 as carbonate in melt inclusions was done on a Nicolet Continuum FTIR (Fourier Transform Infrared) microscope at the Institute of Agriculture and Environment, Massey University in Palmerston North. Total water was measured from the maximum height of the broad absorbance at 3550-3535 cm^{-1} and molecular water from the absorbance at 1630 cm^{-1} wavenumber. Carbonate absorbance was at 1515 and 1430 cm^{-1} and the absorbance heights were averaged (**Figure 2-7**). Background spectra were taken on NaCl and Au disks for transmission and reflectance measurements, respectively before each analysis set. Samples were placed on the NaCl disk for absorbance and reflectance measurements. The thickness for each wafer was determined from interference fringes on reflection spectra.

Collection of spectra, background subtraction and measurements of absorbance heights from baseline were done through OMNIC software provided with the instrument.

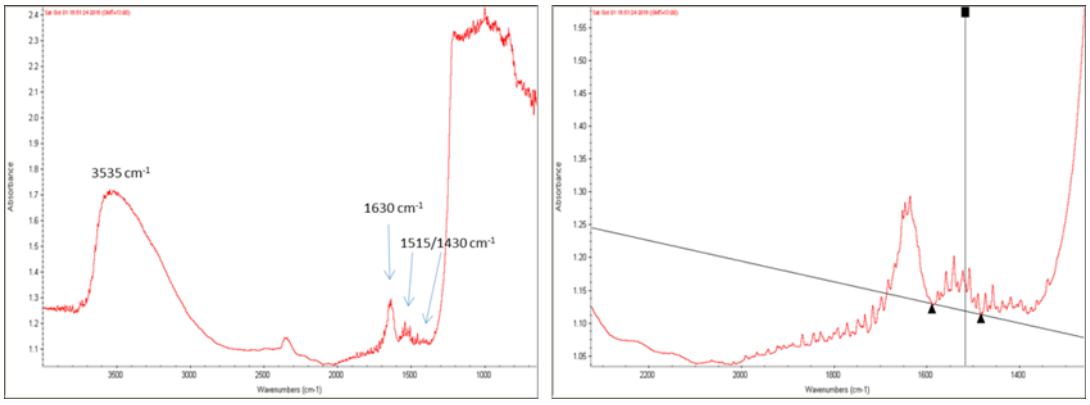

Figure 2-7. Sample spectra for a measurement of melt inclusion by FTIR. Labelled peaks are for total water (3550-3535cm^{-1}), molecular water (1630cm^{-1}) and carbonate (1515 and 1430cm^{-1}). To the left is a narrower band to illustrate peak measurement at 1515cm^{-1}.

Total water as OH and molecular H_2O, molecular H_2O and CO_2 concentrations were calculated using the Beer-Lambert equation:

$$C = {M.W.\times Abs}/{\epsilon\times \rho \times d}$$

Where: C=concentration in weight fraction, M.W.=molecular weight of substance being measured, Abs=intensity of the absorbance (measured height from baseline), ϵ=extinction coefficient (L/mol*cm), ρ=density of the glass (g/L), d=thickness of the sample or path length (cm)

Glass density at room temperature and pressure were calculated using the total mass contribution from constituents in the glass and total volume of constituents considering volume change from 1673 K to 293 K after the method of Thomas Platz provided in the FTIR manual spreadsheet. The parameters used for the density calculations included melt glass (melt

inclusion) composition from microprobe analysis and thermodynamic constants (change in partial molar volume for an increment of T and P) at 1673 K and 1 bar.

Sample wafer thickness or the light path length used for the Beer-Lambert equation was determined using values derived from reflectance spectra for the equation:

$$t = {}^{m}/_{2n(v1 - v2)}$$

Where: t=thickness of the area analysed (cm), m=the number of waves within a selected interval of wavenumbers, v1 and v2=the highest and lowest wavenumbers defining the interval, n=the refractive index of the material (**Figure 2-8**).

The refractive index ranged from 1.49 to 1.60 depending on the silica content of the glass. The absorbance spectra are masked by the reflectance spectra if the wafer is too thin (**Figure 2-8**). In this case, reading the smaller peaks is difficult and sometimes though a signal peak is apparent it is not read.

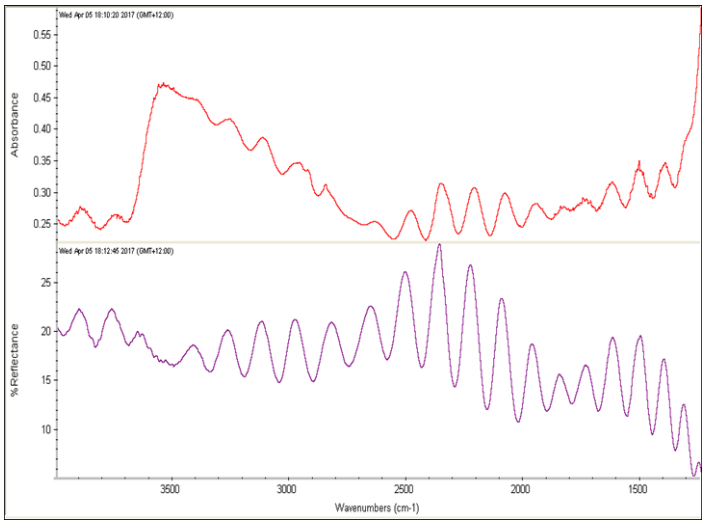

Figure 2-8. Absorbance and reflectance spectra for a very thin wafer where the reflectance signal affects the absorbance signal.

The extinction coefficients (ϵ) used are from literature and are empirical values established from experiments and actual samples (Newman *et al.*, 1986, Dixon *et al.*, 1988, Dixon *et al.*, 1995, Hauri *et al.*, 2002, Mandeville *et al.*, 2002). Different extinction coefficient values for the 3550cm^{-1} and 1630cm^{-1} wavenumbers were used for basalt (Dixon *et al.*, 1988, Dixon *et al.*, 1995), andesite (Mandeville *et al.*, 2002) and rhyolite compositions (Newman *et al.*, 1986, Hauri *et al.*, 2002). The silica values used as range compositions only for the selection here of ϵ (for the Beer-Lambert equation) are: 50-56 wt.% (basalt), 57-65 wt.% (andesite) and >65 wt.% (rhyolite). The extinction coefficients used for the different samples are listed in **Appendix Table 10**. It was shown that ϵ varies linearly with the cation sum Si^{4+} and Al^{4+} (Dixon *et al.*, 1995). **Figure 2-9** shows the ϵ (1630cm^{-1}) versus Si^{4+} +Al^{3+} of standards with the ϵ (1630cm^{-1}) used for the samples and actual sample Si^{4+} +Al^{3+} to show the appropriateness of the chosen constants for the water concentration calculations in this study.

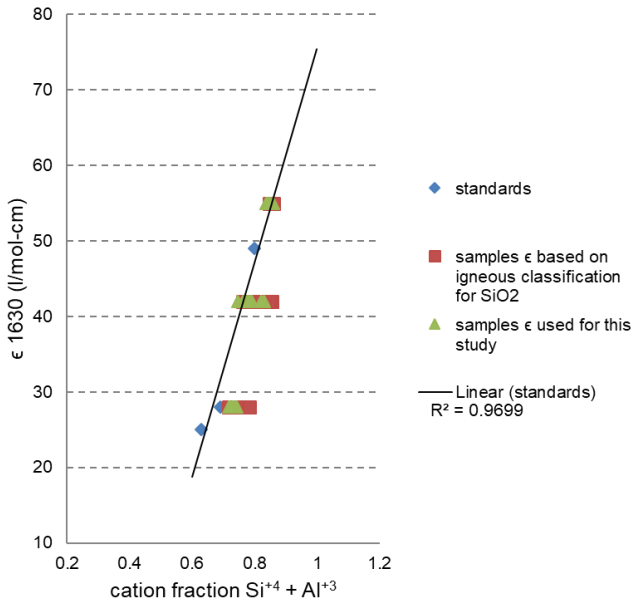

Figure 2-9. Extinction coefficients (ϵ) used for the samples based on the trend established by standards (Dixon *et al.*, 1995).

2.2.6 Melt inclusion data errors and proxy compositions

The error for water measurement using the FTIR technique was estimated to be 15% of determined values (Fine and Stolper, 1985). Repeat measurements on selected melt inclusions were done to see if differences in results are within 15% of the highest value. These repeat measurements were done on some melt inclusions that are large (~50 μm) and show significant target intensities in the spectra. In general, melt inclusions range in the longest diameter from 100 to 20 μm. The resulting spectra from the FTIR when the beam size is smaller than 20 μm is, most of the time, unreadable due to a weak interferogram. Repeat measurements on different wafer thickness and different beam sizes were possible on one melt inclusion from a Wharepu tephra olivine. Wharepu tephra melt inclusions have problems with oversaturated intensities for total water (intensity heights being greater than 1). One melt inclusion weathered grinding to a thinner wafer and measurements were done at 4 different thicknesses. It was also large enough (~100 microns) for the IR beam size to be varied significantly (**Figure 2-10**). The results of the measurements are shown in **Table 2-1**. The first intensities for total water ($3535cm^{-1}$) are oversaturated (> 1) but plotting intensity height versus thickness follows Beer's law and shows good correlation, R^2=0.8875 (**Figure 2-11**). The correlation is better (R^2=0.9903) if smaller beam size results are excluded. For the wafer at 21 μm thickness, the difference between the results of the smaller and larger beam size analysis is 21% of the smaller value. For the wafer at 13 μm thickness the difference between the results of the smaller and larger beam size analysis is 16% of the smaller value. One standard deviation for total water analysis on this melt inclusion (150320-01e-m-mi-ol1-1) is 0.87 wt.%, and is 13% of the largest value and 20% of the smallest value. This study will use an error of 1 standard deviation from the mean value of grouped melt inclusions. As an example, melt inclusions in Wharepu tephra olivines with measured absorbance height and thickness that plot close to the established trend for (150320-01e-m-mi-ol1-1) (**Figure 2-11**) are grouped together and will be plotted with an

error of ± 0.89 wt.% or 1 standard deviation. The error values shown here are close to the error of 15% of the measured value established from the FTIR experiments of Fine and Stolper 1985. Grouping per deposit will be based on mineral host (olivine or pyroxene), whether the host minerals are xenocrysts or in equilibrium with the sample based on equilibrium criteria discussed in Section 2.4.1, and finally whether it follows Beer's law, that is absorbance intensity should increase with thickness at good correlation. For melt inclusions that cannot be grouped, error will be set at 20% of the measured value.

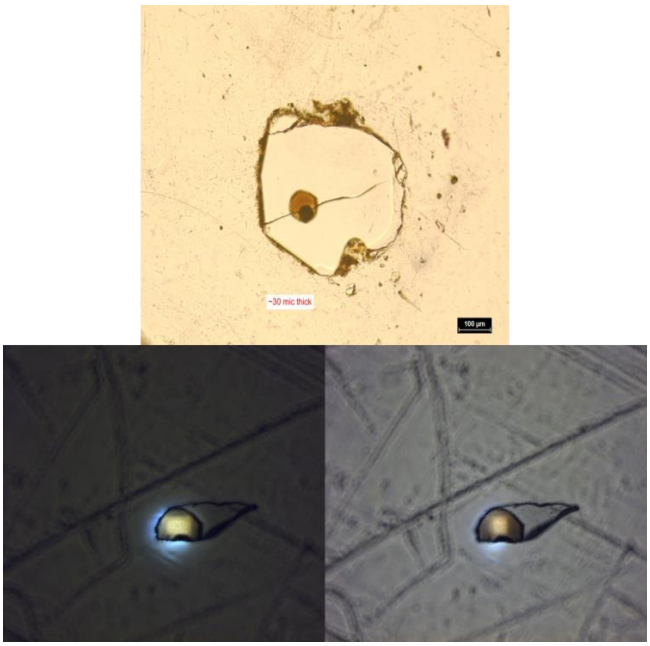

Figure 2-10. Sample 150320-01E-m-mi-ol1-1 (melt inclusion). Photos below are the same melt inclusion in a thinner wafer. Note the position and size of the IR beam.

Table 2-1. Results for one melt inclusion (150320-01E-m-mi-ol1-1) at different thickness and IR beam size (A). Results for melt inclusions grouped based on correlation with the trend established by MI: 150320-01E-m-mi-ol1-1 (B).

A.

		absorbance			wt.%		ppm	
	(μm)	H_2Ot	H_2Omol					
320-01E-m-mi-ol1	**thickness**	**3535 cm^{-1}**	**1630 cm^{-1}**	**H_2Ot**	**H_2Omol**	**OH^-**	**CO_2**	
150320-01e-m-mi-ol1-1a	34	1.568	0.713	4.75	4.86	-0.11	629	
150320-01e-m-mi-ol1-1b	27	1.278	0.537	4.84	4.58	0.26	568	
150320-01e-m-mi-ol1-1c	20	0.841	0.465	4.28	5.32	-1.04	470	smaller beam size
150320-01e-m-mi-ol1-1c2	21	1.115	0.571	5.58	6.43	-0.85	NM	
150320-01e-m-mi-ol1-1d1	13	0.869	0.352	6.70	6.10	0.59	364	
150320-01e-m-mi-ol1-1d2	15	0.815	0.306	5.76	4.87	0.89	NM	smaller beam size
Mean				**5.32**				
1 standard deviation				**0.87**				

*NM: not measured

B.

320-01E olivine group 1								
150320-01e-a-mi-ol4-01	36	1.730	0.7010	4.91	4.47	0.43	0	
150320-01e-a-mi-ol5-01	45	1.597	0.7970	3.63	4.08	-0.45	219	
150320-01e-a-mi-ol7-01	22	1.035	0.4530	4.81	4.73	0.07	229	
150320-01e-m-mi-ol1-1a	34	1.568	0.713	4.75	4.86	-0.11	629	
150320-01e-m-mi-ol1-1b	27	1.278	0.537	4.84	4.58	0.26	568	
150320-01e-m-mi-ol1-1c	20	0.841	0.465	4.28	5.32	-1.04	470	
150320-01e-m-mi-ol1-1c2	21	1.115	0.571	5.58	6.43	-0.85	0	
150320-01e-m-mi-ol1-1d1	13	0.869	0.352	6.70	6.10	0.59	364	
150320-01e-m-mi-ol1-1d2	15	0.815	0.306	5.76	4.87	0.89	0	
150320-01e-m-mi-ol2-1	21	0.819	0.346	4.09	3.89	0.20	133	
Mean				4.93				
1 standard deviation				0.89				

*in red have absorbance height of more than 1

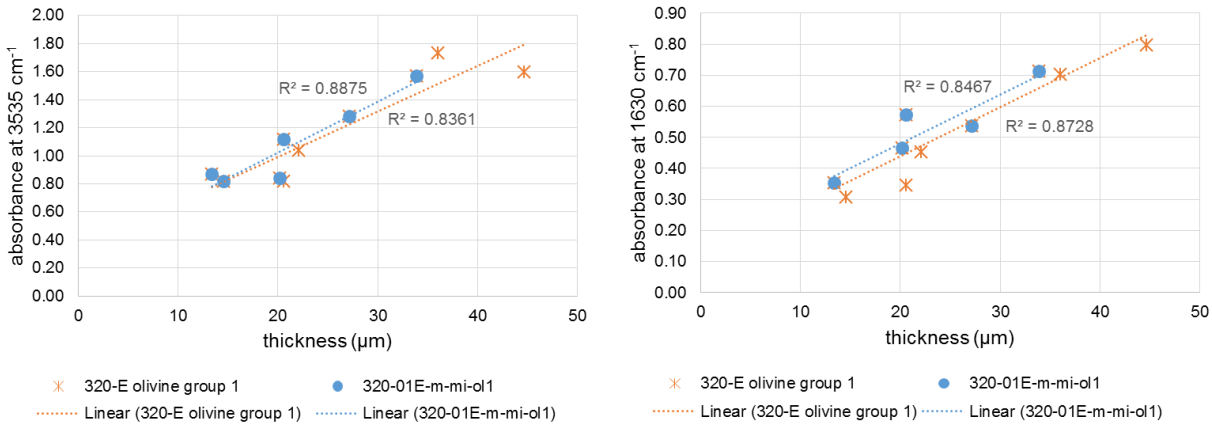

Figure 2-11. Absorbance versus thickness for the melt inclusion in 150320-01E-m-mi-ol1 and melt inclusions in olivine grouped for sample 150320-01E.

The concentration of OH was determined from subtracting molecular water from the total water concentration. Equilibrium trends between OH and molecular H_2O were checked using the equations of Stolper (1982). Some melt inclusions contained high molecular H_2O and does not follow equilibrium distribution for the water species (Stolper, 1982). The values, however, may be representative of the samples and this will be further discussed in Section 4. Molecular water concentrations decreased significantly after homogenization for the samples from Te Maari 1500 A.D. lava flow.

Major elements including Cl and SO_3 were determined for melt inclusions from electron microprobe analysis using the same procedure for groundmass analysis. The crystal wafers were first analysed by FTIR then these were set in epoxide and carbon coated for the microprobe analysis. Some crystal wafers were lost during the sample preparation for microprobe, during grinding to thinner wafers or from handling. This can be seen in the data where melt inclusions have water composition but are without major element, Cl and S compositions. Melt inclusion major element composition is the basis for density, refractive index of the material and choosing extinction coefficients; variables needed in the equations for determining H_2O and CO_2 concentrations by FTIR. The glass density was determined for

the lost melt inclusion wafers by using averaged compositions from melt inclusions with analysis for a specific deposit and host type (**Figure 2-12**). These compositions are referred to here as proxy compositions. Proxy compositions are the average of 4 points having extreme Mg#, SiO_2 and total alkalis ($Na_2O + K_2O$) compositions. **Table 2-2** shows the total number of melt inclusions analysed by FTIR and samples with and without major element analysis, results are listed in **Appendix Table 10**. Water concentrations computed using proxy compositions will be considered but will be noted in the diagrams and treated with caution.

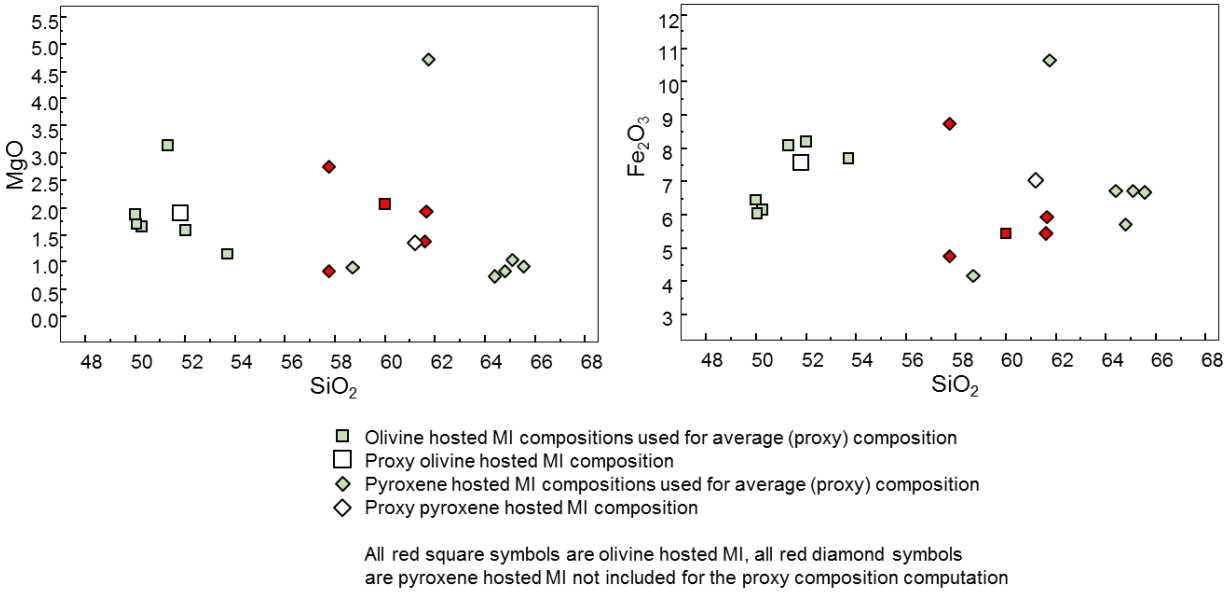

Figure 2-12. Example of MI proxy compositions and actual melt inclusion compositions used to compute the proxies. Proxy compositions are the average of 4 melt inclusion compositions that may represent extreme values, some melt inclusions have repeat analyses (clustered points in the plots). Compositions that deviate too much from the other points, such as the one point for the olivine hosted MI, are not considered.

Table 2-2. Total number of melt inclusion analysis for the different deposits.

Deposits	150319-02	150319-01	150318-03	150320-01E	160727-01-C
MI with FTIR and microprobe analyses	22	5	4	12	22
MI with FTIR only (proxy composition used)*	8	1	0	10	6
Total points	**30**	**6**	**4**	**22**	**28**

*mineral wafer was lost during processing and no microprobe analysis was done, proxy composition was used for density and absorbance coefficient selection

2.3 Data modelling

2.3.1 Equilibrium determination

The thermobarometry models require mineral and melt compositions that are in equilibrium. A groundmass composition, representing liquid composition (Cl), is paired with a mineral composition (Cm) to satisfy a known Kd ($Kd_i = Cm_i/Cl_i$) for a specific element (i). Melt-plagioclase equilibrium was determined from $Kd^{Ca\text{-}Na}$ and $Kd(An\text{-}Ab)^{pl\text{-}liq}$. Experimentally determined $Kd^{Ca\text{-}Na}$ $((X^{pl}_{Ca}/X^{pl}_{Na})/(X^{liq}_{Ca}/X^{liq}_{Na}))$ was found to vary with melt water content (Sisson and Grove, 1993). It can go from 1 for dry melts to 5.5 for water saturated melts (Sisson and Grove, 1993). For the data set, a plagioclase was first assigned a liquid with a matching molar Ca/Na ratio based on $Kd^{Ca\text{-}Na}$ 1.7 to 2. The $Kd(An\text{-}Ab)^{pl\text{-}liq} = X^{pl}_{Ab}X^{liq}_{AlO1.5}X^{liq}_{CaO}/X^{pl}_{An}X^{liq}_{NaO0.5}X^{liq}_{SiO2}$ for the pair was then determined and compared to the required value of 0.27±0.11 to 0.10±0.11 for temperatures > 1050 (Putirka, 2008). Equilibrium between olivine and glass and orthopyroxene and glass were determined from Rhodes diagrams (Rhodes *et al.*, 1979, Putirka, 2008). $Kd(Fe\text{-}Mg)^{min\text{-}melt}$, defined as $(X^{melt}_{Mg}/X^{min}_{Mg})/(X^{melt}_{Fe2+}/X^{min}_{Fe2+})$, has a value of 0.3±0.03 ($Kd(Fe\text{-}Mg)^{ol\text{-}melt}$) for olivines,

0.29±0.06 for orthopyroxene Kd(Fe-Mg)$^{opx\text{-}liq}$, and 0.27±0.03 for clinopyroxenes Kd(Fe-Mg)$^{cpx\text{-}liq}$. This method is also described in Section 3.3.2.

2.3.2 Mineral thermobarometry

The following thermometers and barometers found in Putirka (2008) were used in this study. Standard error of estimate (SEE) is here shown for each model. All equations were derived from a basic thermodynamic equation describing equilibrium reactions for mineral transformations/reactions with melt: $- RT\ln K_{eq} = \Delta G_r$ (where: ΔGr = Gibbs free energy change of reaction; R = gas constant; K_{eq} = equilibrium constant; T = temperature). Substitution of thermodynamic variables and material properties (enthalpy, entropy, volume change, compressibility, thermal expansion) in terms of P and T required derivation of constants from regression equations. Regression constants were based on empirical data gathered from several isobaric experimental data. Regression models were chosen based on accuracy as calibrated from experimental data. Activity coefficients for components in a non-ideal system were considered and addressed by empirical data and activity models. Calculations of liquid and mineral components for input in the equations can be seen in the thermometer and barometer spreadsheets, and Putirka, 2008. Listed below are the relevant equations, please see the reference (Putirka, 2008) for complete explanation, all variable names and equation number.

- Olivine thermometer: equation 15 (SEE: ±60°C):

$$T(°C) = 815.3 + 265.5(Mg\#) + 15.37\left(MgO^{liq}\right) + 8.61\left(FeO^{liq}\right) + 6.646\left((Na_2O + K_2O)^{liq}\right) + 39.16\left(P(GPa)\right) - 12.83\left(H_2O^{liq}\right)$$

  and equation 22 (SEE: ±29°C):

$$T(°C) = \frac{15294.6 + 1318.8\,P(GPa) + 2.4834\left(P(GPa)\right)^2}{8.048 + 2.8352lnD_{Mg}^{ol/liq} + 2.097ln\left(1.5(C_{NM}^{L})\right) + 2.575ln\left(3C_{SiO_2}^{liq}\right) - 1.41NF + 0.222H_2O^{liq} + 0.5P(GPa)}$$

Equation 15 is based only on liquid composition and determines temperature for a liquid saturated with olivine. It is applicable for temperatures between 729-2000°C. Equation 22 is an olivine-melt thermometer and considers the water content of the melt.

- Orthopyroxene thermometer: equation 28a (SEE: ±41°C):

$$\frac{10^4}{T(°C)} = 4.07 - 0.329(P(GPa)) + 0.12\left(H_2O^{liq}\right) + 0.567\ln\left(\frac{X_{Fm_2Si_2O_6}^{opx}}{\left(X_{SiO_2}^{liq}\right)^2\left(X_{FeO}^{liq} + X_{MnO}^{liq} + X_{MgO}^{liq}\right)^2}\right) - 3.06\left(X_{MgO}^{liq}\right) - 6.17\left(X_{KO_{0.5}}^{liq}\right) + 1.89\left(Mg\#^{liq}\right) + 2.57\left(X_{Fe}^{opx}\right)$$

Equation 28a considers orthopyroxene and melt compositions for hydrous melts. It is applicable for temperatures from 750-1600°C.

- Orthopyroxene barometer: equation 29b (SEE: ±2.1 kbar):

$$P(kbar) = 1.788 + 0.0375T(°C) + 1.295\times10^{-3}T(°C)ln\left(\frac{X_{FmAl_2SiO_6}^{opx}}{X_{FmO}^{liq}\left(X_{AlO_{1.5}}^{liq}\right)^2 X_{SiO_2}^{liq}}\right) - 33.42\left(X_{AlO_{1.5}}^{liq}\right) + 9.795\left(Mg\#^{liq}\right) + 36.08\left(X_{NaO_{0.5}}^{liq} + X_{KO_{0.5}}^{liq}\right) + 0.784\left(H_2O^{liq}\right) - 26.2\left(X_{Si}^{opx}\right) + 14.21\left(X_{Fe}^{opx}\right)$$

Equation 29b is an orthopyroxene-melt based barometer for hydrous compositions.

- Clinopyroxene thermobarometers: equations 31 (SEE: ±2.9 kbar):

$$P(kbar) = -40.73 + 358\frac{T(K)}{10^4} + 21.69\frac{T(K)}{10^4}ln\left(\frac{X^{cpx}_{NaAlSi_2O_6}}{X^{liq}_{NaO_{0.5}}X^{liq}_{AlO_{1.5}}\left(X^{liq}_{SiO_2}\right)^2}\right)$$
$$- 105.7\left(X^{liq}_{CaO}\right) - 165.5\left(X^{liq}_{NaO_{0.5}} + X^{liq}_{KO_{0.5}}\right)^2$$
$$- 50.15\left(X^{liq}_{SiO_2}\right)\left(X^{liq}_{FeO} + X^{liq}_{MgO}\right) - 3.178ln\left(X^{cpx}_{DiHd}\right) - 2.205ln\left(X^{cpx}_{EnFs}\right)$$
$$+ 0.864ln\left(X^{cpx}_{Al}\right) + 0.3962\left(H_2O^{liq}\right)$$

32c (SEE: ±1.5 kbar):

$$P(kbar) = -57.9 + 0.0475T(K) - 40.6\left(X^{liq}_{FeO}\right) - 47.7\left(X^{cpx}_{CaTs}\right) + 0.676\left(H_2O^{liq}\right)$$
$$- 153\left(X^{liq}_{CaO_{0.5}}X^{liq}_{SiO_2}\right) + 6.89\left(\frac{X^{cpx}_{Al}}{X^{liq}_{AlO_{1.5}}}\right)$$

and 33 (SEE: ±42°C):

$$\frac{10^4}{T(K)} = 7.53 - 0.14ln\left(\frac{X^{cpx}_{Jd}X^{liq}_{CaO}X^{liq}_{Fm}}{X^{cpx}_{DiHd}X^{liq}_{Na}X^{liq}_{Al}}\right) + 0.07\left(H_2O^{liq}\right) - 14.9\left(X^{liq}_{CaO}X^{liq}_{SiO_2}\right)$$
$$- 0.08ln\left(X^{liq}_{TiO_2}\right) - 3.62\left(X^{liq}_{NaO_{0.5}} + X^{liq}_{KO_{0.5}}\right) - 1.1\left(Mg\#^{liq}\right)$$
$$- 0.18ln\left(X^{cpx}_{EnFs}\right) - 0.027P(kbar)$$

Putirka et al., 2003 thermobarometer (SEE: ±59°C):

$$\frac{10^4}{T(K)} = 4.60 - 4.37 \times 10^{-1}ln\left(\frac{Jd^{cpx}Ca^{liq}Fm^{liq}}{DiHd^{cpx}Na^{liq}Al^{liq}}\right) - 6.54 \times 10^{-1}ln\left(Mg^{liq}\right)$$
$$- 3.26 \times 10^{-1}ln\left(Na^{liq}\right) - 6.32 \times 10^{-3}\left(P(kbar)\right) - 0.92ln\left(Si^{liq}\right)$$
$$+ 2.74 \times 10^{-1}ln(Jd^{cpx})$$

All the thermobarometers are based on clinopyroxene and melt compositions and applicable for hydrous conditions.

- Plagioclase thermometer: equation 23 (SEE: ±43°C):

$$\frac{10^4}{T(K)} = 6.12 + 0.257ln\left(\frac{X_{An}^{pl}}{X_{CaO}^{liq}\left(X_{AlO_{1.5}}^{liq}\right)^2\left(X_{SiO_2}^{liq}\right)^2}\right) - 3.166\left(X_{CaO}^{liq}\right)$$

$$- 3.137\left(\frac{X_{AlO_{1.5}}^{liq}}{X_{AlO_{1.5}}^{liq} + X_{SiO_2}^{liq}}\right) + 1.216\left(X_{Ab}^{pl}\right)^2 - 2.475 \times 10^{-2}\left(P(kbar)\right)$$

$$+ 0.2166\left(H_2O^{liq}\right)$$

Equation 23 is a plagioclase-melt thermometer that considers H_2O in the melt phase.

- Plagioclase barometer: equation 25a (SEE: ±2.47 kbar):

$$P(kbar) = -42.2 + 4.94 \times 10^{-2}T(K) + 1.16 \times 10^{-2}T(K)ln\left(\frac{X_{Ab}^{pl}X_{AlO_{1.5}}^{liq}X_{CaO}^{liq}}{X_{An}^{pl}X_{NaO_{0.5}}^{liq}X_{SiO_2}^{liq}}\right)$$

$$- 382.3\left(X_{SiO_2}^{liq}\right)^2 + 514.2\left(X_{SiO_2}^{liq}\right)^3 - 19.6ln\left(X_{Ab}^{pl}\right) - 139.8\left(X_{CaO}^{liq}\right)$$

$$+ 287.2\left(X_{NaO_{0.5}}^{liq}\right) + 163.9\left(X_{KO_{0.5}}^{liq}\right)$$

Equation 25a considers the exchange between anorthite and albite in plagioclase and melt compositions.

- Plagioclase hygrometer: equation 25b (SEE: ±1.1 wt.%)

$$H_2O(wt\%) = 25.95 - 0.0032T(℃)ln\left(\frac{X_{An}^{pl}}{X_{CaO}^{liq}\left(X_{AlO_{1.5}}^{liq}\right)^2\left(X_{SiO_2}^{liq}\right)^2}\right) - 18.9\left(X_{KO_{0.5}}^{liq}\right)$$

$$+ 14.5\left(X_{MgO}^{liq}\right) - 40.3\left(X_{CaO}^{liq}\right) + 5.7\left(X_{An}^{pl}\right)^2 + 0.108P(kbar)$$

Equation 25b uses plagioclase-melt composition, temperature and pressure to determine melt H_2O content.

The thermobarometer equations have a temperature component for the barometer and a pressure component for the thermometer (Putirka, 2008). In the excel spreadsheets, the pressure from the barometer model can be an input for the thermometer model or users can specify a pressure value. Hydrous and anhydrous compositions can also be a user input. The equations

above are all for hydrous compositions. Errors established for this models (SEE) are shown with the results. The use of the models is further discussed in Section 3.

2.3.3 MELTS modelling

MELTS is a petrological modelling software that uses thermodynamic properties of solids to calculate thermodynamic properties of coexisting liquids, equilibrium is established by minimizing Gibbs free energy for the system (Ghiorso and Sack, 1995, Asimow and Ghiorso, 1998). Composition, amount and thermodynamic properties of minerals and liquids can be determined at user specified temperature, pressure and whole rock compositions. The model will be used to evaluate different petrogenetic processes for the sample set in this study. There are different versions of the general model for specific applications and computer formats. Rhyolite-MELTS (v.1.2.x) (Gualda *et al.*, 2012) will be used here for pressure range scenarios from 0 to 1 GPa. Model input and conditions for MELTS models in Sections 3 to 5 are listed in **Appendix Table 11**.

2.3.4 DCompress modelling

DCompress is a magmatic degassing modelling software developed by Burgisser et al., 2014. It computes the gas and melt volatile composition of five element sets (O-H, S-O-H, C-S-O-H, C-S-O-H-Fe and C-O-H) in magmatic systems at equilibrium conditions (Burgisser *et al.*, 2015). The model uses solubility constants for the different volatile species determined from an empirical equation and mass balance equations. It is calibrated from experiments over the composition range of basalt, phonolite and rhyolite, temperature range from 790 to 1400°C and pressures from atmospheric to 3000 bar.

The model is used here to predict volatile compositions dissolved in the melt and exsolved as a gas phase during magma decompression for an open system volcano. Input parameters can

either be from fumarolic gas data or magmatic volatiles data. Parameters used in Section 4 are listed in **Appendix Table 11**.

2.3.5 Polytopic Vector Analysis (PVA)

PVA Multivariate Unmixing System program was developed by Robert Ehrlich for the interpretation of multi-parameter systems. Polytopic Vector Analysis is a multivariate procedure that can determine the number of sources, the signature of each source and the relative proportion of each source in every sample that is a mixture and does not require access to a database of potential source-fingerprints (Robert Ehrlich). PVA was used to determine end-member compositions for the set of samples in this study. Whole rock compositions were initially tested for possible mixing trends using 2 end-member Langmuir mixing models using extreme compositions as end-members. All possible end-member compositions outside the sample composition cloud were determined using PVA. Whole rock major element compositions were used as input.

Results and Discussions

A view of Red Crater (foreground) and Ngauruhoe (background)

3 Variable magma reservoir depths for Tongariro Volcanic Complex eruptive deposits from 10,000 years to present.

Reformatted and reprinted from Bulletin of Volcanology, Vol. 79, Issue 56. July 2017. With DRC 16 and copyright permission in ***Appendix Table 13.*** *The author of this thesis is responsible for this paper - content, data gathering, approach to data analysis, presentation and interpretation. A completed manuscript was sent to co-authors. Comments and edits from co-authors (supervisors) and journal reviewers and editors improved the manuscript.*

Variable magma reservoir depths for Tongariro Volcanic complex eruptive deposits from 10,000 years to present

Maria Carmencita Arpa*[1], Georg F. Zellmer[1], Bruce Christenson[2], Gert Lube[1], Gregory Shellnutt[3]

[1] Volcanic Risk Solutions, Institute of Agriculture and Environment, Massey University, Palmerston North, New Zealand

[2] National Isotope Centre, GNS Science, Lower Hutt, New Zealand

[3] Department of Earth Sciences, National Taiwan Normal University, Taipei, Taiwan

3.1 Abstract

Mineral, groundmass and bulk rock chemical analyses of samples from the Tongariro Volcanic Complex were made to estimate depths of magma reservoirs for selected eruptive deposits. The sample set consists of two units from the 11,000 cal. yrs. B.P. Mangamate Formation (Te Rato and Wharepu) and more recent deposits from near 1717 cal. yrs. B.P. (Ngauruhoe and Red Crater) to 1975 (Ngauruhoe). The depths of crystallization were determined by established

thermobarometers. Results show that the Mangamate eruptions of Te Rato and Wharepu originated from a deeper magma reservoir of about 28-35 km and likely ascended rapidly, whereas explosive eruption deposits from Ngauruhoe have depths of crystallization in the lower to mid-crust or about 7 to 22 km depth. A Red Crater lava flow had a possible magma reservoir depth from 4 to 9 km. The different eruptions sampled for this study tapped different reservoir levels and the oldest and largest eruptions were sourced from the deepest reservoir.

Keywords: Tongariro Volcano, Ngauruhoe, Mangamate, Thermobarometry, Hygrometry, Magma reservoir

3.2 Introduction

At what depth a magma is stored beneath a volcano has influence on its activity and is an important question in volcanology. Known reservoir depths have implications for interpretation of monitored volcanic activity parameters, such as seismicity and degassing. Complex volcanoes and caldera systems often comprise several magma storage bodies distributed at various depths. Reservoirs of large caldera systems, for example, can have periods of recharge from a deep reservoir (Parks *et al.*, 2012, Moretti *et al.*, 2013). From analysis of several more-recent main explosive events of Vesuvius, it was shown that the magma reservoir migrated from a deeper to a shallower level with time (Scaillet *et al.*, 2008). Analysis of the different deposits from eruptive centres of Taal Volcano show several discrete magma sources, but a common deep source (Miklius *et al.*, 1991).

There are several methods that may be used to determine where magma is stored beneath volcanoes. Seismic tomography utilizing a dense seismic network (Patane *et al.*, 2006, Brenguier *et al.*, 2007), combined with numerical magma property models (Paulatto *et al.*, 2012), for example, can provide high resolution images of magma storage, plumbing structures and magma ascent paths. Petrological techniques, on the other hand, use mineral thermometers

and barometers that are based on thermodynamic properties of minerals crystallizing in equilibrium with the liquid (Lindsley, 1983, Andersen *et al.*, 1993, Ghiorso and Evans, 2008, Putirka, 2008). Other geochemical parameters that have depth implications are the volatile components of magma and oxygen fugacities (Newman and Lowenstern, 2002, Ghiorso and Evans, 2008, Burgisser *et al.*, 2015).

The Tongariro Volcanic Complex in New Zealand is a composite structure comprising at least 12 named eruptive centers including Mt. Ngauruhoe and Te Maari Craters (**Figure 3-1**). The 60 km^3 complex is built from at least 6 cones erupted between 275 – 65 ka B.P. that were overprinted by later eruptions from 25 ka B.P. to present (Hobden *et al.*, 1999, Price *et al.*, 2013). Tongariro is located in the Southern Taupo Volcanic Zone (TVZ) where andesitic volcanism predominates (Cole *et al.*, 2000, Price *et al.*, 2005). The active volcanic arc that includes Tongariro and Ruapehu on the southern end lies about 100 km above the subducting Pacific plate (Reyners *et al.*, 2006). The thickness of crust in the overriding plate in the area of the Taupo Volcanic zone that is north of Tongariro is estimated to be up to 25 km (Stern *et al.*, 2010), or 30 km (Harrison and White, 2006), or 35 km (Reyners *et al.*, 2006), based on various geophysical models.

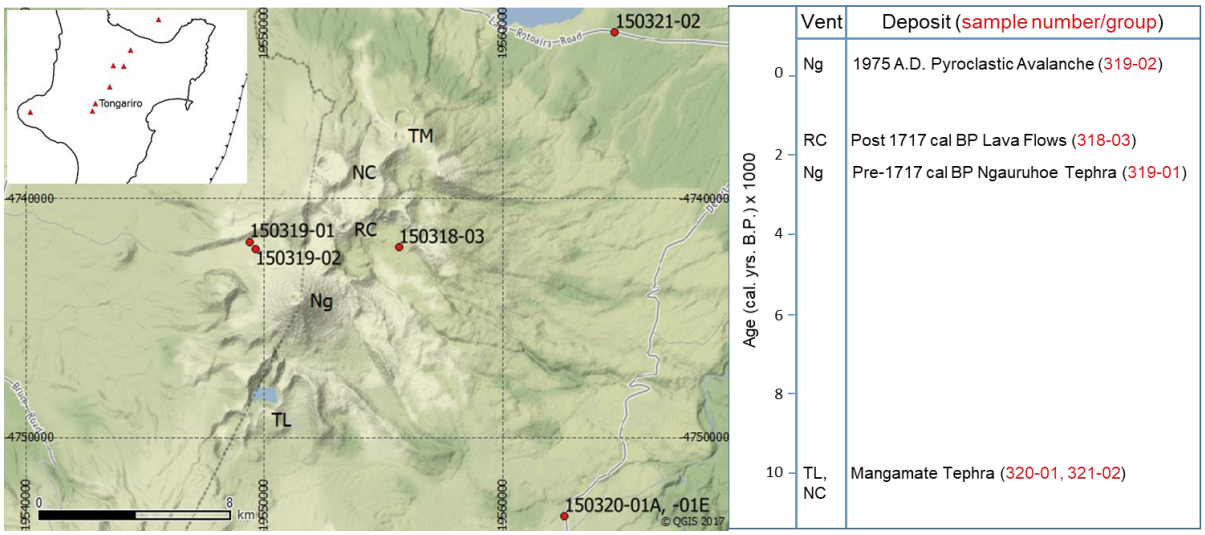

Figure 3-1. Location map for samples in this study. Some of the named eruptive centers are labelled (TL: Tama Lakes, Ng: Ngauruhoe, RC: Red Crater, NC: North Crater, TM: Te Maari Craters). Inset map shows the volcanoes of North Island, New Zealand and the Hikurangi Trench. Stratigraphic positions for the samples are also shown.

This study aims to identify possible depth regions of magma reservoirs beneath Tongariro Volcanic Complex using mineral and groundmass chemistry from selected eruptive deposits from different vents within the complex. The main assumption is that magma has partially crystallized in the reservoirs, as well as during its rise to the surface within an evolving melt. The results will be useful in interpreting magma evolution and petrogenesis for the andesites from Tongariro and will be an important parameter in degassing models of a deep magma source. Previous studies have identified magma reservoir and accumulation depth(s) at Tongariro. Using the clinopyroxene-liquid barometer of Putirka (2008), equilibrium crystallization pressure for an andesite from Ngauruhoe was estimated to be at 5.8 kbar or 21 km of crustal depth (Deering *et al.*, 2011), whereas magnetotelluric studies identified a low resistivity zone representing a magma accumulation zone at 4 - 12 km depth for Tongariro (Hill *et al.*, 2015).

The sample set includes two units (Te Rato and Wharepu) from the 9,780 to 9,700 years B.P. (~11,000 cal. yrs. B.P.) Mangamate Tephra Formation (Topping, 1973, Lowe *et al.*, 2008) and younger units ranging from one that immediately predates the 1717 cal. yrs. B.P. Taupo eruption, up to the present (**Figure 3-1 and 3-2**). These deposits are from eruptions of the following vents: North Crater or Proto North Crater for Te Rato Lapilli (Topping, 1973, Nairn *et al.*, 1998), Tama Lakes area (Topping, 1973) to Lower Tama Lakes and adjacent craters for Wharepu Tephra (Nairn *et al.*, 1998), Ngauruhoe and Red Crater for the more recent eruptions. There are two deposits from Ngauruhoe in this study. One is a tephra lapilli deposit that conformably underlies the 1717 cal yrs. B.P. Taupo pumice and is referred to here as the c. 1717 cal yrs. B.P. Ngauruhoe tephra. The other deposit is from the February 1975 eruption, and consists of cauliflower-textured bombs to lapilli from the phase 1 pyroclastic flow deposits (Nairn and Self, 1978, Lube *et al.*, 2007). The lava flow from Red Crater is post 1717 cal. yrs. B.P. and emplaced towards the Oturere Valley on the southeast flank (Hobden, 1997). Although not included in this study, another post 1717 cal. yrs. B.P. Red Crater lava flow (Hobden, 1997) was recently dated at 200-500 yrs. B.P. using paleomagnetic techniques (Greve *et al.*, 2016). Ages, source vents and sample locations are summarized in **Table 3-1**.

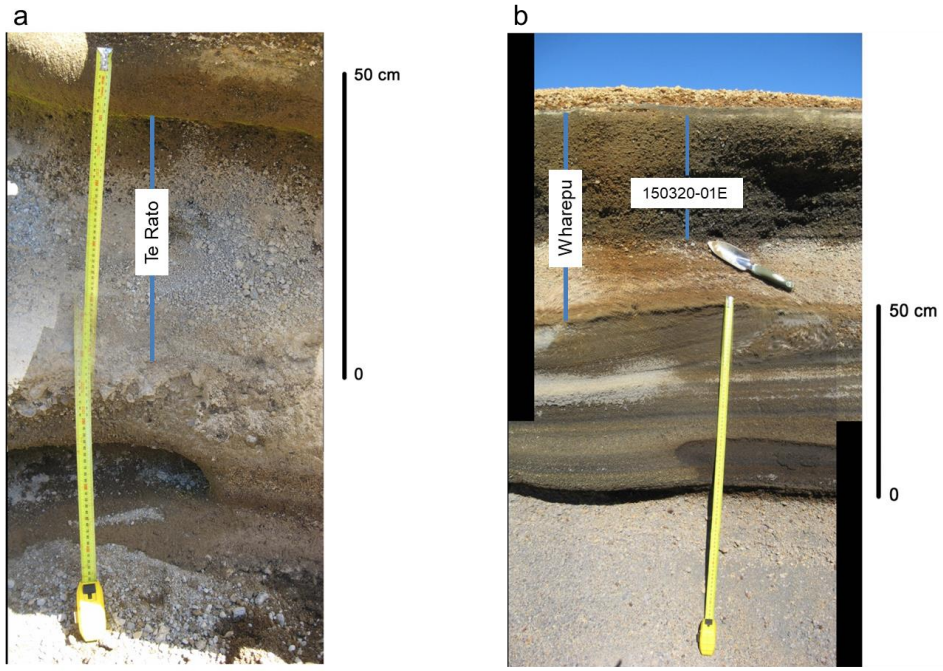

Figure 3-2. Photos showing the two members of the Mangamate formation sampled along the Desert Road outcrop. The oldest member in the formation is Te Rato (a) and the second youngest is Wharepu (b). The Mangamate Formation was deposited from 9,780 to 9,700 years B.P. (Topping, 1973).

Table 3-1. Samples used for this study.

Eruption Center and/or Unit	Sample Type	Age	Sample Number	Location
Te Rato Lapilli	pyroclast	~11,000 cal. yrs. B.P.*	150320-01A, 150321-02	175.733846, -39.220597; 175.752906, -39.079647
Wharepu Tephra (upper gray layer)	pyroclast	~11,000 cal. yrs. B.P.*	150320-01E	175.733846, -39.220597
Ngauruhoe	pyroclast	pre-1717 cal. yrs. B.P.	150319-01	175.61531, -39.14064
Red Crater	lava flow	post-1717 cal. yrs. B.P.**	150318-03	175.67152, -39.14234
Ngauruhoe	pyroclast	1975 A.D.	150319-02	175.61752, -39.14286

* Te Rato Lapilli and Wharepu Tephra are members of the Mangamate Tephra formation, which is dated 9,780 years B.P. (11,125 cal. yrs. B.P.) to 9,700 years B.P. (Topping, 1973)

** Red Crater lava flow relative age is from (Hobden, 1997).

3.3 Methods

3.3.1 Analytical methods

Lava flow samples (150318-03) and individual pyroclasts from tephra fall units (150319-01, 150320-01A, 150321-02, 150320-01E) and scoria-and-ash flow deposits (150319-02) were partitioned for bulk analysis and rock section slabs. Pyroclasts that were large enough had portions taken for both thin sections and bulk rock powders. For samples with smaller lapilli clasts, those showing similar features (color, vesicularity) were grouped (megascopically), and single clasts from each group were processed separately for rock powders and rock sections. Rock powders require an amount of at least 0.6g for the major element analysis used here. The rock powders were prepared at the Soil and Earth Sciences laboratory at Massey University and sent for whole rock major element analysis at the wavelength dispersive (WD) X-ray fluorescence spectrometer (XRF) PANanalytical AXIOS^{max} laboratory at the Department of Earth Sciences, National Taiwan Normal University (NTNU). The samples were cleaned and ground using both agate mortar and pestle for small pyroclasts and Tungsten Carbide mechanical mill for lava and larger pyroclast samples. Thin (30 microns) and thick (100 microns) sections for petrographic and microprobe analysis were prepared at the Mineral Services – Thin Sections Laboratory, National Isotope Centre, GNS Science, Lower Hutt.

Mineral, groundmass glass and bulk groundmass chemistry were determined using a JEOL JXA-8230 Electron Probe Micro-Analyzer (EPMA) equipped with 5 wavelength dispersive X-ray spectrometers (WDS) at the School of Geography, Environment and Earth Sciences, Victoria University of Wellington. A focused beam of 1 micron spot size at an accelerating potential of 15 kV and a beam current of 12 nA was used for mineral analysis. The beam current for glass and groundmass was 8 nA and spot size was varied from 5 to 10 microns for groundmass glass without microlites and 10 to 25 microns for groundmass with microlites, 10

microns were used for most groundmass analysis. Peak counting time was 30 to 15 seconds for all oxides. Backscattered electron images were also taken for photo reference. Analysed mineral phases include plagioclase, clinopyroxene, orthopyroxene, magnetite, and olivine. Additional backscattered electron images and qualitative analysis for mineral identification was done at the Manawatu Microscopy and Imaging Centre, Massey University using a FEI Quanta 200 Environmental Scanning Electron Microscope (SEM) with EDAX module.

This study used preliminary magmatic water data from melt inclusions hosted in olivine and pyroxene crystals to constrain model parameters. Determination of water content was done on a Nicolet Continuum Fourier Transform Infrared (FT-IR) microscope at the Institute of Agriculture and Environment, Massey University in Palmerston North. Total water was determined from the maximum height of the broad absorbance at 3550-3535 cm^{-1} and calculated using the Beer-Lambert equation using extinction coefficients of 63 l mol^{-1} cm^{-1} for basalt (Dixon *et al.*, 1988) and 62 l mol^{-1} cm^{-1} for andesite (Mandeville *et al.*, 2002).

3.3.2 Thermobarometers

This study uses mainly thermometers and barometers of Putirka (2008) listed below:

- Olivine thermometer: equation 15 and 22;
- Orthopyroxene thermometer: equation 28a;
- Orthopyroxene barometer: equation 29b;
- Clinopyroxene thermobarometers: equations 31, 32c and 33, Putirka et al., 2003 thermobarometer;
- Plagioclase thermometer: equation 23;
- Plagioclase barometer: equation 25a;
- Plagioclase hygrometer: equation 25b.

The thermometers are pressure sensitive and the barometers are temperature sensitive (Putirka, 2008), in the model spreadsheets the equations can be solved using the pressure results of the barometer or a user selected pressure. We used a pressure input of 5 kbar for the orthopyroxene, plagioclase and olivine thermometers. A median value of 5 kbar was chosen considering a crustal thickness of 35 km for Tongariro (Reyners *et al.*, 2006). Changing the pressure input to values between 0 to 10 kbar gives results that are within model error. The models can also be used for hydrous and anhydrous conditions. For this study, we used a value of 0.5 wt. % H_2O for the groundmass for all the samples. Initial FTIR data for Ngauruhoe 1975 samples show 0.4 – 1.9 wt.% H_2O in melt inclusions. A 0.5 wt.% H_2O in the groundmass as input in the plagioclase hygrometer of Putirka (2008) gives a magma water content of 0.9 to 1.4 wt.%, close to the value measured in the melt inclusions. The standard errors of estimates for each model (Putirka, 2008) are indicated in **Table 3-6**. Liquidus temperatures were determined using Rhyolite-MELTS (Ghiorso and Sack, 1995, Gualda *et al.*, 2012) from bulk rock compositions and input pressures based on the mineral barometers.

Pairing mineral and groundmass compositions for equilibrium requires known distribution coefficients (Kd). For evaluating melt-plagioclase equilibrium, $Kd^{Ca\text{-}Na}$ and $Kd(An\text{-}Ab)^{pl\text{-}liq}$ were used. Experimentally determined $Kd^{Ca\text{-}Na}$ $((X^{pl}_{Ca}/X^{pl}_{Na})/(X^{liq}_{Ca}/X^{liq}_{Na}))$ was found to be 1 for dry melts to 1.7 for melts with 2 wt.% H_2O and up to 5.5 for water saturated melts (Sisson and Grove, 1993). To pair plagioclase and groundmass compositions in the data set, observed Ca/Na molar ratio of plagioclase was assigned a liquid with computed Ca/Na ratio based on $Kd^{Ca\text{-}Na}$ 1.7 to 2. The observed Ca/Na ratio from a groundmass analysis was then matched to an appropriate plagioclase. The second criteria for equilibrium in plagioclase was from albite-anorthite exchange of $Kd(An\text{-}Ab)^{pl\text{-}liq} = X^{pl}_{Ab}X^{liq}_{AlO1.5}X^{liq}_{CaO}/X^{pl}_{An}X^{liq}_{NaO0.5}X^{liq}_{SiO2}= 0.27 \pm 0.11$ to 0.10 ± 0.11 for temperatures > 1050 (Putirka, 2008). Only plagioclase and liquid pairs that satisfy the equilibrium criteria are presented here. Preliminary FTIR data for the

Ngauruhoe samples and the Wharepu sample show magmatic H_2O contents of ≤ 2 wt. % and the $Kd^{Ca\text{-}Na}$ values for all the samples except Te Rato ranged from 1.0-1.7 consistent with experimental water contents of Sisson and Grove (1993). The Te Rato samples have higher $Kd^{Ca\text{-}Na}$ of up to 2. The test for equilibrium of olivine and orthopyroxene minerals with groundmass/glass was determined from Rhodes diagrams (Rhodes *et al.*, 1979, Putirka, 2008). $Kd(Fe\text{-}Mg)^{Ol\text{-}melt}$, defined as $(X^{melt}_{Mg}/X^{Ol}_{Mg})/(X^{melt}_{Fe2+}/X^{Ol}_{Fe2+})$, of 0.3 ± 0.03 was used for olivines, and $Kd(Fe\text{-}Mg)^{px\text{-}liq}$ of 0.29 ± 0.06 and 0.27 ± 0.03 for orthopyroxenes and clinopyroxenes, respectively. Only mineral and groundmass pairs that complied with the test for equilibrium in the thermobarometer models (Putirka, 2008) were used.

3.4 Results

3.4.1 Mineralogy and textures

All samples are porphyritic with variable phenocryst contents of up to 40% in the lava flows to less than 10% in the tephra, particularly the Te Rato and Wharepu samples. The largest phenocrysts are medium grained (> 1 mm). Microlitic crystals 50 to 100 μm in diameter are also considered here as phenocrysts (microphenocrysts) because in general they are still coarser than the microlitic groundmass. The microlites in the groundmass are generally less than 50 μm, mostly ~10 μm. **Figure 3-3a**, an example of texture, shows the phenocrysts, microphenocrysts and finer groundmass microlites. The groundmass for the samples has variable glass content. Sample 150319-02-a1 from the 1975 proclastic flow of Ngauruhoe has a clear glass groundmass whereas glass in the lava flow is interstitial. **Figure 3-3b** shows the boundary between samples 150319-02-a1 (glass groundmass) and 150319-02-a2 (microlitic groundmass), which are portions of a mingled clast from the Ngauruhoe 1975 eruption. Groundmass texture is summarized in **Table 3-2**. Clasts from Te Rato show mingled bands (**Figure 3-3c and 3-3d**) and Wharepu clasts have bands or lenses (**Figure 3-3e and 3-3f**).

Minerals in the bands are microlitic and for both samples, the vesicles in the bands/lenses are more rounded compared to vesicles in the host (**Figure 3-3c, 3-3d, 3-3e**).

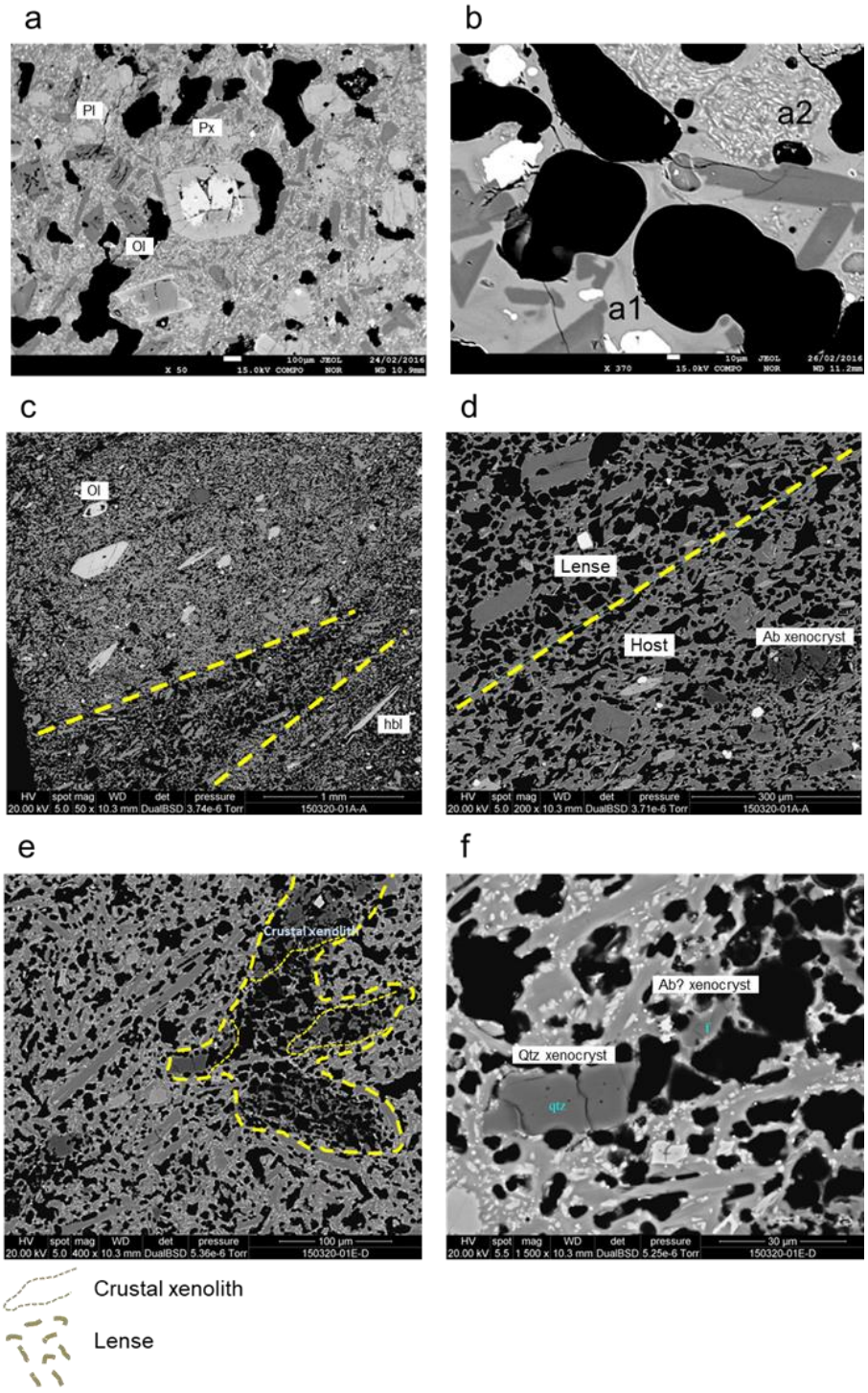

Figure 3-3. Backscattered electron images of samples. The Red Crater lava flow sample (150318-03) showing the larger phenocrysts, microphenocrysts (>50 micron in length) and the microlitic groundmass (a). A mingled pyroclast sample from the 1975 eruption of Ngauruhoe (150319-02-a1/a2) showing the boundary between the

microlitic and the glassy groundmass (b). Banding is common for pyroclasts from Te Rato; the boundary between the lense and host is outlined (c). Note the crustal xenolith within the host and the difference in vesiculation (d). More vesiculated lenses such as the one in the photo are common in pyroclasts from Wharepu, crustal xenoliths within the lense are outlined (thinner dashed line) (e). A quartz xenocryst within the sample shows minor dissolution (f).

Table 3-2. Groundmass characteristics, textures and silica composition ranges. Bulk rock silica is shown for comparison.

Sample Number	Eruption Center and/or Unit	Bulk Rock SiO_2 (wt.%)	Range of Groundmass SiO_2 (wt.%)	Groundmass Texture	
150320-01A-a	Te Rato Lapilli	63.21	64.37 - 67.77	microlitic	host
			65.74 - 69.64	microlitic	band
150321-02-c	Te Rato Lapilli		59.51 - 62.02	microlitic	
150320-01E-b	Wharepu Tephra	54.43	56.90 - 58.60	microlitic	host
			54.62 - 60.40	microlitic	lense
150320-01E-d	Wharepu Tephra		55.00 - 56.70	microlitic	host
			56.34	microlitic	lense
150319-01-e	Ngauruhoe	55.38	60.51 - 63.29	glassy to microlitic	
150319-01-i	Ngauruhoe	55.03	58.32 - 61.39	glassy to microlitic	
150318-03	Red Crater	52.95	56.50 - 60.00	microlitic	
150319-02-a1	Ngauruhoe 1975	55.83	67.57 - 69.8	clear glass	
150319-02-a2	Ngauruhoe 1975	56.24	60.08 - 68.17	microlitic	
150319-02-b2	Ngauruhoe 1975	56.22	61.16 - 65.80	microlitic	
150319-02-d	Ngauruhoe 1975	55.82	60.99 - 64.29	microlitic	

Microlitic groundmass refers to mixed microlites and glass within the area of analysis (beam diameter from 10 to 25 μm).
All compositions are normalized to 100%.

Essential minerals are plagioclase, clinopyroxene, orthopyroxene and olivine for all the samples in the study. Olivine was not analysed in the Te Rato samples, but it was described in the literature (Donoghue *et al.*, 1991, Nakagawa *et al.*, 1998). Amphibole is essential in the Te Rato samples. Plagioclase is rare as large phenocrysts in the Wharepu samples, but common in the groundmass. Fe-Ti oxides are rare in the groundmass of the Red Crater lava flow sample (150318-03), the c. 1717 cal yrs. B.P. Ngauruhoe tephra and Wharepu tephra samples. Fe-Ti oxides can be found as microphenocrysts for these samples. Crustal xenoliths composed mainly of quartz with minor amounts of feldspar (albite and K-feldspar) are found in the Te Rato and

Wharepu clasts. The xenoliths show various stages of dissolution, but often whole quartz and albite minerals were observed with only minor signs of dissolution around the grains (**Figure 3-3d and 3-3f**). Apatite and a Ti oxide, probably rutile, were also found in the Wharepu samples.

3.4.2 Bulk rock, mineral and groundmass compositions

Bulk rock compositions for the sample set are basaltic andesite to dacite, with 52.95 – 63.21 wt. % SiO_2 (**Table 3-3**). The Red Crater lava flow is basaltic andesite while Te Rato clasts are andesitic to dacitic. Groundmass compositions have higher silica content than bulk compositions and range from basaltic andesite to dacite, with 54.62 – 69.80 wt.% SiO_2 (**Table 3-2**). For the Wharepu samples, the groundmass SiO_2 ranges from 54.62 to 58.60 wt.%, close to the bulk composition of 54.43 wt.% SiO_2, but the bulk composition was affected by crustal xenoliths and thus may actually have lower silica contents. The crustal xenoliths are composed mainly of quartz and a new bulk composition for 320-01E-b (Wharepu) was calculated by subtracting 0.5 wt.% silica, which approximates 3% quartz in the sample (**Table 3-3**). The percent area of crustal xenoliths was determined from thin section images of 320-01E-b using ImageJ software. Microlitic groundmass analysis shows a range of compositions (**Table 3-2**). For the Ngauruhoe 1975 sample that has clear glass groundmass, the SiO_2 content has a narrower range of 67.57 to 69.80 wt.%, and it is close to the most evolved microlitic groundmass composition of 68.17 wt.% SiO_2. The entire range of microlitic groundmass for the Ngauruhoe 1975 is from 60.08 to 68.17 wt.% SiO_2 (**Table 3-2**).

Table 3-3. Bulk rock major element compositions for all the samples in this study. Refer to Table 3-1 for age.

	150318-03	150319-01-e	150319-01-i	150319-02-a1	150319-02-a2
SiO_2	52.95	55.38	55.03	55.83	56.24
TiO_2	0.74	0.72	0.77	0.76	0.80
Al_2O_3	15.38	16.49	17.61	16.74	17.70
Fe_2O_3	9.67	8.41	8.69	9.55	8.75
MnO	0.17	0.14	0.14	0.16	0.15

MgO	7.74	6.21	5.69	4.97	4.32
CaO	10.26	9.09	8.48	7.88	7.85
Na_2O	2.37	2.54	2.54	2.68	3.00
K_2O	0.60	0.91	0.93	1.29	1.05
P_2O_5	0.12	0.12	0.13	0.14	0.14
Totals(norm)	100.00	100.00	100.00	100.00	100.00
Totals	100.37	99.97	98.14	100.20	100.85

	150319-02-b2	150319-02-d	150320-01A-a	150320-01E-b	calculated (no quartz) (150320-01E-b)
SiO_2	56.22	55.82	63.21	54.43	52.99
TiO_2	0.79	0.74	0.53	0.79	0.81
Al_2O_3	17.67	17.16	17.64	17.84	18.40
Fe_2O_3	8.80	8.77	5.65	9.43	9.72
MnO	0.15	0.15	0.13	0.15	0.15
MgO	4.39	5.22	2.25	5.47	5.64
CaO	7.80	8.16	5.37	8.66	8.93
Na_2O	2.98	2.82	3.51	2.41	2.49
K_2O	1.05	1.01	1.59	0.72	0.74
P_2O_5	0.14	0.14	0.13	0.12	0.12
Totals(norm)	100.00	100.00	100.00	100.00	100.00
Totals	100.58	100.51	98.20	98.27	100.00

Bulk rock major element compositions for all the samples in this study
Refer to Table 3-1 for sample source vent and age.
All analyses were done at the Department of Earth Sciences, National Taiwan Normal University (NTNU).

Selected mineral compositions are listed in **Table 3-4**, and an example of a single analysis set is shown in **Table 3-5**, with the complete list available as supplementary material (see **Appendix Table 2 and 7**). The clinopyroxenes for all the samples are classified as augite ($Wo_{35.08\text{-}44.49}En_{40.83\text{-}51.53}Fs_{6.65\text{-}22.40}$) and the orthopyroxenes ($Wo_{0.78\text{-}4.95}En_{51.31\text{-}77.19}Fs_{19.52\text{-}47.91}$) are enstatite. Olivines have Fo# that range from 72.33 to 90.89. Plagioclase crystals have $An_{50.16}$ to $An_{92.37}$. The minerals typically show zoning. A zoned olivine in the Red Crater sample has a core composition of $Fo_{87.94}$ and a rim composition of $Fo_{79.22}$. A zoned pyroxene in sample 319-02-a1 (Ng 1975) has an orthopyroxene core ($Wo_{3.40}En_{67.36}Fs_{29.23}$) and a clinopyroxene rim ($Wo_{36.82}En_{43.95}Fs_{19.22}$), while another in sample 319-01-e (Ng) has a more calcic rim ($Wo_{39.37}En_{41.80}Fs_{18.82}$ to $Wo_{41.44}En_{46.68}Fs_{11.88}$). Zoned pyroxenes are also found in the

Red Crater lava flow sample and the 1975 Ngauruhoe sample. Normally zoned plagioclase in the Ngauruhoe 1975 sample can go from $An_{90.98}$ core to $An_{74.43}$ rim.

Table 3-4. Representative mineral and groundmass compositions for all the samples. Molar Mg# = 100*[Mg/(Mg+Fe^{2+}]; molar %An = 100*[Ca/(Ca+Na+K)].

Orthopyroxene	SiO_2	TiO_2	Al_2O_3	FeO	MnO	MgO	CaO	Na_2O	K_2O	Cr_2O_3	Total	Mg#
150321-02-c-opx1	51.67	0.09	0.26	30.24	1.06	18.16	0.38	0.00	0.00	0.00	101.87	51.71
150320-01a-a-opx2	52.38	0.29	1.14	16.62	0.34	27.00	1.62	0.00	0.02	0.00	99.41	74.33
150320-01e-b-opx2	52.95	0.28	0.42	21.44	0.43	23.70	1.59	0.02	0.00	0.08	100.90	66.34
150320-01e-b-opx3	53.41	0.18	0.68	18.28	0.44	26.50	1.53	0.02	0.00	0.03	101.08	72.10
150318-03-opx1	53.81	0.26	0.22	24.05	0.61	23.45	1.44	0.01	0.00	0.06	103.90	63.48
150318-03-opx2	56.22	0.10	0.16	15.37	0.40	28.61	2.06	0.00	0.00	0.00	102.92	76.85
150319-02-a2-opx2	52.12	0.15	1.66	22.62	0.22	21.37	2.45	NA	NA	0.00	100.59	62.75
150319-02-b2-opx1	52.99	0.10	1.20	21.39	0.24	22.56	2.47	NA	NA	0.02	100.97	65.28

Clinopyroxene	SiO_2	TiO_2	Al_2O_3	FeO	MnO	MgO	CaO	Na_2O	K_2O	Cr_2O_3	Total	Mg#
150320-01a-a-cpx1	51.11	0.43	1.53	7.78	0.19	16.21	20.83	0.13	0.00	0.13	98.34	78.80
150320-01a-a-cpx3	50.73	0.52	1.24	8.84	0.24	15.61	21.19	0.15	0.02	0.21	98.74	75.90
150320-01e-ts-cpx1	51.71	0.37	3.32	7.78	0.13	16.10	21.00	0.26	0.01	0.07	100.75	78.68
150319-01-e-cpx2-c	52.02	0.53	0.57	12.05	0.28	15.01	19.67	0.10	0.00	0.00	100.22	68.95
150318-03-cpx2	52.82	0.44	0.86	8.51	0.21	17.55	20.33	0.11	0.01	0.25	101.09	78.62
150318-03-cpx5	52.46	0.38	0.38	11.21	0.38	14.95	21.04	0.10	0.01	0.03	100.93	70.40
150319-02-a2-cpx1	51.62	0.56	0.70	11.67	0.28	16.27	18.92	0.12	0.01	0.09	100.24	71.32

Olivine	SiO_2	TiO_2	Al_2O_3	FeO	MnO	MgO	CaO	Na_2O	K_2O	Cr_2O_3	NiO	Total	Mg#
150320-01e-b-ol2	38.06	NA	NA	22.52	0.31	39.24	0.17	NA	NA	0.00	0.00	100.31	75.65
150320-01e-d-ol1	38.50	NA	NA	19.65	0.27	41.51	0.15	NA	NA	0.03	0.07	100.18	79.02
150319-01-e-ol5	38.67	0.00	0.02	23.31	0.39	40.88	0.17	0.00	0.01	0.02	NA	103.47	75.77
150318-03-ol3-r	38.82	NA	NA	19.68	0.35	42.07	0.22	NA	NA	0.00	0.08	101.23	79.22
150319-02-d-ol1	37.99	NA	NA	25.47	0.37	37.35	0.13	NA	NA	0.00	0.07	101.39	72.33

Plagioclase	SiO_2	TiO_2	Al_2O_3	FeO	MnO	MgO	CaO	Na_2O	K_2O	Total	%An	Comment
150320-01a-a-pl10	52.17	0.00	30.98	0.57	NA	0.15	13.88	3.42	0.13	101.30	68.65	
150321-02-c-pl1-mic	51.58	0.00	30.75	0.76	NA	0.19	14.19	3.34	0.11	100.92	69.68	
150320-01e-b-pl5-mic	52.13	0.02	30.64	0.77	NA	0.21	14.00	3.09	0.11	100.97	70.98	lense
150320-01e-b-pl1-mic	51.12	0.02	31.15	0.66	NA	0.19	14.75	3.12	0.09	101.10	71.96	host
150319-01-e-pl8-mic	54.31	0.02	29.46	0.69	NA	0.20	12.46	3.82	0.21	101.18	63.48	
150319-01-e-pl5-mic	51.02	0.00	31.94	0.56	NA	0.15	15.13	3.01	0.10	101.89	73.11	
150318-03-pl2-c	52.79	0.00	31.40	0.35	NA	0.03	13.57	3.69	0.12	101.96	66.53	
150318-03-pl4	52.95	0.00	30.98	0.36	NA	0.05	13.67	3.74	0.15	101.91	66.32	
150319-02-b2-pl5-mic	54.64	0.00	29.12	0.56	NA	0.08	11.92	4.42	0.22	100.96	59.04	
150319-02-b2-pl6-mic	55.24	0.03	28.36	0.66	NA	0.11	11.39	4.57	0.21	100.57	57.23	

Groundmass	SiO_2	TiO_2	Al_2O_3	FeO	MnO	MgO	CaO	Na_2O	K_2O	Total	Comment
150320-01a-a-gm9	66.61	0.48	16.89	3.45	0.09	0.78	4.80	2.55	2.18	97.94	
150321-02-c-gm4	56.99	0.54	18.08	5.59	0.10	3.50	7.21	1.94	1.13	95.17	
150320-01e-b-gm4	54.23	0.82	15.72	9.47	0.22	7.18	9.09	1.67	0.80	99.28	lense
150320-01e-b-gm7	55.50	0.73	17.78	8.19	0.18	3.38	8.34	2.19	1.12	97.53	host
150319-01-i-gm3	58.33	0.90	16.70	7.92	0.15	3.69	7.53	3.18	1.35	100.02	
150319-01-e-gm8	61.48	1.03	14.55	7.15	0.12	2.67	5.48	2.25	2.33	97.14	
150318-03-gm1	57.78	1.36	14.49	11.11	0.22	3.50	6.66	2.11	1.38	98.75	
150318-03-gm2	56.12	0.64	15.67	8.24	0.20	6.17	9.80	1.72	0.73	99.32	
150319-02-a2-gm4	60.16	1.19	14.51	8.66	0.15	2.33	5.71	2.57	1.67	97.08	
150319-02-a2-gm8	59.89	1.29	14.89	7.86	0.09	1.60	5.35	2.72	2.11	95.91	

Representative mineral and groundmass compositions for all the samples. NA: not analyzed
Microprobe analyses was done at the School of Geography, Environment and Earth Sciences, Victoria University of Wellington.

Table 3-5. Single microprobe analysis run for Wharepu samples. Standard minerals analysed as unknowns before and after each batch of analysis and actual standard compositions for reference are shown. Actual standard values are from (mineralsciences.si.edu/facilities/standards/datasheets.htm 2016).

	SiO_2	TiO_2	Al_2O_3	FeO	MnO	MgO	CaO	Na_2O	K_2O	Cr_2O_3	NiO	Total	comment
							Plagioclase						
1	51.435	0	31.087	0.267		0.127	13.738	3.402	0.097			100.177	plagioclase 01 (NMNH 11590)
2	51.841	0.003	31.1	0.227		0.119	13.807	3.458	0.103			100.658	plagioclase 02 (NMNH 11590)
9	51.121	0.018	31.148	0.655		0.19	14.747	3.116	0.09			101.098	150320-01e-b-pl1-mic
11	51.951	0.007	30.502	0.758		0.174	13.964	3.162	0.107			100.625	150320-01e-b-pl3-mic
12	53.113	0	29.859	0.74		0.182	13.089	3.83	0.11			100.923	150320-01e-b-pl4-mic
13	52.132	0.016	30.637	0.771		0.212	13.998	3.088	0.114			100.968	150320-01e-b-pl5-mic
17	53.504	0.039	28.567	1.126		0.347	13.084	3.562	0.215			100.444	150320-01e-d-pl1-mic
19	53.74	0.059	28.582	1.084		0.327	12.802	3.665	0.246			100.505	150320-01e-d-pl3-mic
23	51.769	0	30.577	0.76		0.205	14.332	3.203	0.111			100.957	150320-01e-d-pl7-mic
25	51.973	0.008	31.238	0.328		0.114	13.739	3.585	0.096			101.081	plagioclase 1 (NMNH 11590)
26	51.801	0	31.216	0.172		0.116	13.888	3.505	0.086			100.784	plagioclase 2 (NMNH 11590)
standard	51.25	0.05	30.91	0.46	0.01	0.14	13.64	3.45	0.18			100.09	Plagioclase, NMNH 11590
							Clinopyroxene						
1	50.34	0.747	8.918	6.732	0.102	16.778	16.097	0.549	0	0.15		100.413	Kakanui
2	50.28	0.753	9.047	6.537	0.125	16.855	16.166	0.569	0.005	0.169		100.506	Kakanui
16	53.084	0.154	0.582	5.422	0.115	17.918	21.97	0.108	0	0.516		99.869	150320-01e-b-cpx1
19	53.959	0.089	0.444	4.384	0.123	18.453	22.337	0.096	0.006	0.656		100.547	150320-01e-b-cpx2
20	53.699	0.114	0.576	4.444	0.128	18.405	22.008	0.125	0.022	0.763		100.284	150320-01e-b-cpx3
26	50.934	0.771	8.855	6.646	0.14	16.843	16.014	0.582	0	0.125		100.91	kakanui1
27	50.585	0.768	8.993	6.738	0.131	16.656	15.901	0.54	0.002	0.162		100.476	kakanui2
standard	50.73	0.74	8.73	6.34	0.13	16.65	15.82	1.27	0			100.41	Kakanui augite, NMNH 122142
							Olivine						
1	39.694			16.852	0.356	44.544	0.019			0.027	0.014	101.506	springwater 01
2	39.769			16.799	0.334	44.332	0.02			0.009	0	101.263	springwater 02
4	38.291			22.023	0.312	39.791	0.158			0.014	0.039	100.628	150320-01e-b-ol1
5	38.063			22.524	0.308	39.242	0.171			0	0	100.308	150320-01e-b-ol2
8	38.504			19.651	0.27	41.508	0.146			0.027	0.069	100.175	150320-01e-d-ol1
9	38.54			19.431	0.294	41.3	0.171			0.015	0.053	99.804	150320-01e-d-ol2
10	38.335			20.619	0.295	40.75	0.16			0.035	0.036	100.23	150320-01e-d-ol3
11	39.645			16.715	0.33	44.519	0.024			0.035	0.032	101.3	springwater 1
12	39.75			17.107	0.324	44.438	0.016			0.02	0.008	101.663	springwater 2
standard	38.95			16.62	0.3	43.58				0.02		99.47	Olivine, USNM 2566
							Groundmass						
1	49.955	4.016	12.096	13.128	0.174	5.077	8.898	1.817	0.851	0.003		96.027	VGA99-01
2	49.657	3.976	12.21	13.234	0.203	4.972	8.925	1.764	0.817	0		95.77	VGA99-02
3	75.266	0.067	11.795	1.089	0.013	0.018	0.422	2.415	4.927	0.009		96.136	VG568-01
4	75.745	0.073	11.879	1.046	0.022	0.026	0.447	2.47	4.953	0.011		96.776	VG568-02
11	59.755	0.39	22.511	5.274	0.077	1.925	2.676	3.057	3.223	0		98.927	150320-01e-b-gm1
13	54.399	1.03	15.24	10.264	0.232	5.521	8.336	1.706	1.054	0.009		97.867	150320-01e-b-gm3
14	54.233	0.816	15.721	9.465	0.221	7.18	9.088	1.665	0.801	0.012		99.265	150320-01e-b-gm4
15	55.097	0.801	19.112	7.671	0.099	2.183	8.478	2.219	1.078	0.012		96.844	150320-01e-b-gm5
17	55.497	0.731	17.778	8.187	0.181	3.381	8.34	2.186	1.119	0		97.498	150320-01e-b-gm7
18	56.4	0.931	15.161	9.687	0.151	4.918	7.572	1.678	1.186	0		97.789	150320-01e-b-gm8
19	56.323	0.803	18.236	6.896	0.117	2.093	8.059	2.25	1.227	0		96.095	150320-01e-b-gm9
20	56.074	0.822	16.744	8.563	0.161	4.029	8.448	1.926	1.052	0		97.913	150320-01e-b-gm10
21	54.612	1.066	14.358	10.264	0.172	5.335	8.326	1.518	1.328	0.007		97.088	150320-01e-d-gm1
22	54.135	1.012	16.209	10.327	0.197	5.16	8.577	1.752	0.96	0.016		98.409	150320-01e-d-gm2
23	53.502	0.864	15.976	8.624	0.146	4.883	7.435	1.73	1.013	0.01		94.317	150320-01e-d-gm3
24	53.979	0.895	16.056	9.389	0.208	5.766	8.212	1.812	0.889	0		97.27	150320-01e-d-gm4
27	53.824	0.724	19.001	7.806	0.154	2.576	7.849	2.231	1.217	0.003		95.495	150320-01e-d-gm7
31	50.581	4.005	12.175	13.089	0.212	4.911	8.906	1.781	0.824	0.016		96.514	VGA99 1
32	50.889	3.961	12.313	13.157	0.172	4.862	8.946	1.717	0.83	0.027		96.884	VGA99 2
33	76.038	0.074	11.829	1.102	0.035	0.035	0.428	2.422	4.906	0.015		96.987	VG568 1
34	76.372	0.075	11.892	1.146	0.042	0.027	0.423	2.498	4.935	0		97.505	VG568 2
standard	76.71	0.12	12.06	1.23	0.03	<0.10	0.5	3.75	4.89			99.29	Glass, Rhyolite NMNH 72854 VG-568
standard	50.94	4.06	12.49	13.3	0.15	5.08	9.3	2.66	0.82			98.8	Glass, Basalt NMNH 113498-1 (A-99)

Microprobe analysis for Wharepu samples. Standard minerals analysed as unknowns before and after each batch of analysis and actual standard values for reference are shown.

Actual standard values are from http://mineralsciences.si.edu/facilities/standards.htm

3.4.3 Pressure and temperature of crystallization

3.4.3.1 Equilibrium conditions and xenocrysts

Mineral and groundmass pairs that met equilibrium conditions were used for the pressure and temperature models. Because microlitic groundmass analysis is bulk (microlites plus glass), the bulk groundmass composition is maintained by the crystallization of microlites and only the interstitial glass (too small for analysis) will have more evolved compositions. The large beam size combines microlite and interstitial glass compositions representing a groundmass composition before microlite crystallization and it can be paired with a phenocryst to determine equilibrium. For the Te Rato and Wharepu samples that are mingled, only the plagioclase and groundmass that are both in the host or both in the lense are matched. The Ca/Na ratio between plagioclase and groundmass for all the samples ranged from 1.0 to 2.0. The Kd (Ab-An) for the plagioclase-groundmass ranged from 0.16 to 0.31. In sample 319-01-e (c. 1717 cal yrs. B.P. Ngauruhoe tephra) only plagioclase microphenocrysts were found to be in equilibrium with the groundmass. More commonly, rim and intermediate zone compositions for plagioclase and plagioclase microphenocrysts are in equilibrium with the groundmass while core compositions are not. $Kd(Fe\text{-}Mg)^{Ol\text{-}melt}$ ranged from 0.266 to 0.332, while $Kd(Fe\text{-}Mg)^{Opx\text{-}melt}$ and $Kd(Fe\text{-}Mg)^{cpx\text{-}melt}$ are from 0.247 to 0.328 and 0.275, respectively (**Table 3-6**).

Table 3-6. Summary of thermobarometry results using different models. Olivine thermometer, orthopyroxene, clinopyroxene and plagioclase thermobarometers, and plagioclase hygrometer are from Putirka (2008). Equations used and corresponding standard errors of estimates (SEE) are shown (Putirka 2008). An initial pressure of 5 kbar

was input for the orthopyroxene and plagioclase thermobarometers and olivine thermometer. A 0.5 wt.% H_2O was assumed for the groundmass/liquid composition input.

Temperature (° C)

	Olivine		Orthopyroxene	Clinopyroxene		Plagioclase	$Kd_{Pl\text{-}liq}^{Ab\text{-}An}$	$Kd_{Ol\text{-}melt}^{Fe\text{-}Mg}$	$Kd_{Opx\text{-}melt}^{Fe\text{-}Mg}$	$Kd_{Cpx\text{-}melt}^{Fe\text{-}Mg}$
	Equation 15* SEE: ± 60˚C	Equation 22 SEE: ± 29˚C	Equation 28a SEE: ± 41˚C	2003 SEE: ± 59˚C	Equation 33* SEE: ± 42˚C	2005, Eqn 23 SEE: ± 43˚C	(0.27 ± 0.11)	(0.3 ± 0.03)	(0.29 ± 0.06)	(0.27 ± 0.03)
1975 Ngauruhoe	1080	1071-1076	1066-1114			1087-1159	0.20-0.26	0.242*-0.263*	0.247-0.328	
Red Crater	1109	1097	1096-1130			1130-1145	0.18-0.30	0.266	0.305-0.323	
Ngauruhoe	1095	1084		1159-1161	1114-1117	1117-1148	0.18-0.21	0.276		0.276-0.277
Wharepu	1139-1151	1135-1153		1178	1121	1215-1216	0.29-0.31	0.266-0.288		0.275
Te Rato						1153-1156 (lense); 1152-1184 (host)	0.16-0.19; 0.17-0.23			

Equations from Putirka (2008), including Putirka et al., 2003, 2005.
*Not included in plots
An initial pressure of 5 kbar was input for the olivine, orthopyroxene and plagioclase thermometers. A 0.5 wt.% H_2O was assumed for the groundmass/liquid composition.

	Pressure (kbar)				H_2O (wt. %)					
	Orthopyroxene Equation 29b SEE: ± 2.1 kbar	2003 SEE: ± 5 kbar	Clinopyroxene Equation 31 SEE: ± 2.9 kbar	Equation 32c SEE: ± 1.5 kbar	Plagioclase Equation 25a SEE: ± 2.47 kbar	Pl hygrometry Equation 25b SEE: ± 1.1 wt.%	$Kd_{pl\text{-}liq}^{Ca\text{-}Na}$	$Kd_{Pl\text{-}liq}^{Ab\text{-}An}$ (0.27 ± 0.11)	$Kd_{Opx\text{-}melt}^{Fe\text{-}Mg}$ (0.29 ± 0.06)	$Kd_{Cpx\text{-}melt}^{Fe\text{-}Mg}$ (0.27 ± 0.03)
1975 Ngauruhoe	3.0-5.6				2.3-5.0	0.9-1.4	1.0-1.7	0.20-0.26	0.247-0.328	
Red Crater					1.2-2.3	0.5-0.7	1.0-1.6	0.18-0.30		
Ngauruhoe		3.3-3.7*	7.1-7.3*	5.4-6.1*	3.5-3.9	1.1-1.3	1.3-1.6	0.18-0.21		0.276-0.277
Wharepu		4.7*	8.5*	5.7*	8.2-8.4	1.3-1.4	1.2-1.3	0.29-0.31		0.275
Te Rato					6.7-7.2 (lense); 7.9-9.3 (host)	2.2 (lense); 2.2 (host)	1.6-2.0; 1.5-2.0	0.16-0.19; 0.17-0.23		

Equations from Putirka (2008), including Putirka et al., 2003.
*The average value was used in the graphs
An initial pressure of 5 kbar was input for the Orthopyroxene and Plagioclase barometers. A 0.5 wt.% H_2O was assumed for the groundmass/liquid composition.

Mineral compositions that do not meet the equilibrium conditions are regarded as xenocrysts. In the Red Crater lava flow sample, olivines with Fo# greater than 87 are not in equilibrium with any of the groundmass compositions based on $Kd(Fe\text{-}Mg)^{Ol\text{-}melt}$. However, a zoned olivine with a high Fo# core and a rim in equilibrium with groundmass may also represent an olivine that fractionated from a liquid, but was later incorporated in the magma before ascent. For the two Ngauruhoe samples, pyroxenes that are not in equilibrium are orthopyroxenes with Mg# greater than 78 and clinopyroxenes with Mg# greater than 75. It should be noted that none of the analysed orthopyroxenes in the c. 1717 cal yrs. B.P. Ngauruhoe tephra are in equilibrium with the groundmass. **Figure 3-4** shows the range of Mg# for the mafic minerals and marks the ones not in equilibrium. In cases where the mineral rim composition is not in equilibrium with the groundmass, such as for a clinopyroxene that has a rim Mg# that is higher than the core, the whole crystal is considered a xenocryst. The limit for the xenocrysts may not be so clear in terms of Mg#. However, using the Mg/Fe^{2+} ratio of a mineral and ideal ratio for the groundmass from Kd (and groundmass Mg/Fe^{2+} with ideal mineral Mg/Fe^{2+}), shows a more distinct separation between xenocrysts and minerals in equilibrium (**Figure 3-5**). Note that no mafic mineral in the glassy sample (319-02-a1: Ng 1975) is in equilibrium with the groundmass glass, but they are in equilibrium with the microlitic groundmass (**Figure 3-5**). In this case, the mingled aphyric magma (319-02-a1: Ng 1975) may have picked up the mafic minerals crystallized from the other magma (319-02-a2: Ng 1975). The incorporation of xenocrysts by rising aphyric magma was proposed for the crystal content of volcanoes in the SW Japan Arc (Zellmer *et al.*, 2013). Plagioclases with compositions greater than An_{84} are not in equilibrium with groundmass for the Ngauruhoe samples based on $Kd(An\text{-}Ab)^{pl\text{-}liq}$ (**Figure 3-6**). However, plagioclase with this high anorthite content is in equilibrium with groundmass for the Red Crater sample. All the mafic minerals analysed for the Mangamate samples are in equilibrium with groundmass.

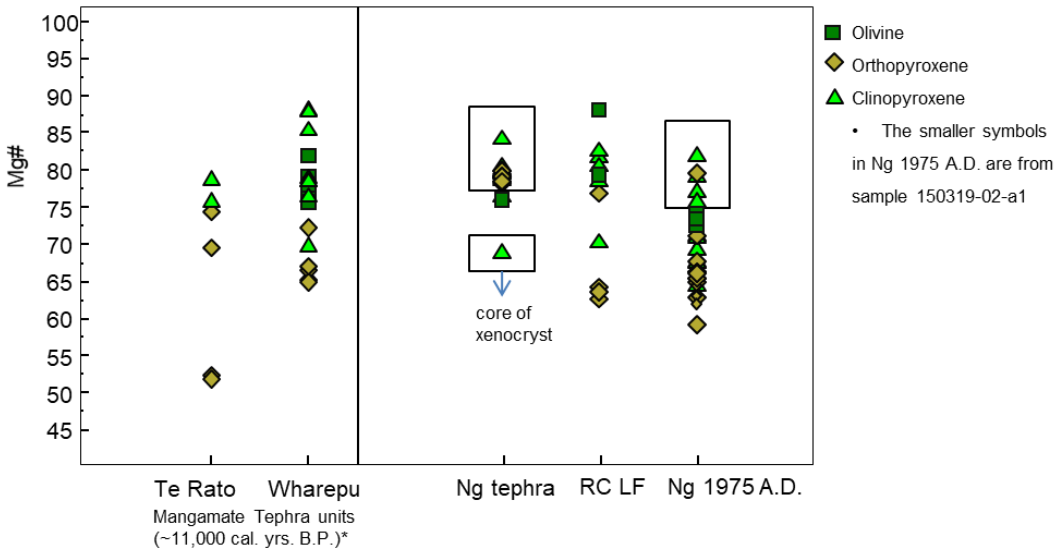

Figure 3-4. Olivine, orthopyroxene and clinopyroxene compositions in terms of molar Mg# for the samples in this study. The grains enclosed in a box are not in equilibrium with any of the analysed groundmass compositions and are considered here to be xenocrysts. Plots were done using Petrograph (Petrelli et al. 2005). Ngauruhoe (Ng); Red Crater Lava Flow (RCLF).

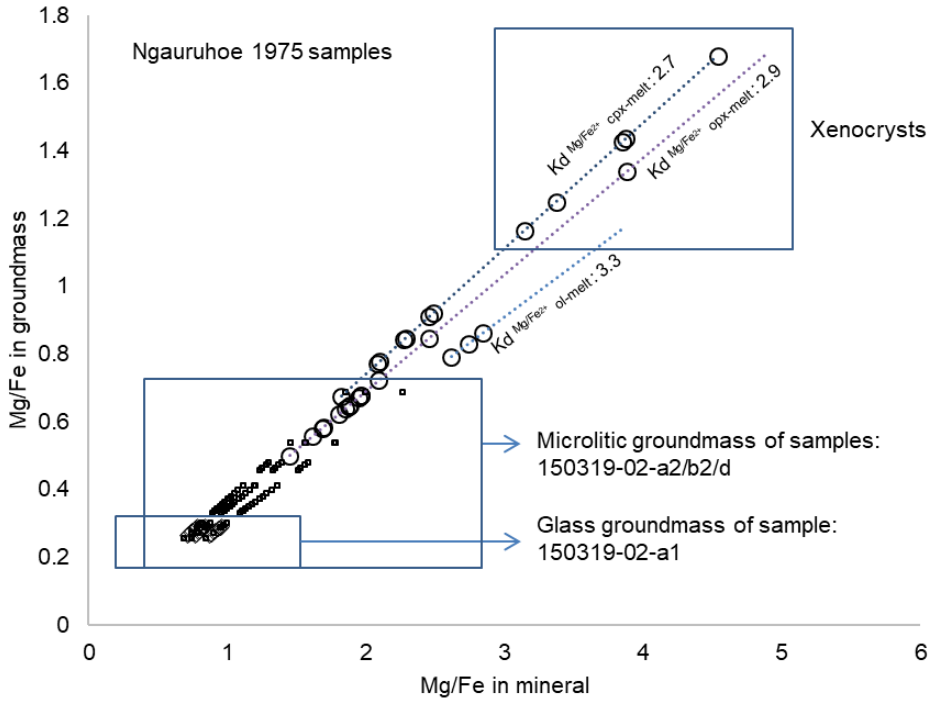

Figure 3-5. All the mafic minerals (olivine, orthopyroxene, clinopyroxene) and groundmass compositions from the Ngauruhoe 1975 samples. The measured Mg/Fe^{2+} ratio in the mineral is paired with a calculated groundmass ratio using Kd values, and measured Mg/Fe^{2+} groundmass ratio is paired with a calculated mineral ratio. The minerals in sample 150319-02-a1 are not in equilibrium with its groundmass, they are however in equilibrium

with the microlitic groundmass from the other samples for this deposit. These minerals can be xenocrysts in the aphyric melt. Minerals considered as xenocrysts are also shown.

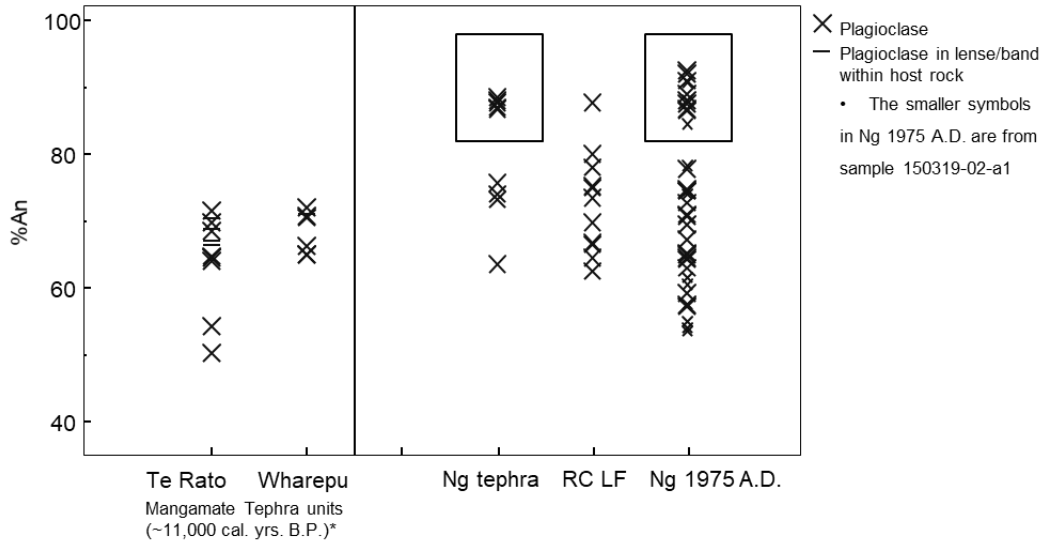

Figure 3-6. Plagioclase compositions in terms of % An for the samples in this study. The grains enclosed in a box are not in equilibrium with any of the analysed groundmass compositions and are considered to be xenocrysts. Abbreviations as in Figure 3-4.

3.4.3.2 Depths and temperatures

In general, the range of crystallization temperatures for all the samples is from 1066 to 1216°C. The sample with the highest temperature is Wharepu Lapilli, a basaltic andesite. Te Rato lapilli, although andesitic to dacitic in composition, has crystallization temperatures of 1152 to 1184°C. Plagioclase from the dacitic bands in the Te Rato clasts show lower crystallization temperatures (1153 to 1156°C). There is no distinct variation in temperature with time. Liquidus temperatures from MELTS model (Ghiorso and Sack, 1995, Gualda *et al.*, 2012) using bulk compositions are all above or near the indicated temperatures except for the Te Rato sample (**Figure 3-7, Table 3-6a**). The liquidus temperature based on bulk composition of a Te Rato clast supports the thermometer model for lower crystallization temperatures of the mingled dacitic magma in this sample. The bulk liquidus temperature would show the average

temperatures for the mingled magma. Probably, more analysis points within the mingled dacite would show even lower crystallization temperatures because there is the effect of various degrees of mixing.

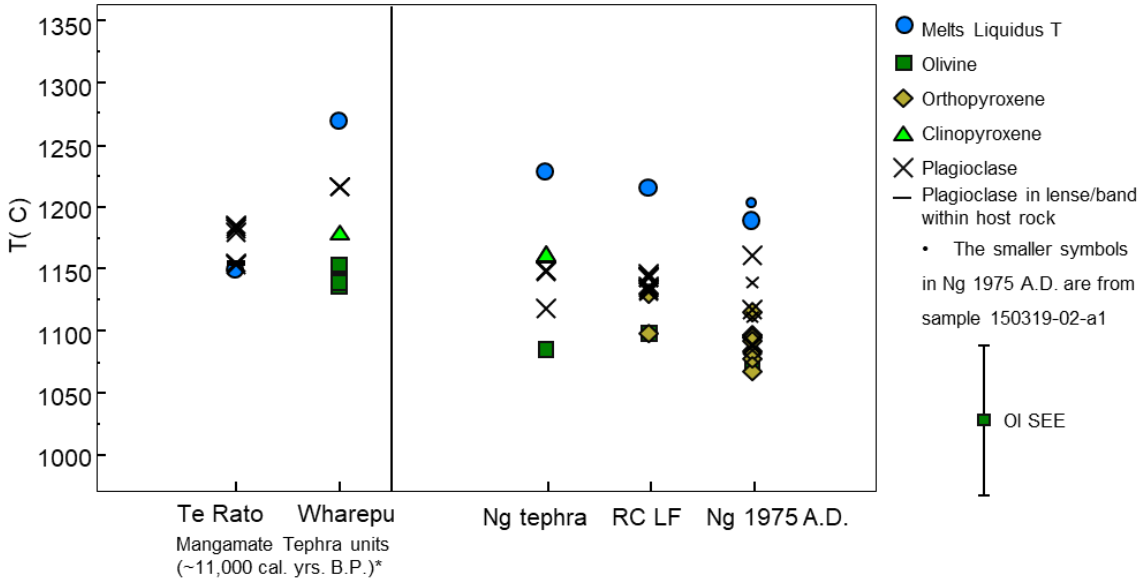

Figure 3-7. Temperatures determined from mineral thermometers using models from Putirka (2008). Standard errors of estimate (SEE) and models used (equations) from Putirka (2008) are listed in Table 3-6, SEE for olivine is shown. Filled circles represent liquidus temperatures for bulk compositions determined from Rhyolite-MELTS (Ghiorso and Sack 1995; Gualda et al. 2012). The deposits are: two units from the Mangamate Tephra (Te Rato and Wharepu), a pre-1717 cal. yrs. B.P. Ngauruhoe tephra, a post-1717 cal. yrs. B.P. lava flow from Red Crater and pyroclasts from the 1975 A.D. eruption of Ngauruhoe (See Table 3-1). Abbreviations as in Figure 3-4.

There is a distinct difference in depth of crystallization between the Mangamate units and the more recent deposits (**Figure 3-8**, **Table 3-6b**). The highest crystallization pressure for Wharepu is from about 8 kbar and for Te Rato it is about 9 kbar. All pressure estimates, including those with probable error for Te Rato, and excluding estimates from the mingled dacite, equate to a depth range of 28 to 35 km (**Figure 3-9**). Assuming a crustal density of 2,700 kg/m^3, this corresponds to the base of the crust for this area (Harrison and White, 2006, Reyners *et al.*, 2006). The range of pressure estimates for the younger Ngauruhoe and Red Crater sourced deposits does not overlap with that of the older Mangamate units (**Figure 3-9**).

Crystallization pressures found for the lenses within Te Rato are 6.7 to 7.2 (n=5) or 25 to 27 km depth. The range of crystallization pressures for the 1975 Ngauruhoe pyroclasts is from 2.3 to 5.6 kbar or 8 to 21 km depth. For the c. 1717 cal. yrs. B. P. Ngauruhoe tephra it is 3.5 to 3.9 kbar or 13 to 14 km depth estimated from plagioclase in equilibrium with groundmass. However, clinopyroxenes in this sample (Ngauruhoe tephra) in equilibrium with bulk composition gives higher pressure estimates of 5.3 to 5.7 kbar (an average for 3 clinopyroxene models) (**Table 3-6b**). Note that the 2003 clinopyroxene model agrees with the plagioclase model. The average from the plagioclase and pyroxene estimates is about 5 kbar and close to the average of estimates from the 1975 Ngauruhoe pyroclast (**Figure 3-9**). The Red Crater lava flow has a crystallization pressure range of 1.2 to 2.3 kbar equivalent to 4 to 9 km depth, the shallowest for the sample set.

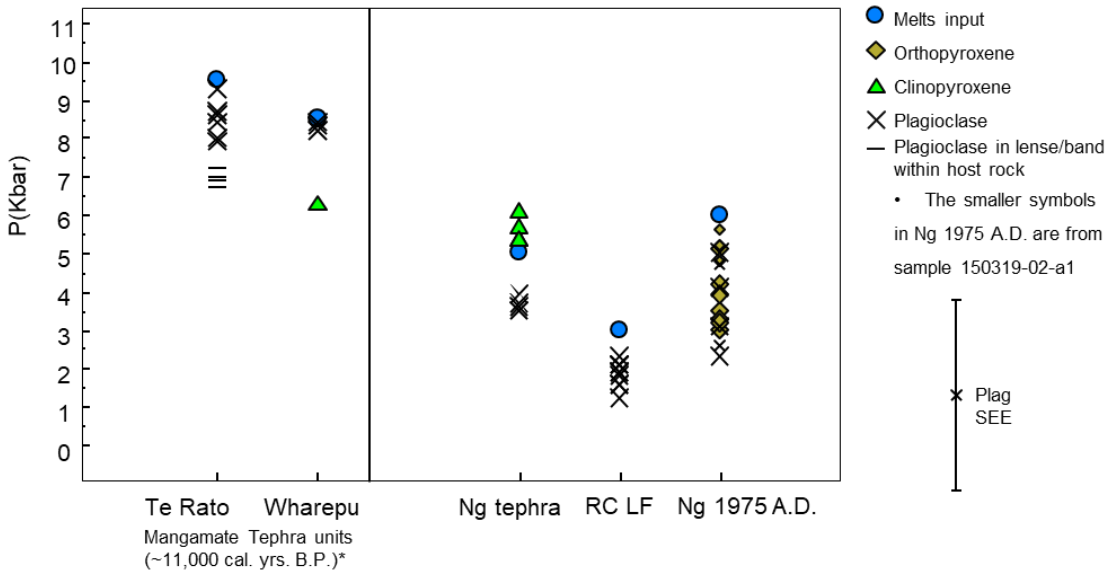

Figure 3-8. Pressures determined from mineral barometers using models from Putirka (2008). Standard errors of estimate (SEE) and models used (equations) from Putirka (2008) are listed in Table 6, SEE for the plagioclase is shown. Filled circles represent input pressures to determine liquidus temperatures from bulk compositions (see Figure 3-7). Abbreviations as in Figure 3-4.

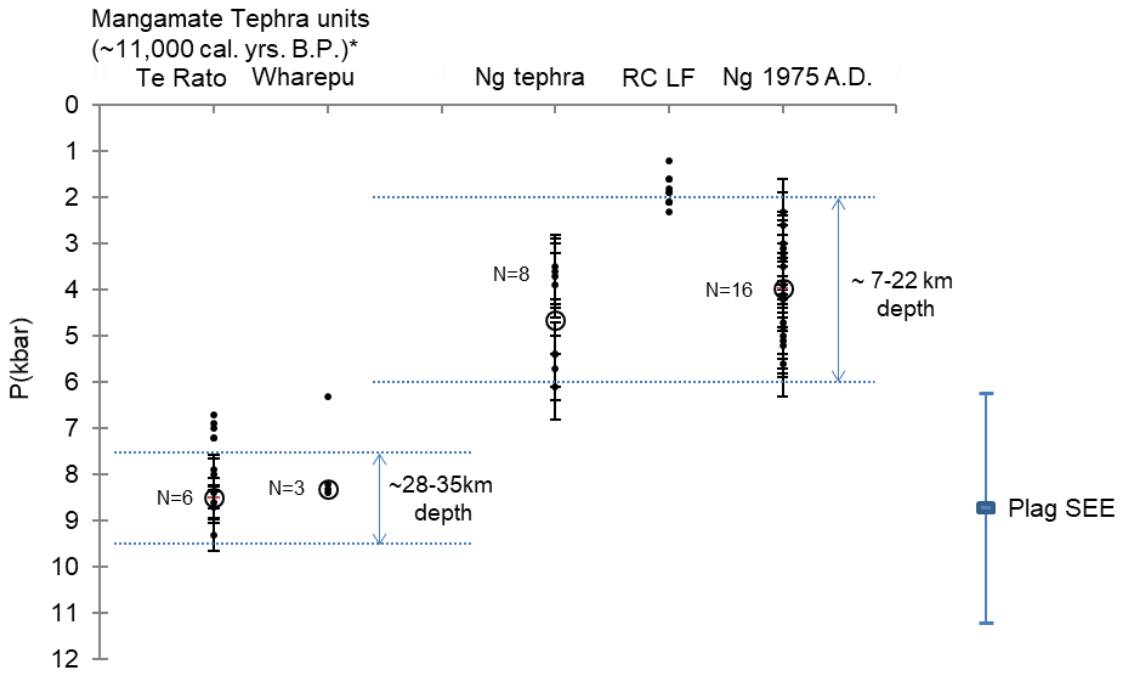

Figure 3-9. Pressures of crystallization for the pyroclast samples showing mean values (large open circle). Pressure values from the lava flow (Red Crater) are not averaged. Probable error is shown for each value for samples with more than 3 points. The dotted line represents 2 standard deviation (2σ) from the mean value for Te Rato and Ngauruhoe 1975 deposits. Equivalent depth using 2700 kg/m^3 crustal density is shown for the range of 2σ from the mean. Modeled pressures from the lenses in Te Rato and the single clinopyroxene estimate from Wharepu are excluded from the average values. Clinopyroxene-bulk and plagioclase-groundmass pressure estimates were averaged for the Ngauruhoe tephra. Abbreviations as in Figure 3-4.

Most of the crystallization pressure estimates are from plagioclase. Only the Ngauruhoe 1975 deposit has pressure estimates gathered from both plagioclase (n=6) and orthopyroxene (n=10). The results from the two minerals in the Ngauruhoe 1975 deposit are in good agreement. The mean pressure estimates from Wharepu clinopyroxenes are lower, but within model standard error of the plagioclase estimates. Equation 31 for the clinopyroxene agrees well with the plagioclase estimate (**Table 3-6b**). The 1975 deposit has water content estimated from melt inclusions in olivine and pyroxene using FTIR that is within the error range of the hygrometry results. The FTIR measurements of 0.4 to 1.9 wt.% H_2O (this study) is within the error range of the hygrometry values (0.9-1.4 +/- 1.1 wt.% H_2O). For the other deposits where there are no available FTIR measurements to confirm hygrometry results, the $Kd_{pl\text{-}liq}^{Ca\text{-}Na}$ (Table 3-6b), may

be used as an indicator of relative magma water content between the samples. $Kd_{pl\text{-}liq}^{Ca\text{-}Na}$ values increase with water content according to the study of Sisson and Grove (1993).

3.5 Discussion

3.5.1 Magma reservoirs

A region of predominant magma storage for the younger samples (Red Crater and Ngauruhoe) is represented by a crystallization depth range of about 4 to 21 km, 7 to 21 km for Ngauruhoe. The narrow range (13 to 14 km) for the older Ngauruhoe tephra probably represents a single magma reservoir that was rapidly evacuated. The resultant deposit does indicate an explosive manner of eruption – pyroclastic fall deposit and glassy groundmass for the pyroclasts. The deeper source for the younger 1975 deposit could be interpreted as a recharge event that resulted in this magmatic eruption. Note that a deeper magma reservoir exists as represented by the Mangamate units. The deepest estimate of 21 km agrees with previous depth estimates of magma accumulation for Ngauruhoe (Deering *et al.*, 2011). The magma reservoir depth estimates for the c. 1717 cal. yrs. B. P. Ngauruhoe tephra (13-14 km) and Red Crater lava flow (4-9 km) also correspond to the low resistivity zone of 4-12 km identified for Tongariro (Hill *et al.*, 2015). Because Red Crater is in the central part of the complex where elevation is higher, it is possible that the basaltic magma cannot easily have the buoyancy to reach the surface and it accumulates at a shallow reservoir until conditions for eruption are met.

Wharepu Lapilli is one of the deeper-sourced Mangamate members originating at greater than 20 km depth according to the study of Nakagawa et al. (1998). It is consistent with the results of this study, which is 30 - 31 km. The magma for Te Rato also originated at lower crustal regions (29 - 34 km), but mingled with more evolved magma at shallower levels. Crystallization depths from the dacitic bands in Te Rato are from 25 to 27 km and possibly shallower. The crystallization depths with respect to the eruption centers are shown in **Figure**

3-10. For all the samples, Wharepu has the highest temperature (1200°C) while the rest have temperatures from 1060 to <1200°C. The deeper sources for Wharepu and Te Rato magmas are consistent with the hotter regions expected at the base of the crust, assuming a crustal thickness of 30 to 35 km in the southern Taupo Volcanic Zone region (Harrison and White, 2006, Reyners *et al.*, 2006).

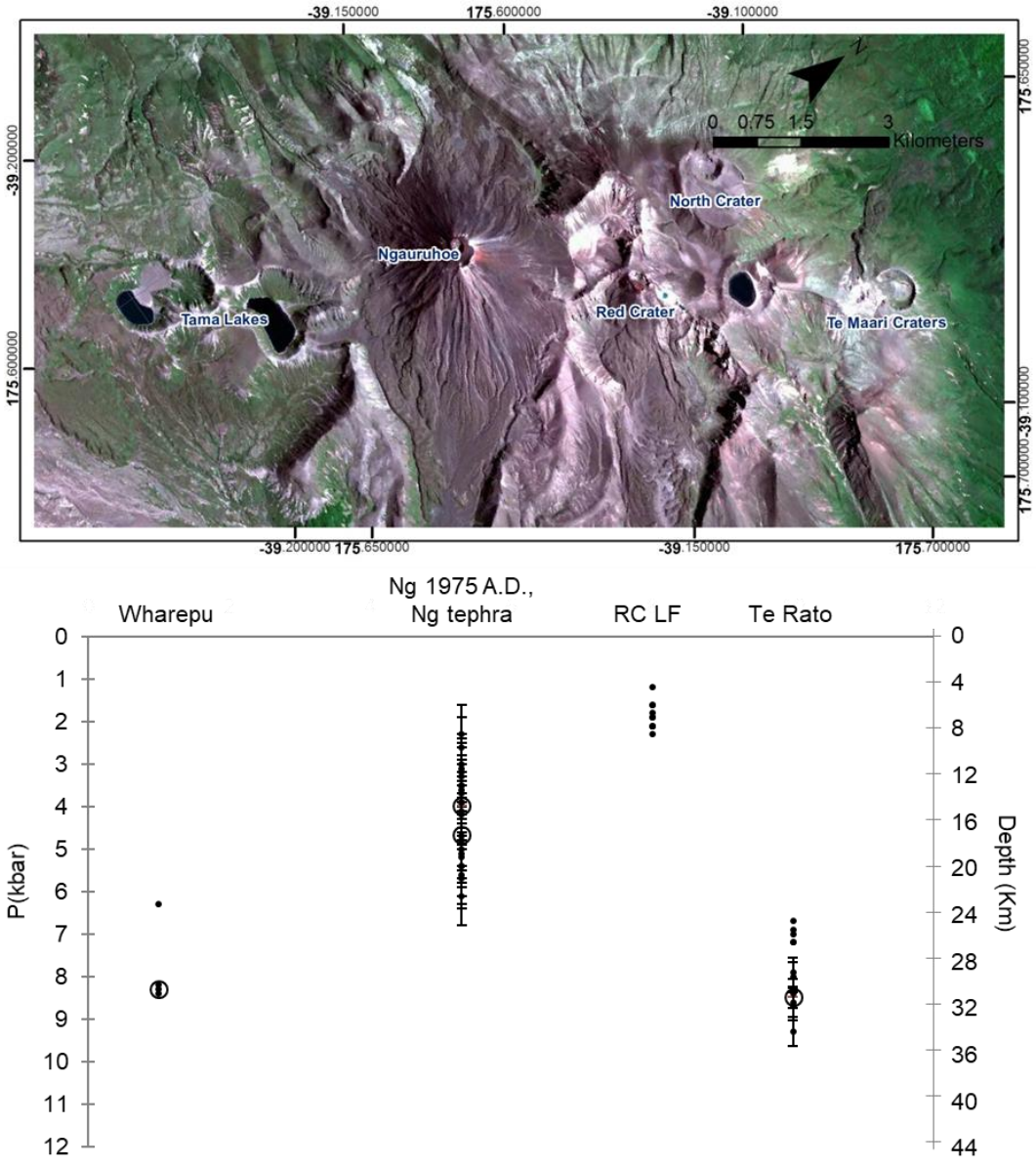

Figure 3-10. Modeled crystallization pressures and equivalent depths with respect to the general location of eruptive vents. Vent names are labelled in the imagery of the Tongariro Volcanic Complex above (note the direction of the North arrow) and the assigned vents for Te Rato tephra (from North Crater) and Wharepu tephra (from Tama Lakes) are based on Topping (1973) and Nairn et al. (1998).

3.5.2 Mingling and vesiculation at different depths for the Mangamate samples

Rapid ascent from the source for the two Mangamate tephras (Te Rato and Wharepu) is indicated by the groundmass textures such as acicular microlitic plagioclase. Rapid growth textures indicating fast ascent rates were previously documented in Nakagawa et al. (1998). Crystallization experiments show that plagioclase crystals are small and swallowtail to spherulitic for decompression crystallization with high decompression rates (Couch *et al.*, 2003). It should be noted that plagioclase crystals are extremely rare as larger phenocrysts in the Wharepu samples, but that they occur commonly as microphenocrysts is a possible indication of fast ascent. Quantified decompression rates done for basaltic magmas positively correlate with eruptive intensity magnitude (Ferguson *et al.,* 2016). High ascent rates are then not unexpected for the Mangamate tephras, because based on tephra distribution and volume, these are one of the largest eruptions from the Tongariro Volcanic Complex (Topping, 1973, Nairn *et al.,* 1998).

Crustal xenoliths and xenocrysts are found both in the Wharepu and Te Rato samples. Crustal xenoliths composed mainly of quartz are found within lenses in the Wharepu samples. The xenoliths, however, show minimal signs of dissolution (**Figure 3-3e and 3-3f**) and only 1 out of 5 groundmass analyses within the lense for Wharepu shows possible assimilation of a more evolved composition (**Figure 3-11a**). One Wharepu lense groundmass composition plots with Te Rato lense groundmass compositions in the K_2O/Na_2O vs. total FeO plot, having significantly higher K_2O/Na_2O ratio and lower total FeO than the rest of the Wharepu groundmass compositions despite having a less silicic composition than the dacitic Te Rato lense groundmass (**Figure 3-11a and 3-11b**). The xenoliths in both samples show minimal dissolution despite having compositions (quartz, albite, alkali feldspar) that would be very

unstable in a basaltic melt. For the andesite-dacite mingling in the Te Rato samples, mixing of compositions is not advanced as there is still a distinct separation of lense and host groundmass compositions at least in terms of major elements (**Figure 3-11a and 3-11b**). The influence of the crustal xenoliths on the Te Rato mingling is less clear. An albitic xenocryst was found within the more primitive host and not within the dacitic lense (**Figure 3-3d**). Because the crustal xenoliths are intact it is unlikely that the melts stalled for a long time within the crust during its rise before eruption.

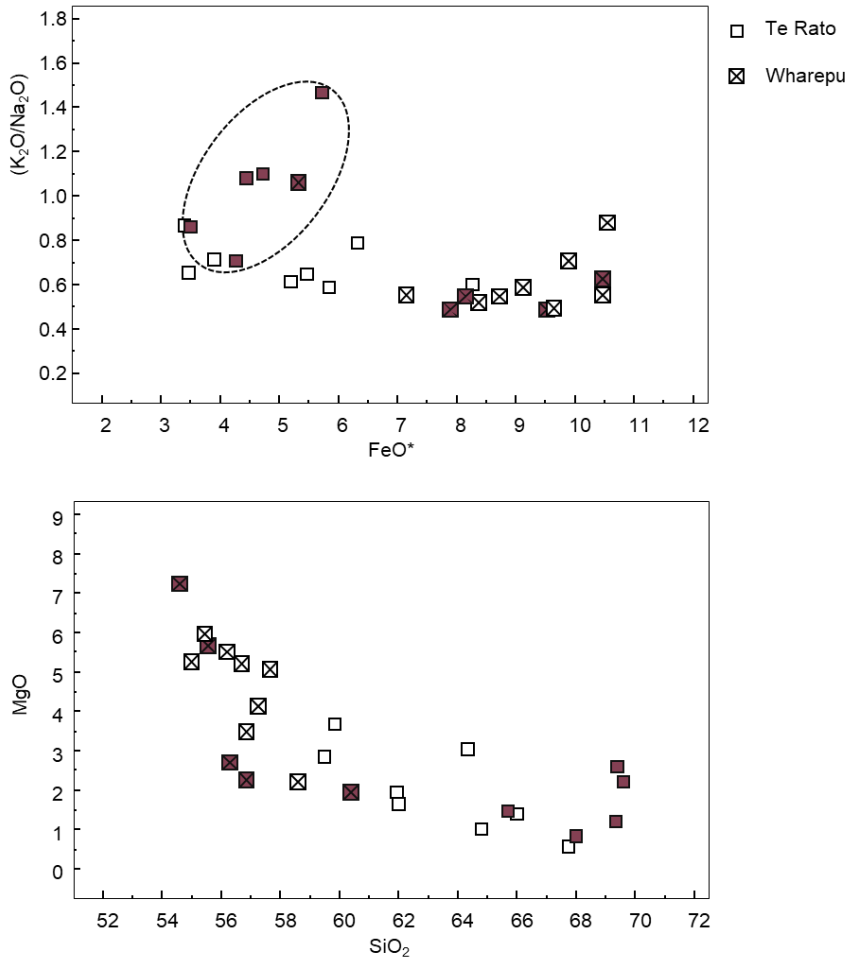

Figure 3-11. Bivariate plots of groundmass compositions for Te Rato and Wharepu, the shaded symbols represent lense groundmass. Te Rato lense groundmass can be separated from the host in the K_2O/Na_2O versus total FeO plot (circled), one lense analysis from Wharepu plot in the same area (a), but not for the MgO versus SiO_2 plot (b). This may imply that the lense in Te Rato is a mingled magma of different composition whereas the lense in Wharepu may be composed of the same magma as the host but modified by incorporation of crustal xenoliths.

Te Rato andesitic magma originating at around 34 km depth mingled with dacitic magma beginning at 27 km and continued to shallower depths. The incorporation of the crustal xenoliths in Wharepu most likely also occurred at shallower depth(s). The result for both samples are lenses with higher degrees of vesiculation and roundness (**Figure 3-3c-f**). Because of the difference in composition, vesiculation dynamics and viscosity are expected to be different for host and lense in the Te Rato sample. It was shown that for crystal-free melts, from basalt to rhyolite, viscosity increases with increasing silica (Takeuchi, 2011). The dacite lense is expected to be more viscous than the lower silica host provided that both magmas were relatively aphyric at the time of mingling. The lense vesiculation shown by the samples is more similar to homogenous-dominated bubble nucleation as determined from the experiments of Mangan and Sisson (2000) and Mangan et al. (2003). Homogenous bubble nucleation occurs in the absence of crystals and other heterogeneities and where degassing is in disequilibrium resulting in delayed vesiculation and retention of more water before being released at higher degrees of saturation (Mangan and Sisson, 2000). Equilibrium conditions show that for a melt containing 1000 mg/kg CO_2, the formation of a separate vapour phase (mainly CO_2 and noble gases), with H_2O only starting to exsolve, is expected at pressures of about 2 kbar (Giggenbach, 1996). The mingled dacite could have been nearly aphyric containing only a few plagioclase crystals at depth (7 kbar). Amphibole crystallization at water saturated conditions, based on amphibole thermobarometry done on Te Rato Lapilli, occurs at an average pressure of 351 MPa (3.5 kb) (Auer *et al.*, 2015). Amphibole crystallization requires a hydrous magma, and water degassing with consequent fine microlite crystallization would have occurred at a lower pressure than 3.5 kb. Vesiculation increases buoyancy and can lead to high exit pressures (Mangan and Sisson, 2000, Mangan *et al.*, 2004), which may have contributed to the high explosivity of the Mangamate eruptions. For the case of Wharepu where most of the material

in the lense is not from melting of the incorporated crustal material or mingled dacitic magma, the crustal material may have contributed mainly volatiles, which resulted in the more significant vesiculation (larger, rounded vesicles) within the lenses. The release of volatiles from the crustal material could be due to thermal metamorphism from heat of intruding plutons (Walther and Orville, 1982).

3.5.3 Thermobarometry results and MELTS model test for the Wharepu samples

As a verification and to have a possible petrologic process for the thermobarometry results, compositions for Wharepu were modeled using Rhyolite-MELTS (Ghiorso and Sack, 1995, Gualda *et al.*, 2012). A composition (less quartz) (**Table 3-3**) calculated for sample 150320-01E-b (Wharepu) was used as a starting composition for the crystallization model. Initial bulk water content was set at 1.0 wt.%, a rounded minimum value from the plagioclase hygrometry (**Table 3-6b**). Ferrous/Ferric iron ratio was set to be 5.4-5.5 to give a resulting oxidation state between NNO and FMQ (ΔNNO: -0.74 to 0.4). The composition was crystallized by equilibrium crystallization at constant pressure (8 kbar) and decreasing temperature from 1300 to 1110ºC. Ascent was then modeled by decompression of the bulk composition from 8 kbar to 0.5 kbar with a decrease in temperature from 1150 to 1135ºC. The model results (**Figure 3-12**) are compared with observed groundmass (host) compositions and plagioclase compositions with modeled crystallization pressures from plagioclase thermobarometry (Putirka, 2008). **Figure 3-12a** shows the track of the liquid as the magma crystallizes at 8 kbar and as the magma melts when it is decompressed from 8 kbar to 0.5 kbar. The model roughly follows the observed trend, although there is some scatter in the observed groundmass composition. Plagioclase compositions used in thermobarometry yield crystallization pressures of 8.4 kbar (**Table 3-6b**). It is also in agreement with plagioclase crystallized at 8 kbar using Rhyolite-MELTS (**Figure 3-12b**). Plagioclase starts crystallizing at 8 kbar and 1180ºC with An content of 71.77, similar to the thermobarometry results of 8.2 to 8.4 kbar and 1216ºC. Starting crystallization at 9 kbar

crystallizes plagioclase with slightly lower An content than the samples (**Figure 3-12b**). Plagioclase An content decreases as it crystallizes at 8 kbar, but increases as the bulk composition is decompressed (**Figure 3-12a**) due to melting of low An plagioclase and clinopyroxene and adjustment to the melt composition. When pressure is decreased from 8 to 0.5 kbar the amount of plagioclase is decreased by half because of melting, however the observed rapid crystallization textures can be due to microlite crystallization during degassing. The MELTS polybaric model produces plagioclase with too high An content that is not seen in the present data. Natural system complexities may not be represented in the model as our input set-up was kept simple and only composition, temperature and pressure were set and no other conditions were imposed. At decompression, clinopyroxene and plagioclase melt starting at 8 kbar, orthopyroxene starts to melt at 2 kbar and olivine crystallizes starting at 1 kbar. **Figure 3-13a** shows the olivine thermometer results in good agreement with the MELTS model temperature and pressure of crystallization of 1136-1135ºC and 1-0.5 kbar, respectively. The olivine temperature plotted in the graph is from equation 15, which is based on a liquid saturated with olivine. Whether the olivine analysed is a xenocryst, that by coincidence has a composition in equilibrium with the melt, is irrelevant when equation 15 is used. The photo of a well formed skeletal olivine (**Figure 3-13b**), which may indicate late and rapid crystallization, also has an orthopyroxene composition near the core and agrees with the model that shows the appearance of olivine at a pressure where orthopyroxene decreases in the magma. Overall, the MELTS model can show a scenario for the thermobarometry results from the Wharepu samples.

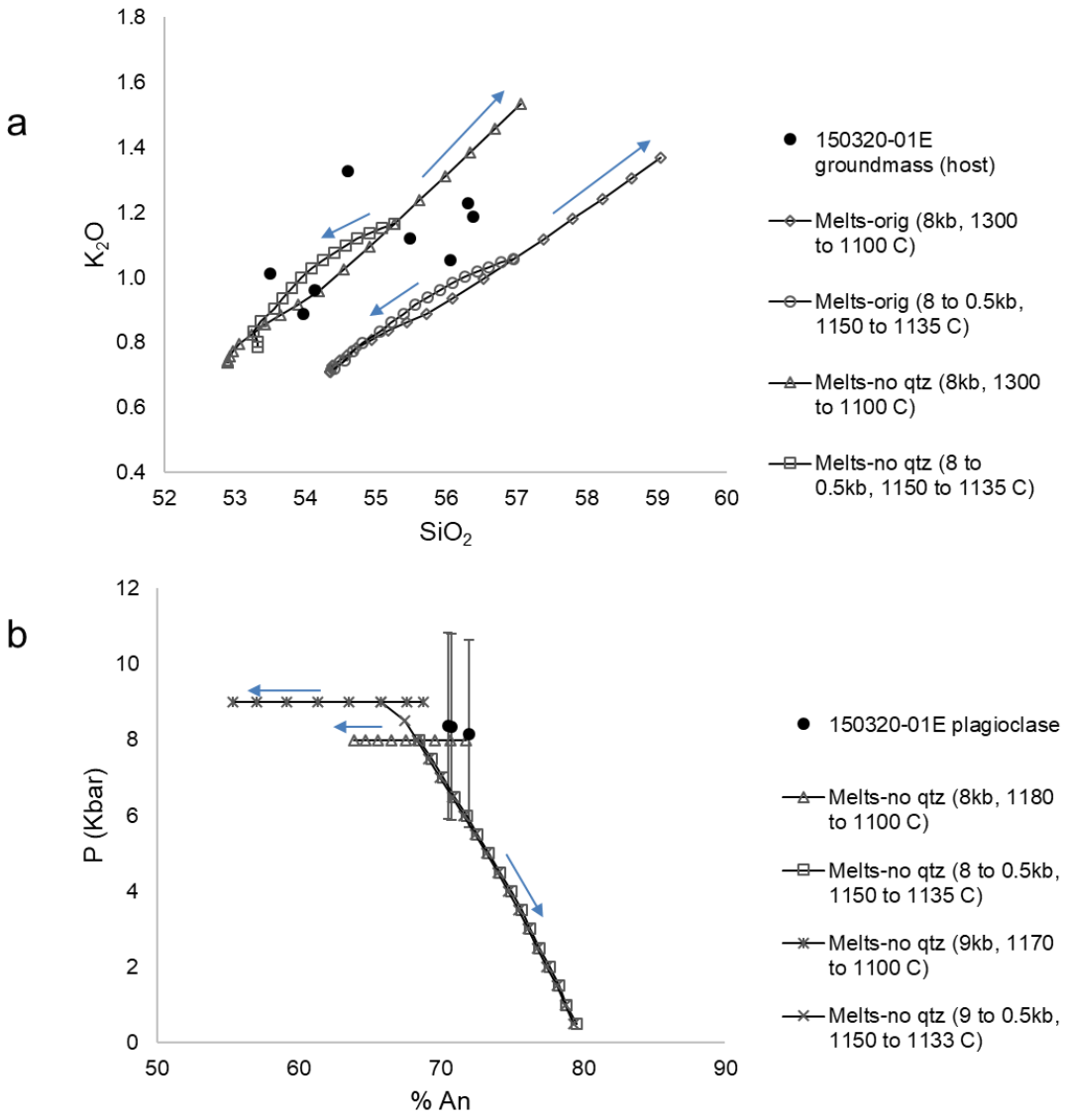

Figure 3-12. Rhyolite-MELTS model for Wharepu compositions. The crystallization and decompression paths of liquid are shown relative to the actual groundmass analysis, model results for the original composition of 320-01E-b is shown for comparison (a). Plagioclase %An composition at pressures for the crystallization and decompression MELTS models starting at 8 kbar and 9 kbar using the calculated bulk composition (b). Pressures from plagioclase used in the thermobarometer are also shown, the error bars represent model SEE. The arrows show the direction from the start to the end composition results for each model.

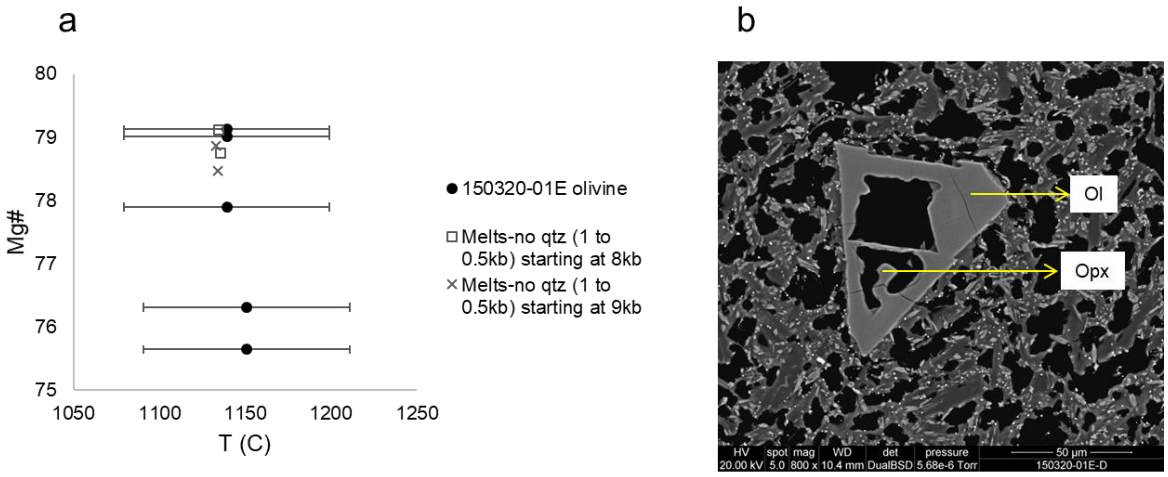

Figure 3-13. Comparison of olivine composition (Mg#) and crystallization temperature from the MELTS model at 0.5 to 1 kbar pressure and the results of liquid (saturated with olivine) thermometer (Equation 15, Putirka (2008)) (a). Error bars are SEE for the thermometer model. Backscattered electron image of a skeletal olivine, the well-formed crystal face with a dissolving orthopyroxene core supports the MELTS model of crystallization of olivine at the expense of orthopyroxene (b).

3.6 Conclusions

The depths of magma accumulation/reservoir regions estimated from depth of crystallization for Tongariro deposits appear to be variable for the different source vents and with time. The deepest sourced (28 - 35 km) samples in this study are the two Mangamate units (Te Rato and Wharepu) erupted at about 11,000 cal. yrs. B.P. Textures show that these magmas ascended rapidly to the surface and that mingling of dacitic magma for the Te Rato event occurred at a shallower depth. The younger deposits have sources at about 4 to 21 km with a predominant region of about 7 to 22 km depth. The shallowest depth of 4 to 9 km is from a Red Crater lava flow. Temperatures of 1216 to 1066°C determined by geothermometry are typical for basaltic to andesitic samples.

The decrease in magma reservoir depth following the highly explosive, high-magnitude Mangamate eruptives coincides with a marked drop in eruption frequency and magnitude across the entire Tongariro Volcanic Centre (Donoghue *et al.*, 1995, Moebis, 2010). Whether

the decrease in magma reservoir depths after the c. 10 ka eruptions is a general feature of the Tongariro Volcanic Centre may be verified in future by additional pressure and temperature of crystallization models for eruptive products of Tongariro and Ruapehu. The results of this study may also reflect not a temporal variation but a spatial variation and subsequent studies can test whether source depths can be linked to tectonic activity and plumbing structure.

Acknowledgments

We thank Bob Stewart, Anja Moebis and Clel Wallace at Massey University and Ian Schipper at Victoria University for their advice and assistance in the laboratory. Sample collection and analyses were funded by GNS Science (Project number 420W4340-00) and IAE, Massey University. We also thank the Associate Editor Judy Fierstein and reviewers Keith Putirka and Kayla Iacovino for their constructive comments and suggestions.

4 Melt inclusion volatile contents from Tongariro deposits: insights on crystallization and magmatic processes

4.1 Abstract

Melt inclusion major element composition including volatiles (H_2O, CO_2, S and Cl), interpreted in terms of host (olivine and pyroxene) crystallization conditions and degassing processes, provide insights on magmatic processes for different eruptions from Tongariro Volcano. Equilibrium crystallization conditions and volatile degassing paths yield different scenarios for eruptions that range from highly explosive to effusive. Crystallization temperature and pressure from mineral components and volatile content of melts from a Te Maari Crater lava flow show possible degassing from a shallow reservoir where xenocrystic olivines were incorporated. Volatile contents, particularly molecular water, may be significant in the resulting explosive eruption that produced the Wharepu Tephra. Volatile composition inputs in crystallization and melting models and volatile composition trends provide possible general magmatic processes for the different deposits from Ngauruhoe and other eruptive centres of Tongariro.

4.2 Introduction

The literature on magmatic volatiles is extensive, because of their importance in understanding and predicting volcanic activity. Magmatic degassing processes are viewed from the perspective of volatiles still dissolved in the magma as melt inclusions (Gerlach *et al.*, 1996, Belkin *et al.*, 1998, Wallace *et al.*, 2003, Metrich and Wallace, 2008, Plank *et al.*, 2013, Lloyd *et al.*, 2014), and from exsolved volatiles measured at the surface (Gerlach, 1986, Taran *et al.*, 1995, Giggenbach, 1996, Allard, 1997, Kazahaya *et al.*, 2002, Aiuppa *et al.*, 2009, Christenson *et al.*, 2010). Magmatic volatile data are interpreted based on the understanding that gas species have different magmatic solubilities that are dependent on pressure, temperature, melt composition and kinetics (Gerlach, 1986, Burnham, 1994, Carroll and Webster, 1994,

Holloway and Blank, 1994, McMillan, 1994, Dixon *et al.*, 1995, Zhang *et al.*, 1995, Giggenbach, 1996), and thus changes in chemistry of volcanic gases are good indicators of a rising magma body. The most recent eruption from Tongariro, the August 2012 at Te Maari Crater, for example, was predicted from time-series fumarolic gas data (Christenson *et al.*, 2013).

Presented here are volatile compositions (H_2O, CO_2, S, Cl) of Tongariro magmas measured from melt inclusions. The melt inclusions are hosted in pyroxene and olivine crystals. The crystallization pressures and temperatures of the host crystals were determined from thermobarometry and crystallization models (Ghiorso and Sack, 1995, Putirka, 2008, Gualda *et al.*, 2012). Volatile compositions and degassing paths were interpreted in terms of host mineral (pyroxene, olivine, xenocrystic or in equilibrium with groundmass), type of deposit and style of eruption, with the objective of determining implications on volcanic hazards. The volatile compositions from past eruptions determined here can be modelled to further understand the present degassing at Tongariro.

The data set consists of 5 deposits from Tongariro Volcano. There are two lava flows (ca. 1500 AD Te Maari LF, post-1717 cal. years BP Red Crater LF) (Topping, 1974, Hobden, 1997), two pyroclast generating eruptions from Ngauruhoe (February 1975 pyroclasts (Ng75 in text), pre-1717 cal. years BP Ngauruhoe tephra (Ng tephra in text)) (Nairn and Self, 1978, Lube *et al.*, 2007), and the Wharepu Tephra of the ca. 11,000 cal. years BP Mangamate formation (Topping, 1973, Lowe *et al.*, 2008). These deposits were selected based on explosivity (VEI: 2-5) (www.volcano.si.edu), volume (0.0034 – 0.2 km^3) (Topping, 1973, Nairn and Self, 1978, Donoghue *et al.*, 1995) and mineral constituents (containing olivine). The deposit from the most explosive (VEI: 5) and largest volume (0.2 km^3) eruption in this set is the Wharepu Tephra (Topping, 1974), whereas the lava flow deposits were from smaller-scale effusive eruptions.

The Ngauruhoe deposits are from vulcanian eruptions of intermediate size and scale (Nairn and Self, 1978, Hobden *et al.*, 2002, Lube *et al.*, 2007).

4.3 Methods

Melt inclusions were selected from olivine and pyroxene crystals retained in the 35 - 60 mesh (<500 μm, >250 μm). The unexposed melt inclusions were photographed and described. Olivine crystals from 3 samples (150320-01e-a (Wharepu), 150319-02-a2 (Ng75), 160727-01-c (Te Maari)) containing partially crystallized melt inclusions (Te Maari) and glassy melt inclusions with shrinkage bubbles were sent to the School of Earth Sciences, University of Tasmania for melt inclusion homogenization. The heating experiment took 2 minutes at 1140 ± 3 °C for sample 150320-01e-a, 1145 ± 3 °C for sample 150319-02-a2, and 1270 ± 3 °C for sample 160727-01-c. The temperatures were based on olivine-liquid thermometer (Putirka, 2008) using previously analysed olivines from the samples and whole rock compositions as liquid. The melt inclusions were analysed for total H_2O, molecular H_2O and CO_3 dissolved in glass by FTIR (Fourier Transform Infrared) using a Nicolet Continuum FT-IR microscope at the Institute of Agriculture and Environment, Massey University, in Palmerston North. The inclusions ranged in diameter from 100 to 20 microns, with the smallest size constrained by minimum beam diameter for the FTIR. Total water and molecular water were measured from the absorbance at 3550 - 3535 cm^{-1} and 1630 cm^{-1}, respectively. Carbonate absorbance was at 1515 and 1430 cm^{-1} and the absorbance heights were averaged. Total H_2O, molecular H_2O, and CO_2 concentrations were calculated using the Beer-Lambert equation:

$$C = M.W.*Abs/ \epsilon * \rho * d$$

where: C=concentration in units of weight fraction, M.W.=molecular weight of substance being measured, Abs=intensity of the absorbance (measured height from baseline),

ϵ=extinction coefficient (L/mol*cm), ρ=density of the glass (g/L), d=thickness of the sample or path length (cm).

The extinction coefficients (ϵ) used are 63 L/mol*cm (3550 cm^{-1}) and 28 L/mol*cm (1630 cm^{-1}) for basalt (Dixon *et al.*, 1988, Dixon *et al.*, 1995), 62 L/mol*cm (3550 cm^{-1}) and 42 L/mol*cm (1630 cm^{-1}) for andesite (Mandeville *et al.*, 2002), and 90 L/mol*cm (3550 cm^{-1}) and 55 L/mol*cm (1630 cm^{-1}) for rhyolite (Newman *et al.*, 1986, Hauri *et al.*, 2002). The silica value range used only for the selection of ϵ in this study are as follows: 50-56 wt.% (basalt), 57-65 wt.% (andesite) and >65 wt.% (rhyolite). It was shown that ϵ varies linearly with the cation sum of Si^{4+} and Al^{3+} (Dixon *et al.*, 1995), and **Figure 4-1** shows the ϵ (1630 cm^{-1}) versus Si^{4+} + Al^{3+} of standards (Dixon *et al.*, 1995) with the ϵ (1630 cm^{-1}) selected for the samples.

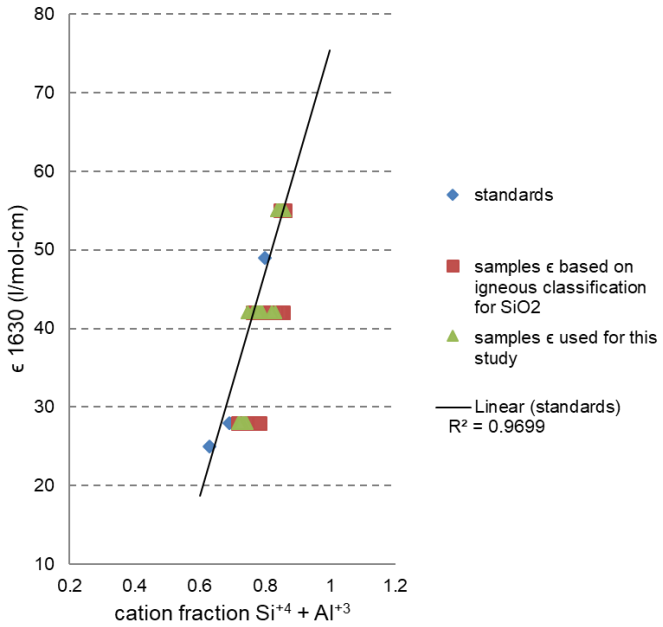

Figure 4-1. Extinction coefficients ϵ (1630 cm -1) variation with cation sum Si^{4+} + Al^{3+} established by standards (Dixon *et al.*, 1995). Cation sum of samples and assigned ϵ for determining molecular water concentration plot well with the established trend.

Major element compositions for melt inclusions and host minerals were measured by electron microprobe using a JEOL JXA-8230 Electron Probe Micro-Analyzer (EPMA) equipped with

5 wavelength dispersive X-ray spectrometers (WDS) at the School of Geography, Environment and Earth Sciences, Victoria University of Wellington. Additional analyses for groundmass and mineral phases (plagioclase, pyroxene, olivine, magnetite and ilmenite) in thin sections were done for the Te Maari sample. The minerals were analysed using a focused beam of 1 μm spot size at an accelerating potential of 15 kV and beam current of 12 nA. A defocused beam at 8 nA current with spot size from 10 to 5 μm was used for melt inclusion glass.

The minerals were polished into wafers to expose the melt inclusion for FTIR measurements. The wafers were then mounted on epoxy and polished for EPMA analysis. During the process of sample preparation some mineral wafers were lost, resulting in some melt inclusions with FTIR data, but without glass composition. Because glass composition is necessary for glass density calculation and selection of ϵ for the Beer-Lambert equation, melt inclusions that were lost were assigned proxy glass compositions. The proxy compositions were either taken from remaining melt inclusions in the mineral host or other melt inclusions from the same type of mineral host (olivine or pyroxene). In most cases, proxy compositions are the average of other melt inclusion compositions from the same type of mineral host in the same deposit. To check for possible errors, an actual composition of 57 wt.% SiO_2 was substituted with extreme values of 75 and 41 wt.% SiO_2 for the computation of water compositions. The results show that 1 standard deviation for the resultant water compositions is within 15% of the actual value. Proxy compositions are used only for the computations of H_2O and CO_2 concentrations and were not used in other element plots. All FTIR data (spectral retrievals and parameters used for the Beer-Lambert equation) are included in **Appendix Table 10** and those with proxy composition are indicated, selected compositions shown in **Table 4-1** are all actual compositions.

Parameters and input conditions for the Rhyolite MELTS (Ghiorso and Sack, 1995, Gualda *et al.*, 2012) and DCompress (Burgisser *et al.*, 2015) models as well as additional data processing can be found in **Appendix Table 11**. For input in the clinopyroxene-liquid thermobarometer

(Putirka, 2008), values for Na_2O in the Te Maari clinopyroxenes were corrected using the equation:

$$Na_2O_{(new)} = (Na_2O_{(measured)} + 0.6306)/1.0145$$

based on regression of reference and average measured Na_2O value from standards Kakanui augite (NMNH 122142), Basalt glass (NMNH 113498-1 A-99) and Rhyolite glass (NMNH 72854 VG-568) with R^2=0.9729 (**Appendix Table 8**). This correction is necessary because Na_2O measurements in the clinopyroxene standard and samples are low and will not yield results in the clinopyroxene thermobarometer.

4.4 Results

4.4.1 Evaluation of melt inclusion and host crystal equilibrium

Melt inclusions for this study are contained in pyroxene and olivine crystals from five deposits of Tongariro Volcano. For the analyses used here, the melt inclusions should ideally show no evidence of crystallization, be comprised of pure glass, and lack bubbles that may contain a fluid phase (Belkin *et al.*, 1998). Glassy melt inclusions were from the more explosive type of deposits (Ngauruhoe pyroclasts and Wharepu tephra), and may represent rapid quenching (Wallace *et al.*, 2003). The melt inclusions from the lava flows (Te Maari and Red Crater), on the other hand, are partially crystallized. Melt inclusions that are not partially crystallized range in silica composition from 49.43 to 65.58 wt.%, whereas partially crystallized melt inclusions have glass compositions of 42.57 to 75.78 wt.% SiO_2 (**Figure 4-2**). **Figure 4-2** shows the range of compositions for all melt inclusions, including homogenized samples, in terms of SiO_2 and Mg#.

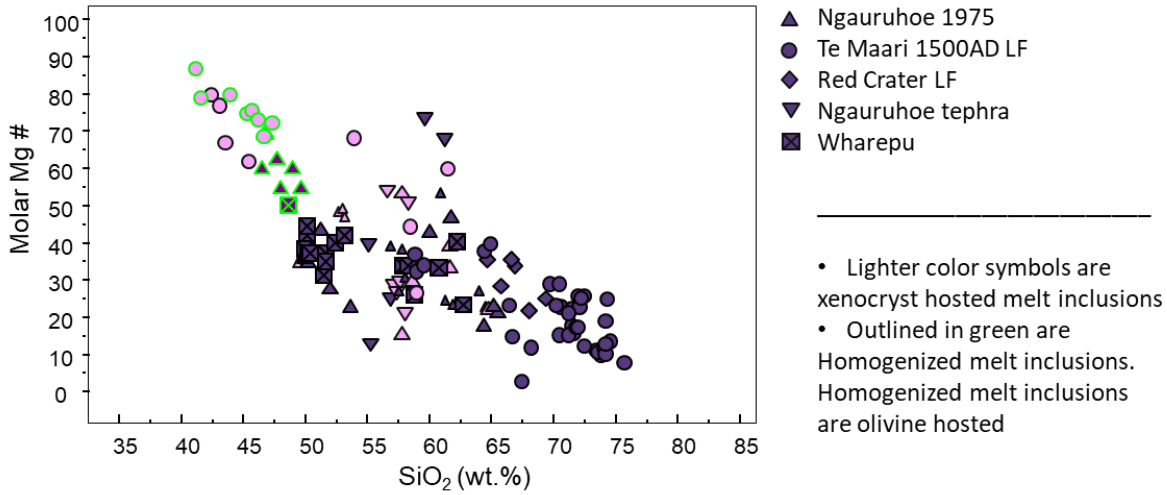

Figure 4-2. Compositional variation in terms of Mg# and SiO_2 for melt inclusions from all the deposits in this study. Pyroxene and olivine hosted melt inclusions are not distinguished by color. Melt inclusions show a wide composition range reflecting different crystal host histories.

Host crystal compositions were evaluated for equilibrium with groundmass and/or whole rock compositions. The equilibrium criteria for olivine-melt and pyroxene (clinopyroxene and orthopyroxene) – melt are from coefficients of distribution, $K_d(Fe\text{-}Mg)^{Ol\text{-}melt} = 0.3 \pm 0.03$, $K_d(Fe\text{-}Mg)^{opx\text{-}liq} = 0.29 \pm 0.06$ and $K_d(Fe\text{-}Mg)^{opx\text{-}liq} = 0.27 \pm 0.03$ (Putirka, 2008). Crystal hosts that are not in equilibrium with groundmass and could possibly be xenocrysts were identified and considered in interpretations. These were not excluded and are shown in plots as symbols with lighter color (also mentioned in plot legends). In general, more olivine than pyroxene host crystals are not in equilibrium with their groundmass. Only in Red Crater and Wharepu samples are all crystal hosts non-xenocrystic. For the Te Maari lava flow, none of the analyzed olivines are in equilibrium with groundmass. Olivines from the Te Maari lava flow have Fo# as high as 91.7. The Te Maari olivines plot with non-xenocrystic olivines from Red Crater (**Figure 4-3**). Selected host mineral and melt inclusion compositions are listed in **Table 4-1**, maximum groundmass and bulk rock Mg# for the samples are also shown. All melt inclusion and host compositions are available in **Appendix Table 7 and 10**.

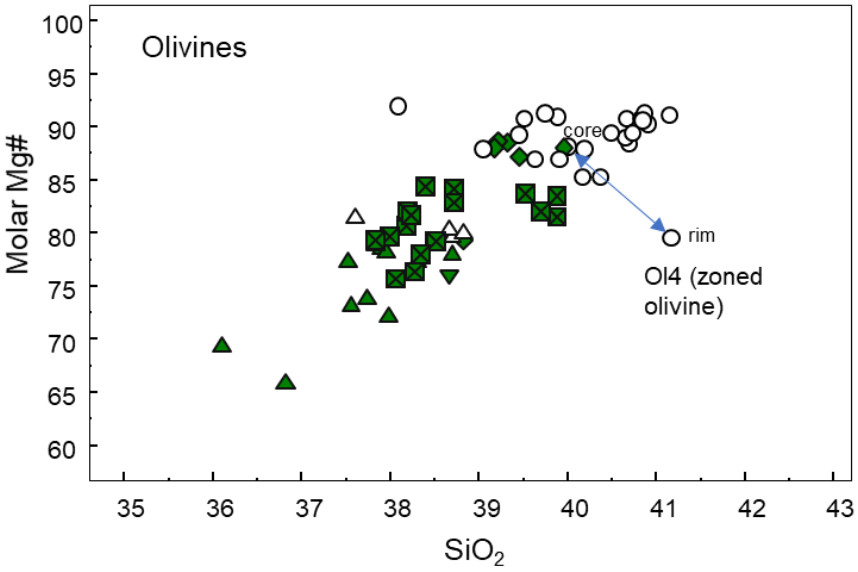

Figure 4-3. Te Maari lava olivine xenocrysts (white circles) plot with Red Crater lava olivines (green diamonds). Note the difference in core and rim composition of a zoned olivine. Deposit symbols are as in Figure 4-2.

Table 4-1. Selected melt inclusion and mineral host compositions.

SiO_2	TiO_2	Al_2O_3	FeO	MnO	MgO	CaO	Na_2O	K_2O	P_2O_5	Cr	Ni	Cl	S	H_2Ot	H_2O molec	O H	CO_2	Total	Sample #	Comment	Host Mg#	MI Mg#	Maximum Mg#		WR Ni
				wt%						ppm	ppm	ppm	Ppm	wt%	wt%	wt%	ppm								ppm
																							WR	GM	
Ngauruhoe 1975 (150319-02)																							54.12	40.70	15 - 26
52.46	0.28	1.16	22.41	0.52	22.26	1.98	-	-	-	130.00	-	-	-					101.08	b2-mi-px1	px	63.91				
65.35	0.86	14.18	5.93	0.11	0.96	3.97	3.34	2.96	-	23.95	-	2350	304	1.21	0.53			97.98	b2-mi-px1-1 *	mi		22.38			
38.71	0.01	-	20.36	0.29	40.80	0.14	-	-	-	-	251.46	-	-					100.33	a2-mi-ol1	ol	78.13				
50.11	0.92	19.65	5.51	0.10	1.73	10.92	2.88	0.62	-	54.74	-	1460	1201	1.79	0.99	0.80		92.89	a2-mi-ol1-1 *	mi		35.86			
37.92	-	-	19.59	0.17	40.13	0.13	-	-	-	75.26	715.09	-	-					98.03	a2-mi-h-ol2	ol	78.51				
47.83	0.78	16.97	8.35	0.14	7.83	9.97	2.56	0.44	-	47.89	-	1415	1130	1.27	0.34	0.92	244	95.27	a2-mi-h-ol2-1 *	mi		62.57			
38.36	-	-	19.67	0.20	39.25	0.13	-	-	-	34.21	345.76	-	-					97.66	a2-mi-h-ol3	ol	78.06				
49.68	0.80	16.18	9.69	0.16	6.64	8.95	2.36	0.62	-	92.37	-	1335	1560	1.35	0.64	0.71		95.59	a2-mi-h-ol3-1 *	mi		55.00			
37.52	-	-	20.15	0.19	38.86	0.15	-	-	-	123.16	801.53	-	-					97.00	a2-mi-h-ol4	ol	77.47				
48.10	0.83	17.75	9.14	0.14	6.27	9.92	2.79	0.48	-	184.74	-	1600	924	0.68	0.00	0.68		95.79	a2-mi-h-ol4-2	mi		55.00			
50.26	0.44	4.36	6.98	0.16	15.89	19.37	0.06	-	-	2894.21	-	-	-					97.93	a2-mi-px4b	px	80.23				
57.75	0.78	16.48	7.76	0.08	0.81	4.32	3.11	1.30	0.07	130.00	-	1400	1572	0.73	0.57	0.16	175	92.98	a2-mi-px4-1	mi		15.67			
37.60	-	-	16.55	0.00	41.23	0.03	0.00	-	-	116.32	-	-	-					95.43	a1-mi-ol3	ol	81.62				
49.43	0.86	18.65	5.41	0.07	1.60	10.62	3.20	0.56	-	-	-	1700	528	0.14				90.66	a1-mi-ol3-1	mi		34.54			
38.82	0.01	-	18.31	0.25	41.14	0.03	0.01	-	-	-	392.90	-	-					98.61	a1-mi-ol7	ol	80.02				
52.97	0.91	20.63	6.33	0.10	3.26	11.61	3.03	0.64	0.03	34.21	-	1710	560	0.51	0.16	0.35		99.78	a1-mi-ol7-1b *	mi		47.98			
51.93	0.21	1.35	16.33	0.40	24.26	1.68	0.01	-	-	246.32	-	-	-					96.21	a1-mi-px1a	px	72.58				
57.39	0.86	15.38	6.14	0.14	2.17	5.56	3.33	1.55	0.09	-	-	1205	738	0.72	0.33	0.39		92.89	a1-mi-px1-1 *	mi		38.62			
57.53	0.86	14.74	5.96	0.12	1.24	4.84	3.35	1.79	0.14	-	-	1260	460	0.84	0.34	0.50		90.79	a1-mi-px1-2	mi		26.99			
52.37	0.19	0.78	17.75	0.31	23.85	1.79	0.00	-	-	280.53	-	-	-					97.07	a1-mi-px4	px	70.54				
64.59	1.02	13.60	6.18	0.05	1.02	4.03	3.50	2.88	0.28	47.89	-	2190	388	0.61	0.29	0.32		97.42	a1-mi-px4-1a	mi		22.66			
Te Maari ~1500 AD lava flow (160727-01)																							63.04	34.80	101 - 118
52.36	0.38	1.72	9.60	0.30	14.92	20.13	0.07	-	-	-	157.16	-	-					99.50	c-mi-px1	px	73.47				
71.52	0.51	14.54	1.71	-	0.20	1.79	3.84	3.32	-	61.58	-	2710	184	0.90	0.79	0.12	84	97.71	c-mi-px1-2	mi		17.45			
52.73	0.31	1.37	10.18	0.27	14.50	20.47	0.05	-	-	54.74	-	-	-					99.87	c-mi-px2	px	71.75				
70.74	0.48	14.06	1.98	0.06	0.32	2.31	3.97	3.07	0.10	-	-	2720	136	2.14	1.68	0.46		97.32	c-mi-px2-1	mi		22.17			
52.32	0.45	1.72	9.65	0.29	14.75	20.07	0.05	-	-	-	282.89	-	-					99.33	c-mi-px7	px	73.15				
72.12	0.53	13.95	1.85	0.06	0.35	1.78	3.54	3.25	-	-	-	2700	104	1.25	1.07	0.18		97.66	c-mi-px7-1	mi		25.40			
51.99	0.41	1.93	10.75	0.38	14.18	19.81	0.08	-	-	143.68	-	-	-					99.54	c-mi-px18	px	70.17				

71.99	0.64	14.12	1.67	0.03	0.19	2.02	3.97	3.03	0.02	75.26	-	2320	104	2.06	1.72	0.34		97.89	c-mi-px18-1 *	mi		16.77			
40.76	-	0.02	10.36	0.13	48.18	0.04	-	-	-	335.26	2522.45	-	-					99.86	c - m i - o l 7	ol	89.24				
59.06	0.53	22.16	1.32	0.12	0.26	5.73	3.84	1.36	0.14	41.05	-	4560	2300	1.63	0.98	0.66		95.55	c-mi-ol7-1a	mi		26.20			
38.12	-	-	7.54	0.11	46.69	0.17	-	-	-	157.37	1870.23	-	-					92.88	c-mi-h-ol1	ol	91.70				
44.10	0.67	13.16	5.79	0.12	12.52	11.55	1.63	0.41	-	998.95	-	1910	1900	1.35	0.35	1.00		90.73	c-mi-h-ol1-1 *	mi		79.41			
39.90	-	-	8.76	0.09	48.38	0.16	-	-	-	321.58	3080.37	-	-					97.73	c-mi-h-ol4	ol	90.78				
45.86	0.76	15.00	5.93	0.10	10.11	12.67	2.17	0.53	-	294.21	-	2000	2404	2.27	0.44	1.83	470	93.93	c-mi-h-ol4-1a	mi		75.26			
39.52	-	-	9.03	0.07	48.45	0.16	-	-	-	574.74	2593.17	-	-					97.64	c-mi-h-ol9	ol	90.54				
46.32	0.66	13.63	7.87	0.15	11.74	10.81	1.87	0.49	-	307.89	-	1495	1840	1.87	0.25	1.62	311	94.16	c-mi-h-ol9-1 *	mi		72.67			
Red Crater post-1717 cal. years BP lava flow (150318-03)																							61.33	57.17	58
52.01	0.28	1.17	10.05	0.35	14.21	20.98	0.18	-	-	6.84	-	-	-					99.22	m i - p x 1	px	71.59				
67.00	2.47	10.53	3.97	0.23	1.12	5.36	1.84	2.41	-	-	-	2010	84	0.38	0.10	0.28		95.11	m i - p x 1 - 1	mi		33.34			
52.51	0.24	1.60	20.89	0.52	22.96	1.25	0.02	-	-	253.16	-	-	-					100.04	m i - p x 2	px	66.21				
65.76	0.80	13.38	5.76	0.09	1.26	4.72	2.08	1.82	-	294.21	-	2090	132					95.89	m i - p x 2 - 1	mi		28.00			
51.93	0.28	1.26	9.73	0.33	14.39	21.81	0.20	-	-	6.84	-	-	-					99.93	m i - p x 3	px	72.50				
64.71	0.74	15.28	3.57	0.13	1.08	4.67	2.00	2.25	-	-	-	1885	14	0.99	0.48	0.51		94.58	mi-px3-1 *	mi		35.06			
69.43	1.08	10.44	5.28	0.08	0.97	3.59	1.46	3.57	-	30.79	-	2365	1110					96.35	mi-px3-2 *	mi		24.70			
51.71	0.41	1.89	9.71	0.34	14.68	20.64	0.23	-	-	47.89	-	-	-					99.61	m i - p x 4	px	72.95				
68.10	0.63	12.85	3.82	0.10	0.58	1.81	1.81	3.36	-	-	-	2830	108	0.90	0.50	0.40		93.32	mi-px4-1	mi		21.37			
66.70	0.74	13.39	4.08	0.05	1.23	3.59	2.08	2.85	-	82.11	-	2010	1780	0.49	0.15	0.34		95.33	mi-px4-2	mi		35.03			
Ngauruhoe pre-1717 cal. years BP tephra (150319-01)																							59.67	46.37	28 - 37
53.63	0.16	1.76	5.25	0.16	19.12	17.92	0.05	-	-	773.16	172.88	-	-					98.18	e - m i - p x 1	px	86.65				
58.30	0.58	15.46	4.85	0.42	2.75	5.26	2.84	1.22	0.04	-	-	680	1672	0.54	0.26	0.28	215	92.20	e-mi-px1-1	mi		50.29			
50.81	0.48	2.95	8.44	0.27	15.95	17.67	0.05	-	-	780.00	-	-	-					96.74	e - m i - p x 4	px	77.11				
56.98	1.21	14.09	8.10	0.17	1.46	4.83	3.66	2.03	0.14	20.53	-	2320	428	0.92	0.42	0.50	0	92.98	e-mi-px4-2	mi		24.35			
52.02	0.33	2.71	6.70	0.18	16.64	20.01	0.03	-	-	2312.63	196.45	-	-					98.98	e - m i - p x 6	px	81.58				
57.22	0.88	18.69	5.96	0.10	1.30	5.14	3.48	1.47	0.02	41.05	-	2560	1236	1.12	0.84	0.27	0	94.77	e-mi-px6-1	mi		27.96			
Wharepu Tephra (150320-01e)																							53.48	57.49	14 - 22
52.17	0.40	1.96	10.69	0.32	14.67	19.73	0.07	-	-	61.58	-	-	-					100.02	a-mi-px7a	px	70.99				
58.11	0.85	14.84	7.77	0.16	2.20	5.70	2.59	1.26	0.07	-	-	2030	904	0.93	0.85	0.08	0	93.92	a-mi-px7-1 *	mi		33.55			
52.21	0.51	2.65	9.18	0.24	15.15	19.97	0.29	0.01	-	184.74	-	-	-					100.24	a-mi-px12a	px	74.64				
62.35	0.79	15.70	5.20	0.09	1.96	5.25	1.54	1.93	-	-	-	1370	338	2.46	1.32	1.14		95.01	a-mi-px12-1 *	mi		40.18			
51.29	-	-	5.80	0.09	16.56	21.29	-	-	-	2983.16	23.57	-	-					95.47	m-mi-px5a	px	83.57				
52.42	0.68	18.77	8.63	0.11	3.21	7.38	2.12	0.59	-	13.68	-	1840	1120	3.06	2.59	0.47	0	94.39	m-mi-px5-1 *	mi		39.89			
38.74	-	-	14.42	0.15	42.82	0.12	-	-	-	225.79	927.26	-	-					96.39	a-mi-h-ol1	ol	84.11				

48.69	0.65	14.09	8.26	0.16	4.56	9.41	0.49	0.33	-	255.44	-	1850	2105	1.86	1.83	0.04	0	87.40	a-mi-h-ol1-1 *	mi		44.21
39.52	-	-	15.70	0.21	44.97	0.04	-	-	-	266.84	825.10	-	-					100.57	a-mi-ol5b	ol	83.63	
50.23	0.68	15.51	7.17	0.09	2.42	11.38	2.00	0.54	-	112.89	-	2200	2314	2.44	2.88	-0.45	219	90.77	a-mi-ol5-2 *	mi		37.53
51.62	0.74	16.16	6.70	0.11	1.94	11.10	2.19	0.57	-	218.95	-	2415	2344	2.63	3.20	-0.57	193	91.94	a-mi-ol5-3 *	mi		33.93
38.02	-	-	18.59	0.12	40.52	0.10	-	-	-	109.47	408.62	-	-					97.42	m-mi-ol1a	ol	79.53	
50.17	0.76	16.49	6.91	0.12	3.07	9.58	1.18	0.69	-	75.26	-	2185	1962	6.70	6.10	0.59	364	89.65	m-mi-ol1-1d1 *	mi		44.21
38.25	-	-	16.56	0.13	41.03	0.11	-	-	-	-	416.48	-	-					96.13	m-mi-ol2	ol	81.54	
50.45	0.81	16.69	7.15	0.12	2.32	10.09	0.97	0.60	-	-	-	2410	1996	4.09	3.89	0.20	133	89.89	m-mi-ol2-1	mi		36.69
37.85	-	-	18.69	0.15	39.98	0.12	-	-	-	68.42	377.19	-	-					96.84	m-mi-ol3	ol	79.23	
51.67	0.79	17.03	6.10	0.09	1.84	9.22	0.96	0.80	-	102.63	-	1940	2068	2.03	1.72	0.30	0	89.18	m-mi-ol3-1	mi		34.90

* more than one measurement point was taken and compositions were averaged; - is not analysed or not detected

in comment: pyroxene (px), olivine (ol), melt inclusion (mi)

Maximum Mg# for whole rock and groundmass for the deposits except Te Maari lava flow were taken from Arpa et. al., 2017

The melt inclusion data, as analysed and without composition recalculation, are first described in terms of equilibrium with host. This is important as deviation from equilibrium may be due to a certain component diffusion process or errors in analysis/sample preparation. Conventional corrections were constructed based on particular processes that caused disequilibrium (such as olivine crystallization or dissolution) (Danyushevsky *et al.*, 2000), processes that may not necessarily apply to the samples.

Melt inclusions in the Te Maari lava flow olivine and pyroxene crystals are partially crystallized, and the residual glass in these non-homogenized melt inclusions are not in equilibrium with the host crystal. The low Mg# for the melt inclusions may indicate olivine fractionation; these plot to the left of the equilibrium field in the Rhodes diagram (**Figure 4-4A**) (Rhodes *et al.*, 1979, Putirka, 2008). Pyroxene-hosted melt inclusions on the other hand show low MgO, high SiO_2 and low CaO/Al_2O_3 ratios and may indicate pyroxene crystallization (Belkin *et al.*, 1998). Partially crystallized melt inclusions show crystallites commonly forming a rim along the melt inclusion wall. Equilibrium between mineral host and melt is demonstrated by heated melt inclusions (**Figure 4-4A**). Heating incorporated the crystallites back into the melt (homogenization). Overheating may cause the host olivine to melt, resulting in higher Mg# for the melt inclusion as shown in **Figure 4-4A** where some melt inclusions plot to the right of the equilibrium field. Pyroxene hosted melt inclusions were not homogenized, and other ways will be employed to determine undifferentiated melt compositions.

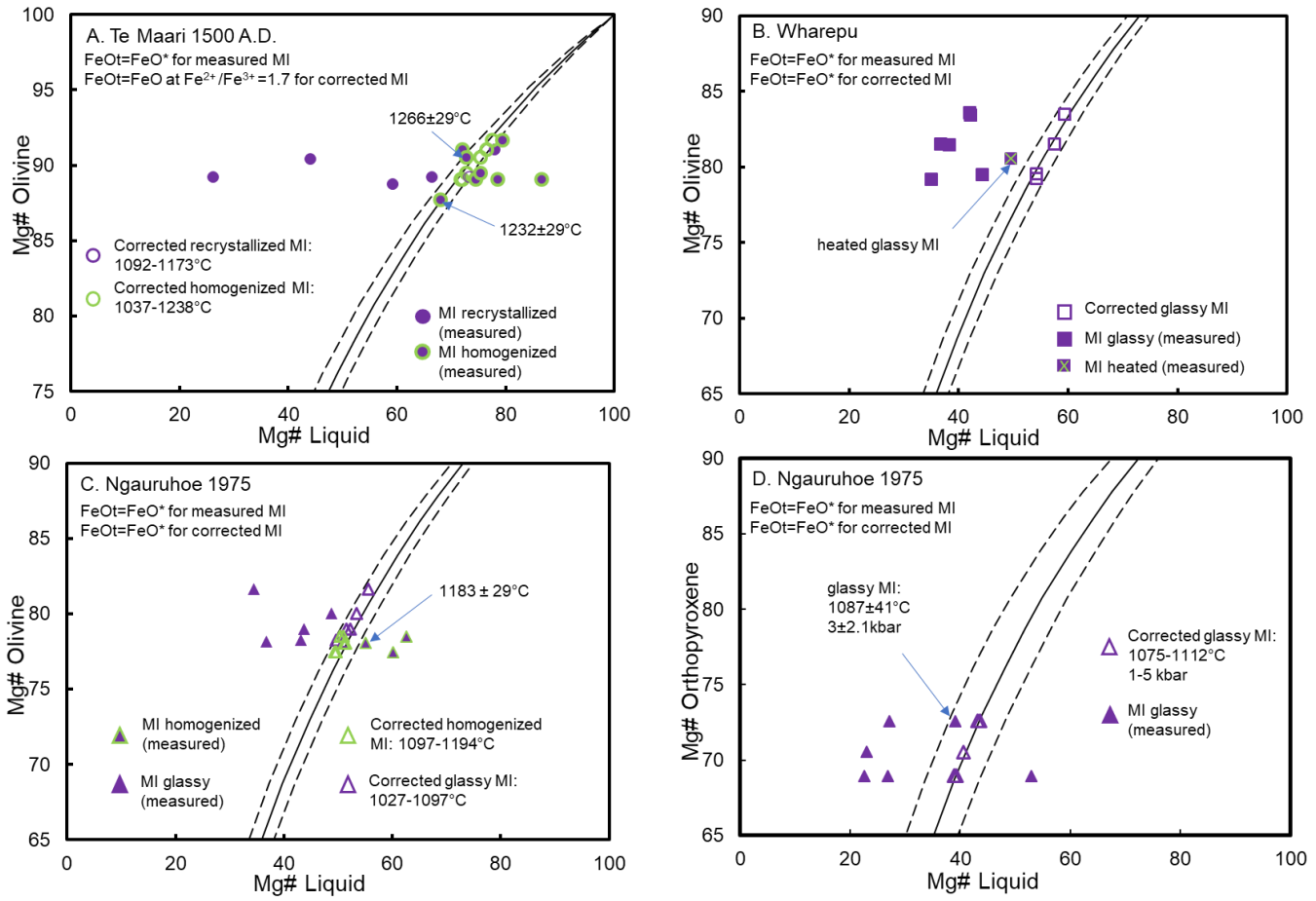

Figure 4-4. Melt inclusion composition for the different samples plotted in Rhodes diagram, symbols and colour scheme as for **Figure 4-2**. A) Homogenized melt inclusions within the equilibrium range were used for the olivine-melt geothermometer, results are shown. Geothermometer results using corrected (to equilibrium) homogenized melt inclusion compositions are listed. B) Note that the heated glassy melt inclusion is close to equilibrium. C) Note that an unmodified melt inclusion composition plots close to equilibrium range and was used for the ol-liq thermometer. D) An unmodified glassy melt inclusion, plotting within the equilibrium field was used for the orthopyroxene-liquid thermobarometer. The result is within the range for temperature and pressure using corrected glassy melt inclusion compositions.

None of the melt inclusions in olivine from Wharepu are in equilibrium with the host despite the melt inclusions being glassy (**Figure 4-4B**). The Mg# of the melt inclusions are too low for the host. Melt inclusions in pyroxenes, however, for Wharepu, are in equilibrium with the host. There is a distinct separation in melt inclusion composition for the olivine hosted and pyroxene hosted melt inclusions when plotted on Harker diagrams (**Figure 4-5**).

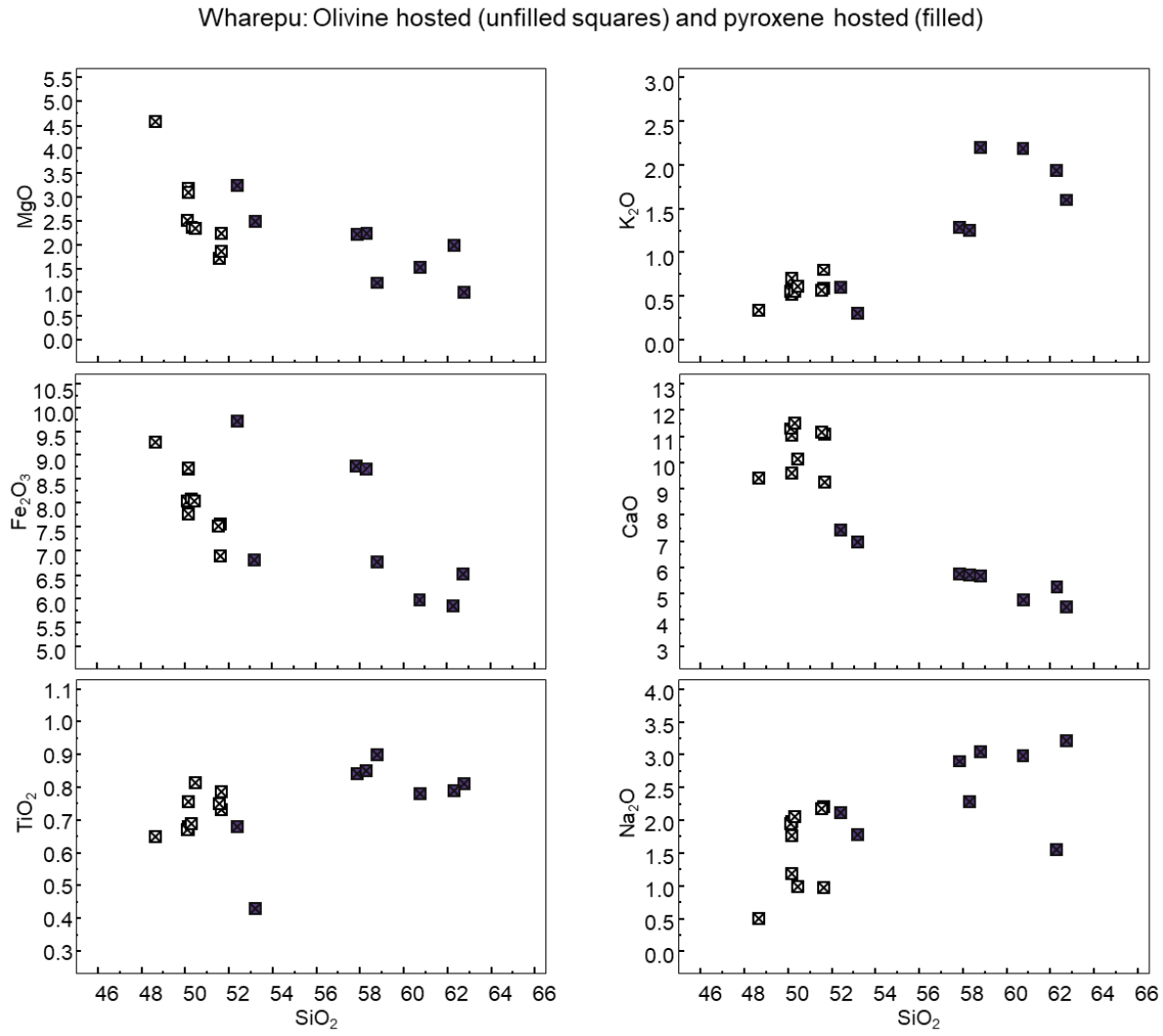

Figure 4-5. Olivine hosted and pyroxene hosted melt inclusions from Wharepu. All values are in wt.%.

Corrections were applied on melt inclusion compositions to bring it in equilibrium with the host. Equilibrium conditions between melt inclusion and host crystal are illustrated in **Figure 4-4** (**A-D**), it shows both the original data and compositions where the Petrolog (Danyushevsky *et al.*, 2000) correction to the olivines was applied (**Appendix Table 12**). Although there is no apparent Fe loss observed in the melt inclusions, there may be exchange of Mg between melt and host affecting compositions (Danyushevsky *et al.*, 2000). The input for Fe^{2+}/Fe^{3+} in Petrolog corrections for olivine-hosted melt inclusions were estimates from R-MELTS models (**Appendix Table 11**). The selected R-MELTS models closely reproduce measured compositions and observed mineral phases. These models resulted in relative redox states that range from; ΔNNO +1.85 to +0.25 (Te Maari), ΔNNO -0.19 to -0.43 (Wharepu), and ΔNNO -0.44 to -1.72 (Ngauruhoe1975). The correction for orthopyroxene-hosted melt inclusions from Ngauruhoe 1975 (**Figure 4-4 D**) was done by either adding (2.5 to 7%) or subtracting (13%) the orthopyroxene host to arrive at $Kd(Fe\text{-}Mg)^{Opx\text{-}melt}$ of 0.286 to 0.291. Corrected to equilibrium values and measured values in terms of MgO and SiO_2 are shown in **Figure 4-6**. Petrolog correction on the Wharepu melt inclusions however, significantly increased both Mg# and SiO_2, and an alternative composition correction for equilibrium was done using modelled ideal values. This correction and further evaluation of equilibrium are discussed in the following.

In addition to the Petrolog corrected values for Wharepu melt inclusions, a composition (MI calc) was calculated from olivine addition to a bulk (liquid) composition (**Table 4-2**). Using an R-MELTS model (Ghiorso and Sack, 1995, Gualda *et al.*, 2012) (**Appendix Table 11**), a bulk composition (calculated Wh in Section 3) started to precipitate olivine (step 19 ol) at 1120°C and 5 kbar. The composition of the crystallized olivine (step 19 ol) was added to a melt inclusion composition (average, N:9) representing dissolution of olivine. An addition of 5.8% olivine (step 19 ol) is required to increase the $Kd(Fe\text{-}Mg)^{Ol\text{-}melt}$ of 0.16 (average MI – step 19

ol) to 0.28. The results and reference values for comparison are presented in **Table 4-2** and plots are shown in **Figure 4-7**. The MI (calc) composition however, may not be necessary and is probably not a good corrected value as neither olivine recrystallization nor significant Fe loss (values that plot off the trend) were observed (**Figure 4.7**). In fact, it may be the composition of the olivine host that may need correction. Majority of olivine hosts for the melt inclusions show lower Fe values probably due to preparation of very thin wafers, ≤ 30 μm (**Figure 4.8**). Although no similar pattern was observed for the Te Maari olivine hosts, which are also of similar thickness. The R-MELTS olivines plot along the trend defined by sample olivines analysed from thick sections (~100 μm). This composition (R-MELTS olivine) and not the olivine host composition was used for the correction.

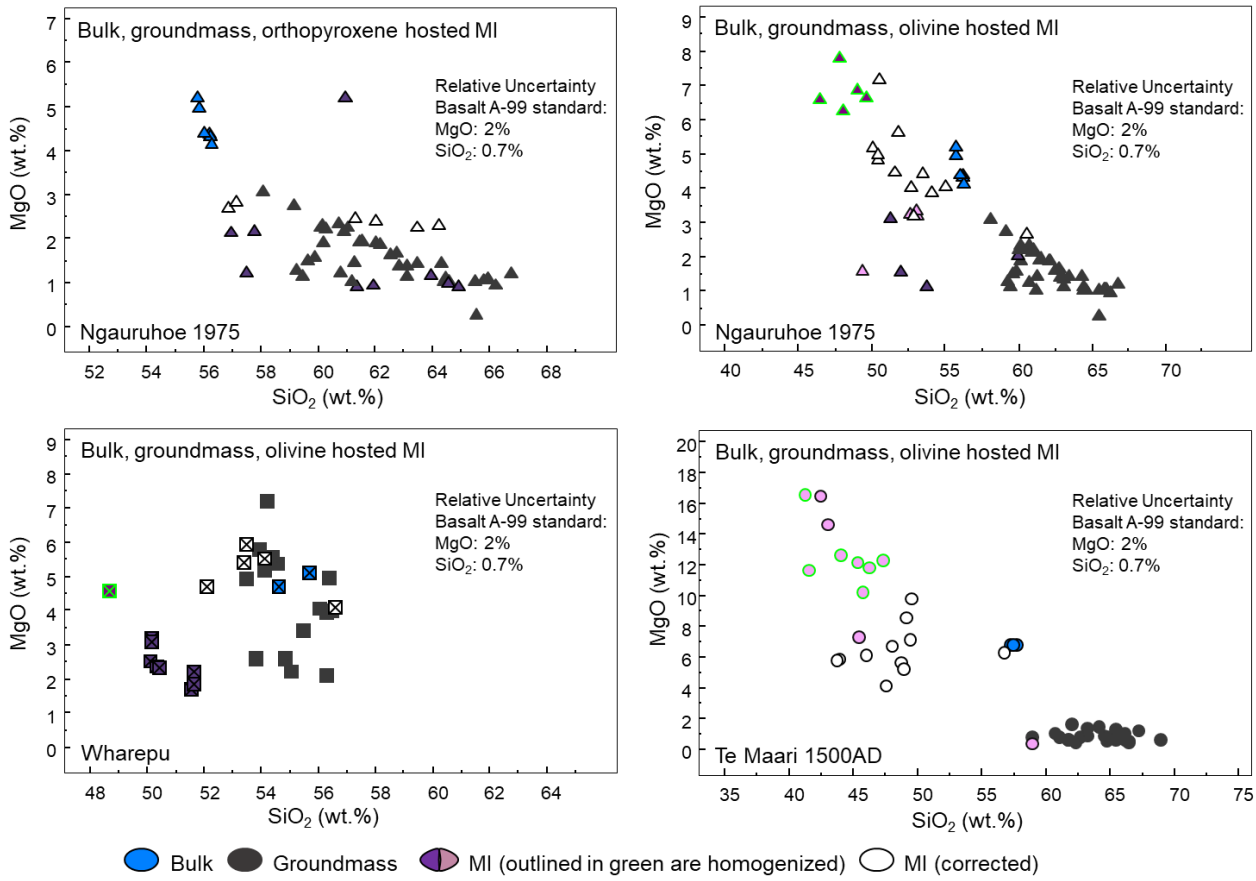

Figure 4-6. Melt inclusion compositions calculated to equilibrium and plotted with bulk, groundmass and measured melt inclusions (heated and unheated).

Table 4-2. Different melt compositions (bulk, groundmass, melt inclusion, modelled) for Wharepu samples and a calculated composition (MI (calc)) after adding an olivine composition.

	Bulk[b]	Groundmass		R-MELTS Liq[c]	Melt inclusion (MI)[d]		Difference	R-MELTS Ol[c]	MI (calc) addition of	Difference
wt% oxide		average (N:15)	2ϭ (STD)	step 19	average (N: 9)	2ϭ (STD)	MI-MELTS liq	step 19 Ol	5.8% step 19 Ol	MI(calc)-R-MELTS liq
SiO_2	52.70	55.05	2	50.06	50.70	1	0.65	39.55	50.06	0.00
TiO_2	0.81	0.89	0.3	0.77	0.73	0.1	-0.04		0.68	-0.08
Al_2O_3	18.32	17.01	3	17.38	15.93	2	-1.46		15.00	-2.38
Fe_2O_3	1.36			1.29	1.10		-0.20		1.03	-0.26
FeO	7.48			7.10	6.07		-1.03	16.58	6.68	-0.42
MnO	0.15	0.22	0.3	0.14	0.13	0.1	-0.02	0.12	0.13	-0.02
MgO	5.61	4.23	3	5.32	2.48	1	-2.85	43.54	4.86	-0.47
CaO	8.88	7.71	2	8.44	10.68	2	2.24	0.21	10.07	1.63
Na_2O	2.48	2.07	0.9	2.35	1.69	1	-0.66		1.59	-0.76
K_2O	0.74	1.25	0.9	0.70	0.60	0.2	-0.10		0.56	-0.13
P2O5	0.12			0.11						
H2O[a]	1.38			6.33	6.70				6.7	
FeO (total)	8.69	8.93	2		7.05	1			7.60	
SUM	100	97.48		100	96.79			100	97.37	

Kd	Kd (0.3±0.03)
Bulk-RMELTS Ol	0.29
RMELTS liq-RMELTS Ol	0.29
MI (average)-RMELTS Ol	0.16
MI(calc)-RMELTS Ol	0.28

[a] H_2O content is from plagioclase hygrometry (for the bulk composition), and the maximum measured water content for the melt inclusion. Non-homogenized melt inclusion compositions were normalized to 100% with 6.7 wt.% H_2O

[b] Calculated bulk composition where 0.5% SiO_2 was subtracted and normalized to 100%. Fe_2O_3 and FeO compositions were estimated to give model results that best represent the samples (see Section 3.5.3).

[c] R-MELTS model (Appendix Table 11) at 1120°C and 5kbar where olivine starts to crystallize (labelled step 19 in table), composition for liquid and olivine in equilibrium are shown in table

[d] Average composition for non-homogenized melt inclusions hosted in olivines. Fe_2O_3 and FeO compositions were estimated based on proportions from R-MELTS models. The water content is the maximum measured in the melt inclusions.

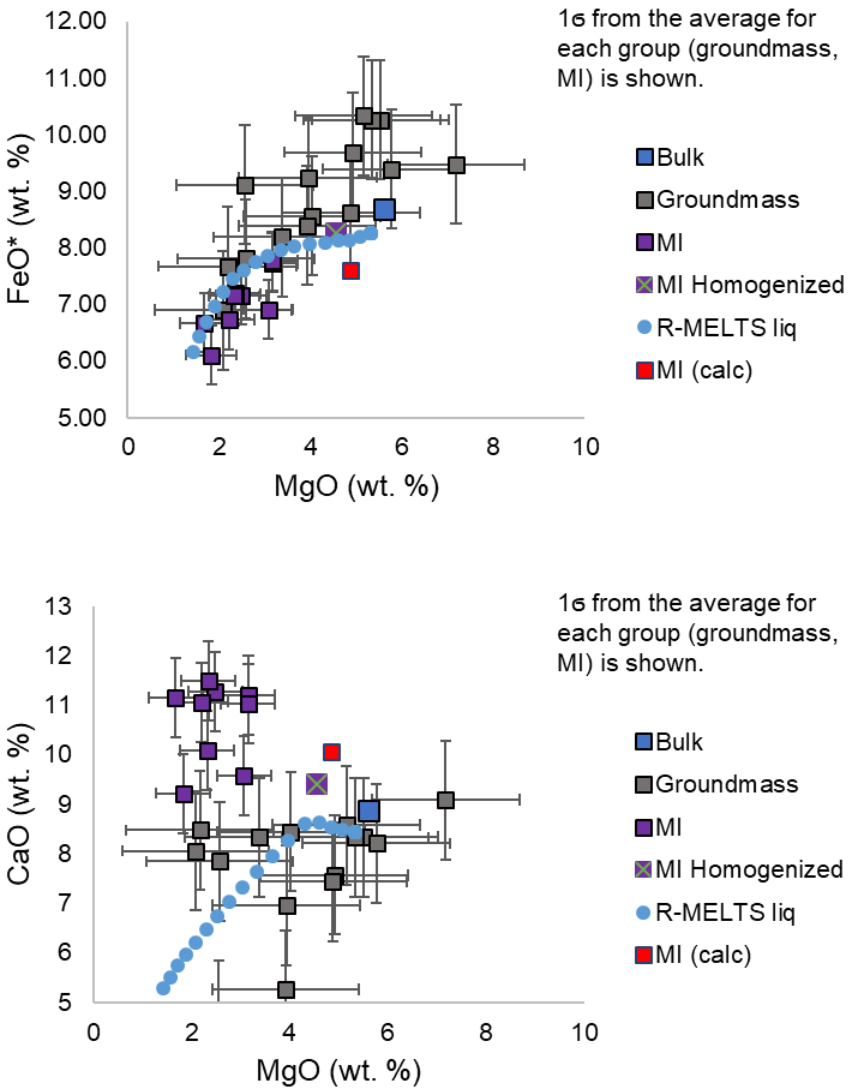

Figure 4-7. Comparison of several compositions representing melt (measured and modelled) from Wharepu.

The possible errors in some olivine host compositions, for all deposits with melt inclusion analysis, are likely due to the small and very thin wafers, a result of a necessary sample preparation as the melt inclusions are small. Mounting in epoxide then re-polishing of the small wafers may have resulted in deviations from an ideal smooth horizontal surface. Variations in sample tilt, x-ray take off angle, and surface roughness are among the sources of error in microprobe analysis (Lifshin and Gauvin, 2001). The observed compositional differences are unlikely due to instrumental error because melt inclusions were analysed in 3 widely separated

sessions (months), and all analysis of a basaltic glass standard (Basalt NMNH 113498-1 (A-99)) as unknown (**Appendix Table 8**) for all the different sessions have 1 standard deviation (1 σ) of 0.16 for CaO (N:49), 0.09 for MgO (N:49) and 0.23 for FeO (N:49) and relative uncertainty ([1 σ/reference value]*100) of 1.75% (CaO), 1.72% (MgO), 1.7% (FeO).

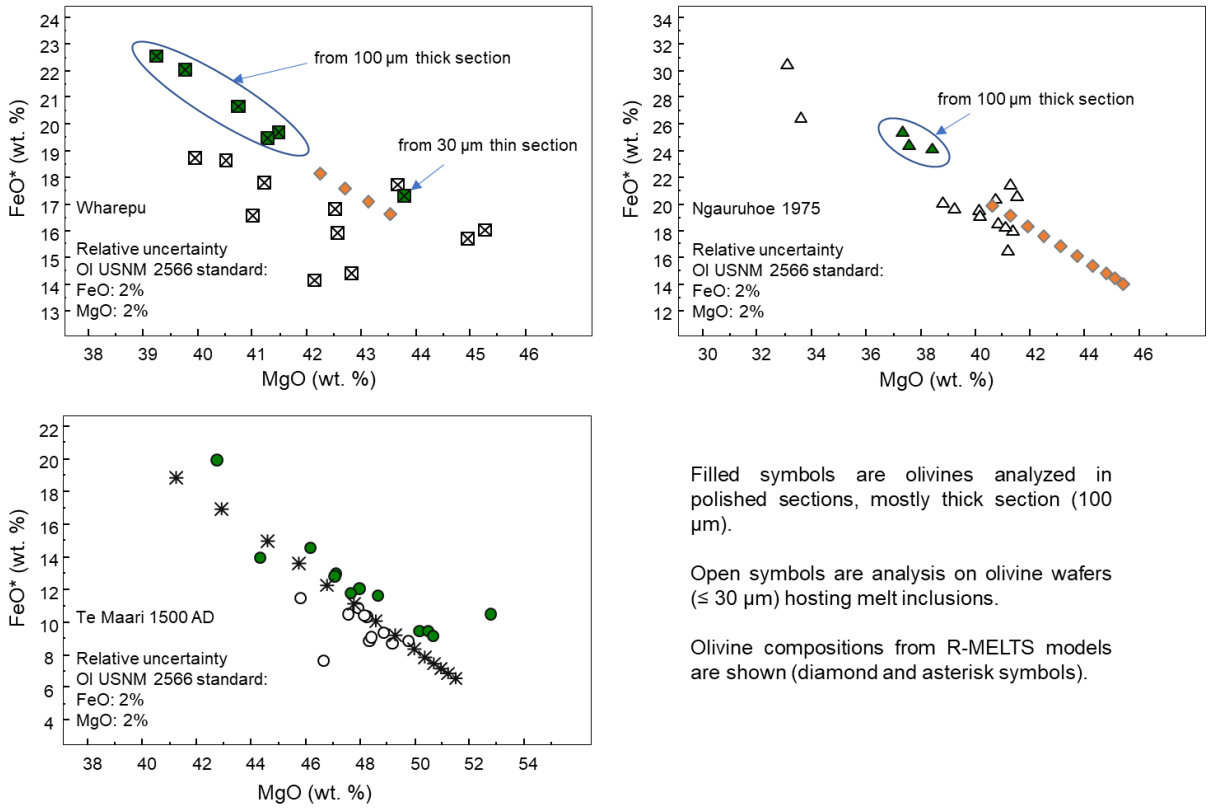

Figure 4-8. Olivine analysis from polished slides and thin wafers. Modelled olivine compositions from R-MELTS (models discussed in **Section 4.5.1**) are also shown.

All melt inclusions from Wharepu have low major element totals (90.77±1 wt.%, average N:9) for anhydrous composition. The maximum H_2O content from this sample group is 6.7 wt. % whereas plagioclase hygrometry produced a value of 1.4 wt.% H_2O at 8 kbar (Arpa *et al.*, 2017). From the results shown on **Table 4.2** it appears that there was significant addition of

water, loss of MgO, and addition of CaO (**Figure 4-7**). These changes likely occurred at lithostatic pressures very much less than 8 kbar, in consideration of the hygrometry results.

The measured (not recomputed) melt inclusion compositions in equilibrium or close to equilibrium with the host mineral were used for additional thermobarometry considerations for determining magmatic processes. Homogenization experiments give actual changes in composition and are preferred over correction computation. Over-heating and under-heating can be checked from the results (whether equilibrium was reached) and can be minimally corrected. Volatiles data (H_2O, CO_2) measured by FTIR are preferred for interpretation in this study over Petrolog (model used was Danyushevsky, 2001) corrected values. The increase in H_2O in a corrected value for a melt inclusion with the highest H_2O content in Te Maari is 18% and within the 20% error considered for the FTIR analysis in this study.

4.4.2 H_2O, CO_2, S, Cl melt inclusion compositions and effect of homogenization

H_2O values for the samples except for Wharepu are below the average value (~4 wt. %) for water in subduction zone magmas (Plank *et al.*, 2013) whereas Cl is high compared to values from other arc volcanoes (Metrich and Wallace, 2008). The complete data can be found in **Appendix Table 7 and 10**. The melt inclusions with the highest H_2O content come from the Wharepu deposit. The maximum total water measured for Wharepu is 6.7 wt.%, and this is more than 4 wt.% higher than the highest H_2O value (2.27 wt.%) for Te Maari melt inclusions, and the second highest for the different deposits (**Figure 4-9**). For the other deposits (Ngauruhoe and Red Crater) in this study, the total water content ranges from 0.14 to 1.95 wt.%. The highest S values for the different deposits ranged from 1780 to 3888 ppm. There is no clear trend in S between deposits because the range for each deposit is quite large. Cl concentrations, for Te Maari inclusions, however, are significantly higher than for those of the other deposits. Excluding melt inclusions from possible xenocrysts, the highest Cl value for Te

Maari is 4790 ppm, whereas for the rest of the deposits, maximum values are from 2510 to 2950 ppm. There are very few measurements for CO_2 because for the very thin wafers/small melt inclusions, some of the FTIR spectra were masked by a reflectance signal or the interferogram is weak due to a small beam diameter, making the CO_2 peak difficult to read. The CO_2 values for the different deposits range from 215 to 470 ppm.

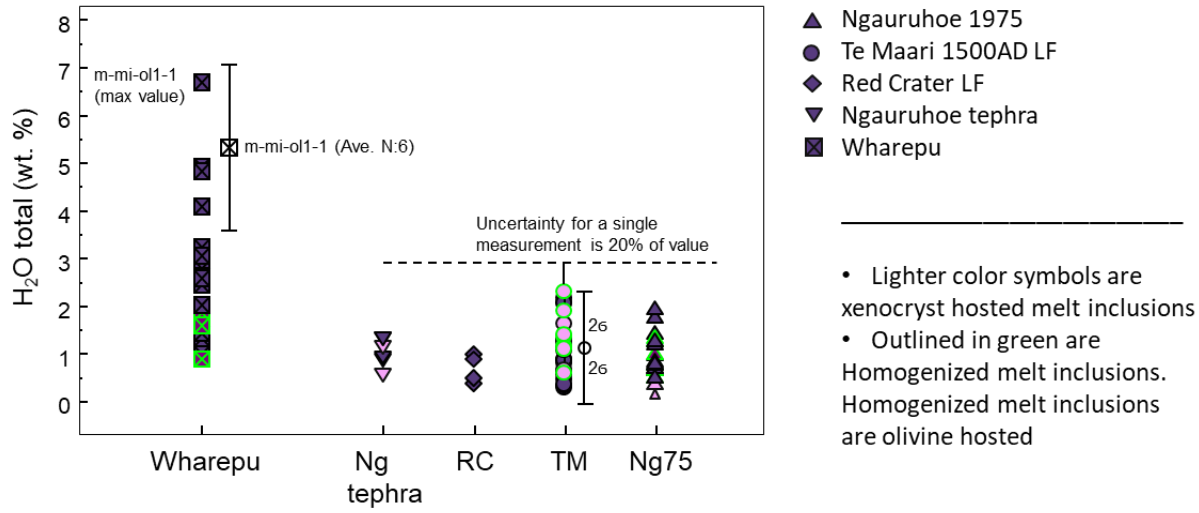

Figure 4-9. Variation in total H_2O for the different deposits. The deposits have water contents below the average of 4 wt.% for arc magmas (Plank *et al.*, 2013) except for Wharepu. The plotted values are the average for 2-3 times repeat analysis. For MI m-mi-ol1-1, only the best value is plotted (average value for repeat analyses (N=6) is shown with 2σ error) because some measurements have saturated H_2O spectra resulting in lower values (see Methods **Table 2-1**). For an error of 20% of the value, the highest measured value would have a range of 6.7 ± 1.3 wt.%.

Olivine grains from 3 samples (Te Maari, Wharepu and Ng75) in the data set were sent for melt inclusion homogenization. Only the Te Maari melt inclusions among the samples for homogenization are partially crystallized (**Figure 4-10**). Melt inclusions from Wharepu and Ng75 are glassy, but some contain bubbles (**Figure 4-10**). As previously described, melt inclusions from the lava flow samples are partially crystallized. This is consistent with crystallization in melt inclusions that were cooled at a slower rate (Wallace *et al.*, 2003).

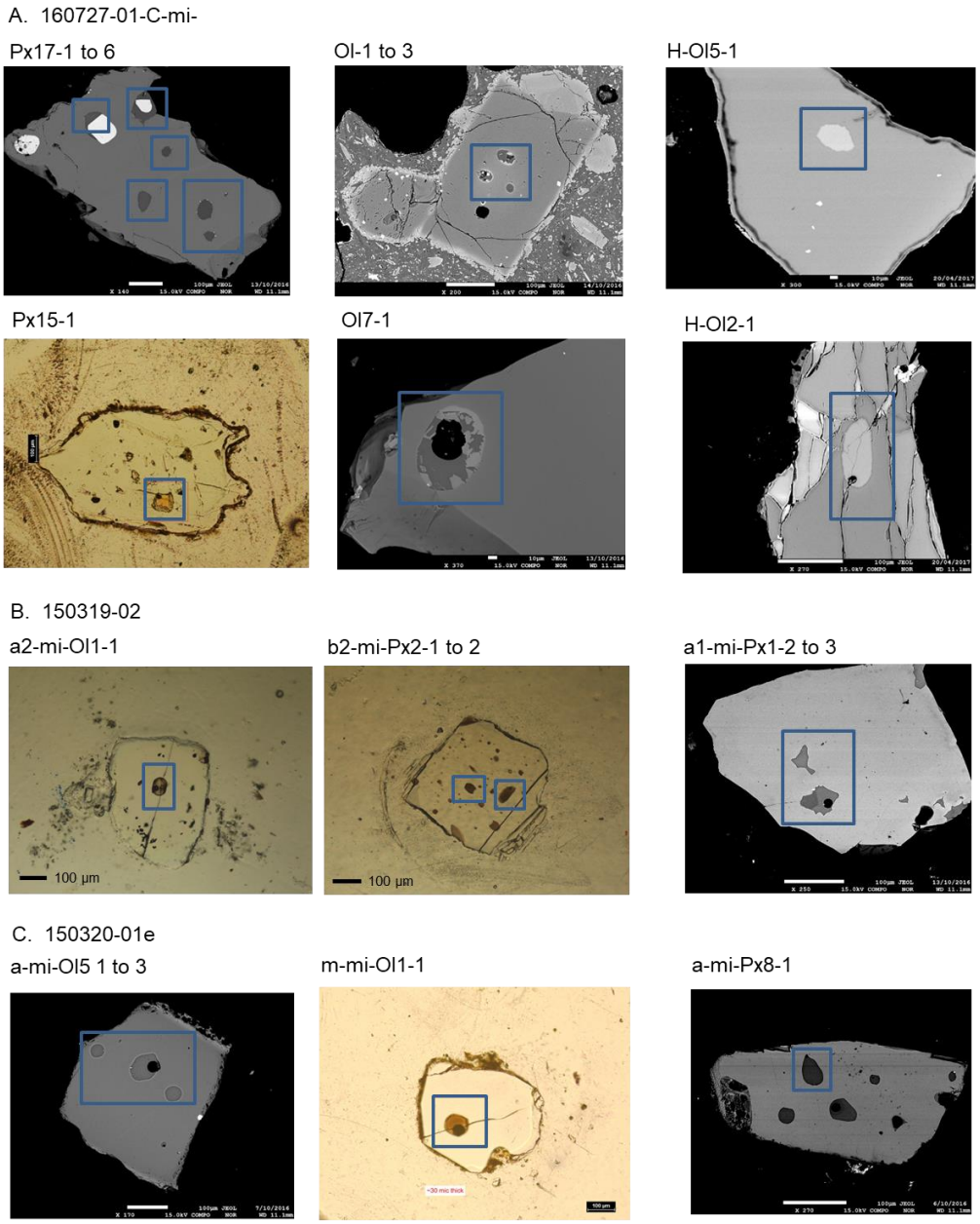

Figure 4-10. Melt inclusions from Te Maari 1500 A.D. lava flow (A) showing crystallite formation along the border. Homogenized melt inclusions are also shown, labelled H. The fractured state of H-Ol2-1 is due to polishing of thin wafers. Naguruhoe 1975 (B) and Wharepu (C) unheated melt inclusions, the glass is free of crystallites.

Water speciation is significantly changed between the partially crystallized (unhomogenized) and homogenized melt inclusions from Te Maari. It is only the proportion between molecular water and hydroxyl that is affected and there is no significant difference in total water content between the sample groups (homogenized and unhomogenized), likely indicating that water is

not taken in by the crystallites. For Te Maari, the proportion of molecular water in the homogenized melt inclusions ranges from 16 to 26% of the total water content, whereas in the unhomogenized inclusions it is very high – from 27 to 98% with an average of 72% of the total water. The proportion of molecular water for unhomogenized Wharepu melt inclusions is also high (55 to 100%), but homogenized samples almost have the same range of values (60 to 98%). The same is observed for the melt inclusions from Ng75. The proportion of molecular water in the homogenized melt inclusions is not very different from the unhomogenized samples from Ng75. Presenting the data in terms of the relationship between molecular H_2O, OH and silicate melt (mole fraction of O based on SiO_2) (Stolper, 1982) and comparing with values representing constants that describe water speciation in experimentally heated rhyolitic glass (Zhang *et al.*, 1995), only homogenized inclusions from Te Maari and Ngauruhoe plot in near equilibrium range and none for the Wharepu samples (**Figure 4-11**).

The average CO_2 content of homogenized melt inclusions from Te Maari is 364 ppm (N:3, maximum: 470 ppm) larger than the average for non-homogenized inclusions which is 140 ppm (N:3, maximum 178 ppm), probably indicating incorporation of CO_2 from bubbles during homogenization. Heated melt inclusions that were partially crystallized (Te Maari samples) also have lower Cl and higher S concentrations. The average S concentration in olivine hosted homogenized melt inclusions is 1926±666, N:7 (2162±253, N:6) whereas for non-homogenized melt inclusions, it is 286±583, N:14 (133±71, N:13). The increase in S values for the homogenized inclusions is more pronounced than changes in Cl values. Some crystallites were probably S bearing phases.

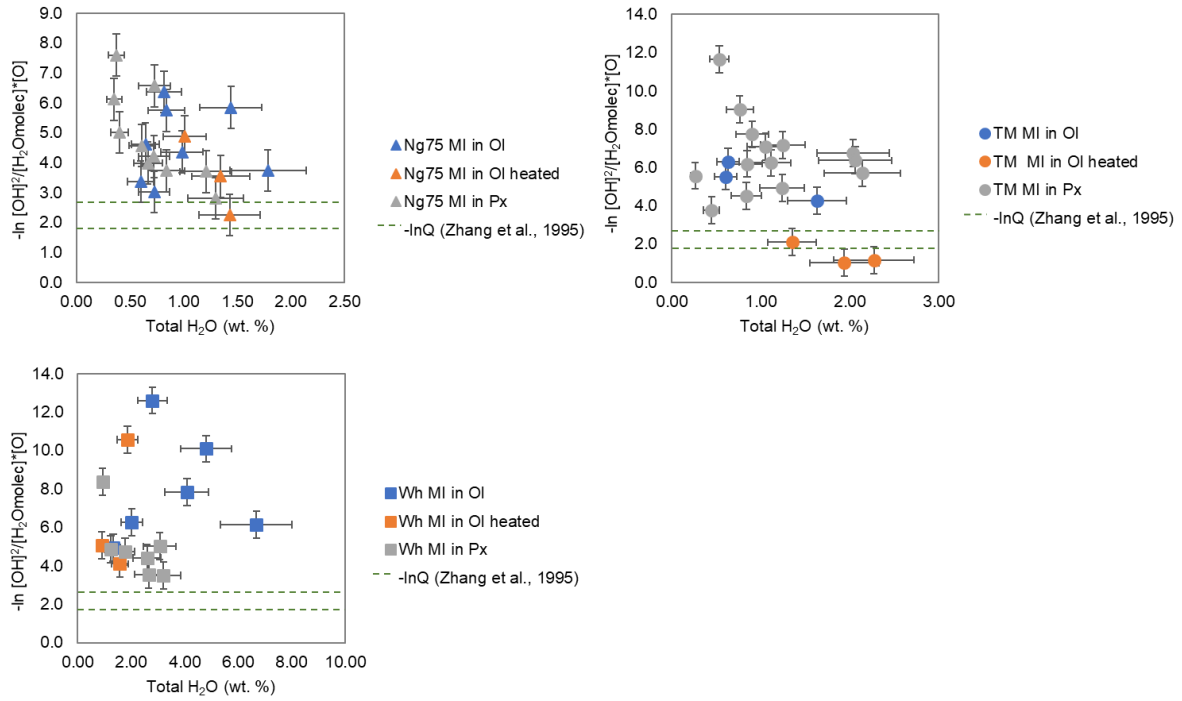

Figure 4-11. Evaluation of OH-H_2Omolec equilibrium in silicate, after Stolper (1982) and Zhang et al. (1995). Water speciation equilibrium range based on heating experiments on rhyolites are from Zhang et al., (1995). Ngauruhoe 1975 deposit (Ng 75), Te Maari (TM), Wharepu (Wh). Error bar for total water is 20% of value, vertical error bar (0.7) is propagated error using 20% FTIR measurement error.

4.5 Discussion

4.5.1 Crystallization environments

Temperature and pressure of crystallization pathways for the host minerals were constrained by equilibrium crystallization models. Thermobarometry models (Putirka, 2008) were applied only to melt inclusions that are in equilibrium with the host and host crystals that are in equilibrium with groundmass or bulk rock compositions. Redox conditions (Hutchison, 1973, Ghiorso and Evans, 2008) were only determined for the Te Maari samples. Finally, the temperature, pressure and redox results were used to constrain models using Rhyolite MELTS (Ghiorso and Sack, 1995, Gualda *et al.*, 2012) to further estimate possible crystallization/melting environments. The results are summarized in **Table 4-3**.

Table 4-3. Summary of thermobarometry results.

	Temperature (° C)					Pressure (kbar)		H2O (wt.%)					
	Ol host-MI		Opx host-MI	Pl-gm 2005, Eqn 23*	Ti-Fe oxide	Opx host-MI	Pl-gm	Pl hygrometry	melt inclusion ol and px hosted	Kd $_{Pl\text{-}liq}$ (0.27 ± 0.11)	Kd $_{Ol\text{-}melt}$ (0.3 ± 0.03)	Kd $_{opx\text{-}melt}$ (0.29 ± 0.06)	Relative Iron redox state
	Eqn 15 SEE: ± 60˚C	Eqn 22 SEE: ± 29˚C	Eqn 28a SEE: ± 41˚C	SEE: ± 43˚C		Eqn 29b SEE: ± 2.1 kbar	Eqn 25a SEE: ± 2.47 kbar	Eqn 25b SEE: ± 1.1 wt.%	±20%				Ti-Fe oxide DNNO
1975 Ngauruhoe	1169	1183	1087-1094	1087-1159**		3.0	2.3-5.0**	0.9-1.4**	0.14-1.95	0.20-0.26**	0.343	0.226-0.242	
Te Maari 1500AD LF	1229-1284	1223-1301		1110-1209	891-1292		6.4-11.0	1.5-1.8	0.27-2.27	0.16-0.26	0.278-0.357		0.59-2.75
Wharepu	host-MI not in equilibrium			1215-1216**		not in equil	8.2-8.4**	1.3-1.4**	0.9-6.7	0.29-0.31**			

*Equations from Putirka (2008), including Putirka et al., 2003, 2005. Fe-Ti oxide thermometer is from Ghiorso and Evans (2008)

**In Arpa et al., 2017
An initial pressure of 5 kbar was input for the olivine and plagioclase models. A 0.5 wt.% H_2O was assumed for the groundmass composition and actual H_2O measured was used for the melt inclusion (liquid)

4.5.1.1 Te Maari

The mineral components of the Te Maari lava flow indicate a wide range of crystallization pressures and temperatures reflecting ascent history and a likely incorporation of xenocrystic olivine crystals. Plagioclase thermobarometry (Putirka, 2008) indicates crystallization at relatively high pressures, (11.0 to 6.4 ± 2.47 kbar or 41 to 24 km depth) and at temperatures from 1110 to 1209 ± 43 ºC. Fe-Ti oxide thermometer (Ghiorso and Evans, 2008) from analysis of magnetite and ilmenite exsolusion textures indicate temperatures as high as 1292 ºC and an oxidizing environment ($0.59 < \Delta NNO \leq 2.25$). Homogenized melt inclusions in equilibrium with the host olivine give temperatures of 1223-1301 ± 29 ºC using the Ol-liq thermometer (equation 22) of Putirka (2008). These samples were homogenized at 1270 ± 3 ºC. The closest liquidus temperature to the above geothermometer results, for a basaltic melt inclusion (160727-01-c-mi-h-ol1-1, homogenized), is 1357 ºC, modelled using Rhyolite MELTS (Ghiorso and Sack, 1995, Gualda *et al.*, 2012) at 1 kbar pressure and the actual water composition of the melt inclusion (1.35 wt.%). Starting from liquidus temperature (1357 ºC), during fractional crystallization, $Fo_{92.12}$ olivine starts crystallizing at 1277 ºC. Fractionated and equilibrated olivine recreates the forsterite content ($Fo_{91.7 - 87.7}$) of olivine hosts for the melt inclusions up to 1117 ºC. The liquid approximately recreates olivine-hosted melt inclusions for fractional crystallization down to this temperature (**Figure 4-12**). The relative redox state decreases from ΔNNO +1.85 (at 1357 ºC) to +1.62 (at 1117 ºC) and is within the range determined from Fe-Ti oxide thermometer. The modelled liquid compositions do not however, recreate the groundmass and partially crystallized pyroxene-hosted melt inclusion compositions, which are higher in silica. Olivine can crystallize at higher pressure (8 kbar) using the same input parameters, but the liquidus temperature is too high and fractional

crystallization down to 1100 ºC still results in a significantly lower silica liquid compared to groundmass compositions. Comparing unhomogenized olivine-hosted and pyroxene-hosted melt inclusion compositions shows that, assuming the same degree of recrystallization, the olivine-hosted melt inclusions started at a more primitive composition (**Figure 4-13**). This could imply that the melt inclusions were trapped in different environments.

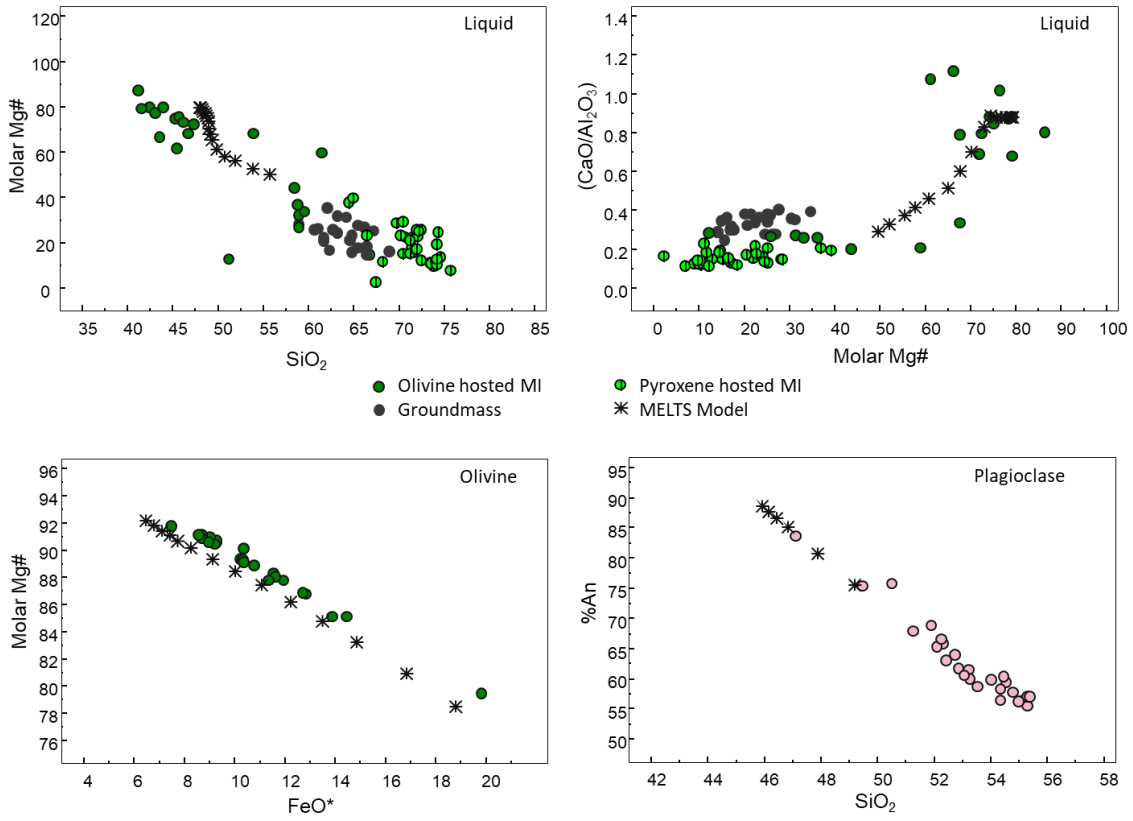

Figure 4-12. Rhyolite MELTS model (fractional crystallization at 1 kbar) results for Te Maari 1500AD lava flow. Model input is listed in Appendix Table 11.

Pyroxene compositions cannot be recreated from the 1 kbar olivine melt inclusion crystallization model discussed above. In the different models tried, pyroxenes can easily crystallize at high pressures. Based on major element trends, the composition of a partially crystallized olivine-hosted melt inclusion (160727-01-c-mi-ol1-1b) may be close to a non-crystallized composition of a pyroxene-hosted melt inclusion (**Figure 4-13**). This composition

was found to be in equilibrium with the pyroxene hosts (Kd_{cpx}: 0.280 - 0.294). Using an H_2O of 1 wt.% and 160727-01-c-ol1-1b as input for a clinopyroxene-liquid model (equation 32c) (Putirka, 2008), crystallization pressures range from 7.2 – 13.1 ± 1.5 kbar (27 to 49 km depth). These values agree with the plagioclase thermobarometry results. The melt trapped in the pyroxenes crystallizing from a fractionated magma at great depths crystallized within the host during the rise of the magma to the surface. Because the compositions of the residual glass in the crystallized melt inclusions are similar to bulk groundmass compositions (microlites plus interstitial glass), the groundmass composition can be regarded as the residual composition from the crystallization of phenocrysts. This may indicate that the magma of bulk composition (160727-01-c-ol1-1b) ascended as a single batch (isolated system). Finally, to reconcile the scenario from the pyroxenes with the olivines that crystallized at 1 kbar from a primitive melt would require the olivines to be xenocrysts. These olivines crystallized and settled within a shallow chamber (~3-4 km depth) and were later incorporated by a rising magma originating at greater depths.

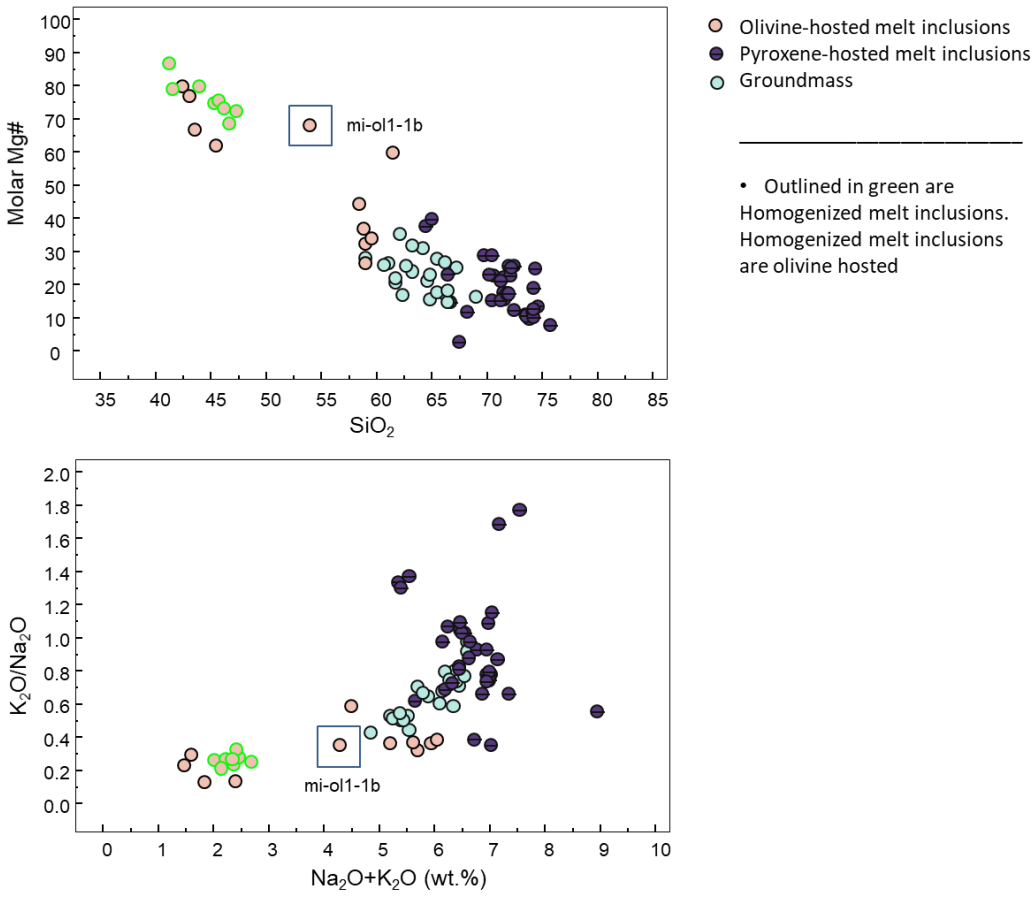

Figure 4-13. Differences in major element compositions between olivine-hosted and pyroxene-hosted melt inclusions. Homogenized melt inclusions in olivines have the most primitive composition. The pyroxene melt inclusions have the most evolved compositions because these are analysis of residual glass from partially crystallized inclusions. Melt inclusion (mi-ol1-1b) in olivine (in square) may represent a parental composition, a composition that is not recrystallized for the pyroxene melt inclusions. Bulk groundmass compositions plot along the trend established by the melt inclusions.

4.5.1.2 Ngauruhoe 1975

Modelling suggests that magmas from the 1975 Ngauruhoe eruption were derived from the interaction between a hotter magma and partial melting of a cooler crystallized magma. Temperature and pressure are constrained by thermobarometry. The homogenized melt inclusions, however, have Mg# that are too high for the host olivine, and non-homogenized inclusions have values that are too low. Only one is close to equilibrium values (K_d: 0.343) and

resulted in a temperature of 1183 ºC. A melt inclusion (n=1) in equilibrium with orthopyroxene gives a crystallization pressure of 3 kbar and temperature of 1087 ºC. The best model for the equilibrium crystallization of a melt inclusion composition (150319-02-a2-mi-h-ol2-1) to produce melt inclusion and olivine host compositions requires high water content (1.95 wt.%) and a reducing environment (-0.87 < ΔNNO ≤ -1.72) (**Appendix Table 11**) at 4 kbar. The amount of water used (1.95%) is not the amount measured in this melt inclusion, but the highest measured for Ngauruhoe 1975 to represent an undegased composition. For this model, the liquidus temperature is 1213 ºC and olivine (Fo_{84}) starts crystallizing at 1203 ºC. Crystallization of lower Fo_{82} olivine occurs at 1163 ºC and is closer to the composition of olivine hosts ($Fo_{81.6-66}$). Other phases are orthopyroxene, clinopyroxene and plagioclase, with compositions similar to the actual sample (**Figure 4-14**). Modelled liquid compositions agree with melt inclusion composition for crystallization down to 1003 ºC, but the modelled water content is too high (2.0-5.2 wt.%). Pyroxene hosted melt inclusion and bulk groundmass compositions however, were not reproduced. Equilibrium melting (1000 increased to 1150 ºC) of a bulk rock composition at 4 kbar, low water content (0.5 wt.%) and FeO/Fe_2O_3 = 6.04 (**Appendix Table 11**) produces liquid compositions similar to groundmass, melt inclusions in pyroxenes and low anorthite plagioclase crystals in the samples (**Figure 4-14**). Based on these models for Ng75, it is possible that a cooling/crystallizing magma body in a region around 4 kbar melts a previously emplaced degassed intrusion, and the melts and their crystal components are mixed prior or during ascent leading to eruption.

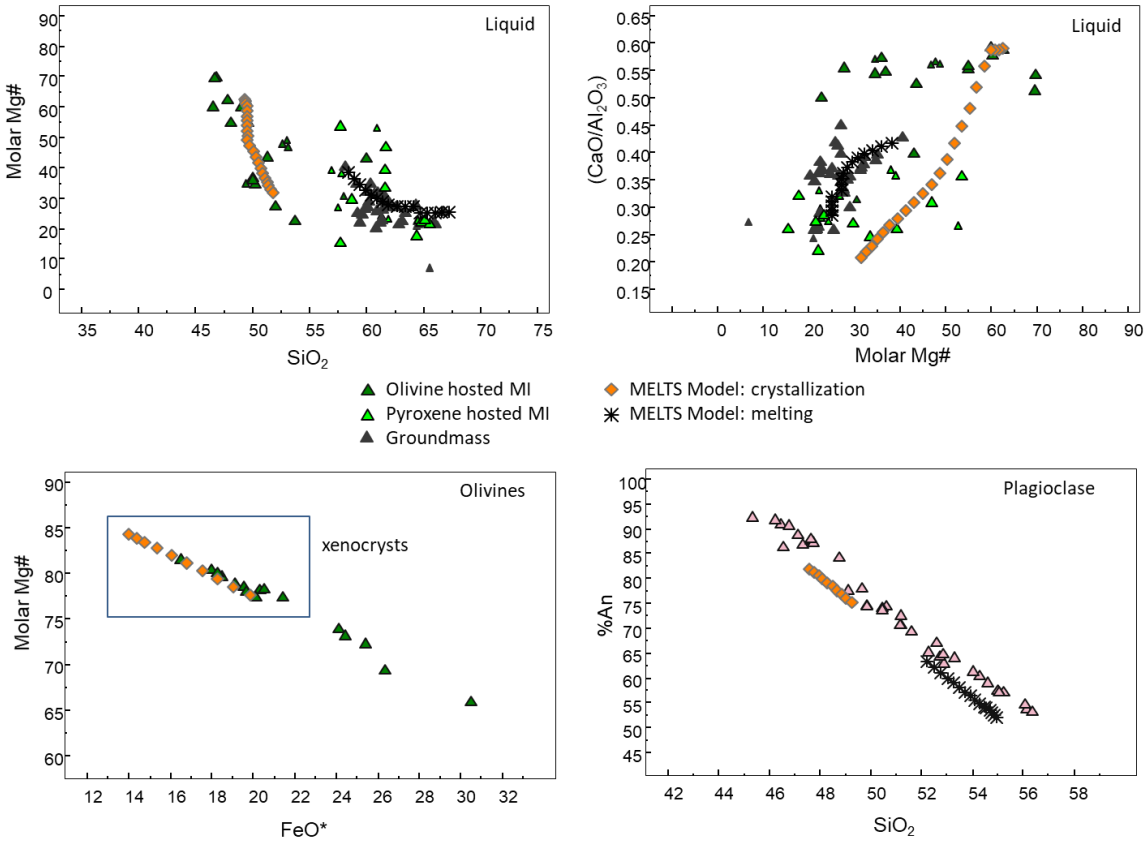

Figure 4-14. Rhyolite MELTS model results (equilibrium melting and crystallization at 4kbar) for Ngauruhoe 1975 pyroclasts. Model input is listed in Appendix Table 11.

4.5.1.3 Wharepu lapilli

Melt inclusions in olivines are not in equilibrium with the host. The Mg# is lower than what is required for equilibrium even for the homogenized inclusions; note that non-homogenized inclusions are already glassy. Crystallizing a melt inclusion composition (150320-01e-m-mi-ol1-1) from 10 kbar to 0.5 kbar crystallizes olivine only at 0.5 kbar and the Fo# is too low compared to actual samples. In this case, temperature and pressure constraints for the model are based on the parameters derived for Wharepu (Arpa et al. 2017). The bulk composition with quartz subtracted is considered, together with the maximum water content for Wharepu melt inclusions in this study (6.7 wt.%) (**Appendix Table 11**). Compositions are normalized to 100% and oxide compositions are adjusted to accommodate the high amount of water. Batch

crystallization from 1300 down to 900 ºC at 5 kbar crystallized $Fo_{81.8\text{-}79.9}$ olivine at 1120 to 1090 ºC, within the range of actual olivine compositions. The resulting liquid is similar to the range of Mg# for the melt inclusions and groundmass, but lower in silica (**Figure 4-15**). Plagioclase is not crystallized. Polybaric batch crystallization of Wharepu starting from 8 kbar produces all the crystal components in the sample, but olivine crystallizes only from 1 kbar (Arpa *et al.*, 2017). Increasing the water content to 6.7 wt.% allows for crystallization of olivine at a higher pressure. A slightly reducing environment ($-0.43 < \Delta NNO \leq -0.19$) and higher water content are needed to crystallize olivine in this case. The high amount of water in Wharepu will be discussed in the next sections. Among the samples, it is the only one where the measured water from melt inclusions do not agree with the results from plagioclase hygrometry (**Table 4-3**).

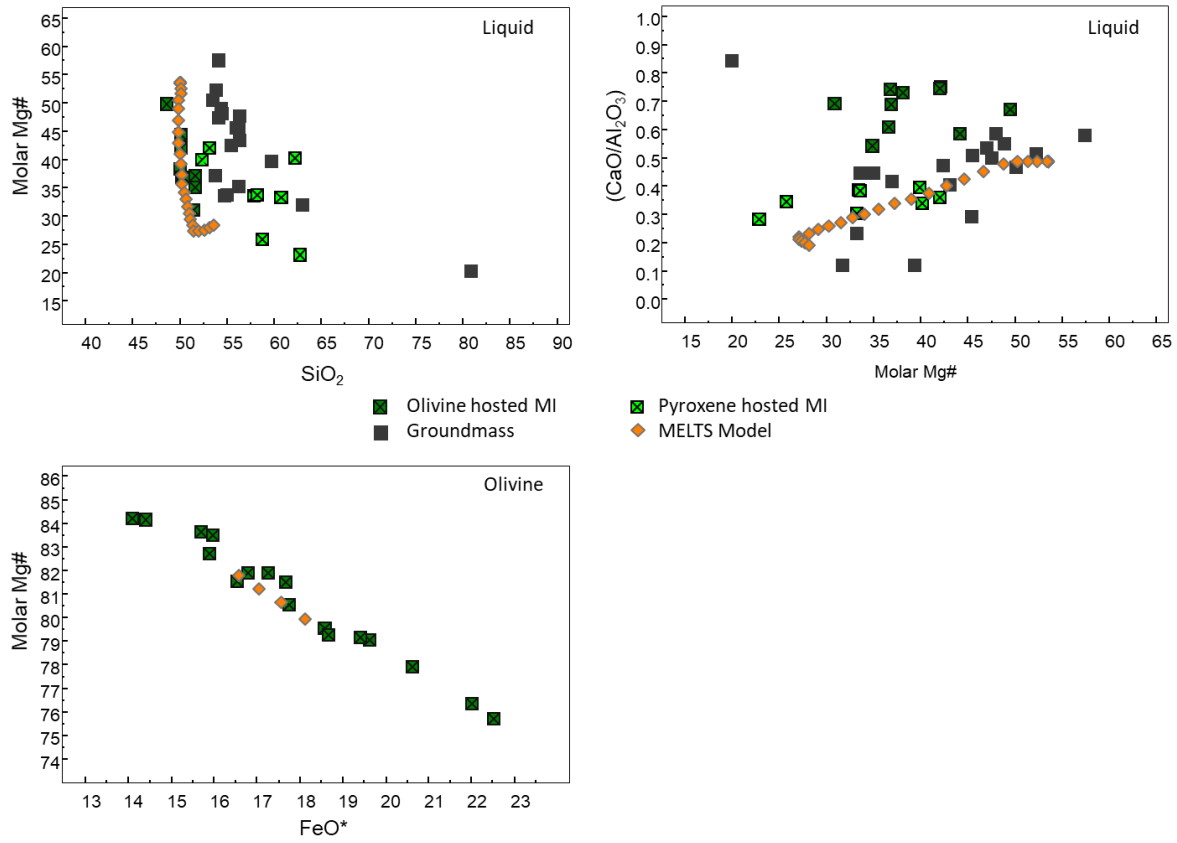

Figure 4-15. Rhyolite MELTS model (equilibrium crystallization at 5 kbar) results for Wharepu tephra. Model input is listed in Appendix Table 11.

4.5.2 Water speciation in the samples

Water can be dissolved in the silicate glass as molecular water and hydroxyl (OH) (Stolper, 1982). The predominant species at low total water content is OH, and equilibrium conditions were determined (Stolper, 1982). Different models (Stolper, 1982, Burnham, 1994) of water dissolution in the aluminosilicate glass are summarized in McMillan (1994). Water dissolution mechanisms in magmatic melts have been extensively studied and involve consideration of temperature, pressure and equilibration kinetics (McMillan, 1994). The data reported here are not sufficient for selecting a possible dissolution mechanism, however, we observe a difference in water speciation between glassy (homogenized) and partially crystallized melt inclusions in the Te Maari lava flow.

Unhomogenized melt inclusions from Te Maari show a disequilibrium distribution for water speciation such that molecular water is too high. Total water in the homogenized samples is not significantly different from total water in unhomogenized samples, but molecular water in the homogenized samples is lower and the distribution roughly follows equilibrium (**Figure 4-16A**) according to the model of Stolper (1982). Higher H_2Omolec/OH values were found for slowly cooled melt inclusions (Wallace *et al.*, 2003) and heating experiments show that the abundance of molecular H_2O and OH is dependent on total water content and cooling rate (Zhang *et al.*, 1995). This explains the high molecular H_2O concentration in the slowly cooled inclusions from the lava flow and the lowering of molecular H_2O concentrations relative to OH when the partially crystallized inclusions were heated then quenched rapidly during homogenization experiments. High H_2Omolec/OH for slowly cooled melt inclusions also emphasizes that the molecular water content of Wharepu melt inclusions are anomalously high considering that these samples naturally rapidly cooled being deposited as tephra.

Speculations can also be made on the effect of the dissolution of crystallites during homogenization. Microprobe analysis of unhomogenized melt inclusions sometimes trend towards contamination of plagioclase, sometimes pyroxene and olivine. Crystallites may take up cations (Na, Mg, Fe, Al) resulting in the preference of water in the residual silicate glass for the molecular form. When the crystallites were dissolved, cations were incorporated in the silicate melt and bonded with OH.

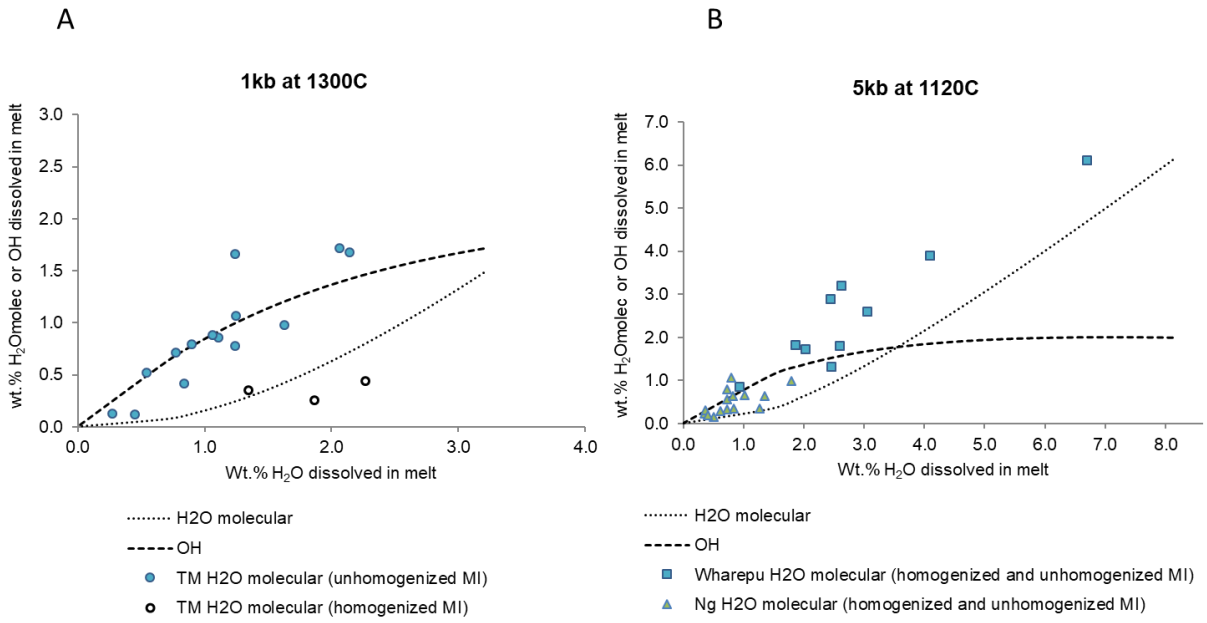

Figure 4-16. VolatileCalc (Newman and Lowenstern, 2002) models of equilibrium concentrations between OH and H_2O molecular (lines) for Te Maari (A) and Wharepu and Ngauruhoe 1975 (B) for the indicated pressure and temperature. The points represent wt. % H_2O molecular and total H_2O in homogenized and unhomogenized melt inclusions. Note that homogenized Te Maari melt inclusions H_2O molecular content follows the equilibrium trend.

Isobaric models in VolatileCalc (Newman and Lowenstern, 2002) give the dissolved water species in the melt at a given temperature and pressure for a basaltic composition. Using 1 kbar and 1300 ºC (values from the crystallization model) as input in VolatileCalc for a basaltic composition (SiO_2: 48 wt.%), the molecular H_2O composition for the homogenized samples in Te Maari follow the modelled molecular water trend (**Figure 4-16A**). Homogenization moved the values for the Te Maari samples towards equilibrium. Modelling for Wharepu at 5 kbar,

1120 ºC and 49 wt.% SiO_2, shows lower molecular water values than the trend revealed by the samples. Ngauruhoe 1975 samples can be plotted on this model as well, because the input parameters are similar (**Figure 4-16B**).

4.5.3 Modelled volatile compositions in melt and gas phases

Solubility models can be used to determine parameters described by the data set and to estimate volatile compositions that were not measured. Isobaric models in VolatileCalc, for example, give CO_2 values dissolved in the melt for a corresponding range of H_2O in the melt. Because there are only few measurements for CO_2 in the data set, we can derive additional values from models. For a range of H_2O from 0 – 2.4 wt.% in the melt for Te Maari, from the VolatileCalc isobaric model at 1 kbar described in the previous section, the corresponding CO_2 values are from 326 to 680 ppm. The highest measured CO_2 in the melt inclusions for Te Maari is 470 ppm. The values are appropriate for melt entrapment at 1 kbar (~ 3-4 km). The highest measured for Wharepu is 364 ppm CO_2. The VolatileCalc model for Wharepu at 5 kbar gives CO_2 values in the melt of 678 to 2825 ppm for the H_2O range of 6.7 to 0 wt.%. There appears to be CO_2 loss in the magma before melt entrapment.

Melt volatile data were used to construct plots that show volatile trends for melt and gas phases using DCompress (Burgisser *et al.*, 2015). DCompress considers 5 element (C-S-O-H-Fe) components in magmatic systems and can be used to determine equilibrium between gas and melt up to 3 kbar (Burgisser *et al.*, 2015). Here, DCompress was used to model melt H_2O, CO_2 and S in Te Maari and Wharepu for up to 3 kbar. The results are compared to VolatileCalc models and actual values.

The volatile content (modelled and actual) of the Te Maari 1500AD lava flow, a product of an effusive eruption, and Wharepu Tephra, from an explosive eruption, are here compared. All CO_2 and total H_2O values for Te Maari and Wharepu are plotted (**Figure 4-17)** with

DCompress models and range of compositions from VolatileCalc for a given pressure. The CO_2 and H_2O content of Te Maari melt inclusions modelled for entrapment at 1kbar follows the equilibrium degassing trend. The Wharepu melt inclusions, considered entrapped at 5kbar, are below the range of compositions from VoltileCalc and are considered degassed in terms of CO_2. In terms of H_2O however, the values plotted at 5kbar can be projected to the equilibrium degassing trend established by DCompress starting at 3kbar (**Figure 4-17**). CO_2 starts degassing at a much higher pressure than H_2O (Gerlach, 1986). The fCO_2gas/CO_2melt for the two deposits when projected to higher pressures appear to converge, and this may indicate a similar CO_2 content for the source of Te Maari and Wharepu magmas. The CO_2 content in undegassed magma may be as high as 4000 - 3000 ppm at greater than 5 kbar (**Figure 4-17**).

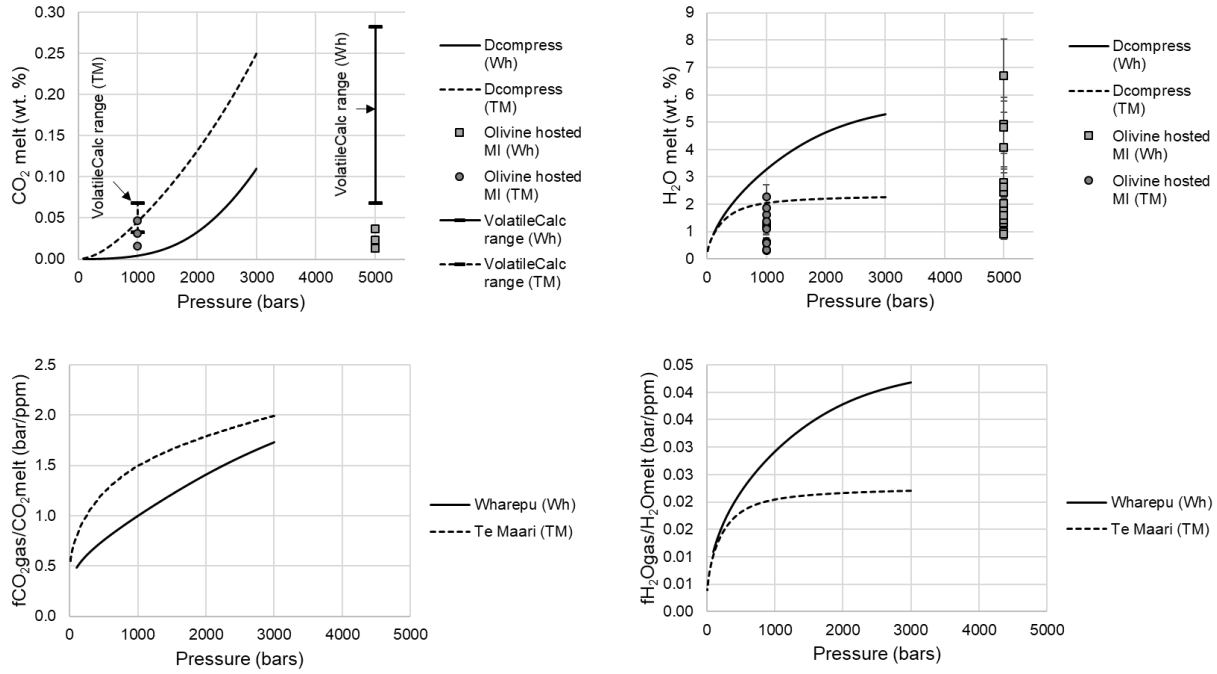

Figure 4-17. DCompress model results for Te Maari (Basalt 1 in Appendix Table 11) and Wharepu (Basalt 3 in Appendix Table 11) CO_2 and H_2O compositions. Measured values and VolatileCalc results are shown.

Values of sulphur dissolved in melt from the Dcompress models for TeMaari are close to measured values for homogenized melt inclusions from olivine xenocrysts and are only higher

depending on the CO_2 input (**Figure 4-18**). Note a difference in S concentrations in homogenized and non-homogenized melt inclusions, with one outlier from each group, as mentioned in Section 4.4.2. A CO_2 input of 2500 ppm is close to the maximum CO_2 value of 2220 ppm at 3 kbar from VolatileCalc. The sulphur model is only for Te Maari where the pressures involved are less than 3 kbar.

Magmatic volatile parameters may be used to set up magma decompression plots for an equilibrium gas phase that may be useful for the present degassing at Te Maari. Because the composition of a presently degassing magma is not known, models were set-up to represent both basaltic and rhyolitic compositions. The rhyolite model uses the same water content as measured (2.27 wt. %), but CO_2 (1125 ppm) was determined from a rhyolite isobaric (3 kbar) degassing model from VolatileCalc, and the temperature is lower at 1110 ºC. DCompress inputs are found in **Appendix Table 11**. The resulting trend of the gas phase for CO_2(gas) versus CO_2/H_2O (gas) (**Figure 4-19**) follows the trend determined by high temperature volcanic gas compositions from different arc volcanoes (Fischer, 2008).

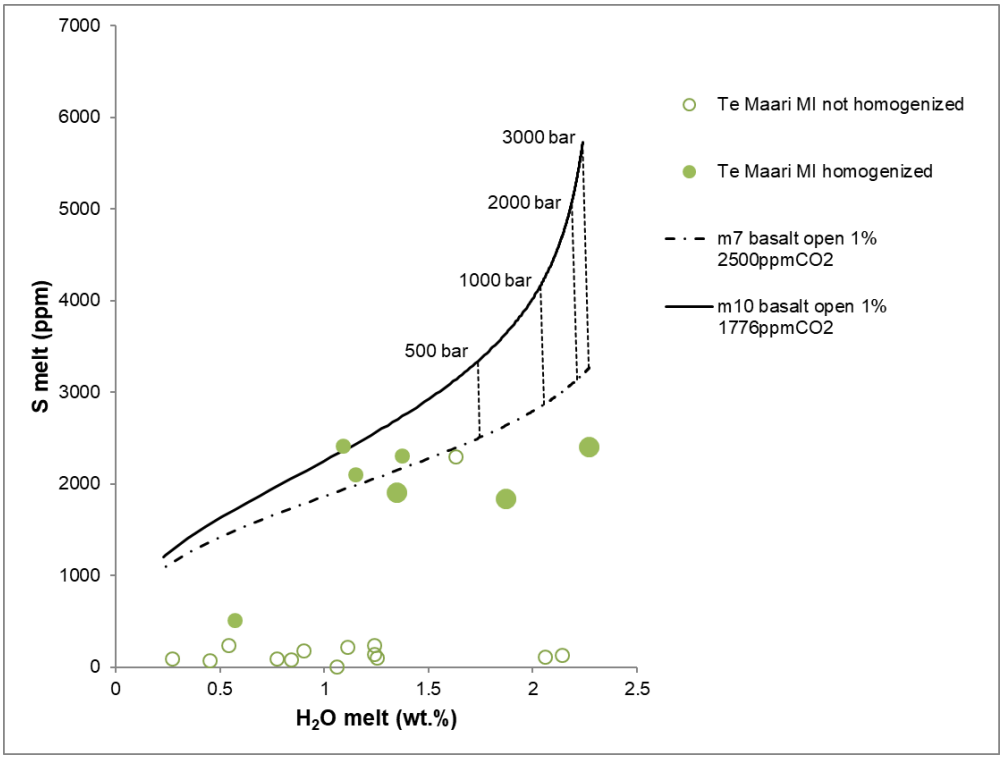

Figure 4-18. Models for open system degassing of basalt using Dcompress (Burgisser *et al.*, 2015), showing the variation of S and H_2O dissolved in the melt as the magma is decompressed starting from 3000 to 10 bar. Measured S and H_2O in homogenized melt inclusions in Te Maari show possible region of melt inclusion entrapment for a crystallizing magma. Large symbols are for melt inclusions with molecular H_2O and OH in equilibrium.

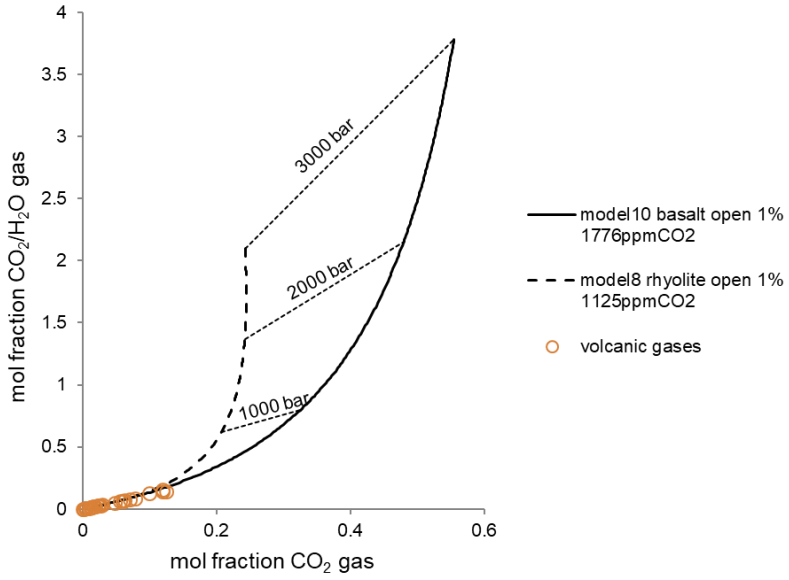

Figure 4-19. Models using Dcompress (Burgisser *et al.*, 2015) for open system degassing of basalt (m10 in Figure 4-13) and rhyolite as magma is decompressed from 3000 to 10 bar. Mole fraction of CO_2 and H_2O in the gas phase are shown. The model follows the trend established by fumarole gas measurements summarized in Fischer (2008).

4.5.4 Eruption style and volatile content

Summarized here are possible implications on volcanic activity for the 3 deposits (Wharepu, Ngauruhoe 1975, Te Maari) based on volatile contents. The melt inclusion data for Ngauruhoe tephra and Red Crater are too few (n=4) to describe clear trends. Conditions were compared between Te Maari 1500AD LF, which is from an effusive eruption, and Wharepu tephra, the product of the highest explosivity and highest volume eruption in the data set. Many studies relate volatiles, whether by their effect on changing viscosity by degassing (Blundy and Cashman, 2005), disequilibrium degassing (Mangan and Sisson, 2000, Mangan *et al.*, 2004) or an accumulated vapour phase (Gerlach *et al.*, 1996), to explosive eruptions.

The main difference between the trends in volatile composition between Te Maari 1500AD lava and Wharepu Tephra is that TeMaari follows equilibrium degassing. Wharepu, in contrast, shows disequilibrium in the distribution of the water species (molecular and OH), and CO_2 compositions that are lower than what was predicted from equilibrium degassing models (**Figure 4-17**). It appears that Wharepu magma degassed CO_2 at >5 kbar and gained H_2O at lower pressure (regassed). Hydrogen can diffuse through olivine to the melt inclusion in timescales of hours based on experiments (Gaetani *et al.*, 2012), whereas O_2 diffusion, re-equilibration of fO_2 between inclusion and surrounding melt, is slower with timescales of hours to days (Gaetani *et al.*, 2012, Hartley *et al.*, 2017). In Wharepu, molecular H_2O is higher than what is expected at equilibrium favouring diffusion of H^+ at lower lithostatic pressure after entrapment. This also implies a shorter time for freezing of the melt inclusions. Plagioclase hygrometry indicates a total H_2O content of 1-1.4 wt% at 8.4 ± 2 kbar (Arpa *et al.*, 2017). There was then an increase in total H_2O content to up to 6.7 wt.% at lithostatic pressures less than 8 kbar (≤ 5 kbar) based on the models for olivine host crystallization shown.

Although melt inclusions can gain meteoric H_2O by diffusion and passage through cracks (Wallace *et al.,* 2003), the proportion of molecular H_2O is high in all analysed Wharepu inclusions and these were inspected for fractures. Ascent and cooling was also fast (tephra deposit) providing little time to equilibrate and exchange diffusively with hydrothermal water. Water can also come from dehydration at depth of the crustal micro-xenoliths found in the tephra samples. The texture around the xenoliths are more vesiculated (76% vesicles compared to 35% vesicles) implying volatile contribution from the xenolith. However, it also suggests that volatiles were released in bubbles. Xenolith dissolution based on major element analysis of groundmass were also found to be insignificant. Water contributed by an underplated hydrous intrusion in a deep reservoir is also possible. At high pressures and total water content, molecular H_2O is the predominant species (Holloway and Blank, 1994). It cannot explain however, the disagreement with plagioclase hygrometry results (for Wharepu) where crystallization pressures are high, but total water is significantly lower (**Table 3-6**) than what is measured in melt inclusions. In this study, the isotopic characteristic of the melt inclusion water was not determined, and the origin/source for the H_2O enrichment cannot be identified with more certainty. Regardless of origin however, high ascent rates in an extensional environment (Nairn *et al.,* 1998, Nakagawa *et al.,* 1998), combined with possible addition of H_2O to the magma may be factors explaining the explosivity of the Wharepu eruption.

The melt inclusion volatile contents plotted in the H_2O-S-Cl system shows the degassing trend as crystallization pressures for the mineral hosts decrease (**Figure 4-20**). It shows a decreasing water content from the deeply sourced magmas (Wharepu) to the shallow reservoir for Te Maari, and the S/Cl ratio remains relatively constant. Water measured from Te Maari melt inclusions in olivines may represent water fugacities at the 1kbar deep chamber. However, because the olivines are xenocrysts it cannot be determined if the inclusions crystallized and cooled in the reservoir or during lava transport, the latter case makes the water content subject

to diffusive loss by equilibration with the degassing flow (Hartley *et al.*, 2015). At shallower depths, S starts to degas leading to relative enrichment of Cl in the melt, traced by the path of decreasing S/Cl ratio (Lloyd *et al.*, 2014). Figure 4-20 also shows the different histories for the olivines and pyroxenes in Te Maari. The pyroxene hosted melts appear to have degassed S. However, this does not agree with the melts trapped at high pressure. Water content for the pyroxene hosted melt inclusions is similar to the olivine hosted melts implying that these were not degassed in terms of water. In the case where pyroxene-hosted melt inclusions may have equilibrated with external melt H_2O at the shallow (1kbar) reservoir, the changes will be small because the degassing model for Te Maari (**Figure 4-17**) shows that water only significantly decreases after 1kbar. To have low S values, it may be possible that S was incorporated in a separate phase, as inclusions comprising Fe and S were found in the pyroxenes and in groundmass. It was demonstrated, although only for olivines, that homogenized Te Maari melt inclusions show, in general, higher S compared to non-homogenized inclusions.

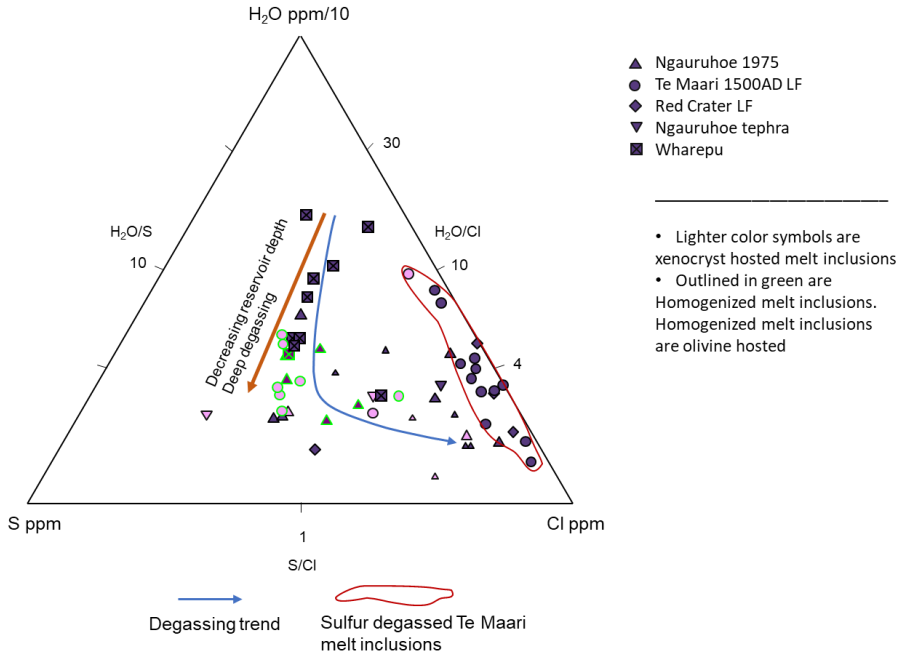

Figure 4-20. Decreasing mineral host crystallization depth follows degassing trend. Pyroxene-hosted melt inclusions from Te Maari are outlined, these show low S content for the same range of H_2O content in the olivine (xenocrysts) hosted melt inclusions.

Insights into the relative redox state of the Te Maari lava can be gained from co-existing magnetite and ilmenite (exsolution lamellae) compositions. These compositions were input into the Fe-Ti thermometer of Ghiorso and Evans (2008) and resulted in values from 0.59 to 2.75 ΔNNO. These values are consistent with an oxidizing condition for arc magmas (Carmichael and Ghiorso, 1986). The less oxidizing value of 0.59 ΔNNO at a lower temperature (891 ºC) may represent a decrease in redox state as the magma cooled. Note that from bulk Fe^{3+}/Fe^{2+} of the lava sample (slowly cooled at the surface), determined by wet chemistry methods (Hutchison, 1973), the relative redox state is ΔNNO -1.2 ± 0.5 to -1.5 ± 0.6. The decrease in oxidation state may be primarily influenced by degassing of sulphur and other volatiles at near surface. Sulphur degassing significantly affects the relative Fe redox state of magmas (Carmichael and Ghiorso, 1986, Gaillard *et al.*, 2015).

Ngauruhoe melt inclusion volatiles (H_2O, S and Cl) appear intermediate between Wharepu and Te Maari. The variability among the 3 volatile species for Ngauruhoe may imply convective degassing in the magma reservoir region. The reservoir is likely stable for a long period to accommodate multiple intrusions that result in crystallization and melting. The eruptive history of Ngauruhoe, a well formed stratovolcano and highest peak in the Tongariro Volcanic Complex, can go back to 7,000 cal. years BP (Moebis *et al.*, 2011). Component (minerals and glass) compositions for the Ngauruhoe pyroclasts can be modelled by both crystallization and melting, probably in a convecting chamber (Stevenson and Blake, 1998, Beckett *et al.*, 2014).

4.6 Conclusions

Volatile composition from melt inclusions for selected deposits from Tongariro Volcano were interpreted in relation to host mineral crystallization environments. Different magmatic conditions were derived for deposits produced from different eruption styles. High water content was measured for the explosively erupted Wharepu Tephra. More important than high water content, it is high in molecular water and shows a trend that is not consistent with equilibrium water speciation. Disequilibrium features in terms of water speciation and mineral-melt compositions may have implications on processes that produce explosive eruptions. A shallow reservoir, where magma incorporated xenocrysts is implied for the Te Maari 1500AD magma. The magma originated from a deep source and stalled at this shallow reservoir where it starts to significantly degas. The degassing and magma reservoir processes for Ngauruhoe may be more complex and may imply melting and crystallization in the reservoir. It appears that the distinct volatile compositions for the deposits are consistent with differences in the manner of magmatic and volcanic activity.

5 Models of storage and differentiation for Tongariro Volcano magmas and its relation to the Southern Taupo Volcanic Zone

5.1 Abstract

Petrological processes that can produce the c. 10 ka to present andesites in Tongariro Volcano are interpreted relative to storage depths and ascent/degassing paths. The deposits are from different vents within the volcanic complex and were deposited from explosive to effusive eruptions. Whole rock major, trace and isotope compositions, groundmass and mineral compositions, and melt inclusion volatile contents show that more differentiated magmas can be derived from a common basaltic source, but there may be specific magma differentiation paths for each deposit. A basalt may differentiate to andesite by crystallization at depth, and an andesite may be stored at a shallower reservoir where it can be melted to produce dacite. Basaltic magmas from deep reservoirs can also be tapped for eruption or be stored at shallow reservoirs where it either batch crystallize or fractionate crystals before eruption. Trace element, Sr and O isotope compositions show influence of crustal assimilation, but it does not determine major element compositions. Ascent path conditions that affect magma compositions may be dependent on local structure controls on the volcano based on comparison with Ruapehu and consideration of regional magmatism.

5.2 Introduction

Tongariro Volcano in the North Island of New Zealand is part of the Southern Taupo Volcanic Zone, which is within a larger area of Quaternary volcanism and tensional tectonics (Central Volcanic Region) southwest of the Havre Trough and Lau Basin back-arc systems (**Figure 5-1**) (Karig, 1974, Stern, 1985). The Southern Taupo Volcanic Zone, which also includes Ruapehu Volcano, partly comprise a volcanic arc that formed from the subduction along the Hikurangi Trench (Karig, 1974, Stern, 1985, Rowland and Sibson, 2001, Smith and Price,

2006). The Kermadec subduction zone system continues south to the Hikurangi Trench where convergence between the Australian and the Pacific Plates changes from oceanic to continental-oceanic in New Zealand forming a NE-SW trending volcanic arc, with melt generation occurring 80-100 km above the subducted slab (Karig, 1974, Stern, 1985, Hamilton, 1988, Reyners *et al.*, 2006, Smith and Price, 2006, Stratford and Stern, 2006). The continental crust, particularly below Taupo Volcanic Zone in the Central Volcanic Region, is thinned by back-arc extension (Harrison and White, 2006, Stern *et al.*, 2006, Stratford and Stern, 2006, Stern *et al.*, 2010), but basaltic intrusions in the lower crust places the crust-mantle boundary at 20-25 km (Stern *et al.*, 2010) or 30 and 35 km depths (Harrison and White, 2006, Reyners *et al.*, 2006). These basalts are expected to be generated in a mantle modified by the subduction process.

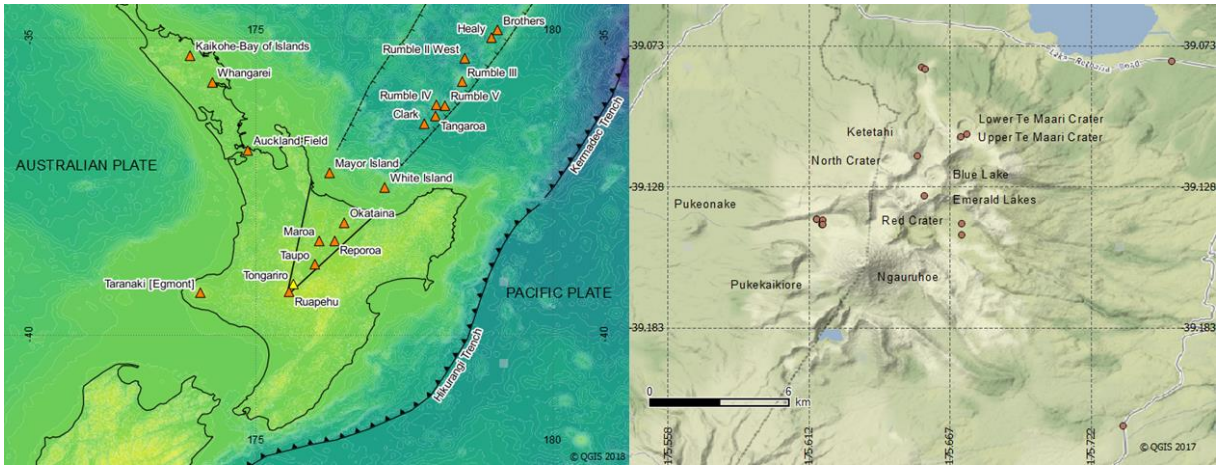

Figure 5-1. Regional tectonic setting for Tongariro Volcano showing the Central Volcanic Region (solid line) and the Havre Trough Back-Arc Basin (bounded by dashed hachured lines) (left). Tongariro Volcanic Complex, named eruptive vents are labelled (right) and sample sites are shown (red circles).

Studies of arc magmatism have shown contributions from the subducting slab, overriding crust and mantle (Mysen and Boettcher, 1975, Hildreth and Moorbath, 1988, Tatsumi, 1989, Peacock, 1990, Ryan *et al.*, 1995, Yogodzinski and Kelemen, 1998, Castillo and Newhall, 2004, Grove *et al.*, 2006, Behn *et al.*, 2011, Till *et al.*, 2012). Flux/dehydration melting is a

predominant process beneath volcanic arcs where fluids from dehydration of the subducted sediments and oceanic crust enables melting in the mantle wedge (Grove *et al.*, 2006, Till *et al.*, 2012). Melting of subducted sediments and down-going slab can also occur (Yogodzinski and Kelemen, 1998, Behn *et al.*, 2011). Decompression melting of the mantle due to extension in a back-arc results in less hydrous melts, but may interact with shallower hydrated mantle (Kamenetsky *et al.*, 1997).

The Southern Taupo Volcanic Zone is in a region where there is significant crustal extension to the northeast, but it is also part of the volcanic arc being about 100 km above the slab (Reyners *et al.*, 2006). A large reservoir of silicic volcanism (Taupo Volcanic Zone) is located towards the northeast in the more extensional environment (Cole, 1981). Andesitic magmatism in the Southern Taupo Volcanic Zone was shown to be the result of assimilation and/or fractional crystallization from a common parental magma (Gamble *et al.*, 1990, Graham *et al.*, 1995, Price *et al.*, 2005). In this study, we evaluate andesite petrogenesis in a volcanic complex plumbing system by looking at Tongariro Volcano magmas. Tongariro is a good area to study the effects of transitional tectonic environments on arc magmatism (**Figure 5-1**).

The samples were selected based on different eruption styles for deposits with ages determined from previous studies (**Table 5-1**). These samples are from the last 16,000 years, with detailed discussions on deposits from c. 10,000 years to present. Petrogenesis will be evaluated for deposits from explosive to effusive eruptions and from different vents within the complex. Compositions will also be compared to those of Ruapehu for the same period of magmatic activity to see spatial variations that may be related to regional volcano-tectonic settings. Magmatic differentiation in Tongariro samples will be interpreted relative to depths of magma reservoirs and magmatic volatile contents to consider petrologic processes for a moving magma, and to have insights on volcanic hazards.

Table 5-1. Samples for this study. Source vent names are also labelled on the Tongariro imagery in Figure 5-1. The samples are listed from youngest (top) to oldest.

Sample main	Source Vent/Unit	Longitude (Easting)	Latitude (Southing)	Comment	Mineralogy (* with microprobe)
150319-02	1st phase 1975 PF Ngauruhoe	175.61752	-39.14286	Pyroclast (bomb)	*(pl, cpx, opx, ol, mt)
150829-03	1st phase 1975 PF Ngauruhoe	175.61765	-39.14295	Pyroclast (bomb)	
1954	1954 Ngauruhoe lava flow			Lava Flow	nt
150317-01	[a]1500AD Upper Te Maari LF	175.65614	-39.08202	Lava Flow	*(pl, cpx, opx, ol, mt, il)
160727-01	[a]1500AD Upper Te Maari LF	175.65726	-39.08273	Lava Flow	
150318-02	[b]post-1.8 ka Taupo Red Crater LF	175.65710	-39.13176	Lava Flow	pl, px, ol
150318-03	[b]post-1.8 ka Taupo Red Crater LF	175.67152	-39.14234	Lava Flow	*(pl, cpx, opx, ol)
150424-01	[a]Red Crater LF (Oturere lava flow)	175.67155	-39.14675	Lava Flow	Pl, px, ol, ox
150319-01	pre-1.8 ka Taupo tephra Ngauruhoe?	175.61531	-39.14064	Tephra	*(pl, cpx, opx, ol)
150829-01	[b]Ngauruhoe lava flow, group 2, pre-1.8 ka Taupo	175.61548	-39.14074	Lava Flow	nt
150318-01	[c]agglutinate North Crater	175.65448	-39.11628	Pyroclast (bomb)	*(pl, cpx, opx, mt, il)
150116-01/ 150320-01A	Te Rato (~11,000 cal. yrs. B.P.): North Crater[a]; Proto-NC, TM craters[d]	175.73384	-39.22060	Tephra	*(pl, cpx, opx, ol, hbl, mt)
150321-02	Te Rato: North Crater[a]; Proto-NC, TM craters[d]	175.75290	-39.07965	Tephra	
150320-01B	Oturere: Tama Lakes-Ng area[a]; Saddle Cone, Half Cone[d]	175.73384	-39.22060	Tephra	pl, px, ol, ox
150320-01C	Waihohonu (above fine ash layer, middle coarse layer): Tama Lakes-Ng area[a]; Saddle Cone, Half Cone[d]	175.73384	-39.22060	Tephra	pl, ol
150320-01D	Wharepu (lower brown layer): Tama Lakes[a,d]	175.73384	-39.22060	Tephra	pl, px, ol
150320-01E	Wharepu (upper gray layer): Tama Lakes[a,d]	175.73384	-39.22060	Tephra	*(pl, cpx, opx, ol)
150320-01F	Poutu (~11,000 cal. Yrs. B.P.): Blue Lake[a]; Ngauruhoe area[d]	175.73384	-39.22060	Tephra	pl, px, hbl
150321-01A	[c]RT3 lower orange brown lapilli layer: Lower Te Maari	175.75290	-39.07965	Tephra	pl, cpx, opx, ox
150321-01E	[c]RT3 orange brown lapilli layer: Lower Te Maari (~16,000 cal. yrs. B.P.)	175.75290	-39.07965	Tephra	pl, cpx,opx, ol, ox

Ages/vents are from [a] Topping, 1974; [b] Hobden, 1997; [c] Topping, 1974, Shane et al., 2008, Lowe et al., 2008; [d] Nairn et al., 1998
nt = no thin section

5.3 Methods

Portions of lava and bomb size pyroclasts and individual lapilli were analysed for whole rock major element compositions using a wavelength dispersive (WD) X-ray fluorescence

spectrometer (XRF) PANalytical AXIOS^{max} at the Department of Earth Sciences, National Taiwan Normal University (NTNU). Trace element compositions were determined by Inductively Coupled Plasma Mass Spectrometer (ICPMS) on dissolved samples at National Taiwan University (NTU). Additional whole rock major element analysis was done at the X-Ray Centre of the University of Auckland using PANalytical Axios 1kW X-ray fluorescence spectrometer. Selected samples were sent and analysed for whole rock Oxygen and Hydrogen isotopic compositions at the Stable Isotope laboratory, Department of Geological Sciences, University of Cape Town. Analyses were done by conventional vacuum extraction line using ClF_3 as the reagent (Harris and Ashwal, 2002). The same set of samples were analysed for Sr ($^{87}Sr/^{86}Sr$), Nd ($^{143}Nd/^{144}Nd$) and Pb ($^{208}Pb/^{204}Pb$, $^{207}Pb/^{204}Pb$, $^{206}Pb/^{204}Pb$) isotopes using a Nu plasma II-ES multicollector inductively coupled plasma mass spectrometer at the College of Engineering and Physical Sciences, University of New Hampshire.

Mineral and groundmass major element compositions, also presented in Sections 3 and 4, are from electron microprobe analysis using a JEOL JXA-8230 Electron Probe Micro-Analyzer (EPMA) equipped with 5 wavelength dispersive X-ray spectrometers (WDS) at the School of Geography, Environment and Earth Sciences, Victoria University of Wellington. Melt inclusion major element and volatile compositions, as presented in Section 4, are from the microprobe laboratory at Victoria University and FTIR (Nicolet Continuum FTIR) analysis at the Institute of Agriculture and Environment, Massey University, Palmerston North.

5.4 Whole rock major and trace element compositions

All samples are calc-alkaline and range from basalt to dacite (**Figure 5-2)**. These are from at least 6 vents within Tongariro Volcanic Complex, and eruption styles range from explosive to effusive for eruptions in the last 16,000 years. One tephra clast is a basalt, and another classifies as dacite (SiO_2: 63.21 wt.%). The basalt is a tephra clast from a lower unit of Wharepu tephra

and the dacite is a mingled pumice from Te Rato, both are members of the 10 ka Mangamate Formation. All samples listed in **Table 5-1** plot mostly along a single trend for major elements that can originate from the basalt sample.

Trace element abundances are enriched relative to primordial mantle (**Figure 5-3A**) and shows a typical arc pattern. The samples have values for Nb, Hf, Zr, Sm close to average MORB (**Figure 5-3B**), but are enriched relative to MORB in incompatible elements such as Rb, Ba, Th, U, K and La. Relative to an average lower continental crust (**Figure 5-3C**), the samples are depleted in Ba, but remain enriched in Rb, Th, U, and become slightly more enriched in Ti and heavy rare earths. Rare earth element abundances relative to Chondrite (**Figure 5-3D**) show no large variations between samples and a gentle negative slope from light to heavy REE with no significant depletion of middle REE. This pattern does not reflect the typical pattern for low degree partial melting or involvement of an eclogite source (**Figure 5-3D**) where heavy REE are fractionated in the source (Winter, 2001). The complete list of whole rock major and trace elements is found in **Appendix Tables 2 and 3**.

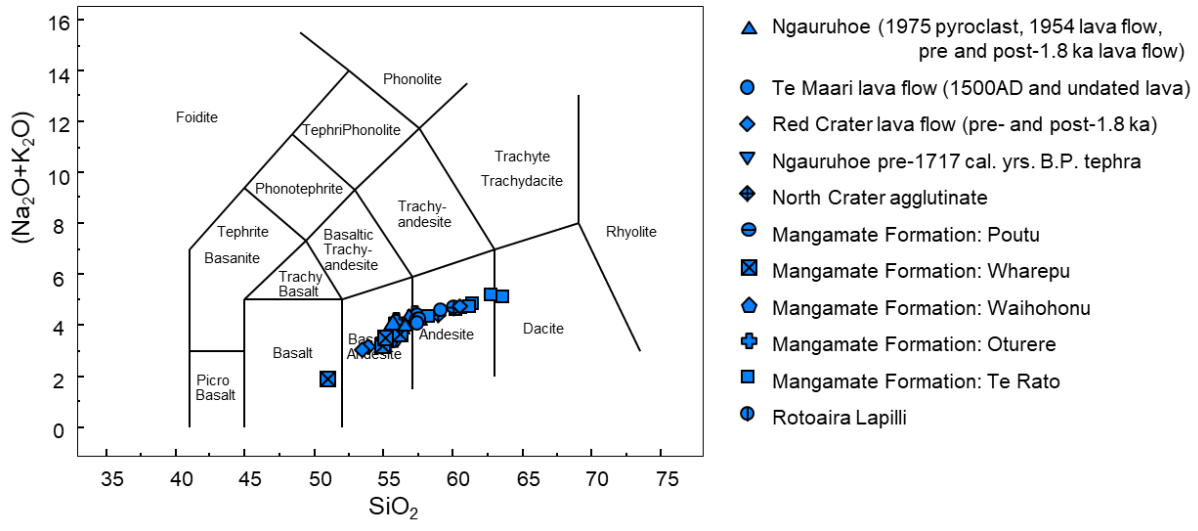

Figure 5-2. Total alkalis versus silica classification for igneous rocks after Le Bas et al., 1986. Plotted using Petrograph (Petrelli *et al.*, 2005).

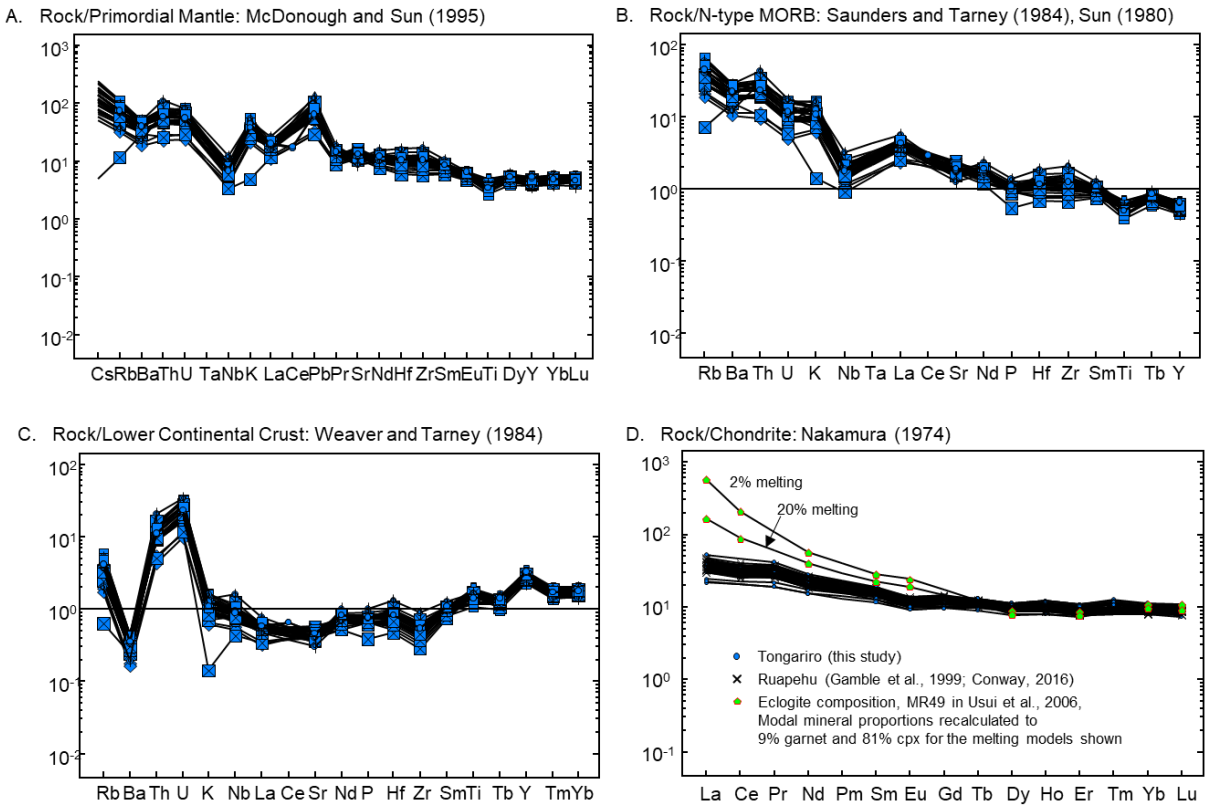

Figure 5-3. Trace element variations relative to standard average compositions. Symbols are as for **Figure 5-2**. Plotted using Petrograph (Petrelli *et al*., 2005)

Caution should be taken in interpreting the Te Maari bulk composition in terms of elements fractionated in olivine crystals. The addition of olivine xenocrysts have increased Ni in the whole rock sample, and compositions show significantly higher Ni concentrations relative to the rest of the samples (**Figure 5-4**). Using the mass balance function (after Stormer and Nichols, 1978) in Petrograph (Petrelli *et al.*, 2005) with an undated Upper Te Maari lava sample (150421-02) as starting composition and adding a xenocryst olivine composition, an addition of 5.97% olivine is needed to produce the Te Maari lava flow sample composition (160727-1C). The mass balance is in terms of 10 major elements without considering Ni. Nickel is considered in a 2-end member mixing model (mixing model function, after Langmuir et al., 1978, in Petrograph), using 150421-02 and olivine (in TM 1500 AD lava) compositions in

terms of Ni and MgO (**Figure 5-5**). The mixing model shows an addition of 5.94% to 6.12% olivine. About 3% olivine was estimated from 1 thin section view. None of the randomly sampled olivines in the Te Maari samples were found to be in equilibrium with groundmass with respect to Mg and Fe.

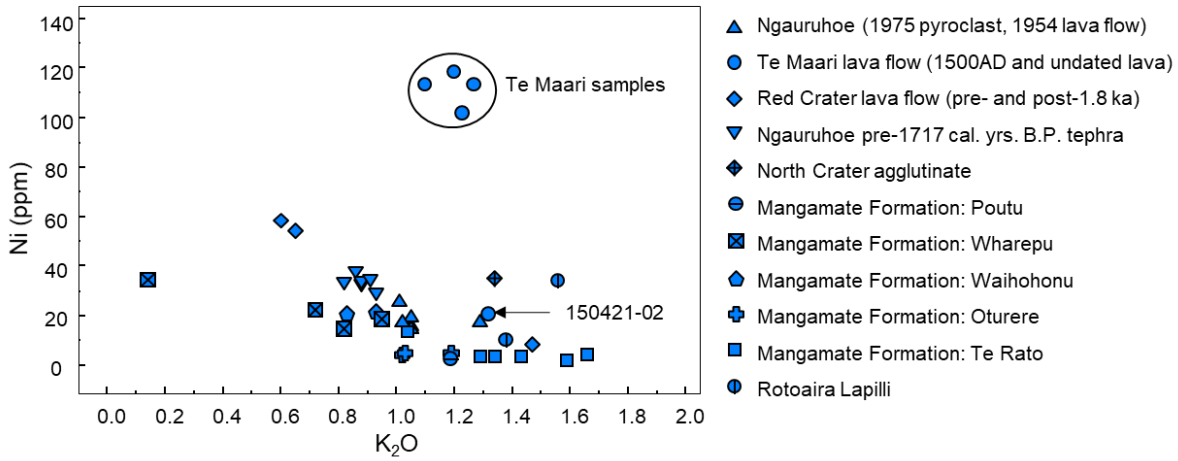

Figure 5-4. Off trend, significantly higher Ni values for Te Maari whole rock compositions.

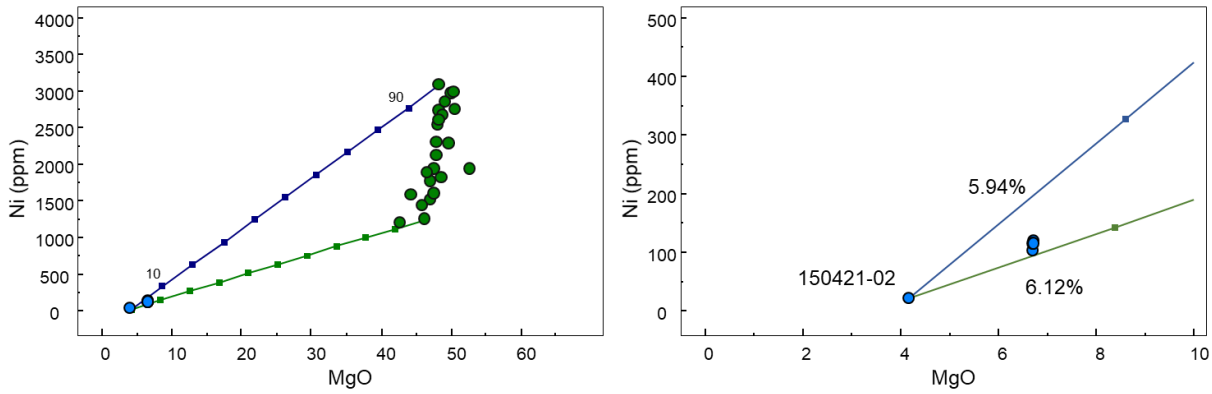

Figure 5-5. Two end-member mixing models showing the proportion (5.94-6.12%) of olivine (green circles) added to Te Maari 1500AD lava flow samples (clustered blue circles). This agrees with mass balance results of 5.97% using all the major elements.

5.5 Radiogenic isotope compositions

Before evaluation of differentiation processes and relationships between sample compositions, it is important to assess whether the samples show a common source based on coherence of isotopic composition. It will also show where the samples plot relative to known sources (mantle, MORB, continental crust). Radiogenic isotopes of Sr and Nd (**Table 5-2**) are used to characterize the source of magmas because their parent elements have different compatibilities in the mantle (White, 2013). Pb isotopes (**Table 5-2**) may be used to identify sources with different characteristic subducted sediments (Castillo and Newhall, 2004). **Figure 5-6A** shows a narrow composition range for Pb isotopes despite one sample being affected by inclusion of a crustal xenolith as shown by its higher total Pb. The source magma for all the samples is higher in radiogenic Pb compared to the East Pacific Rise MORB sources (Ito *et al.*, 1987) and is close to the composition of an average upper crust (Rudnick and Goldstein, 1990). Ngauruhoe crustal xenoliths (Price *et al.*, 2010) are plotted for comparison. The sample compositions plot to the right of the 4.45 Ga geochron (**Figure 5-6B**) suggesting an enriched source.

Table 5-2. Sr, Nd and Pb isotope compositions for selected samples. Mean (M) standard errors (SE) are shown.

Sample	$^{87}Sr/^{86}Sr$	2 SE (M)	e_{Nd}	$^{143}Nd/^{144}Nd$	2 SE (M)	$^{208}Pb/^{204}Pb$	2 SE (M)	$^{207}Pb/^{204}Pb$	2 SE (M)	$^{206}Pb/^{204}Pb$	2 SE (M)	Comment
150318-03	0.704589	0.000008	3.68	0.512826	0.000006	38.7594	0.0026	15.6376	0.0007	18.8316	0.0006	RC post-1.8 ka LF
150319-01-e	0.704950	0.000012	1.84	0.512732	0.000004	38.7860	0.0016	15.6443	0.0004	18.8460	0.0004	Ng pre-1.8 ka tephra
150319-02-a1	0.705774	0.000010	1.36	0.512707	0.000006	38.7919	0.0021	15.6472	0.0005	18.8457	0.0005	Ng 1975 pyroclast
150319-02-b2	0.705712	0.000012	1.38	0.512709	0.000004	38.7819	0.0020	15.6481	0.0006	18.8345	0.0005	Ng 1975 pyroclast
150319-02-a2	0.705642	0.000009	1.54	0.512717	0.000009	38.7925	0.0011	15.6471	0.0004	18.8495	0.0004	Ng 1975 pyroclast
150320-01A-b	0.705254	0.000009	2.18	0.512750	0.000005	38.7906	0.0014	15.6443	0.0004	18.8421	0.0004	Te Rato pumice
150320-01A-h	0.705123	0.000012	2.65	0.512774	0.000004	38.7860	0.0019	15.6440	0.0005	18.8433	0.0005	Te Rato pumice
150320-01E-a	0.704884	0.000007	2.03	0.512742	0.000004	38.7712	0.0017	15.6409	0.0005	18.8287	0.0005	Wharepu tephra
150320-01E-e	0.704978	0.000013	1.61	0.512721	0.000005	38.7972	0.0014	15.6434	0.0004	18.8495	0.0005	Wharepu tephra
160727-01-C	0.705405	0.000010	1.63	0.512721	0.000005	38.7990	0.0021	15.6485	0.0006	18.8556	0.0005	Te Maari 1500AD LF

Analysis done at the College of Engineering and Physical Sciences, University of New Hampshire.

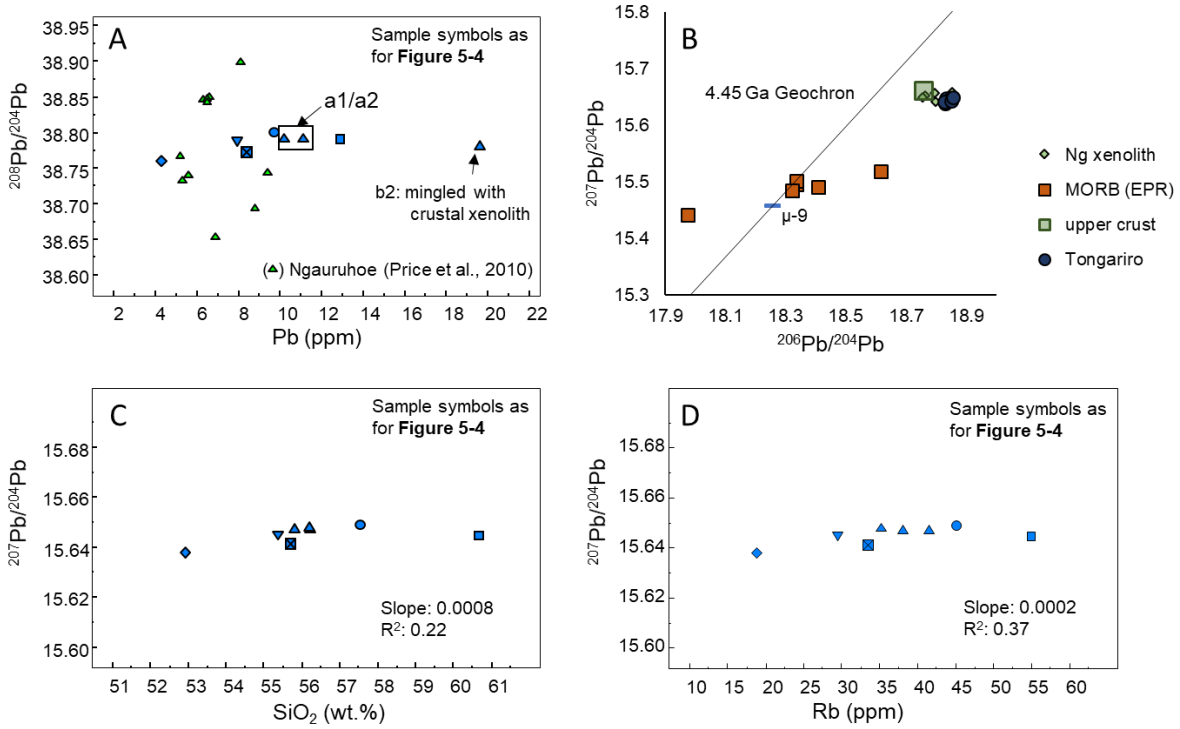

Figure 5-6. A narrow range in Pb isotopes support a common source. One sample is enriched in total Pb, likely a crustal contribution, Ngauruhoe samples (green triangles) from Price et al., 2010 are shown for comparison. Samples 150319-02-a1, a2 and b2 from Ngauruhoe 1975 are indicated, symbols are as for **Figure 5-4** (A). Radiogenic Pb values relative to known sources: MORB (EPR) (Ito *et al.*, 1987), upper crust (Rudnick and Goldstein, 1990); crustal xenoliths from Ngauruhoe (Price *et al.*, 2010) are also plotted. The 4.45 Ga geochron represents present day Pb isotope values (B). Very low correlation and only a slight positive trend between $^{207}Pb/^{204}Pb$ and differentiation indicators such as SiO_2 (C) and Rb (D).

A Ngauruhoe crustal xenolith was used to approximate an upper-crust composition, or the composition of sediments subducted along the Hikurangi Trench. It is used as an end-member composition in a 2 end-member mixing model in the $^{87}Sr/^{86}Sr$ versus $^{143}Nd/^{144}Nd$ plot (**Figure 5-7**), after the equation of Langmuir et al. (1978). This mixing model and another between an East Pacific Rise (EPR) MORB source (Ito *et al.*, 1987) and an actual bulk sediment composition near the Kermadec subduction segment (Plank and Langmuir, 1998) represent

well the sample compositions. The r ~ $[(Nd/Sr)_1/(Nd/Sr)_2]$ (Langmuir *et al.*, 1978) for the models is 0.6 and close to the $(Nd/Sr)_1/(Nd/Sr)_2$ of 0.577 for 2 extreme compositions in the sample set. This shows a source composition that is intermediate between a depleted MORB mantle (DMM) and an enriched mantle (EM2) as also shown in **Figure 5-8**. Enriched mantle (EM2) reflects contributions of subducted upper crust sediments and fluids to the mantle (Zindler and Hart, 1986). A contribution from sediments is reflected by the mixing models with respect to Sr and Nd isotopes, and the sediment source is common for the magmas as implied from the lack of variability in the Pb isotopic compositions.

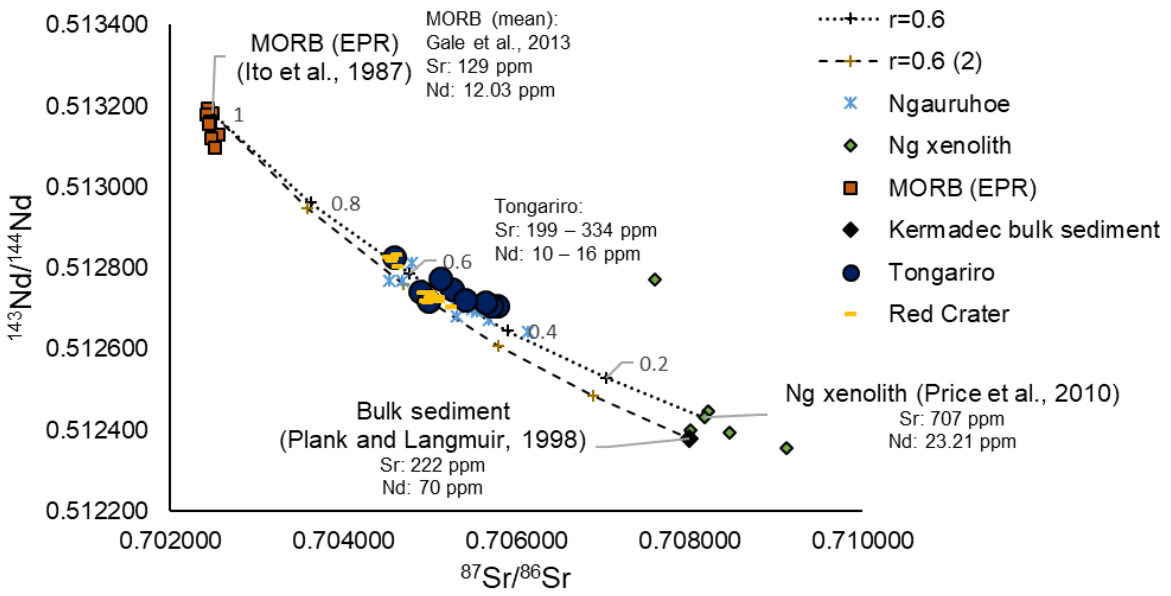

Figure 5-7. Mixing line between MORB (EPR) (Ito *et al.*, 1987) and Kermadec bulk sediments, gray diamond, (Plank and Langmuir, 1998) and between MORB (EPR) and a Ngauruhoe crustal xenolith (Price *et al.*, 2010) to approximate subducted sediments closer to the study area. Mean values for MORB are shown (Gale *et al.*, 2013). The mixing lines represent well the sample compositions. Deposits from Ngauruhoe (Price *et al.*, 2010) and Red Crater (Shane *et al.*, 2017) are shown for comparison.

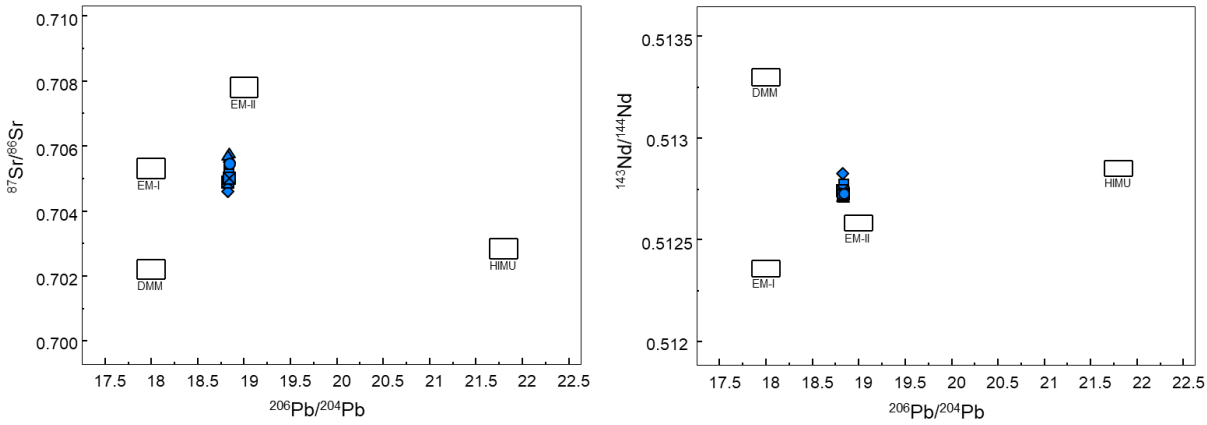

Figure 5-8. Sample isotopic composition relative to established mantle sources: Depleted MORB Mantle (DMM), Enriched Mantle I (EMI), Enriched Mantle II (EMII), Hi-μ mantle (HIMU). Plotted using Petrograph with mantle end-members from Hart et al., 1992 (Petrelli *et al*., 2005)

5.6 Crystallization models

It was shown that andesites from the Taupo Volcanic Zone can be derived from a similar basaltic parental magma and that variability in composition is due to local fractionation pathways (Gamble *et al.*, 1990). Isotopic compositions presented in the previous section show that the samples from the last 10,000 years define a common source. Geochemical correlation for magmatic sources may also be done by looking at trace element ratios and major element trends. Zr/Nb ratio for most of the samples, excluding 2 outliers, are constrained within the narrow range of Wharepu samples (20.7-26.4) (**Figure 5.9 A**). The Zr/Nb ratio for Tongariro deposits (for the same period) from previous studies (Pahoka-Mangamate (Nakagawa *et al.*, 1998), North Crater (Shane *et al.*, 2008), Ngauruhoe (Price *et al.*, 2010), Red Crater (Hobden, 1997, Shane *et al.*, 2017) and Te Maari (Hobden, 1997)) show a larger range (**Figure 5.9 B and C**) for the Mangamate members and certain Red Crater samples. However, this may be mainly due to different laboratory calibrations, and more recent analyses show a common range for the data. Representative Ruapehu compositions (Hackett, 1985, Gamble *et al.*, 1999,

Conway, 2016) is distinguished from Tongariro in terms of Ba/La ratio. For only 10-20% melting, Ba/La in melt should be similar to Ba/La in source and Ba should be enriched with increasing contribution of fluids from slab dehydration (Castillo and Newhall, 2004). Based on trace element ratios and isotope compositions, the Tongariro samples in this study imply a common source, distinct from the closest volcano (Ruapehu), and therefore petrogenetic processes relating magma compositions within the sample set may be evaluated.

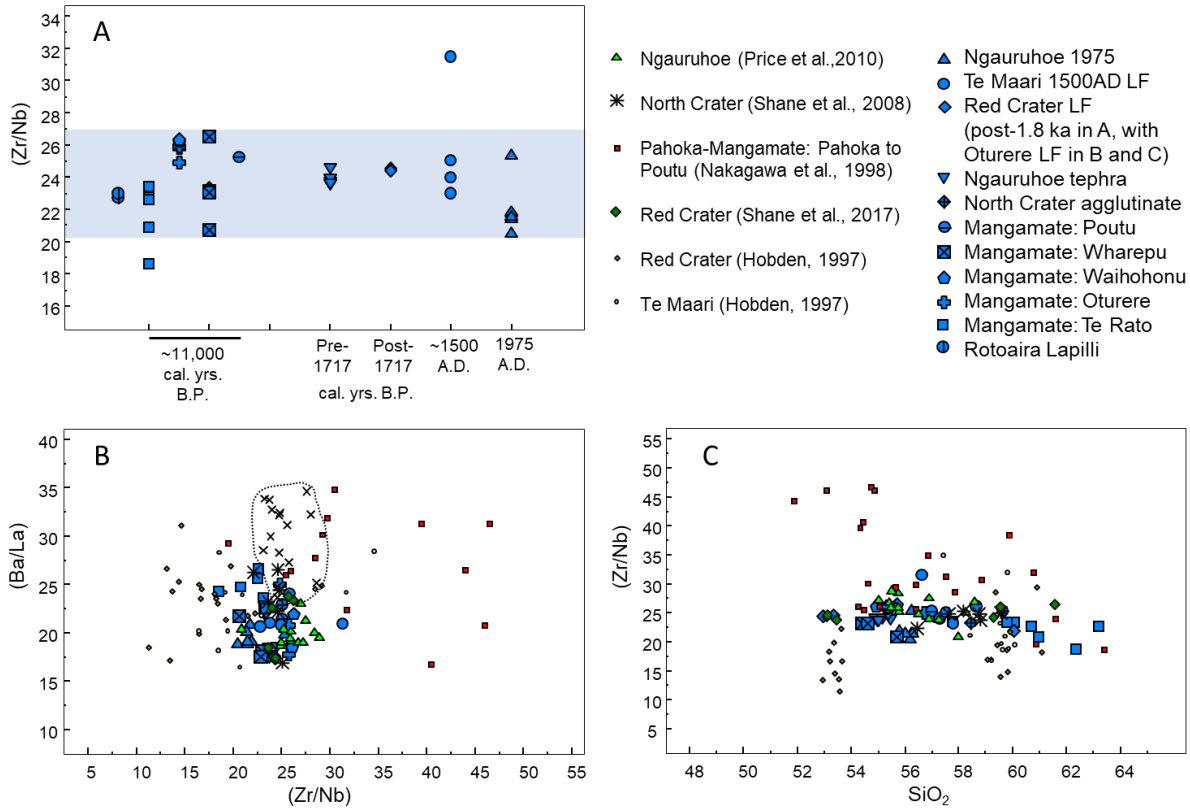

Figure 5-9. A distinct magmatic source for the samples in this study constrained by trace element ratios. The range for Zr/Nb ratio for samples is narrow (A). Ruapehu samples (x symbol, enclosed by a dashed line) can be distinguished by higher Ba/La ratios, data from Hacket, 1985; Gamble et al., 1999; Conway, 2016 (B). Data for Tongariro from previous studies are plotted with the sample set, all recent data sets plot within the range of the samples for this study.

In a subduction zone setting, parental basalts are produced by partial melting of a metasomatized mantle (Winter, 2001). Geophysical models show that, there is a large reservoir

of subduction related intrusions in the lower crust below the Taupo Volcanic Zone (Harrison and White, 2006, Reyners *et al.*, 2006, Stern *et al.*, 2006). Crystallization models of basalts at lower crustal depths may be done to derive residual melt compositions. The sample set has a single basalt composition, which was used for a starting composition in major element Rhyolite MELTS models (Ghiorso and Sack, 1995, Gualda *et al.*, 2012).

Whole rock Wharepu (lower brown unit: 150320-1D-C) and Red Crater (150318-03, post 1.8 ka) compositions were crystallized by decreasing temperature at 10kbar using Rhyolite-MELTS (Ghiorso and Sack, 1995, Gualda *et al.*, 2012) to see variations in residual liquid compositions. Sample 1D-C was modelled for equilibrium and fractional crystallization. From thermobarometry, Wharepu, Te Rato (andesite, not the mingled dacite) and Te Maari have plagioclase crystals that have equilibrated at 8-10 kbar (~30-37km) (Sections 3 and 4). Red Crater lava flow has plagioclase crystals that have equilibrated at 1-2 kbar (~4-7 km) (Section 3), but it has a primitive composition relative to the other samples, which may be possible if the deeply sourced magma stalled at a shallow reservoir and crystallized as a close system. **Table 5-3** lists the resultant solid phases for the models, crystallization of garnet (because it is not supported by trace element variations) was suppressed in all the runs. The results for Red Crater do not recreate the plagioclase An (An_{62-79}) content observed in the sample. It is proposed here that specific for the Red Crater sample, the magma ascended to a shallow reservoir (1-2 kbar) where it crystallized, in agreement with plagioclase thermobarometry results.

Table 5-3. Mineral phases for the different crystallization models.

150320-1D-C		150318-03
Equilibrium	Fractional	Equilibrium
clinopyroxene	clinopyroxene	clinopyroxene
orthopyroxene	oxide	orthopyroxene
spinel	spinel	apatite
feldspar (An_{65-74})	feldspar (An_{52-75})	feldspar (An_{47-57})

The crystallization modelling was undertaken to test whether the more evolved compositions in the sample set can be recreated by the modelled liquid compositions. The tracks of the residual liquids are shown in **Figure 5-10**, plotted with sample whole rock compositions, Wharepu, Te Rato and Red Crater microlitic groundmass compositions and glass groundmass (free from microlites) of a Ngauruhoe75 pyroclast (150319-02-a1). The result for K_2O shows that a basalt source with K_2O values between 318-3 and 1D-C is needed to recreate observed K_2O values. The low K_2O in 1D-C may be due to a slightly weathered state of the sample as the total for major elements (95.35%) is at the low acceptable value and some K_2O may have been lost. However, the sample is considered here because it has passed a criterion for weathering in terms of major elements (**Figure 2-4**) and trace element trends do not indicate low values from weathering (**Figure 5-3**). In terms of other major elements, more evolved compositions in the sample set can be approximated by the crystallization models, but it would take up to 80% crystallization to produce higher SiO_2 compositions.

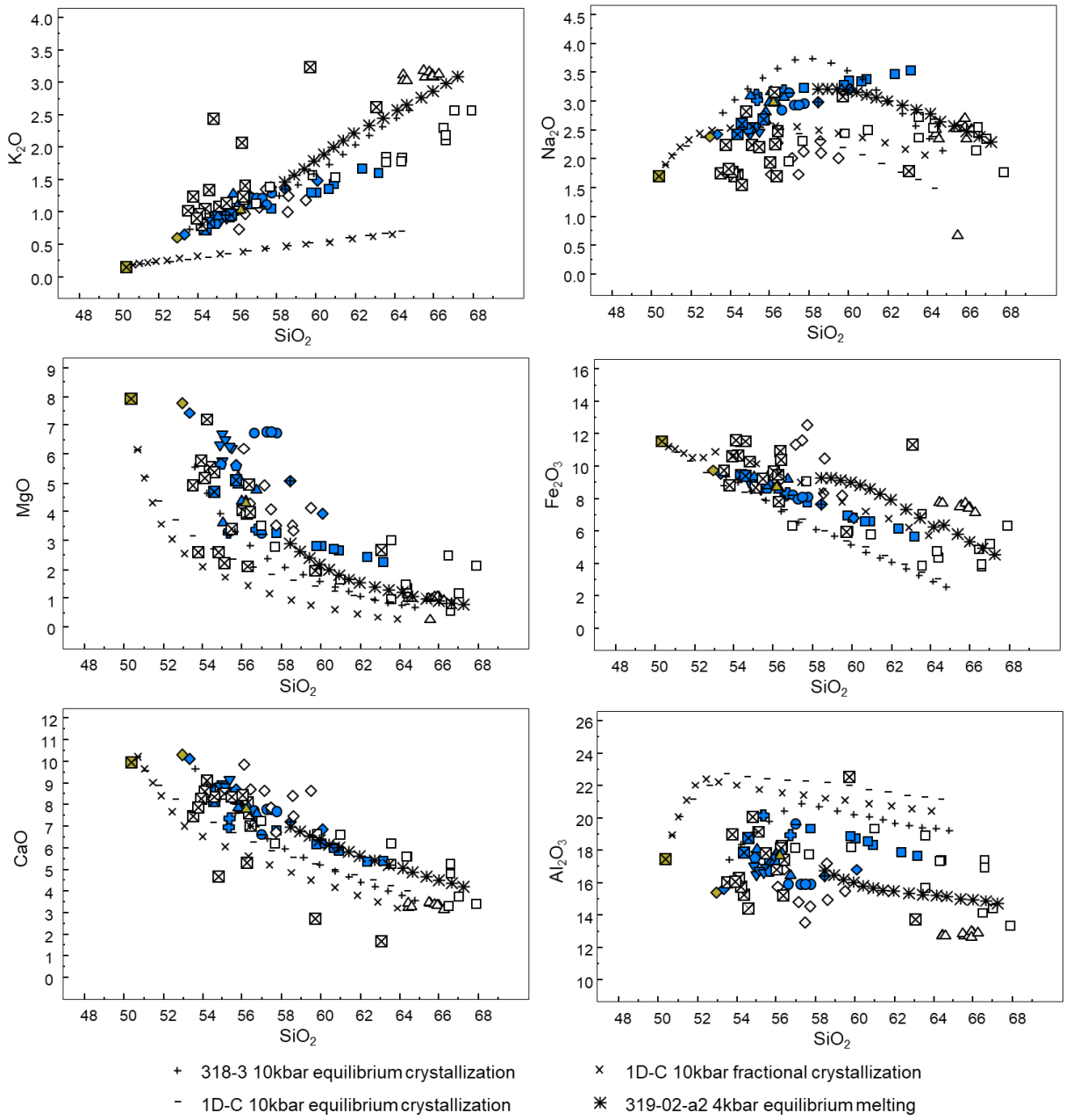

Figure 5-10. Track of liquid for different Rhyolite MELTS model results. Symbols for whole rock compositions (blue) are the same as in Figure 5-2. Starting compositions that were crystallized or melted are filled yellow. Unfilled symbols following whole rock scheme are groundmass. Only the microlite-free groundmass of Ngauruhoe75 is plotted to represent melting of a degassed intrusion after the model in Section 4.5.1.2.

Residual melts from crystallization can move to shallower depths and crystallize. It was shown that the dacite mingled with andesite in the Te Rato sample yielded lower crystallization pressures for the component plagioclase (Section 3). The best fitting model to the highest silica compositions (whole rock and groundmass) is melting of a basaltic andesite composition at 4 kbar (**Figure 5-10**). A residual melt, of basaltic andesite to andesite composition, from crystallization of basalt at 10kbar can move to a shallower depth and crystallize. Partial melting of this andesite will result in a liquid of dacitic composition. This was the scenario for the Ngauruhoe model at 4 kbar in Section 4, results are plotted in **Figure 5-10**. It recreates well the glass groundmass for Ngauruhoe at only 30 to 35% melting. It was shown in other studies that partial melting of ponded more evolved and still hot intrusions can produce dacite to rhyolite compositions (Vogel *et al.*, 2006).

A specific process (melting or crystallization) and depth of magma should be considered for each deposit. Each deposit will have a scenario such as what was done for a bulk composition of Wharepu (Section 3: equilibrium crystallization then polybaric melting), for bulk Ngauruhoe75 at 4 kbar (Section 4: crystallization and melting), and a melt inclusion composition for Te Maari that represent a basaltic magma that rose to 1kbar pressure, stalled and crystallized (Section 4). These specific scenarios can approximate both liquid and crystal compositions. A single process cannot represent all the samples, but it can show that all 10 ka deposits may be related to a single basaltic source, and that the crystallization and melting scenarios does not require input of assimilated country rock (greywacke).

MgO proxy (MgO compositions from the crystallization models for 20 to 100% liquid fraction) for melt fraction was used to plot results from trace element models using the equilibrium and fractional crystallization equations that describe trace element enrichment or depletion in liquid (White, 2013):

Equilibrium crystallization: $C_i^l/C_i^o = 1/(DX+(1-X))$

Fractional crystallization: $C_i^l/C_i^o = (1-X)^{D-1}$

where C_i^l is the concentration of element i in liquid, C_i^o is the original concentration, D is coefficient of distribution and X is fraction crystallized (0 to 1)

Bulk distribution coefficient D for different elements were derived for 150320-01D-C and 150318-03. Distribution coefficients between elements and the different minerals in basalt were taken from White, 2013, and are shown in **Figure 5-11**.

The trace element models show that the sample set compositions can be produced at 10 kbar lithostatic pressure with equilibrium or fractional crystallization of a basaltic source (**Figure 5-11**). Maximum degree of crystallization for the trace element models is 60 to 70%. Basement (Torlesse and Waipapa) compositions were plotted for comparison (Graham, 1985, Price *et al.*, 2010). In the La, Nb and Zr models, to better represent the samples, a basaltic source (such as the Red Crater lava composition) with higher concentrations for these trace elements is required. The model that best represent the data is for Ba. Alternatively, models (crystallization and/or melting) at lower pressures (<10kbar) may better represent the samples as discussed in the major element models. The enrichment in the source may also indicate minor contributions from melting of surrounding basement rock.

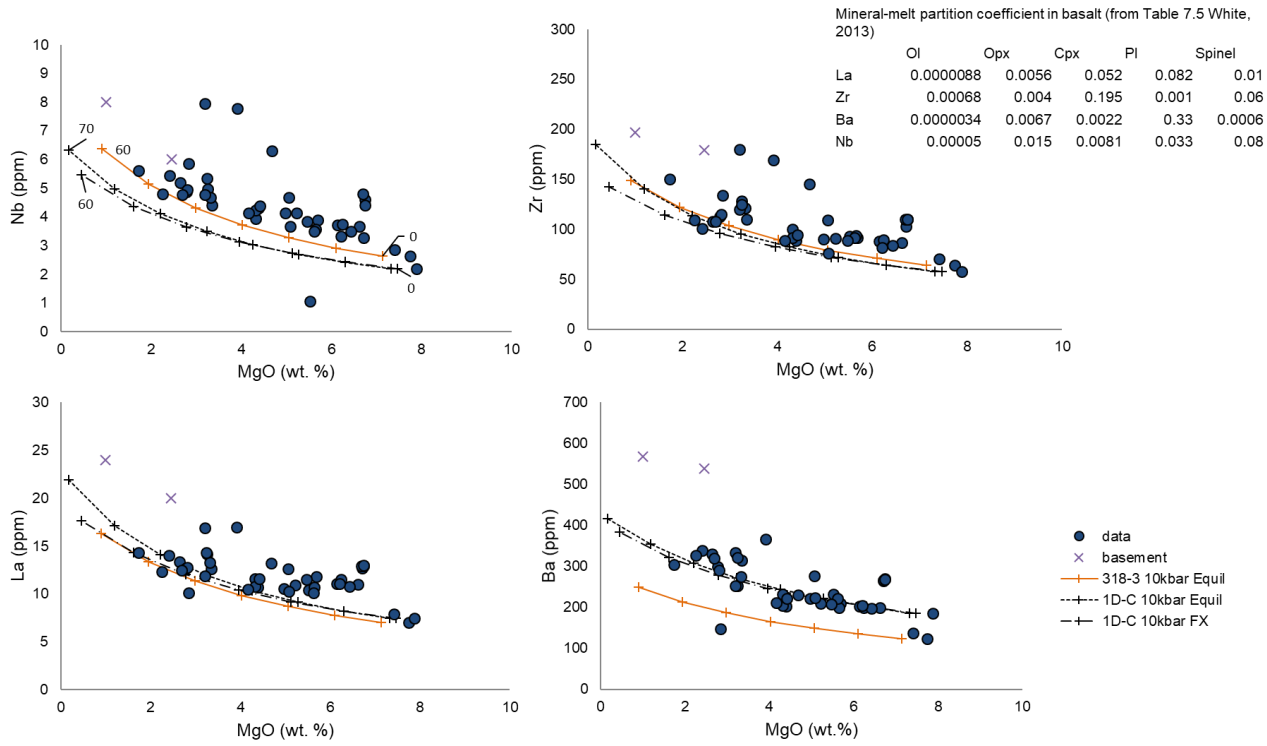

Figure 5-11. Crystallization models describing trace element partitioning in the liquid as composition 01D-C (normative composition: 5% olivine, 7% clinopyroxene, 8% spinel, 17% orthopyroxene, 63% plagioclase) and 318-03 (normative composition: 5% olivine, 25% clinopyroxene, 1% spinel, 20% orthopyroxene, 49% plagioclase) are crystallized. The numbers represent percent crystallized (0 to 60 and 70%) indicated in the Nb plot. MgO is used to proxy for melt fraction based on mass and liquid composition from Rhyolite-MELTS models.

5.7 Differentiation and shallow degassing

Variations in the concentration of the different gas species is a good indicator of magma depth because of their different solubilities in silicate melt and K_2O is a good indicator of magma differentiation. **Figure 5-12** shows variable Cl/K_2O ratio for the melt inclusions with values that are between 0.8 to 0.05 as melt compositions evolve. The observed Cl/K_2O ratios are higher than values obtained from basalts produced by melting of unaltered mantle. It was shown that the Cl/K_2O ratios for uncontaminated MORB and OIB mantle sources are less than 0.1 (Lassiter *et al.*, 2002).

The Cl/S ratio is almost constant in lower K_2O samples (more basaltic samples). The preference of Cl relative to S in higher K_2O samples may reflect the higher solubility of Cl in more alkali-rich melts (Carroll and Webster, 1994). However, the increase in Cl relative to S in higher K_2O samples is likely more influenced by degassing, where S degasses before Cl in magma (Giggenbach, 1996). The samples in the Cl-S-K_2O system therefore show influence of both degassing and differentiation. Low Cl, high K_2O values represent evolved magma at low pressure environments (degassed). It also shows degassing and microlite crystallization in groundmass.

The degassing trend in **Figure 5-12** shows increasing Cl/S ratio as S is degassed followed by decreasing Cl/K_2O ratio as K increases in the melt. Olivine-hosted melt inclusions from Wharepu have almost constant Cl, S and K_2O values. Wharepu pyroxene-hosted melt inclusions show slight variability in Cl/S ratios as S values decrease and melt compositions increase in K_2O (**Figure 5-12A**). Because the high K_2O melt inclusions are hosted in pyroxenes, some S may have leaked through the crystal structure, or S may have formed a separate phase (FeS) as observed in some samples. It must be considered however, that the melt inclusions for this sample are not recrystallized and that the manner of eruption can rapidly quench melt inclusions making post entrapment volatile loss unlikely (Wallace *et al.*, 2003). In contrast, the olivine-hosted melt inclusions for Te Maari (1500AD lava) show an increase in Cl/S ratio due to both decrease in S and increase in Cl. This may reflect crystallization of the olivine host in a magma that is moving to a shallower depth and degassing S. However, as stated earlier, the decrease in S may be due to precipitation of a S bearing phase as most of the inclusions in Te Maari with lower S are partially crystallized (non-homogenized) (**Figure 5-12B**). It must also be noted that the Te Maari olivines are xenocrysts from olivine crystallization in a shallow reservoir. The trend may also imply slow ascent resulting in melt inclusions that were cooled slowly and crystallized. Te Maari pyroxene-hosted melt inclusions are partially

crystallized and plot in the high K_2O composition, within the field of all sample groundmass compositions.

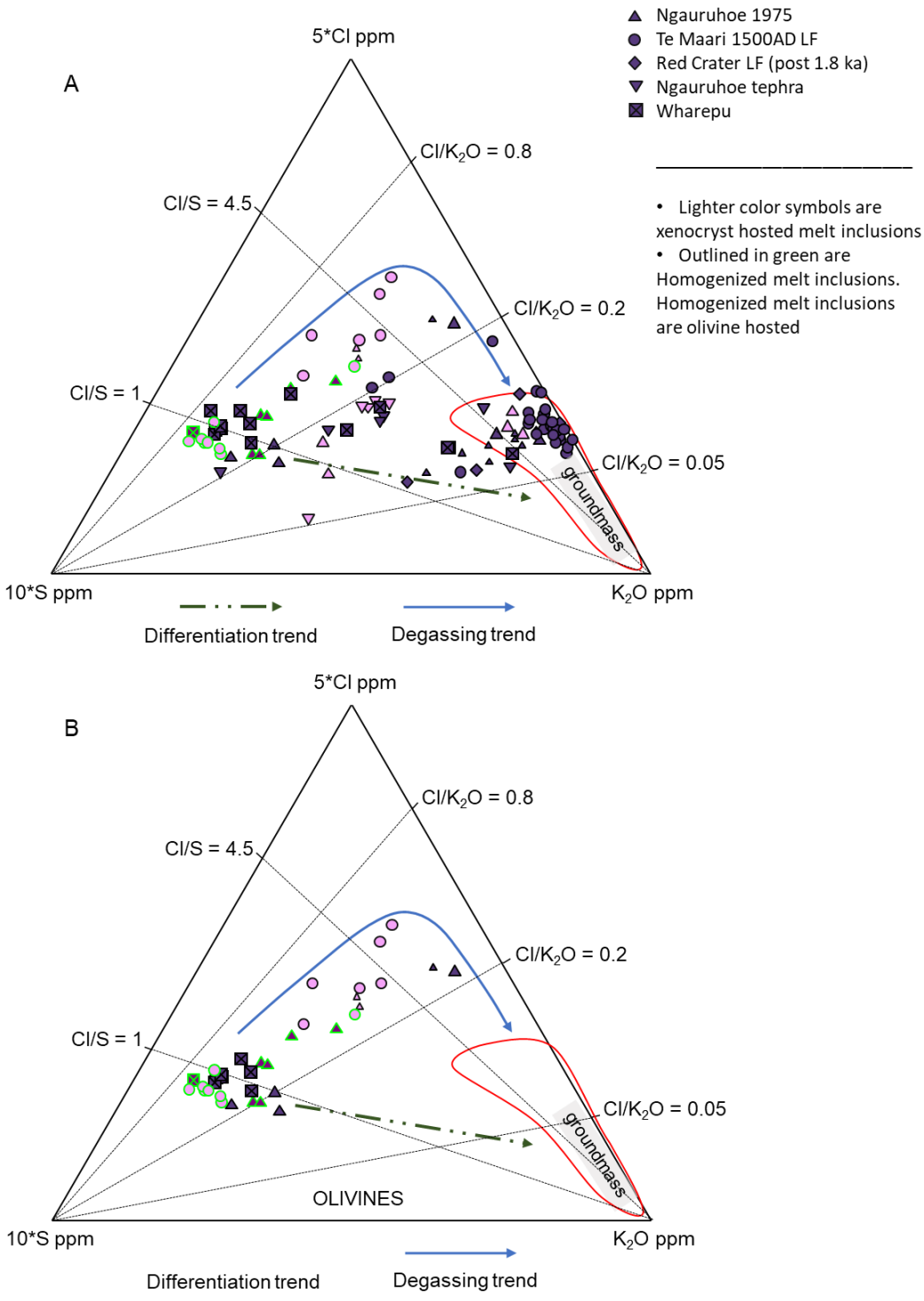

Figure 5-12. Cl-S-K_2O system showing degassing of S then Cl, and differentiation – low to high K_2O. Melt inclusion compositions are plotted. Groundmass (outlined in red) have evolved and degassed compositions (A). Emphasis on olivine-hosted melt inclusions (B).

5.8 Shallow reservoir magmas and evaluation of crustal assimilation

Crystallization models, show that higher SiO_2 (andesitic) compositions may be derived from basalts in the lower crust (10 kbar). However, it does not explain all the chemical variations in the samples. Previous studies emphasized the significance of assimilation of the surrounding crust in the TVZ (Gamble *et al.*, 1990, Graham *et al.*, 1995, Price *et al.*, 2005). In this section, how the compositions for this set of samples were altered by assimilation of basement will be evaluated.

Crustal assimilation can be evaluated from the distribution of $\delta^{18}O$ between samples mingled with crustal xenoliths and selected basaltic and andesitic samples using an AFC (Assimilation Fractional Crystallization) model. The AFC model is at minimum a 3 component problem that considers country rock, magma and minerals where the heat for assimilation is provided by latent heat of crystallization (Taylor and Sheppard, 1986):

$$\delta_m-\delta_o=([\delta_a-\delta_o]+\Delta/R)(1-f^{-R/(R-1)})$$

where: R=mass material assimilated/mass material crystallized; $\Delta=\delta$crystal-δmagma; $\delta_m=\delta^{18}O$ of the magma; δ_o=initial $\delta^{18}O$ of the magma; $\delta_a=\delta^{18}O$ of assimilated material; f=fraction of liquid remaining

Because isotope data is for bulk rock and crystals have not been separated for analysis, the value of 0.2‰ for Δ was based on values that range from 0.1 to 0.3‰ from the study of Taylor and Sheppard, 1986 (White, 2013). Initial $\delta^{18}O$ is 7.6‰ and the $\delta^{18}O$ of assimilated material is 11‰ based on the Torlesse and Waipapa basement (Blattner and Reid, 1982, Graham *et al.*, 1995). MgO wt.% is used to substitute for percentage of crystallization. MgO values were derived from crystallization (fractional crystallization) of bulk composition 150320-01D-C by decreasing temperature from 1300°C to 1000°C at constant pressure using Rhyolite-MELTS

(Ghiorso and Sack, 1995, Gualda *et al.*, 2012). Because the shallowest reservoir for this set of samples is 1 kbar (4 km) and the deepest 10 kbar (37 km), fractional crystallization was done at these pressures. The higher pressure also approximates the level of the base of the crust where basaltic intrusion were interpreted to accumulate (Reyners *et al.*, 2006) In **Figure 5-13**, the sample that plots above R=0.5 is a juvenile clast from Ng75 that is mingled with a crustal xenolith, the same sample that is high in total Pb (**Figure 5-6**). Other juvenile samples from Ng75 plot at $R \leq 0.5$. Basaltic andesite lava flows from Red Crater and Te Maari also have higher $\delta^{18}O$. Considering that there are xenocrystic olivines (**Figure 5-4 and 5-5**) in the Te Maari sample, the actual bulk $\delta^{18}O$ should be even higher if the olivines were removed. Unaltered olivines in basalt magma will mostly have $\delta^{18}O < 7$ (Bindeman, 2008), and iddingsite alteration was not observed in the samples. Based on $\delta^{18}O$, the samples most affected by assimilation of basement are the Te Maari and Red Crater lava flows and the Ngauruhoe (Ng75) sample that was mingled with crustal xenolith. A Te Rato banded pumice, which has andesite and dacite bands plot close to R=0.1. Whole rock δD and $\delta^{18}O$ values are listed in **Table 5-4**. Shallow reservoir basaltic andesite to andesite samples show some degree of assimilation in terms of $\delta^{18}O$, but the highest silica sample in this data set (Te Rato banded pumice) plots at a lower R indicating a lower mass of assimilated material. This may imply that the dacite bands in the Te Rato pumice was not a product of mixing between basaltic melts and high silica melts from partial melting of the surrounding basement (Torlesse and Waipapa).

Table 5-4. Whole rock δD and $\delta^{18}O$ of selected samples from Tongariro. Refer to Figure 2-3 for sample photos.

Samples	wt.% water	δD	$\delta^{18}O$	Comment
150319-02-a1	0.08		8.1	Ngauruhoe 1975 pyroclast
150319-02-a2	0.06		7.6	Ngauruhoe 1975 pyroclast
160727-01-c	0.06		8.0	Te Maari 1500AD lava flow
150320-01E-e	0.27	-115.5	7.8	Wharepu Tephra
150318-03	0.05		7.9	Red Crater lava flow (post-1.8 ka)

150320-01A-h	0.66	-87.2	7.9	Te Rato pumice
150319-01-e	0.11		7.6	Ngauruhoe tephra (pre-1.8 ka)
150319-02-b2	0.06		8.7	Ngauruhoe 1975 pyroclast

Whole rock analysis was done at the Stable Isotope Laboratory, Department of Geological Sciences, University of Cape Town

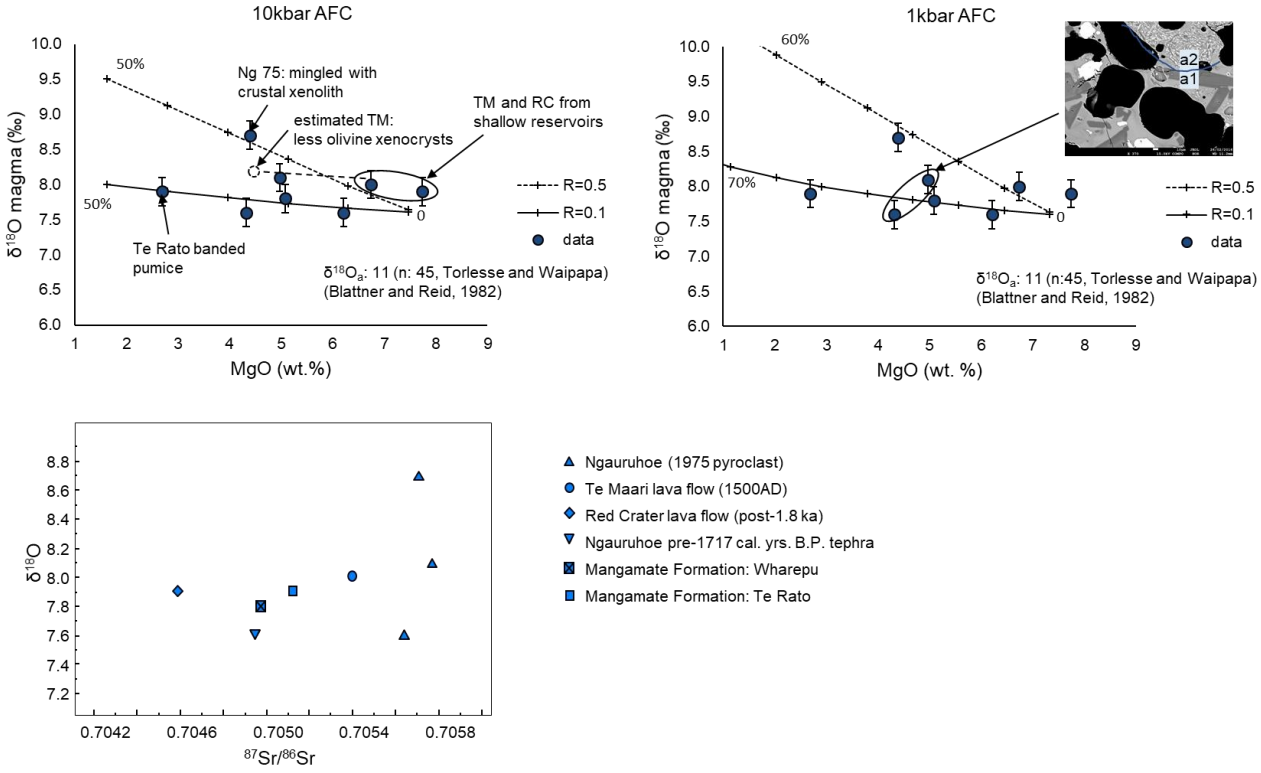

Figure 5-13. $\delta^{18}O$ versus MgO for AFC model at 10 and 1 kbar, MgO approximating percent crystalized, labelled in the liquid track. Note that sample a1 (Ng75) is not a crustal xenolith, SEM image shown in $\delta^{18}O$ versus MgO for 1 kbar. The samples are distinguished by symbol in $\delta^{18}O$ versus $^{87}Sr/^{86}Sr$ isotopes.

5.9 Differentiation model and regional relevance

5.9.1 Comparison with Ruapehu

Tongariro and Ruapehu both belong to the Southern Taupo Volcanic Zone. They form the apex of a spreading zone that opens along a northeast line. Rifting rates are regarded to decrease southwest, and measured rates around Taupo is about 8±2 mm/yr (Darby *et al.*, 2000). Tongariro lies northeast of Ruapehu and southwest of Taupo. Based on the assumption that rifting has more influence on the magmatism of Tongariro than Ruapehu, compositional differences between eruptive deposits for a similar period were evaluated.

Ruapehu magma compositions erupted between 18 ka to present (Hackett, 1985, Gamble *et al.*, 1999, Conway, 2016), based on major and selected trace elements, are similar to Tongariro, but have higher K and Ba concentrations (**Figure 5-14**). For an andesite SiO_2 range, K_2O is higher for Ruapehu. Crustal xenoliths found with the Ngauruhoe 1975 deposits, analysed for this study, appear to be a mixing end member composition in terms of Ba and K_2O for this composition range. Possible end members considering 10 major element compositions were determined using the Polytopic Vector Analysis (PVA) program by Robert Ehrlich (Johnson *et al.*, 2002). Conditions set were the same for Tongariro and Ruapehu models, model default conditions and 5 end members were chosen for both. PVA has a "DENEG" condition, default value of 0.05, which means that the program will continue iteration until convergence and none of the mixing proportions for the end members are more negative than 0.05. Five end members resulted in acceptable Klovan/Miesch Coefficient of Determination (KMCD) values (Johnson *et al.*, 2002). Both model runs gave results that satisfied conditions after 2 iterations. Crustal xenoliths (this study and Price et al., 2010) and basement compositions (Graham, 1985, Price *et al.*, 2010) are plotted with sample compositions and end member results (**Figure 5-15**). Not all end members can be real, but results show that a high K_2O low MgO end member is required

for Ruapehu. Studies done on Ruapehu deposits show assimilation of crustal xenoliths resulting in higher K_2O (Conway, 2016). The low silica end member for both volcanoes are not high Al basalts. Majority of basalts from the TVZ cannot be related to high Al basalts (Graham *et al.*, 1995). The high silica end member for Ruapehu follow closer the crustal xenolith compositions. Magmatic source characterization, also shown in **Figure 5-9B**, identified distinct magma sources for Ruapehu and Tongariro. Although the 2 volcanoes have a similar mantle source based on Zr/Nb ratio (**Figure 5-14**) and isotopes, higher values for Ba/La and K_2O (for the same SiO_2 range) for Ruapehu magmas may imply a larger influence of subduction related fluids in the source or greater degree of crustal assimilation compared to Tongariro.

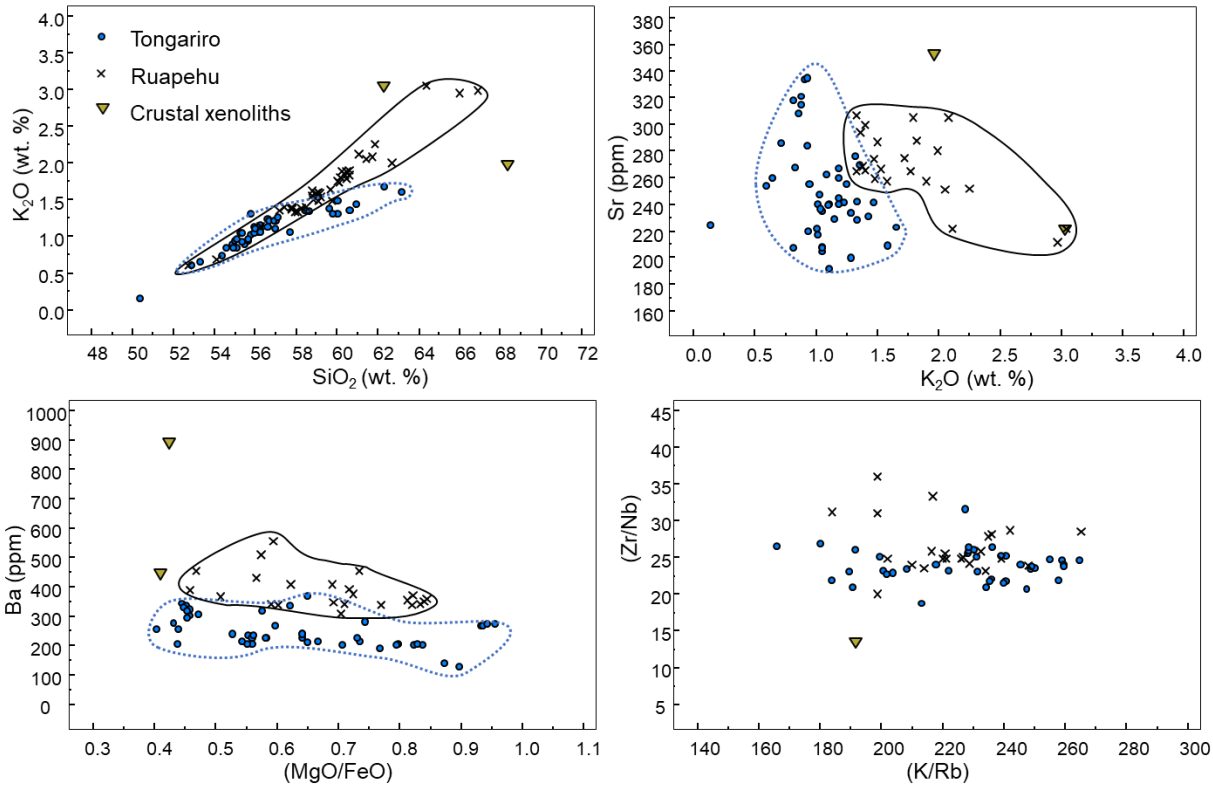

Figure 5-14. Major and trace element differences between Tongariro and Ruapehu (Hackett, 1985; Gamble et al., 1999; Conway, 2016) for deposits from ~16 ka to present. Crustal xenolith compositions are from this study.

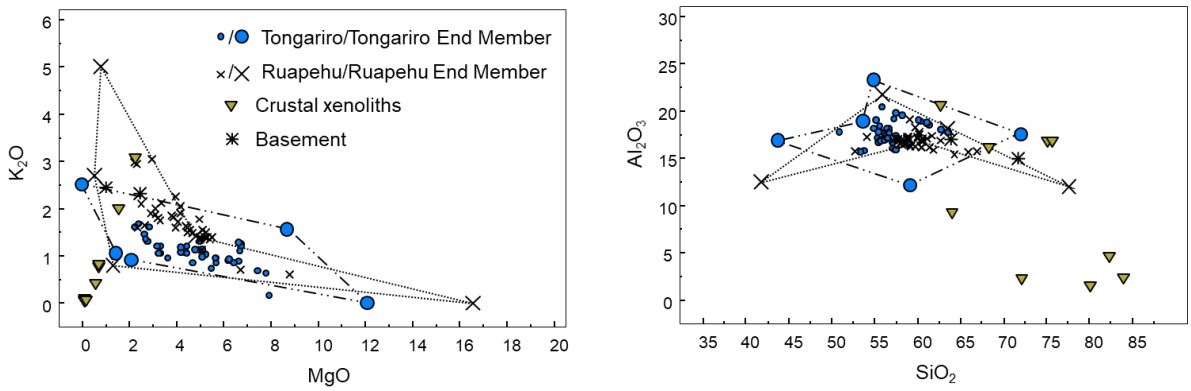

Figure 5-15. Possible mixing end-members to describe compositions of Tongariro and Ruapehu (Hackett, 1985; Gamble et al., 1999; Conway, 2016) based on 10 major element concentrations. Crustal xenolith compositions are from this study and Price et al., 2010, basement compositions are from Graham (1985).

5.9.2 Differentiation model

The model starts at the lower crust where it is given that there is a large accumulation of basalt intrusions (Harrison and White, 2006, Reyners *et al.*, 2006, Stern *et al.*, 2006). This is a large reservoir and assimilation of lower crustal material have minimal effect as shown from sample isotopic compositions such as negligible enrichment in Pb isotope relative to SiO_2 (**Figure 5-6**), in addition to REE pattern, and major element models. Most of the samples do not show a significant country rock contribution based on δO^{18}, and enrichment of incompatible elements in the basalts is likely from the subduction processes whether from the dehydration of subducted crust and sediments or melting of sediments (Tatsumi, 1989, Peacock, 1990, Ryan *et al.*, 1995, Behn *et al.*, 2011). Island arc primary basalts are enriched in δO^{18} (6.1 ± 1.1 ‰) relative to MORB (δO^{18}: 5.7±0.2 ‰) (Harmon and Hoefs, 1995) due to the subduction process. Subducted continental sediment contribution to primary basalt in a region where continental crust is absent can increase $^{87}Sr/^{86}Sr$ from a range of 0.703696 - 0.703834 (Mayon Volcano) (Castillo and Newhall, 2004) to a range of 0.70443 – 0.70472 (Taal Volcano) (Mukasa *et al.*, 1994). The Tongariro samples have $^{87}Sr/^{86}Sr$ values of 0.704589 to 0.705774 and a minimum

δO^{18} of 7.6 ‰, values that likely reflect influence of subducted continental sediment with only minor contribution from assimilation of the overriding continental crust.

Derivative melts from the basalts can be modelled by equilibrium and fractional crystallization. Settling of crystals in the reservoirs is expected and it can be argued that everything should be fractional crystallization, but compositions can be represented by equilibrium melting/crystallization. Convection or turbulence in the chambers probably can result in remixing of the settled crystals. It was shown that injection of new magma into a chamber with crystal mush results in mixing of crystals and injected melt, and that mixing will be more efficient before an eruption or magma ascent (Bergantz *et al.*, 2015). Lastly, in the lower crust scenario, there are variability in the basalt (Wharepu basalt) to basaltic andesite (for the Red Crater sample) magmas based on trace elements and radiogenic isotopes.

The basalt bodies may crystallize or melt from heat of crystallization and the derivative melts rise because of buoyancy (Annen *et al.*, 2006). The rise can be incremental or deeply-sourced existing melts can be tapped by rifting, in the latter case primitive compositions can be erupted or rise to shallow reservoirs. A major rifting event opens pathways for the magma to rise from this deep reservoir to the surface, as was modelled for the Mangamate eruptions (Nakagawa *et al.*, 1998).

The melts can rise and store in different magma chambers or be erupted to the surface (**Figure 5-16**). A rising magma from a deep source can intersect more differentiated melts at shallower or intermediate reservoirs. The more differentiated, andesitic or dacitic melts are extracted melts from crystallization or melting of basalt-basaltic andesite magmas. A rising magma may pass through and mingle with these melt reservoirs producing banded pumice deposits. The dacite mingled in a Te Rato pumice, for example, shows a shallower crystallization depth for the magma (**Figure 3-8**). Depending on the path, a clear path may take basaltic melts from a

deep reservoir to a shallow reservoir. Stalling of melts may probably depend on magma buoyancy and volume. Whether a magma erupts can also depend on the flux of new magma and size of the chamber (Karlstrom *et al.*, 2010). The Red Crater basaltic andesite lava flow sampled in this study most likely originated from a deep source and ascended relatively undifferentiated before being stored in a shallow chamber. The Te Maari lava flow passed through a shallow chamber before eruption, and it incorporated olivine xenocrysts. The possible difference between the two pathways is that rifting is more developed in Red Crater and the magma probably had a clearer path.

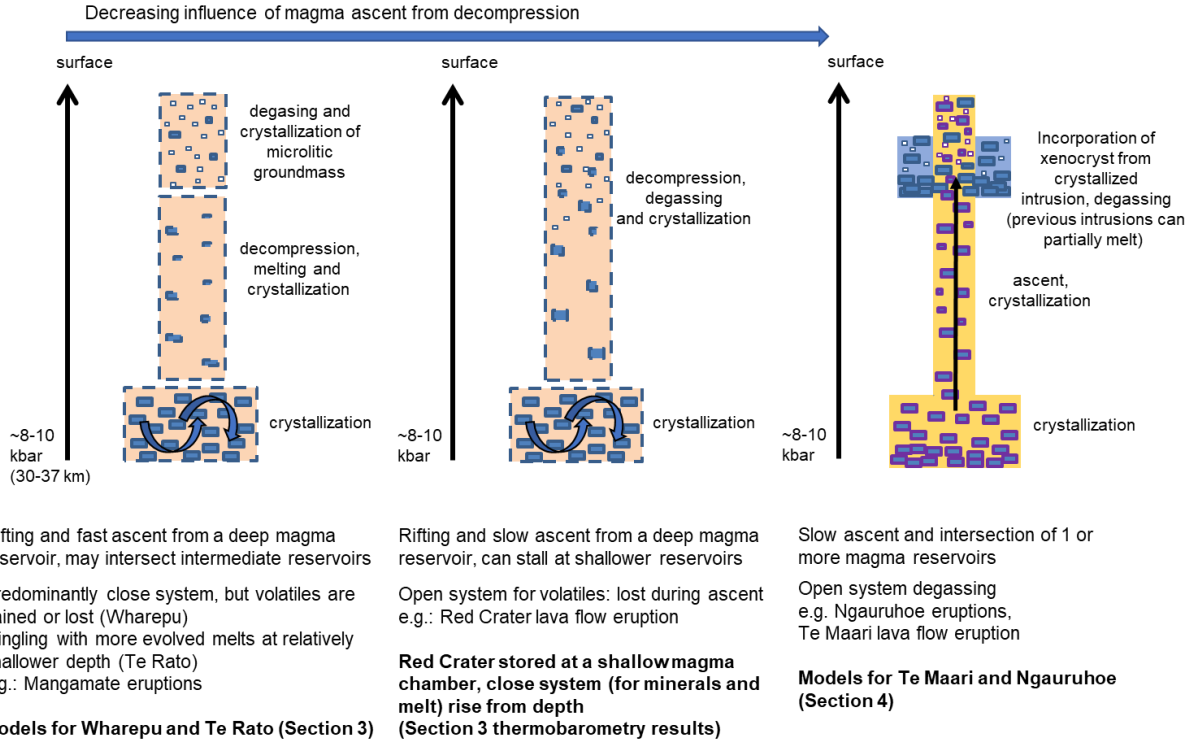

Figure 5-16. Possible effects of rifting, decompression and ascent rates on magmatic processes. Curved arrows represent turbulence in the magma chamber, mixing the settled crystals, before ascent.

Tongariro is on the margin of large silicic caldera systems to the northeast. These caldera systems are regarded as having a large magma reservoir of crystal mush. The model for silicic magmatism in Taupo caldera, northeast of Tongariro, require crystallization of a large crystal mush reservoir (Charlier *et al.*, 2005, Deering *et al.*, 2011). Basaltic magma intrusions underplate the silicic crystal mush because of density difference (Bachmann and Bergantz, 2003).

Many models show basaltic magma ponding below and on the sides of the mush body. Magma transport process is facilitated through dikes and it is a factor in the growth of large igneous bodies (Karlstrom *et al.*, 2010). The Taupo Volcanic zone is a rifted area and rifting is propagating southward (Darby *et al.*, 2000). The relevance of a growing crystal mush scenario in the mid-crust for Tongariro is that some intermediate depth basaltic-andesitic sources for Tongariro may be on the fringes of the large silicic crystal mush (**Figure 5-17**). This model states the significance of local structures to magmatism.

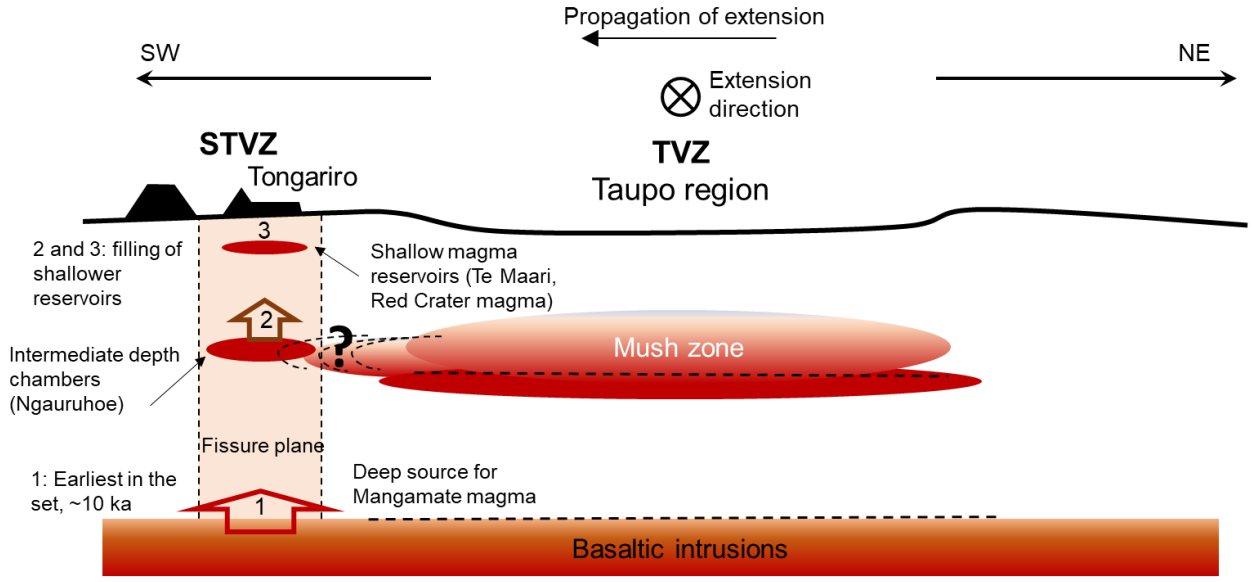

Figure 5-17. A conceptual model for magma storage regions below Tongariro.

5.10 Conclusions

Basaltic to andesitic samples erupted from the last 10 ka from Tongariro Volcano may have a common batch of mantle derived basalt sources in the lower crust. The basalts may vary depending on the degree and frequency of melt extraction causing variations in trace elements. Andesites and dacites are derivative melts from melting and crystallization processes on the basalts. Contributions from the surrounding country rock is minimal and show more significantly on trace and isotope data for samples that are in close contact with crustal xenoliths or in magmas that have incorporated xenocrysts. Whole rock major and trace element variations can be modelled from melting and or crystallization without assimilation. Compositional variations determined for the samples from different eruptive centres may reflect tectonic controls that may variably determine ascent paths, storage conditions, tapping of melts and petrological processes.

6 Conclusions, recommendations and volcanic hazards implications

6.1 Conclusions and summary

The objectives of this thesis as stated in the introduction are 1) to constrain the depths of magma crystallization and storage, 2) determine volatiles content and derive degassing processes during their ascent, and 3) to get an overall picture of magmatic processes that resulted in the Tongariro eruptions. The results show that the shallowest reservoir is at ~4 km depth (1.2 kbar) and the deepest is at ~30-37 km (~8-10 kbar), and intermediate reservoirs are at ~14 km depth. These depths are for the sample set consisting of basalt to dacite. These are consistent with possible magma storage regions for the Taupo Volcanic Zone from literature. A basalt accumulation in the lower crust and base of the crust was interpreted from geophysical data (Harrison and White, 2006, Reyners *et al.*, 2006, Stern *et al.*, 2010). Possible magma accumulation regions were presented by other studies from geophysical and petrological perspectives (Deering *et al.*, 2011, Hill *et al.*, 2015). It was shown, from literature, that andesitic melts can be extracted from dry basalt at lower crustal pressures, and that dacite can be extracted from more hydrous basalts, explaining both the andesitic volcanism in the Southern Taupo Volcanic Zone (STVZ) and the dacite accumulation in the upper crust that formed a silicic mush for the Central Taupo Volcanic Zone (Deering *et al.*, 2011). Results in Sections 3 and 4 have shown that basaltic magma from Tongariro, within the STVZ, also can be stored in the upper crust. This is not uncommon as basalts originating at great depths can also stall in shallow reservoirs within a rift zone, as for Kilauea Volcano (Gerlach, 1986, Edmonds *et al.*, 2013). A summary figure (**Figure 6-1**) is here presented.

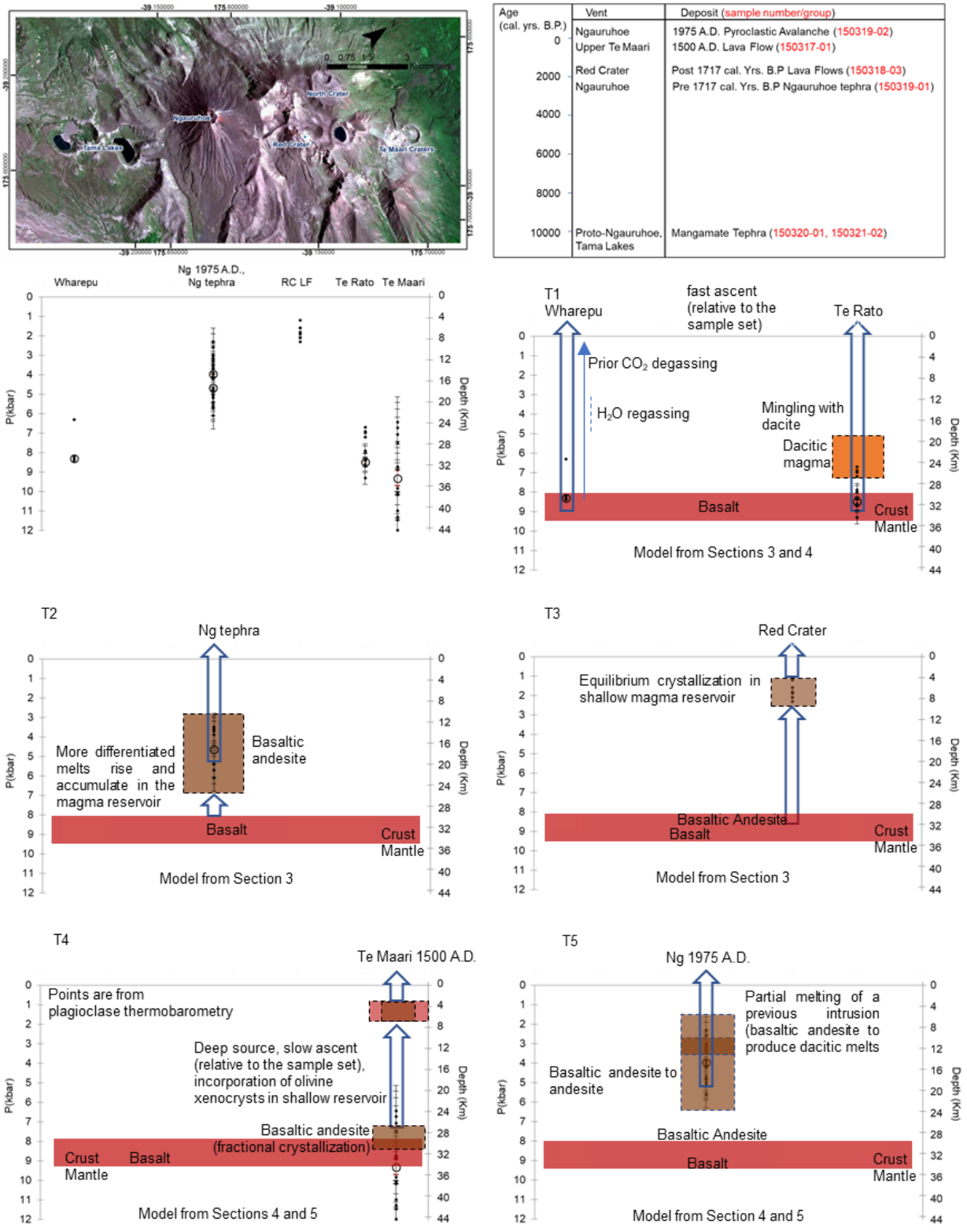

Figure 6-1. Summary illustration for magma depths from different eruption periods and vents. Magma composition and modelled processes from the results section are indicated.

Because magma reservoirs are found at different depths below Tongariro Volcano, the effect of pressure must be considered in magma differentiation and its resultant products including volatiles. Water, for example, will accumulate in a magma differentiating (partially crystallizing) in a deep reservoir (Te Rato) whereas it will degas from a magma crystallizing in a shallow reservoir (Te Maari and Red Crater lava in this study). A magma differentiating from basalt to dacite before mingling with a deeper sourced basaltic melt extracted by a rifting event resulted is a mingled pumice (Te Rato) and a highly explosive eruption. Subsequent basaltic eruptions (Wharepu) were enriched in molecular water and also produced highly explosive eruptions. A sudden decrease in pressure and rapid ascent of magma originating from a deep source, which destabilize minerals and increase melt fraction based on thermodynamic modelling (Rhyolite MELTS) may also have contributed to increasing eruption explosivity.

The average total H_2O for the different deposits is 1.5 wt.% (n: 110, 1σ: 1.3 wt.%). This value is below the average for mafic arc magmas (4 wt %) (Plank *et al.*, 2013), arc basalts (2-4 wt %) and continental arc andesites – dacites (2-5 wt %) (Schmincke, 2004). Wharepu tephra has the highest measured total H_2O at 6.7±1.3 wt.% (average for repeat measurements: 5.3 wt. %, n: 6), higher than modelled H_2O (1.4 ± 1.1 wt.%) from hygrometry for this deposit (**Figure 6-1**). It was shown in Section 4 that water speciation in Wharepu is in disequilibrium, favouring molecular water. It was then inferred that there may have been re-equilibration with external melt to increase H_2O in the melt inclusion prior to freezing. The source of additional water cannot be determined in this study (**Figure 6-2**). It can either be a contribution from more volatile rich melts or assimilated fluid from country rock. The possibility of a hydrothermal water contribution however, cannot be explored from the present data. Future analyses can look at the isotopic composition (particularly δD, $\delta^{18}O$) of the volatiles in melt inclusions. The melt inclusions should be from host crystals that are not xenocrysts.

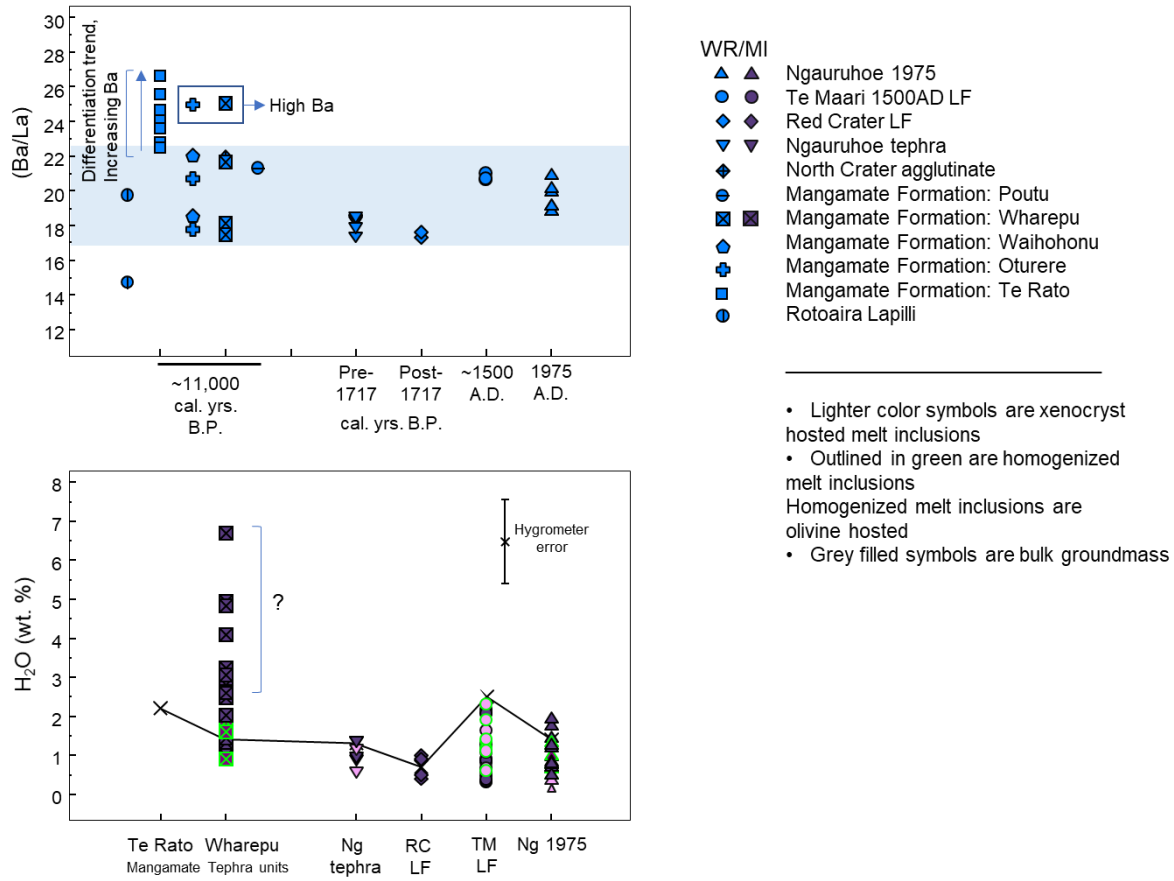

Figure 6-2. Subduction related fluid enrichment should be similar for the ~ 10 ka deposits that are related to a common source as supported by trace element ratios in this figure (Ba/La) and in the text. The large difference in total H_2O content between Wharepu Tephra and the rest of the samples may imply involvement of processes that enriched source values. Connected (X) symbols are H_2O values from plagioclase hygrometry.

Shallower level magma reservoirs for Tongariro mainly degas in an open system vent (Ngauruhoe, Te Maari, Red Crater). Magma differentiation in multiple level reservoirs, when the environment is stable to maintain these reservoirs such that there are no major rifting events, produce discrete partially crystallized magma bodies. Passing of ascending hotter magma through these reservoirs can result in partial melting of the previous magma intrusions and or incorporation of settled crystals (xenocrysts).

All the samples in this study, covering a period of ≥ 10 ka, appear to source from a basalt reservoir in the lower crust. This may be a large reservoir that is being replenished by mantle melts. Composition values and trend analyses in the previous section (Section 5), such as trace element ratios (Ba/La and Zr/Nb) that have narrow ranges for all the samples, indicate a common source. However, the trend in Ba/La ratio displayed by Te Rato mingled pumice (whole rock analysis) shows preferred enrichment in Ba. Enrichment of Ba ($Kd(Ba)^{cpx\text{-}melt}$: 0.0022) relative to La ($Kd(La)^{cpx\text{-}melt}$: 0.052) was probably from fractionation of clinopyroxene at higher pressure, emphasizing the importance of pressure regimes for magma crystallization (**Figure 5-11** in Section 5). The range in Ba/La (**Figure 6-2**) is the result of whole rock analysis of banded pumice and is consistent with the conclusions. It reflects magma mixing/mingling for the different proportions of andesite and dacite in the pumice (see discussion in **Section 3**).

The 10 ka to present eruptive deposits from different depth magma reservoirs can be traced by magmatic process (crystallization and melting) to a single or similar composition basalt to basaltic andesite magmas. The period for the samples is within the differentiation time scale of 30 ky for an arc magma (Asmerom *et al.*, 2005). It is also within the latest stage of cone building in Tongariro, which started at 25 ka (Hobden, 1997). A comparison with older deposits for the 275 - 340 ka (Hobden *et al.*, 1999, Gamble *et al.*, 2003) history of Tongariro will require comparison not only of whole rock compositions, but also of mineral content, melt and volatile compositions to determine trends in source characteristics and differentiation processes. For an initial assessment, however, comparison with older Tongariro samples were done.

The samples were compared to older deposits going back to 210 ka using data from Hobden (1997). The sample compositions from this study coincide with the range of compositions from Hobden (1997) for the period 0 to 20 ka (**Figure 6-3**). Because the compositions are whole rock, the elements - K, Rb, Ba were considered as these are minimally fractionated in olivines, which can be xenocrysts. In addition, Ba being mobile in aqueous fluids is important in

evaluation of subduction zone magmas. It appears that higher Ba values are predominant in the older deposits, although the range for the periods overlap. It may be that contributions from decompression melting to flux melting increase with time or that assimilation was more significant in the past. Interpretation of temporal variations in this scale (up to 210 ka), however, requires a more careful evaluation of processes involved. If there are differences in Ba with time, it is important for future studies to also evaluate H_2O and Cl for the much older magmas.

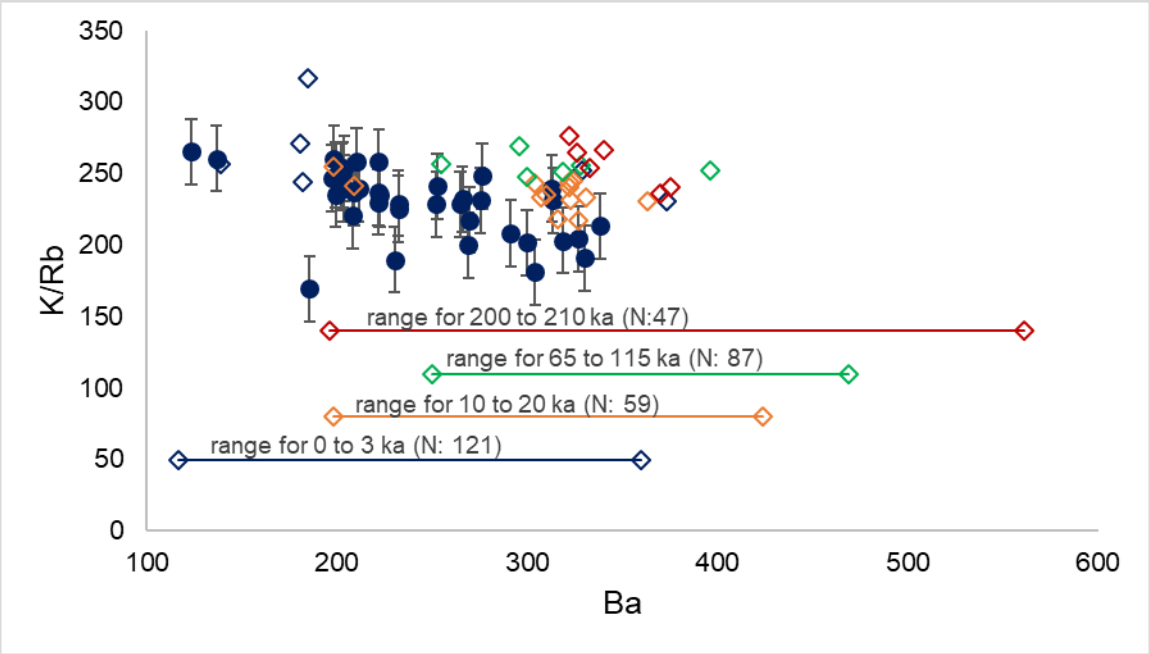

Figure 6-3. Tongariro samples from this study are shown as filled blue circles; error bars represent 1 standard deviation from the average K/Rb ratio (this study). Colored diamonds are data from Hobden (1997). The period from 1 to 3 ka are represented by samples from Ngauruhoe and Red Crater; the 10 to 20 ka period include samples from Te Maari, young SW Oturere, Young Pukekaikiore, North Crater, Blue Lake, Pukeonake, Young NE Oturere; the 65 to 115 ka period have deposits from Tongariro Trig and SW Oturere; finally, Tama Lake (Tama 2) deposits represent the 200 to 210 ka period (Hobden, 1997).

6.2 Volcanic complex, rifted continental arc and volatiles

Ascent dynamics that appear to influence magma differentiation can be explored further by detailed studies of smaller, local structures within the volcano complex. Structures within a

volcano edifice have been shown to influence magma and magmatic gases path ways to surface, such as for Mammoth Mountain (Hill and Prejean, 2005) and Taal Volcano (Zlotnicki *et al.*, 2008). It is more the norm that alignment and pattern in volcanic centres are structurally controlled. This is seen in volcanic fields such as the Macolod Corridor, which includes Taal Volcano Complex (Forster *et al.*, 1990, Oles *et al.*, 1995) and large caldera systems as for Long Valley Caldera and surrounding volcanoes (Hildreth, 2004). Voluminous tephra eruptions (including the Mangamate eruptions) from aligned vents within the Taupo Volcanic Centre at ~10 ka were attributed to a regional rifting event (Nairn *et al.*, 1998, Nakagawa *et al.*, 1998). Although detailed structural analyses of the Tongariro Graben, within which the Tongariro Volcano Complex is situated, shows that extension within the last 20 ka is mainly a tectonic process, there is a small percentage of extension associated to volcanic eruptions (Gomez-Vasconcelos *et al.*, 2017). Detailed analysis of structures (minor faults, fractures where gases are emitted, lineaments) on the volcano complex itself however, may show connections to larger structures and magma pathways at subsurface.

It was shown that the average H_2O content of Tongariro magmas are lower than the average for mafic magmas of subduction zone volcanoes (Plank *et al.*, 2013). The modelled CO_2 values for non-degassed magma from Tongariro is 4000 - 3000 ppm and the highest measured S is 3888 ppm, both are close to the upper values for CO_2 (~3000 ppm) and S (~4000 ppm) for arc basalts and basaltic andesites (Metrich and Wallace, 2008). Cl values are here compared to values for oceanic-crust back-arc basalts (Lau Basin) in the Tonga subduction system - north of Tongariro (Kent *et al.*, 2002), alkali intraplate basalts affected by an ancient subduction (Hudgins *et al.*, 2015), and rifted continental arc basalts (Rowe *et al.*, 2009).

Tongariro is part of a rifted continental arc south of the Havre Trough and Lau Basin back-arc systems. The Cl/K_2O values (0.31-0.58) for the Valu Fa Ridge (VFR) in the Lau Basin are attributed to the addition of a slab fluid component (Kent *et al.*, 2002). For reference, the

Cl/K_2O ratio of N-MORB is 0.032 (Michael, 1988), and less than 0.1 in deeper enriched sources of OIB (Lassiter *et al.*, 2002). Tongariro magmas have Cl/K_2O values (**Figure 6-4**) that are within the range of VFR and lower than some ratios for the Central Lau Spreading Center (CLSC). VFR is closer to the arc front whereas CLSC is regarded to have minimal slab input and a large range in Cl attributed to seawater contamination (Kent *et al.*, 2002). In comparison, alkali intraplate basalts of the western branch of the East African Rift (**Figure 6-4**) plot close to the lower values of Cl/K_2O for Tongariro. These magmas were not contaminated by seawater but had a mantle source that was metasomatized by a ~700 Ma subduction (Hudgins *et al.*, 2015). Cl/K_2O ratios for calc-alkaline basalts from the high Cascades (Rowe *et al.*, 2009) also plot on the lower boundary for the Tongariro ratios. These comparisons were done to emphasize the significance of a subduction component to the generated primary basalts for Tongariro.

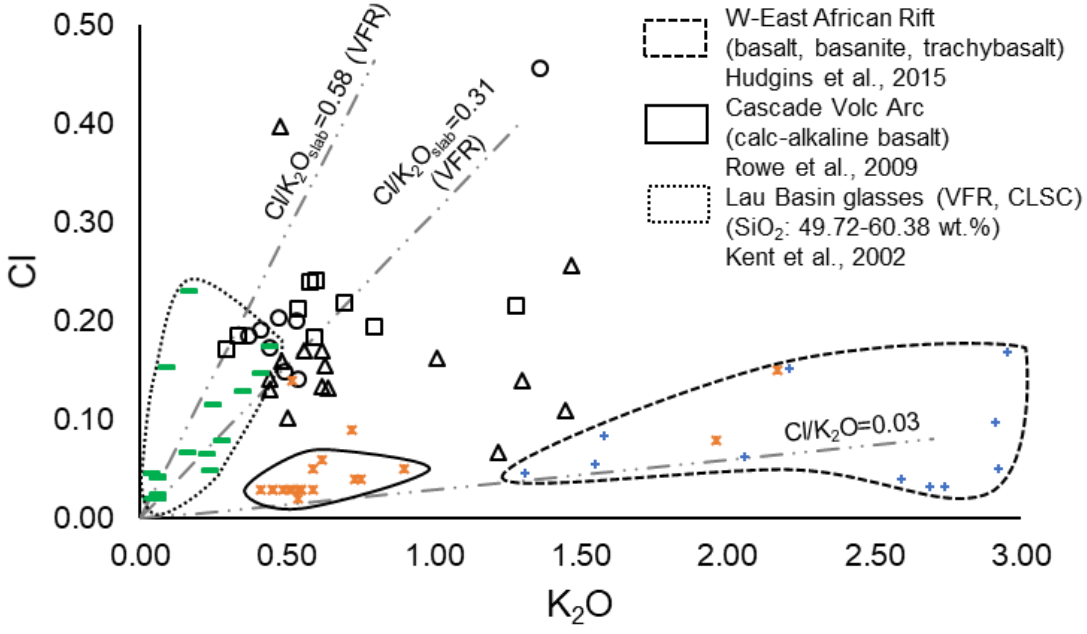

Figure 6-4. Comparison of Cl/K_2O ratios between Tongariro melt inclusions (open symbols: circles (Te Maari 1500AD), triangles (Ng 1975), squares (Wharepu)), Western-East African Rift basalts (cross symbol), Cascade calc-alkaline basalt (asterisk), and Lau Basin glasses (dash). Note that only the olivine-hosted melt inclusions that were homogenized are plotted for Te Maari.

6.3 Relative ascent rates and hazard implications

It is more likely that the ascent rate of magmas that produce tephra (pyroclastic) deposits is higher than lava flow producing eruption. This is based on the nature of the eruption and textures (mineral and glass) in the lava and pyroclast. Textural characteristics indicating fast ascent for the Mangamate Tephra have been observed in a previous study (Nakagawa *et al.*, 1998) and in samples for this study. Textures indicating rapid crystallization (swallow tail, skeletal texture) as well as minimal dissolution in crustal micro-xenoliths were observed.

Compositional disequilibrium may also be an indicator of fast ascent. Ascent rates cannot be quantitatively determined from the data in this study. However, a possible time range may be deduced based on the processes attributed to sample composition in comparison to experimentally determined rates. For example, from an H^+ diffusion experiment, H_2O in a melt inclusion increased from 0.37 wt. % to 3.9 wt. % (equilibrated with external melt) at 1250°C in 22 hours (Gaetani *et al.*, 2012). Accepting that H^+ diffusion in Wharepu occurred at $\leq$ 5 kbar lithostatic pressure, after entrapment of melt inclusion (crystallization pressure modelled in Section 4), resulting in an increase in H_2O from 1.4 to 6.7 wt.% (hygrometry results at 8 kbar versus melt inclusion FTIR data, **Figure 6-2**), the Wharepu melt inclusions equilibrated with external melt H_2O at a depth where H_2O remained dissolved in the melt. The magma then ascended rapidly, such that it did not equilibrate with external liquid that is exsolving/degassing H_2O on its way to the surface. The magma was erupted as tephra and the melt inclusions were quenched rapidly.

Before the 1991 eruption of Pinatubo Volcano, moving magma was tracked to the surface from seismic data (Harlow *et al.*, 1996, White, 1996). Shallow long period earthquakes followed deep long period earthquakes (28-35 km) within 1 hour and a phreatic eruption occurred after

2 hours (White, 1996). White (1996) attributed it to CO_2 gas exsolved at depth, as CO_2 can start to be released at greater than 30 km depth (Stolper *et al.*, 1987). It is not unlikely therefore, that Wharepu melt inclusions were degassed in terms of CO_2 as discussed in Section 4.5.3. The deep long period earthquakes, observed for Pinatubo in 26 May 1991, were interpreted to be basaltic magma at the base of the crust. This magma batch reached the surface on June 7, rising from 35 to 40 km in 11.5 days (White, 1996). The ascent velocity is 0.04 m/s, averaged for the 40 km thick crust. Last phase decompression, starting from a shallower depth can have higher ascent rates, and magma may have stages of ascent as it accelerates to the surface (Lloyd *et al.*, 2014). Using volatile species diffusion from melt embayments in olivines, an averaged ascent velocity starting from about 10 km for Fuego Volcano basaltic magma is about 11-17 m/s (Lloyd *et al.*, 2014). As observed from recent eruptions, magma moving from the base of the crust to the surface is possible, and ascent rate for a Mangamate eruption, with magma originating at the base of the 30-35 km thick crust, may be hours to a few days, likely hours based on disequilibrium features.

Time scales for ascent based on element diffusion in minerals is a post-eruption assessment. Pre-eruption ascent rate estimates will be based on real-time monitored data together with measured and modelled parameters. An assumed depth of magma chamber combined with conduit dimensions, magma fluid properties, and empirical data from fluid dynamic experiments (James *et al.*, 2006) can be used to determine possible magma ascent rates before eruption. Thus, a contribution of this study to hazard assessment is a petrologically determined picture of the magma plumbing system of Tongariro, particularly reservoir depths.

Appendices

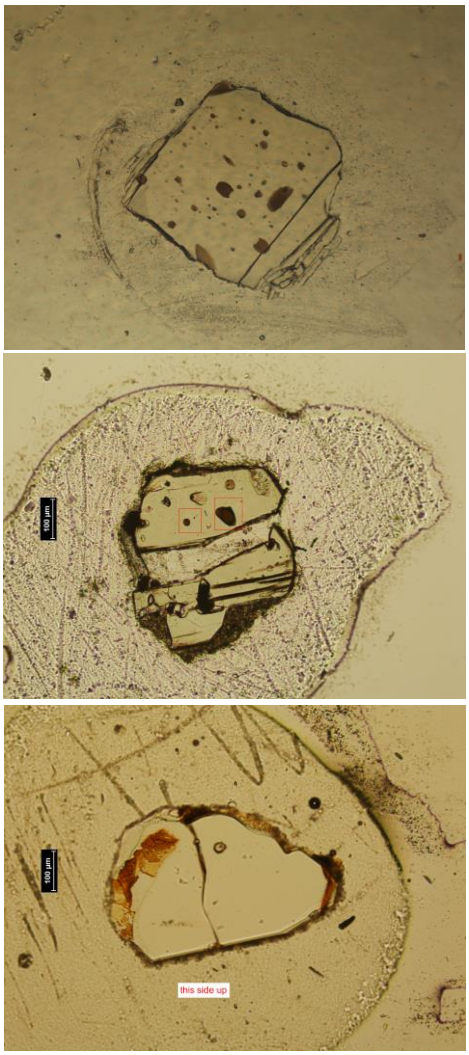

Pyroxene and olivine crystal wafers with exposed melt inclusions mounted on crystal bond (right after polishing). Example of samples that were analysed for melt inclusion water content, but were lost during pre-microprobe preparation

Appendix Table 1. Complete list of samples.

		Waypoints			Sub-Samples	
Sample main	Source/Unit	Station	Longitude (Easting)	Latitude (Southing)		Comment
150116-01*	Te Rato	WP1	175.73384	-39.2206	150116-01-a	lapillus for powder
					150116-01-b	lapillus for powder
					150116-01-c	lapillus for thin section
					150116-01-d	lapillus for thick section
					150116-01-e	lapillus for thin section
					150116-01-f	lapillus for thick section
					150116-01-g	lapillus for mineral separates
					150116-01-h	lapillus for mineral separates
150116-01	Te Rato	WP1	175.73384	-39.2206	150116-01-a	lapillus for powder
					150116-01-b	lapillus for powder
					150116-01-c	lapillus for thin section
					150116-01-d	lapillus for thick section
					150116-01-e	lapillus for thin section
					150116-01-f	lapillus for thick section
					150116-01-g	lapillus for mineral separates
					150116-01-h	lapillus for mineral separates
150317-01	1500AD UTeMaari LF	WP3	175.65614	-39.08202	150317-01	50 g for powder 50 g for mineral separates slab for thin section slab for thick section
150318-01	agglutinate NC	WP7	175.65448	-39.11628	150318-01	50 g for powder 50 g for mineral separates slab for thin section slab for thin section, w/ enclave slab for thick section
150318-02	post 1.8ka RC LF (aa)	WP10	175.6571	-39.13176	150318-02	50 g for powder 50 g for mineral separates slab for thin section slab for thick section
150318-03	post 1.8ka RC LF (aa-blocky)	WP11	175.67152	-39.14234	150318-03	50 g for powder 50 g for mineral separates

						slab for thin section
						slab for thick section
150319-01	pre 1.8ka tephra Ngauruhoe?	WP12	175.61531	-39.14064	150319-01-a	single lapillus for powder
					150319-01-b	single lapillus for powder
					150319-01-c	single lapillus for powder
					150319-01-d	portion of lapillus for powder
					150319-01-d	slab of lapillus for thin section
					150319-01-d	slab of lapillus for thick section
					150319-01-e	portion of large lapillus for powder
					150319-01-e	crust of large lapillus for thin section, with enclave
					150319-01-e	slab of large lapillus for thin section
					150319-01-e	slab of large lapillus for thick section
					150319-01-e	portion of large lapillus for mineral separates
					150319-01-f	lapillus for thin section
					150319-01-g	lapillus for thick section
					150319-01-h	large lapillus for mineral separates
					150319-01-i	single lapillus for powder
					150319-01-i	slab of lapillus for thin section
					150319-01-i	slab of lapillus for thick section
					150319-01-i	portion of lapillus for mineral separates
150319-02	1st phase 1975 PF Ngauruhoe	WP13	175.61752	-39.14286	150319-02-a1	light portion for powder
					150319-02-a1/a2	slab for thin section
					150319-02-a1/a2	slab for thick section
					150319-02-a1	portion for mineral separates
					150319-02-a2	dark portion for powder
					150319-02-a2	portion for mineral separates
					150319-02-b1	light portion for powder
					150319-02-b1/b2	slab for thin section
					150319-02-b1/b2	slab for thick section

			150319-02-b2	dark portion for powder
			150319-02-b2	portion for mineral separates
			150319-02-c	pyroclast for powder
			150319-02-c	pyroclast for thin section
			150319-02-c	pyroclast for thick section
			150319-02-c	pyroclast for mineral separates
			150319-02-d	pyroclast for powder
			150319-02-d	pyroclast for thin section
			150319-02-d	pyroclast for thick section
			150319-02-d	pyroclast for mineral separates
			150319-02-e1	enclave for powder
			150319-02-e2	dark portion for powder
			150319-02-e2	dark portion for mineral separates
			150319-02-e1/e2	slab for thin section
			150319-02-e1/e2	slab for thick section
			150319-02-f	pyroclast for powder
			150319-02-f	portion for mineral separates
150320-01A	Te Rato	WP1	150320-01A-a	lapillus for powder
			150320-01A-a	lapillus for thin section
			150320-01A-b	lapillus for powder
			150320-01A-c	lapillus for thin section
			150320-01A-d	lapillus for thick section
			150320-01A-e	lapillus for thin section
			150320-01A-f	lapillus for thick section
			150320-01A-g	lapillus for mineral separates
			150320-01A-h	lapillus for mineral separates
150320-01B	Oturere	WP1	150320-01B-a	lapillus for powder
			150320-01B-a	lapillus for thin section
			150320-01B-b	lapillus for powder
			150320-01B-b	lapillus for thin section
			150320-01B-c	lapillus for powder
			150320-01B-c	lapillus for thin section
			150320-01B-d	lapillus for thin section
			150320-01B-e	lapillus for thick section
			150320-01B-f	lapillus for thin section
			150320-01B-g	lapillus for thick section
			150320-01B-h	lapillus for thin section

					150320-01B-i	lapillus for thick section
					150320-01B-j	lapillus for mineral separates
					150320-01B-k	lapillus for mineral separates
					150320-01B-l	lapillus for mineral separates
150320-01C	Waihohonu (above fine ash layer, middle coarse layer)	WP1			150320-01C-a	lapillus for powder
					150320-01C-b	lapillus for powder
					150320-01C-c	lapillus for powder
					150320-01C-d	lapillus for thin section
					150320-01C-e	lapillus for thick section
					150320-01C-f	lapillus for thin section
					150320-01C-g	lapillus for thick section
					150320-01C-h	lapillus for thin section
					150320-01C-i	lapillus for thick section
					150320-01C-j	lapillus for mineral separates
					150320-01C-k	lapillus for mineral separates
					150320-01C-l	lapillus for mineral separates
150320-01D	Wharepu (lower brown layer)	WP1	175.73384	-39.2206	150320-01D-a	lapillus for powder
					150320-01D-b	lapillus for powder
					150320-01D-c	lapillus for powder
					150320-01D-d	lapillus for thin section
					150320-01D-e	lapillus for thick section
					150320-01D-f	lapillus for thin section
					150320-01D-g	lapillus for thick section
					150320-01D-h	lapillus for thin section
					150320-01D-i	lapillus for thick section
					150320-01D-j	lapillus for mineral separates
					150320-01D-k	lapillus for mineral separates
					150320-01D-l	lapillus for mineral separates
150320-01E	Wharepu (upper gray layer)	WP1	175.73384	-39.2206	150320-01E-a	lapillus for powder
					150320-01E-b	lapillus for powder
					150320-01E-b	lapillus for thin section
					150320-01E-c	lapillus for powder
					150320-01E-d	lapillus for thin section
					150320-01E-e	lapillus for thick section
					150320-01E-f	lapillus for thin section

					150320-01E-g	lapillus for thick section
					150320-01E-h	lapillus for thin section
					150320-01E-i	lapillus for thick section
					150320-01E-j	lapillus for mineral separates
					150320-01E-k	lapillus for mineral separates
					150320-01E-l	lapillus for mineral separates
150320-01F	Poutu	WP1	175.73384	-39.2206	150320-01F-a	lapillus for powder
					150320-01F-a	lapillus for thin section
					150320-01F-b	lapillus for powder
					150320-01F-b	lapillus for thin section
					150320-01F-c	lapillus for powder
					150320-01F-d	lapillus for thin section
					150320-01F-e	lapillus for thick section
					150320-01F-f	lapillus for thin section
					150320-01F-g	lapillus for thick section
					150320-01F-h	lapillus for thin section
					150320-01F-i	lapillus for thick section
					150320-01F-j	lapillus for mineral separates
					150320-01F-k	lapillus for mineral separates
					150320-01F-l	lapillus for mineral separates
150321-01A	RT3 lower orange brown lapilli layer	WP14	175.7529	-39.07965	150321-01A-a	lapillus for powder
					150321-01A-a	lapillus for thin section
					150321-01A-b	lapillus for powder
					150321-01A-c	lapillus for powder
					150321-01A-d	lapillus for thin section
					150321-01A-e	lapillus for thick section
					150321-01A-f	lapillus for thin section
					150321-01A-g	lapillus for thick section
					150321-01A-h	lapillus for thin section
					150321-01A-i	lapillus for thick section
					150321-01A-j	lapillus for mineral separates
					150321-01A-k	lapillus for mineral separates
					150321-01A-l	lapillus for mineral separates
150321-01B	RT3 gray layer	WP14	175.7529	-39.07965	150321-01B-a	mineral separates
					150321-01B	mineral separates
150321-01C	RT3 orange brown lapilli layer	WP14	175.7529	-39.07965	150321-01C-a	lapillus for powder
					150321-01C-b	lapillus for powder

					150321-01C-c	lapillus for powder
					150321-01C-d	lapillus for thin section
					150321-01C-e	lapillus for thick section
					150321-01C-f	lapillus for thin section
					150321-01C-g	lapillus for thick section
					150321-01C-h	lapillus for thin section
					150321-01C-i	lapillus for thick section
					150321-01C-j	lapillus for mineral separates
					150321-01C-k	lapillus for mineral separates
					150321-01C-l	lapillus for mineral separates
150321-01D	RT3 gray coarse ash and lapilli, including the laminated gray layer	WP14	175.7529	-39.07965	150321-01D-a	mineral separates
					150321-01D	mineral separates, gray laminated ash layer
150321-01E	RT3 orange brown lapilli layer	WP14	175.7529	-39.07965	150321-01E-a	lapillus for powder
					150321-01E-b	lapillus for powder
					150321-01E-c	lapillus for powder
					150321-01E-d	lapillus for thin section
					150321-01E-e	lapillus for thick section
					150321-01E-f	lapillus for thin section
					150321-01E-g	lapillus for thick section
					150321-01E-h	lapillus for thin section
					150321-01E-i	lapillus for thick section
					150321-01E-j	lapillus for mineral separates
					150321-01E-k	lapillus for mineral separates
					150321-01E-l	lapillus for mineral separates
150321-02	Te Rato	WP14	175.7529	-39.07965	150321-02-a	lapillus for powder
					150321-02-b	lapillus for powder
					150321-02-c	lapillus for thin section
					150321-02-d	lapillus for thick section
					150321-02-e	lapillus for thin section
					150321-02-f	lapillus for thick section
					150321-02-g	lapillus for mineral separates
					150321-02-h	lapillus for mineral separates
150421-01	Lower Te Maari, top most lava layer	WP15	175.67345	-39.10789	150421-01	50 g for powder 50 g for mineral separates

						slab for thin section slab for thick section
150421-02	Upper Te Maari, thermal area	WP18	175.67125	-39.10898	150421-02	50 g for powder 50 g for mineral separates slab for thin section slab for thick section
150424-01	Oturere lava flow	WP22	175.67155	-39.14675	150424-01	50 g for powder 50 g for mineral separates slab for thin section slab for thick section
150829-01	Ngauruhoe lava flow, pre-Taupo	WP26	39.14074	175.61548	150829-01	50 g for powder slab for thin section
150829-02	Ngauruhoe lava flow, post-Taupo	WP27	39.14109	175.61789	150829-02	50 g for powder slab for thin section
150829-03	1st phase 1975 PF Ngauruhoe	WP28	39.14295	175.61765	150829-03-a1/a2	slab for thin section
					150829-03-a2	50 g for powder slab for thin section
					150829-03-b	slab for thin section
					150829-03-c1/c2	50 g for powder
					150829-03-c1	
1954	1954 Ngauruhoe lava flow				a	50 g for powder slab for thin section
					b	50 g for powder slab for thin section
					c	50 g for powder slab for thin section
160727-01	1500AD U Te Maari LF	WP29			160727-01-a	50 g for powder slab for thin section
					160727-01-b	50 g for powder slab for thin section
					160727-01-c	50 g for powder slab for thin section slab for thick section

Appendix Table 2. Complete list of whole rock major element analysis. Shaded rows are standards analysed as unknown. Samples in red have high LOI and were not considered in plots

Sample name	SiO_2 (%)	TiO_2 (%)	Al_2O_3 (%)	Fe_2O_3 (%)	MnO (%)	MgO (%)	CaO (%)	Na_2O (%)	K_2O (%)	P_2O_5 (%)	LOI (%)	TOTAL (%)
150116-01-a*	61.35	0.57	17.54	5.97	0.13	2.37	5.25	3.41	1.63	0.14	1.63	99.99
150116-01-a	58.84	0.61	18.28	6.66	0.13	2.72	6.03	3.27	1.27	0.13	2.24	100.17
150116-01-b	58.37	0.62	18.39	6.76	0.13	2.74	5.98	3.20	1.26	0.13	2.65	100.23
150116-01-b*	59.56	0.59	17.90	6.38	0.13	2.58	5.69	3.30	1.40	0.14	2.42	100.09
150317-01	56.86	0.73	15.90	8.10	0.14	6.73	7.68	2.83	1.24	0.14	0.13	100.48
150318-01	58.43	0.72	16.33	7.63	0.14	5.06	7.19	2.97	1.34	0.14	0.52	100.46
150318-02	53.79	0.75	15.69	9.58	0.16	7.47	10.15	2.43	0.66	0.13	-0.17	100.64
150318-03	53.14	0.74	15.44	9.70	0.17	7.77	10.30	2.38	0.60	0.12	-0.22	100.15
150319-01-a	54.15	0.74	16.13	8.73	0.15	6.51	8.72	2.36	0.84	0.12	2.10	100.55
150319-01-b	54.64	0.73	16.55	8.51	0.15	6.04	8.45	2.38	0.86	0.12	1.96	100.39
150319-01-c	53.78	0.74	16.53	8.62	0.15	6.11	8.61	2.39	0.86	0.12	2.05	99.97
150319-01-d	54.13	0.72	16.30	8.59	0.15	6.31	8.57	2.43	0.81	0.12	1.63	99.77
150319-01-e	55.36	0.72	16.48	8.40	0.14	6.21	9.09	2.54	0.91	0.12	0.40	100.37
150319-01-i	54.01	0.76	17.28	8.53	0.14	5.58	8.32	2.49	0.91	0.13	1.96	100.10
150319-02-a1	55.95	0.76	16.78	9.57	0.16	4.98	7.89	2.69	1.29	0.14	0.07	100.27
150319-02-a2	56.72	0.81	17.85	8.82	0.15	4.36	7.92	3.03	1.06	0.14	-0.20	100.65
150319-02-b1	68.07	0.58	15.92	4.30	0.08	1.57	2.39	4.55	1.95	0.13	0.37	99.90
150319-02-b2	56.55	0.80	17.77	8.85	0.15	4.41	7.85	3.00	1.06	0.14	-0.06	100.52
150319-02-c	56.56	0.80	17.79	8.84	0.15	4.35	7.85	3.03	1.05	0.14	-0.15	100.40
150319-02-d	56.11	0.75	17.25	8.81	0.15	5.25	8.20	2.84	1.02	0.14	-0.18	100.33
150319-02-e1	90.79	0.02	3.22	0.90	0.09	0.24	4.58	0.28	0.15	0.07	0.04	100.37
150319-02-e2	56.44	0.78	17.92	8.60	0.15	4.17	7.97	3.02	1.05	0.14	-0.11	100.13
150319-02-f	56.26	0.80	17.92	8.91	0.15	4.43	7.79	3.01	1.03	0.14	-0.28	100.16
150320-01A-a	62.07	0.52	17.32	5.54	0.13	2.21	5.28	3.45	1.56	0.12	1.60	99.80
150320-01A-b	59.00	0.59	17.95	6.41	0.13	2.62	5.82	3.23	1.31	0.14	2.65	99.85
150320-01B-a	53.13	0.93	19.29	8.65	0.13	3.12	6.62	2.98	0.98	0.15	4.37	100.34
150320-01B-b	56.06	0.87	18.66	8.18	0.13	3.31	7.11	3.14	1.17	0.14	1.59	100.36
150320-01B-c	53.83	0.89	19.54	8.37	0.12	3.23	7.13	2.93	1.00	0.15	3.23	100.42
150320-01C-a	55.91	0.75	16.67	8.54	0.14	5.53	8.65	2.76	0.97	0.12	0.23	100.26
150320-01C-b	53.90	0.77	17.20	8.80	0.14	5.54	8.31	2.48	0.81	0.13	2.06	100.13
150320-01C-c	55.43	0.74	16.61	8.56	0.14	5.59	8.63	2.71	0.93	0.12	0.60	100.06
150320-01D-c	48.07	0.72	16.63	10.99	0.14	7.51	9.47	1.61	0.14	0.07	4.31	99.66
150320-01E-a	55.30	0.76	17.26	8.81	0.15	5.04	8.21	2.65	0.94	0.11	0.96	100.20
150320-01E-b	53.49	0.77	17.53	9.26	0.15	5.37	8.51	2.37	0.70	0.11	1.97	100.24
150320-01E-c	53.63	0.81	18.34	9.16	0.14	4.59	7.99	2.54	0.81	0.12	2.04	100.18

150320-01F-a	46.60	0.83	19.58	8.55	0.11	3.33	6.01	2.32	0.63	0.14	11.87	99.98
150320-01F-b	54.96	0.79	18.86	7.87	0.13	3.09	6.37	3.02	1.15	0.14	3.59	99.97
150320-01F-c	39.05	0.92	21.48	9.59	0.10	3.15	4.91	1.59	0.28	0.15	18.37	99.60
150321-01A-a	55.98	0.77	17.91	6.81	0.12	3.01	4.97	2.88	1.29	0.17	6.46	100.36
150321-01A-b	48.45	0.87	19.80	7.71	0.12	3.52	5.51	2.22	0.69	0.18	10.95	100.02
150321-01A-c	51.83	0.83	18.75	7.59	0.12	3.70	5.81	2.52	0.93	0.16	8.03	100.26
150321-01C-a	47.78	0.83	19.52	8.44	0.11	4.71	5.51	1.92	0.61	0.16	10.56	100.14
150321-01C-b	49.25	0.82	19.44	8.26	0.11	4.45	5.87	2.06	0.66	0.16	9.15	100.23
150321-01C-c	48.82	0.81	19.15	8.16	0.11	4.32	6.02	2.04	0.68	0.16	9.81	100.09
150321-01E-a	57.91	0.76	17.67	6.41	0.12	2.71	4.95	3.10	1.49	0.14	4.75	100.01
150321-02-a	56.65	0.68	18.93	7.55	0.14	3.18	6.63	3.14	1.02	0.13	1.94	99.99
150321-02-b	57.33	0.49	19.66	5.29	0.12	1.62	4.73	3.33	1.24	0.15	6.12	100.11
150421-01	59.77	0.74	17.18	7.14	0.13	3.66	6.74	3.27	1.36	0.14	0.17	100.29
150421-02	58.77	0.77	16.93	7.53	0.13	4.19	7.18	3.17	1.33	0.14	0.17	100.31
150424-01	60.29	0.72	16.84	6.78	0.12	3.92	6.83	3.21	1.48	0.13	-0.03	100.29
20160727-1a	57.32	0.70	15.82	7.91	0.14	6.74	7.74	2.92	1.20	0.13	0.16	100.78
20160727-1b	57.81	0.71	15.83	8.03	0.14	6.70	7.63	2.94	1.27	0.14	0.02	101.20
20160727-1c	57.55	0.71	15.85	8.02	0.14	6.74	7.71	2.92	1.10	0.14	0.09	100.96
BRC-2	54.13	2.22	13.85	13.67	0.20	3.58	7.10	3.15	1.70	0.35	0.09	100.04
AGV-2	59.12	1.02	17.29	6.68	0.10	1.73	5.10	4.21	2.67	0.47	1.46	99.86

Whole rock analysis done at the wavelength dispersive (WD) X-ray fluorescence spectrometer (XRF) PANalytical AXIOS^{max} laboratory at the Department of Earth Sciences, National Taiwan Normal University (NTNU)

150318-03	53.05	0.742	15.13	9.82	0.16	7.797	10.33	2.4	0.63	0.121	-0.18	100.22
150829-01	55.08	0.872	18.11	9.37	0.154	3.649	8.4	3.11	0.94	0.138	0	100.05
150829-02	56.75	0.838	16.48	9.23	0.152	4.788	7.63	3.08	1.11	0.145	-0.32	100.11
150829-03-a2	56.1	0.795	17.27	8.85	0.143	4.17	7.84	3.17	1.15	0.141	0.03	99.92
150829-03-c1	61.52	0.765	20.11	5.82	0.067	2.205	1.5	3.62	2.99	0.189	1.09	100.17
1954-a	56.04	0.736	16.93	8.84	0.145	5.062	8.19	2.87	1.11	0.131	0	100.26
1954-b	56.13	0.747	16.9	8.88	0.145	5.078	8.16	2.86	1.1	0.135	-0.18	100.16
1954-c	56.64	0.786	17.01	8.27	0.134	4.404	7.7	2.98	1.18	0.143	0.41	99.86
SY-2	59.8	0.131	11.92	6.18	0.303	2.55	7.85	4.24	4.46	0.436	1.054	99.24
Ou-1	58.01	0.428	14.92	8.84	0.123	4.523	6.39	2.46	0.21	0.046	3.28	99.32

Whole rock analysis done at the X-Ray Centre using PANalytical Axios 1kW X-ray fluorescence spectrometer at the University of Auckland

Standards	SiO2	TiO2	Al2O3	Fe2O3	MnO	MgO	CaO	Na2O	K2O	P2O5
BIR-1										
S.D.	0.18	0.004	0.04	0.02	0.001	0.02	0.03	0.03	0.001	0.001
R.V.	47.96	0.96	15.50	11.32	0.175	9.70	13.30	1.82	0.03	0.021
±	0.19	0.01	0.15		0.003	0.08	0.12	0.05	0.00	0.001
Relative Uncertaintity	0.37	0.44	0.26	0.17	0.47	0.21	0.20	1.63	2.84	6.77

* Fe2O3t for BIR-1 = 2.06+(1.111*8.34)

SDC-1										
S.D.	0.17	0.00	0.03	0.01		0.03	0.00	0.04	0.01	0.00
R.V.	65.80	1.01	15.80	6.32		1.69	1.40	2.05	3.28	0.16
±	0.43	0.04	0.34	0.23		0.10	0.07	0.09	0.10	0.03
Relative Uncertaintity	0.26	0.49	0.21	0.20		1.65	0.33	1.85	0.27	1.30
AGV-2										
R.V.	59.30	1.05	16.91	6.69		1.79	5.20	4.19	2.88	0.48
±	0.70	0.22	0.21	0.13		0.03	0.13	0.13	0.11	0.02
SY2-1										
R.V.	60.53	0.14	12.14	6.38	0.32	2.71	8.02	4.34	4.48	0.43
OU-1										
R.V.	58.25	0.44	15.14	8.99	0.13	4.73	6.49	2.46	0.22	0.05

Appendix Table 3. Complete list of whole rock trace element analysis.

	150116-01-a*	150116-01-b*	150116-01-a	150116-01-b	150317-01	150318-02	150318-03	150319-01-a	150319-01-b	150319-01-c
Sc	15.6	17.1	18.0	18.3	27.2	38.7	34.6	37.5	33.8	35.5
Ti	3197	3395	3483	3544	4126	4257	4106	4261	4188	4238
V	131	145	153	152	190	240	236	240	227	232
Cr	14.4	13.5	12.8	13.2	189	222	246	215	171	195
Co	12.4	14.5	14.5	14.9	49.0	47.6	53.8	30.6	29.2	29.0
Ni	3.77	3.49	3.01	3.22	101	54.1	58.1	36.8	32.0	32.8
Rb	64.6	62.2	53.3	51.3	44.8	20.8	18.8	28.5	29.3	28.1
Sr	222	230	233	233	240	259	253	307	320	314
Y	17.7	18.2	18.1	18.6	19.9	18.3	16.7	17.5	17.5	17.7
Zr	101	108	113	115	103	70.0	64.1	86.3	87.7	89.2
Nb	5.44	5.19	4.88	4.94	3.28	2.86	2.63	3.68	3.71	3.74
Cs	4.07	3.88	3.21	2.99	2.30	0.88	0.78	1.36	1.41	1.40
Ba	338	330	300	291	265	137	124	200	203	199
La	14.0	13.4	12.7	12.8	12.7	7.94	7.05	11.0	11.1	11.5
Ce	29.0	27.8	25.8	26.1	27.3	17.6	15.9	23.6	24.7	25.1
Pr	3.57	3.45	3.27	3.35	3.55	2.39	2.17	3.03	3.12	3.22
Nd	14.0	13.8	13.2	13.5	15.0	10.6	9.76	12.7	13.1	13.6
Sm	3.02	3.03	2.92	3.00	3.51	2.71	2.53	2.99	3.06	3.17
Eu	0.824	0.826	0.843	0.862	0.936	0.829	0.777	0.859	0.874	0.903
Gd	3.00	3.05	2.96	3.06	3.54	3.01	2.78	3.09	3.13	3.20
Tb	0.495	0.511	0.498	0.517	0.577	0.516	0.478	0.517	0.525	0.537
Dy	2.96	3.06	3.03	3.14	3.50	3.19	2.99	3.16	3.18	3.28
Ho	0.641	0.663	0.667	0.685	0.749	0.702	0.655	0.681	0.681	0.704
Er	1.86	1.96	1.96	2.03	2.14	2.00	1.88	1.97	1.97	2.03
Tm	0.282	0.303	0.300	0.311	0.321	0.302	0.284	0.291	0.293	0.303
Yb	1.88	1.98	2.01	2.06	2.08	1.96	1.81	1.91	1.92	1.98
Lu	0.293	0.311	0.315	0.324	0.317	0.295	0.279	0.288	0.292	0.301
Hf	2.77	2.98	3.06	3.14	2.83	2.01	1.86	2.50	2.49	2.55
Pb	14.6	13.3	12.7	12.9	8.74	4.89	4.33	8.49	8.49	8.55
Th	6.42	6.17	5.82	5.93	4.55	2.24	1.83	3.88	3.98	4.02
U	1.61	1.60	1.53	1.56	1.11	0.550	0.484	0.896	0.924	0.934

Whole rock analysis done by Inductively Coupled Plasma Mass Spectrometer (ICPMS) on dissolved samples at National Taiwan University (NTU). Values are in ppm. Text in red are possible erroneous values based on standards analysed as unknown (values at the end of the table).

Appendix Table 3 continued

	150319-01-d	150319-01-e	150319-01-i	150319-02-a1	150319-02-b1	150319-02-b2	150319-02-c	150319-02-d	150319-02-e1	150319-02-e2
Sc	33.6	32.9	32.0	28.2	10.6	25.8	26.8	28.3	0.56	27.3
Ti	4027	3980	4336	4054	3159	4176	4257	4032	51.70	4083
V	221	219	229	191	79	198	202	199	4.24	194
Cr	170	171	136	59.4	25.0	46.4	45.6	80.9	0.08	46.0
Co	29.5	45.5	27.1	26.0	9.6	94.9	36.4	39.3	1.5	22.2
Ni	32.6	33.7	28.1	17.7	9.08	19.5	14.9	26.0	2.30	14.7
Rb	27.7	29.6	29.7	41.5	84.8	35.2	36.2	35.5	5.74	36.3
Sr	317	333	334	199	351	204	207	221	75.8	206
Y	17.1	17.3	17.6	21.7	17.0	20.1	20.6	19.4	1.03	20.7
Zr	83.7	81.7	91.3	90.3	85.6	88.6	91.6	90.6	2.57	88.9
Nb	3.51	3.33	3.88	4.14	6.50	4.32	4.24	4.14	0.19	4.14
Cs	1.37	1.38	1.43	1.72	4.94	1.79	1.79	1.66	0.24	1.78
Ba	197	204	210	222	438	202	204	209	26	212
La	10.8	11.1	11.8	10.6	21.5	10.7	10.8	10.9	0.49	10.5
Ce	23.4	23.6	25.4	23.3	44.4	23.3	23.7	23.7	1.2	22.8
Pr	2.99	3.05	3.25	3.07	5.33	3.03	3.09	3.10	0.15	2.96
Nd	12.6	12.7	13.5	13.3	20.6	12.9	13.1	13.2	0.53	12.6
Sm	2.94	2.94	3.15	3.29	4.11	3.15	3.21	3.17	0.12	3.08
Eu	0.851	0.857	0.902	0.940	0.994	0.882	0.905	0.897	0.071	0.870
Gd	3.02	3.08	3.20	3.55	3.67	3.34	3.42	3.31	0.10	3.30
Tb	0.508	0.512	0.530	0.610	0.561	0.568	0.589	0.558	0.023	0.547
Dy	3.05	3.10	3.21	3.78	3.15	3.52	3.61	3.43	0.16	3.46
Ho	0.662	0.670	0.693	0.832	0.645	0.770	0.793	0.751	0.041	0.762
Er	1.91	1.93	1.99	2.42	1.80	2.22	2.29	2.16	0.15	2.20
Tm	0.285	0.286	0.303	0.369	0.267	0.340	0.347	0.328	0.024	0.332
Yb	1.85	1.86	1.94	2.38	1.69	2.19	2.25	2.12	0.27	2.17
Lu	0.282	0.283	0.298	0.368	0.249	0.335	0.343	0.326	0.063	0.333
Hf	2.40	2.39	2.62	2.57	2.45	2.53	2.59	2.55	0.08	2.43
Pb	7.96	7.98	9.06	11.1	44.3	19.6	9.47	9.00	2.20	9.03
Th	3.79	3.73	4.15	3.60	8.14	3.67	3.76	3.72	0.24	3.74
U	0.864	0.870	0.955	0.837	1.80	0.850	0.869	0.856	0.127	0.821

Whole rock analysis done by Inductively Coupled Plasma Mass Spectrometer (ICPMS) on dissolved samples at National Taiwan University (NTU). Values are in ppm. Text in red are possible erroneous values based on standards analysed as unknown (values at the end of the table).

Appendix Table 3 continued

	150319-02-f	150320-01A-a	150320-01A-b	150320-01B-a	150320-01B-b	150320-01B-c	150320-01C-a	150320-01C-b	150320-01C-c	150320-01D-a
Sc	27.2	13.0	16.8	23.9	22.6	23.4	31.4	30.8	30.1	35.3
Ti	4442	2694	3254	5180	4607	4950	4328	4265	4169	3915
V	209	112	141	206	199	205	229	215	223	178
Cr	48.4	7.65	12.8	3.25	5.29	4.46	74.5	71.6	74.2	52.2
Co	40.7	10.7	14.1	22.3	18.7	19.1	107.2	28.1	28.9	28.6
Ni	17.9	1.74	3.17	3.62	4.41	4.14	20.1	20.5	21.5	12.5
Rb	35.9	64.7	55.0	37.0	42.7	37.1	35.8	29.1	33.7	17.9
Sr	216	208	227	239	239	247	290	267	283	265
Y	21.1	15.8	17.7	22.8	21.2	21.9	18.1	18.2	17.4	15.7
Zr	94.7	109	108	128	110	121	92.9	93.7	91.7	71.8
Nb	4.39	4.80	4.78	4.97	4.42	4.68	1.07	3.57	3.49	2.74
Cs	1.80	4.07	3.71	2.09	2.43	2.08	1.89	1.56	1.81	2.30
Ba	222	327	319	252	314	275	232	199	222	203
La	11.6	12.3	12.5	14.2	12.6	13.3	10.4	10.7	10.1	7.78
Ce	25.2	25.2	27.0	30.4	25.6	26.1	21.8	22.1	21.2	13.5
Pr	3.24	3.08	3.26	3.81	3.43	3.63	2.84	2.94	2.78	2.10
Nd	13.7	12.1	13.1	15.7	14.2	15.0	11.9	12.3	11.7	9.01
Sm	3.29	2.60	2.89	3.62	3.30	3.47	2.82	2.90	2.75	2.22
Eu	0.916	0.710	0.754	0.979	0.938	0.977	0.825	0.813	0.816	0.686
Gd	3.47	2.62	2.92	3.79	3.48	3.67	3.00	3.05	2.94	2.45
Tb	0.572	0.420	0.477	0.620	0.574	0.602	0.498	0.505	0.486	0.417
Dy	3.60	2.58	2.93	3.86	3.58	3.77	3.11	3.14	3.04	2.65
Ho	0.787	0.562	0.645	0.844	0.780	0.821	0.681	0.682	0.666	0.591
Er	2.28	1.68	1.89	2.44	2.25	2.36	1.96	1.99	1.91	1.70
Tm	0.338	0.257	0.292	0.364	0.342	0.354	0.296	0.294	0.288	0.254
Yb	2.23	1.75	1.95	2.34	2.22	2.28	1.90	1.92	1.86	1.63
Lu	0.345	0.278	0.309	0.356	0.342	0.350	0.293	0.292	0.287	0.249
Hf	2.61	2.91	2.94	3.40	2.99	3.24	2.56	2.58	2.54	2.06
Pb	9.35	13.5	12.9	12.1	10.8	11.5	8.21	8.17	7.92	5.83
Th	4.00	5.91	5.87	5.52	5.09	5.25	4.06	4.08	3.95	2.93
U	0.898	1.64	1.56	1.36	1.19	1.28	1.05	1.04	1.03	0.62

Whole rock analysis done by Inductively Coupled Plasma Mass Spectrometer (ICPMS) on dissolved samples at National Taiwan University (NTU). Values are in ppm. Text in red are possible erroneous values based on standards analysed as unknown (values at the end of the table).

Appendix Table 3 continued

	150320-01D-c	150320-01E-a	150320-01E-b	150320-01E-c	150320-01F-a	150320-01F-b	150320-01F-c	150321-01A-a	150321-01A-b	150321-01A-c
Sc	45.1	29.4	35.6	21.6	23.9	20.6	28.7	20.0	24.7	30.7
Ti	3847	4031	4620	4346	4473	4123	5603	4507	5208	4730
V	214	216	247	159	185	167	220	146	176	235
Cr	232	87.8	127	54.7	13.4	2.15	20.7	35.3	79.1	51.7
Co	33.8	24.9	29.6	16.5	16.9	15.8	17.4	16.4	19.8	26.8
Ni	33.9	18.2	21.8	14.5	5.40	2.12	6.51	9.62	20.2	15.9
Rb	33.9	33.6	26.9	35.9	22.2	41.0	9.6	58.0	29.2	29.7
Sr	33.9	254	285	206	229	244	208	229	223	302
Y	33.9	18.0	21.2	18.7	19.0	19.4	23.3	21.9	20.0	20.4
Zr	33.9	75.9	88.7	145	128	120	150	180	177	96.4
Nb	33.9	3.67	3.84	6.31	4.98	4.77	5.79	7.96	8.00	4.02
Cs	33.9	1.96	1.68	1.96	1.30	2.36	0.52	2.97	1.51	1.59
Ba	33.9	223	208	230	170	253	97	333	206	221
La	33.9	10.3	11.5	13.2	11.1	11.9	13.8	16.9	15.1	11.3
Ce	33.9	21.4	23.0	30.1	21.1	25.1	23.3	45.2	46.4	24.8
Pr	33.9	2.78	3.14	3.82	3.56	3.37	5.03	4.74	4.66	3.16
Nd	33.9	11.7	13.2	15.6	14.6	13.7	20.4	18.8	18.6	13.0
Sm	33.9	2.76	3.16	3.63	3.38	3.20	4.69	4.18	4.24	3.08
Eu	33.9	0.782	0.882	0.949	0.938	0.889	1.20	1.02	1.12	0.879
Gd	33.9	2.95	3.42	3.56	3.45	3.29	4.67	4.10	4.07	3.34
Tb	33.9	0.492	0.570	0.582	0.575	0.546	0.766	0.655	0.661	0.555
Dy	33.9	3.10	3.62	3.55	3.57	3.41	4.71	3.98	4.00	3.49
Ho	33.9	0.682	0.800	0.746	0.773	0.742	1.00	0.844	0.835	0.765
Er	33.9	1.98	2.30	2.15	2.24	2.18	2.84	2.43	2.39	2.21
Tm	33.9	0.293	0.345	0.323	0.340	0.331	0.430	0.368	0.362	0.338
Yb	33.9	1.90	2.23	2.12	2.22	2.16	2.83	2.43	2.43	2.17
Lu	33.9	0.290	0.342	0.323	0.341	0.333	0.422	0.367	0.359	0.328
Hf	33.9	2.19	2.50	3.89	3.49	3.25	4.01	4.68	4.65	2.58
Pb	33.9	8.45	10.0	15.7	12.2	11.6	14.0	18.5	17.7	8.76
Th	33.9	4.04	4.09	6.79	5.95	5.63	6.70	8.56	8.08	4.27
U	33.9	0.93	1.02	1.39	1.32	1.36	1.72	1.71	1.47	1.07

Whole rock analysis done by Inductively Coupled Plasma Mass Spectrometer (ICPMS) on dissolved samples at National Taiwan University (NTU). Values are in ppm. Text in red are possible erroneous values based on standards analysed as unknown (values at the end of the table).

Appendix Table 3 continued

	150321-01C-a	150321-01C-b	150321-01C-c	150321-01E-a	150321-01E-b	150321-01E-c	150321-02-a	150321-02-b	150421-01	150421-02
Sc	23.9	26.7	25.8	26.5	25.7	19.5	10.3	21.7	23.8	21.8
Ti	4659	4870	4661	4439	4715	3827	2690	4156	4497	3965
V	160	174	168	167	169	181	81	168	184	160
Cr	91.6	110	111	123	119	6.3	b.d.	41.3	58.1	83.3
Co	19.1	21.6	19.7	20.1	19.3	16.5	6.9	31.1	29.0	51.1
Ni	31.9	30.6	21.7	33.5	24.9	2.33	b.d.	13.0	17.1	20.3
Rb	25.8	28.0	27.2	21.8	22.1	39.3	47.8	52.4	47.2	57.1
Sr	200	223	223	174	188	242	236	277	269	275
Y	17.4	18.5	17.2	15.5	16.5	19.0	19.8	20.5	21.5	20.7
Zr	156	154	145	134	147	106	150	125	127	126
Nb	6.80	6.75	6.35	5.85	6.25	4.30	5.62	5.34	5.05	4.85
Cs	1.34	1.45	1.40	1.15	1.15	1.99	8.31	8.89	9.28	8.89
Ba	183	199	192	148	161	281	304	321	313	330
La	12.3	12.8	11.9	10.1	11.4	11.4	14.3	14.3	13.7	13.8
Ce	27.8	29.0	25.8	20.1	22.5	23.7	29.7	30.8	30.0	29.6
Pr	3.80	3.93	3.61	3.16	3.51	3.12	3.83	3.91	3.86	3.74
Nd	15.3	15.9	14.6	12.8	14.1	12.7	15.0	15.8	15.9	15.2
Sm	3.57	3.69	3.42	3.05	3.29	2.94	3.23	3.59	3.64	3.46
Eu	0.935	0.981	0.911	0.783	0.862	0.868	0.901	0.958	0.985	0.899
Gd	3.43	3.60	3.33	2.96	3.18	3.08	3.25	3.63	3.76	3.56
Tb	0.564	0.591	0.547	0.498	0.531	0.510	0.522	0.590	0.606	0.581
Dy	3.42	3.61	3.34	3.00	3.19	3.18	3.24	3.57	3.74	3.60
Ho	0.717	0.755	0.700	0.623	0.669	0.702	0.703	0.769	0.804	0.773
Er	2.03	2.15	1.98	1.76	1.87	2.05	2.08	2.22	2.32	2.23
Tm	0.311	0.323	0.298	0.264	0.281	0.315	0.322	0.333	0.346	0.336
Yb	2.04	2.16	1.99	1.72	1.85	2.07	2.17	2.15	2.27	2.21
Lu	0.304	0.318	0.296	0.252	0.273	0.315	0.341	0.329	0.347	0.334
Hf	4.09	4.05	3.78	3.51	3.84	2.82	3.84	3.29	3.29	3.40
Pb	16.0	16.3	14.9	13.3	14.5	11.3	15.2	12.4	9.56	11.8
Th	7.05	6.88	6.35	5.77	6.47	4.74	6.88	5.49	5.41	5.74
U	1.35	1.34	1.23	1.05	1.15	1.14	1.54	1.32	1.32	1.40

Whole rock analysis done by Inductively Coupled Plasma Mass Spectrometer (ICPMS) on dissolved samples at National Taiwan University (NTU). Values are in ppm. Text in red are possible erroneous values based on standards analysed as unknown (values at the end of the table).

Appendix Table 3 continued

	150424-01	150319-02-a2	150318-01	160727-01-a	160727-02-b	160727-03-c	BCR-2	AVG-2	R. V. BCR-2	±	R. V. AVG-2	±
Sc	18.44	28.39	22.31	28.99	27.39	28.35	32.06	11.74	33	2	13	1
Ti	4464	4665	3775				13315	5926	13500	300	6300	1300
V	136	220	162	198	191	198	403	113	416	14	120	5
Cr	28.93	54.18	131.90	471.53	407.03	400.05	11.58	11.74	18	2	17	2
Co	15.25	63.40	23.59	58.88	47.25	47.20	93.40	39.96	37	3	16	1
Ni	7.92	15.77	34.82	117.58	112.65	113.08	10.79	15.89			19	3
Rb	66.24	38.05	44.67	45.33	44.81	45.33	46.08	67.44	48	2	68.6	2.3
Sr	240.05	233.55	240.85	265.58	253.66	260.55	337.45	655.15	346	14	658	17
Y	21.10	22.62	18.39	22.69	22.50	22.74	35.29	19.10	37	2	20	1
Zr	169.10	100.40	108.80	109.80	110.10	110.13	192.20	238.60	188	16	230	4
Nb	7.78	3.93	4.68	4.57	4.78	4.45	12.80	13.61			15	1
Cs	9.18	9.80	7.96	2.23	2.13	2.18	0.97	7.40	1.1	0.1	1.16	0.08
Ba	366.36	232.44	276.36	269.67	266.12	269.09	678.90	1107.00	683	28	1140	32
La	17.01	11.63	12.61	12.87	12.93	13.04	24.82	37.39	25	1	38	1
Ce	43.63	25.90	29.13	28.95	29.05	29.33	57.98	74.47	53	2	68	3
Pr	4.56	3.38	3.47	3.63	3.66	3.68	6.90	8.21	6.8	0.3	8.3	0.6
Nd	17.96	14.17	14.04	15.19	15.20	15.51	28.95	30.56	28	2	30	2
Sm	3.96	3.44	3.21	3.58	3.58	3.63	6.71	5.57	6.7	0.3	5.7	0.3
Eu	1.03	0.97	0.84	1.00	1.00	1.02	2.03	1.67	2	0.1	1.54	0.1
Gd	3.85	3.72	3.26	3.71	3.72	3.77	6.85	4.56	6.8	0.3	4.69	0.26
Tb	0.62	0.62	0.53	0.60	0.60	0.61	1.07	0.65	1.07	0.04	0.64	0.04
Dy	3.77	3.91	3.23	3.60	3.59	3.63	6.47	3.50				
Ho	0.80	0.85	0.69	0.76	0.76	0.77	1.36	0.68	1.33	0.06	0.71	0.08
Er	2.31	2.46	1.99	2.15	2.18	2.21	3.77	1.83			1.79	0.11
Tm	0.35	0.38	0.30	0.32	0.33	0.33	0.55	0.26	0.54		0.26	0.02
Yb	2.31	2.43	1.95	2.10	2.13	2.15	3.44	1.63	3.5	0.2	1.6	0.2
Lu	0.35	0.37	0.30	0.32	0.32	0.32	0.51	0.25	0.51	0.02	0.25	0.01
Hf	4.44	2.75	2.86	2.92	2.96	2.95	4.93	5.18	4.8	0.2	5.08	0.2
Pb	17.81	10.16	10.99	9.65	9.66	9.75	13.62	17.43	11	2	13	1
Th	8.16	4.02	4.81	4.56	4.64	4.64	6.00	6.14	6.2	0.7	6.1	0.6
U	1.76	0.92	1.12	1.12	1.14	1.16	1.68	1.87	1.69	0.19	1.88	0.16

Whole rock analysis done by Inductively Coupled Plasma Mass Spectrometer (ICPMS) on dissolved samples at National Taiwan University (NTU). Values are in ppm. Text in red are possible erroneous values based on standard values analysed as unknown.
Shaded columns are standards analyzed as unknown and reference values (R. V.).

Appendix Table 3 continued

	160519-01	150318-03	150829-02	150829-01	1954-a	1954-b	1954-c	150829-03-c1	150829-03-a2	SY-2	Ou-1	R.V. SY2-1	R.V. OU-1
Sc	46	36	41	36	23	30	31	13	34	15	28		33
V	235	257	233	249	215	226	205	107	223	48	217	50	222
Cr	111	273	179	14	82	81	59	53	51	4	16	10	28
Ni	56	74	47	19	38	38	27	29	29	17	22	10	13
Rb	ND	5	24	16	21	22	24	105	23	217	ND	219	2
Sr	331	269	191	219	239	238	259	220	228	268	105	273	109
Y	24	17	23	23	19	20	20	28	20	135	20	129	21
Zr	126	64	97	83	89	90	102	252	96	417	49	282	55
Nb	ND	ND	ND	ND	ND	ND	ND	2	ND	20	ND	29	2
Cs	16	4	12	18	7	5	14	23	13	10	12		0
Ba	160	157	225	201	234	236	266	885	237	425	138	464	124
La	22	16	28	30	18	18	21	44	13	87	8	76	5
Ce	34	34	32	38	45	28	41	84	38	163	19	176	12
Nd	17	7	7	8	11	4	12	26	3	68	ND		7
Pb	0	2	5	6	6	7	5	30	6	94	2	86	4
Th	3	5	7	5	5	5	3	18	5	376	4	382	2
U	3	ND	3	1	ND	4	3	4	1	272	2		
Zn	83	78	87	82	79	81	75	71	81	251	73	250	74
Cu	34	64	36	38	47	31	18	27	39	13	69	5	62
Ga	18	15	18	19	17	18	19	26	18	28	14		14
S	30	161	94	27	138	134	84	521	184	206	113		
Cl	203	470	463	524	435	497	408	ND	890	65	ND		

Whole rock analysis done at the X-Ray Centre using PANalytical Axios 1kW X-ray fluorescence spectrometer at the University of Auckland. Values are in ppm. Text in red are possible erroneous values based on standard values analysed as unknown.
Shaded columns are standards analyzed as unknown and reference values (R.V.).
Non-detected (ND)

Appendix Table 4. Whole rock FeO and Fe_2O_3 determination results

Sample	wt. sample (g)	vol. titrant (ml)	N of titrant	FeO (wt. %)	(Total) FeO*	Fe_2O_3 (wt.%)
160727-01-C	0.525	4.15	0.0997	5.662532714	7.13	1.648839647
	0.525	4.15	0.1087	6.173694143		1.074500963
160727-01-A	0.498	3.94	0.0997	5.667464518	7.04	1.542174699
	0.498	3.94	0.1087	6.179071145		0.967335793
160727-01-B	0.514	4.54	0.0997	6.327245195	7.14	0.913207647
	0.514	4.54	0.1087	6.898410759		0.271448586
Average (ABC)				6.151403079		1.069584556
Standard Dev				0.46117114		0.496151519
Te Maari LF				6.2 +/- 0.5		1.1
150319-01-E	0.507	3.07	0.0997	4.337628432	7.48	3.530754571
	0.507	3.07	0.1087	4.729189675		3.090798118
Average				4.533409053		3.310776345
Ngauruhoe AF				4.5 +/- 0.5		3.3
FeO* from W.R. XRF						

Appendix Table 5. Whole rock δD and $\delta^{18}O$ analysis laboratory report.

December 6th 2016 new silicate Zn

SAMPLES	δD raw	δD corr	δD corr2	δD corr3	P	V mass 2
CTMP2010	-16.96	-9.5	-8.9	-9.0	44.7	5.170
CTMP2010	-13.90	-6.4	-5.8	-5.7	44.5	5.176
Ave CTMP	**-15.43**	**-8.0**	**-7.4**	**-7.4**	**44.6**	**5.173**
RMW	-131.37	-124.8	-124.2	-131.7	37.1	4.236
RMW	-130.84	-124.3	-123.7	-131.1	45.0	5.062
Ave RMW	**-131.1**	**-124.5**	**-123.9**	**-131.4**	**43.18**	**4.912**
Revised equation		(-7.4+((X+7.4)*((-lowstd act-7.4)/(-low std obs-7.4))))				

CTMP2010 = -7.4; RMW = -131.4

	Standard	δD raw	δD cor	δD corr2	δD corr3	δD corr4	Wt sample	P	Mass 2 V	mg water	wt.% water	$\delta^{18}O$
A	Bulk Serina kao 1	-65.4	-58.3	-57.7	-60.9	-56.9	15.20	38.3	4.264	1.65	10.85	
B	Bulk Serina kao 2	-65.6	-58.5	-57.9	-61.1	-57.1	15.00	37.3	4.316	1.67	11.12	
C	Bulk Serina kao 3	-66.0	-58.9	-58.3	-61.6	-57.6	15.20	39.4	4.646	1.80	11.82	
					-61.0	**-57.0**						
	Samples											
1	150319-02-a1	no gas					100.45	0.1	0.220	0.09	0.08	8.1
2	150319-02-a2	no gas					100.52	0.1	0.155	0.06	0.06	7.6
3	160727-01-c	no gas					100.70	0.1	0.166	0.06	0.06	8.0
4	150320-01E-e	-119.9	-113.3	-112.7	-119.5	-115.5	100.24	4.8	0.695	0.27	0.27	7.8
5	150318-03	no gas					100.00	0.1	0.121	0.05	0.05	7.9
6	150320-01A-h	-93.6	-86.8	-86.2	-91.2	-87.2	100.27	14.6	1.712	0.66	0.66	7.9
7	150319-01-e	no gas					100.25	0.1	0.281	0.11	0.11	7.6
8	150319-02-b2	no gas					100.19	0.1	0.144	0.06	0.06	8.7

Notes: The standard bulk Serina Kao is a pure kaolinite from the Serina mine near Cape Town; its δD values is -57 (Harris et al., Econ Geol, 1999)

CTMP2010 and RMW are 2 water standards used to calibrate the raw data to the SMOW scale. Their δD values are -7.4 and -131.4
Raw data are corrected vs the ref gas value (δD corr), then adjusted so that CTMP2010 = -7.4 (δ corr2), then 'stretched' so that RMW = -131.4
The silicates are adjusted (δD corr 4) so that kaolinite = -57.

V mass 2 = voltage measured on the mass 2 collector prior to analysis at constant volume. CTMP2010 and RMW are 2 mg exactly.

The voltage per mg is used to determine the mg water and then the wt.% water.

Laboratory report for whole rock δD and $\delta^{18}O$ analysis done at the Stable Isotope laboratory, Department of Geological Sciences, University of Cape Town. Shaded columns are final data.

Appendix Table 6. Whole rock $^{87}Sr/^{86}Sr$, $^{143}Nd/^{144}Nd$, $^{206}Pb/^{204}Pb$, $^{207}Pb/^{204}Pb$, $^{208}Pb/^{204}Pb$ values.

Sample	$^{87}Sr/^{86}Sr$	2 SE (M)	e_{Nd}	$^{143}Nd/^{144}Nd$	2 SE (M)	$^{208}Pb/^{204}Pb$	2 SE (M)	$^{207}Pb/^{204}Pb$	2 SE (M)	$^{206}Pb/^{204}Pb$	2 SE (M)
150318-03	0.704589	0.000008	3.68	0.512826	0.000006	38.7594	0.0026	15.6376	0.0007	18.8316	0.0006
150319-01-e	0.704950	0.000012	1.84	0.512732	0.000004	38.7860	0.0016	15.6443	0.0004	18.8460	0.0004
150319-02-a1	0.705774	0.000010	1.36	0.512707	0.000006	38.7919	0.0021	15.6472	0.0005	18.8457	0.0005
150319-02-b2	0.705712	0.000012	1.38	0.512709	0.000004	38.7819	0.0020	15.6481	0.0006	18.8345	0.0005
150319-02-a2	0.705642	0.000009	1.54	0.512717	0.000009	38.7925	0.0011	15.6471	0.0004	18.8495	0.0004
150320-01A-b	0.705254	0.000009	2.18	0.512750	0.000005	38.7906	0.0014	15.6443	0.0004	18.8421	0.0004
150320-01A-h	0.705123	0.000012	2.65	0.512774	0.000004	38.7860	0.0019	15.6440	0.0005	18.8433	0.0005
150320-01E-a	0.704884	0.000007	2.03	0.512742	0.000004	38.7712	0.0017	15.6409	0.0005	18.8287	0.0005
150320-01E-e	0.704978	0.000013	1.61	0.512721	0.000005	38.7972	0.0014	15.6434	0.0004	18.8495	0.0005
160727-01-C	0.705405	0.000010	1.63	0.512721	0.000005	38.7990	0.0021	15.6485	0.0006	18.8556	0.0005

Analysis done at the College of Engineering and Physical Sciences, University of New Hampshire.

Appendix Table 7. Microprobe analysis for mineral, groundmass and melt inclusions for selected deposits.

No.	Sample		SiO_2	TiO_2	Al_2O_3	FeO	MnO	MgO	CaO	Na_2O	K_2O	P_2O_5	Cr_2O_3	SrO	NiO	Cl	SO_3	Total	Mg#	%An	%Ab	Wo	En	Fs	Sr ppm	Cr ppm	Ni ppm	Cl ppm	S ppm
	150318-03 (Red Crater LF)																												
22	150318-03-pl1		53.58	0.01	30.77	0.33	-	0.03	13.13	3.92	0.15	-	-	0.00	-	-	-	101.93		64.35	34.78				0	0	0	0	0
23	150318-03-pl2-c		52.79	0.00	31.40	0.35	-	0.03	13.57	3.69	0.12	-	-	0.00	-	-	-	101.96		66.53	32.75				0	0	0	0	0
24	150318-03-pl2-r		53.92	0.00	30.31	0.31	-	0.03	12.62	4.10	0.14	-	-	0.00	-	-	-	101.42		62.47	36.69				0	0	0	0	0
25	150318-03-pl3		50.84	0.00	32.09	0.43	-	0.18	15.39	2.76	0.07	-	-	0.00	-	-	-	101.76		75.19	24.41				0	0	0	0	0
26	150318-03-pl4	plagioclase (pl)	52.95	0.00	30.98	0.36	-	0.05	13.67	3.74	0.15	-	-	0.00	-	-	-	101.91		66.32	32.80				0	0	0	0	0
27	150318-03-pl5		49.28	0.00	32.92	0.51	-	0.17	16.35	2.25	0.04	-	-	0.00	-	-	-	101.52		79.84	19.91				0	0	0	0	0
28	150318-03-pl6-mic		47.90	0.00	34.00	0.56	-	0.14	17.47	1.33	0.04	-	-	0.00	-	-	-	101.43		87.70	12.06				0	0	0	0	0
29	150318-03-pl7-mic		49.95	0.00	32.65	0.52	-	0.18	15.78	2.44	0.05	-	-	0.00	-	-	-	101.57		77.92	21.77				0	0	0	0	0
30	150318-03-pl8-mic		52.16	0.01	30.71	0.77	-	0.49	14.03	3.32	0.11	-	-	0.00	-	-	-	101.59		69.60	29.78				0	0	0	0	0
31	150318-03-pl9-mic		51.19	0.00	31.67	0.59	-	0.19	14.97	2.97	0.07	-	-	0.00	-	-	-	101.64		73.31	26.29				0	0	0	0	0
32	150318-03-pl10-mic		50.81	0.01	32.13	0.56	-	0.18	15.24	2.78	0.06	-	-	0.00	-	-	-	101.77		74.94	24.70				0	0	0	0	0
7	150318-03-opx1		52.27	-	-	21.94	0.63	22.01	2.49	-	-	-	0.00	-	0.00	-	-	99.33	64.13			4.95	60.96	34.09	0	0	0	0	0
8	150318-03-opx2		52.10	-	-	23.23	0.52	21.81	1.08	-	-	-	0.04	-	0.00	-	-	98.77	62.61			2.17	61.25	36.58	0	260	0	0	0
6	150318-03-opx1		53.81	0.26	0.22	24.05	0.61	23.45	1.44	0.01	0.00	-	0.06	-	-	-	-	103.90	63.48			2.72	61.75	35.53	0	397	0	0	0
8	150318-03-opx2		56.22	0.10	0.16	15.37	0.40	28.61	2.06	0.00	0.00	-	0.00	-	-	-	-	102.92	76.85			3.83	73.91	22.27	0	0	0	0	0
11	150318-03-cpx5		52.46	0.38	0.38	11.21	0.38	14.95	21.04	0.10	0.01	-	0.03	-	-	-	-	100.93	70.40			41.58	41.13	17.29	0	171	0	0	0
5	150318-03-cpx1		51.54	0.57	1.25	6.69	0.13	16.73	21.77	0.11	0.01	-	0.74	-	-	-	-	99.54	81.68			43.30	46.32	10.39	0	5049	0	0	0
7	150318-03-cpx2		52.82	0.44	0.86	8.51	0.21	17.55	20.33	0.11	0.01	-	0.25	-	-	-	-	101.09	78.62			39.56	47.52	12.92	0	1704	0	0	0
9	150318-03-cpx3	pyroxene (px)	53.83	0.33	0.68	7.69	0.22	18.00	20.44	0.13	0.00	-	0.43	-	-	-	-	101.74	80.67			39.70	48.64	11.65	0	2949	0	0	0
10	150318-03-cpx4		51.68	0.56	1.06	6.37	0.14	17.10	21.92	0.09	0.01	-	1.00	-	-	-	-	99.92	82.71			43.25	46.94	9.81	0	6856	0	0	0
8	150318-03-mi-px1		52.01	0.28	1.17	10.05	0.35	14.21	20.98	0.18	0.00	-	0.00	-	-	-	-	99.22	71.59			43.17	40.68	16.14	0	7	0	0	0
9	150318-03-mi-px2		52.51	0.24	1.60	20.89	0.52	22.96	1.25	0.02	0.00	-	0.04	-	-	-	-	100.04	66.21			2.53	64.54	32.93	0	253	0	0	0
10	150318-03-mi-px3		51.93	0.28	1.26	9.73	0.33	14.39	21.81	0.20	0.00	-	0.00	-	-	-	-	99.93	72.50			44.13	40.51	15.37	0	7	0	0	0
11	150318-03-mi-px4		51.71	0.41	1.89	9.71	0.34	14.68	20.64	0.23	0.00	-	0.01	-	-	-	-	99.61	72.95			42.43	42.00	15.57	0	48	0	0	0
9	150318-03-ol3-c	olivine (ol)	39.98	-	-	11.94	0.21	48.81	0.18	-	-	-	0.04	-	0.19	-	-	101.35	87.94						0	294	1493	0	0
10	150318-03-ol3-r		38.82	-	-	19.68	0.35	42.07	0.22	-	-	-	0.00	-	0.08	-	-	101.23	79.22						0	0	660	0	0

10	150318-03-mi-ol2		39.47	-	-	12.24	0.09	46.52	0.19	-	-	-	0.03	-	0.16	-	-	98.70	87.14						0	233	1289	0	0
11	150318-03-mi-ol3		39.32	-	-	10.97	0.10	46.72	0.19	-	-	-	0.04	-	0.21	-	-	97.55	88.36						0	246	1627	0	0
12	150318-03-mi-ol4		39.24	-	-	10.66	0.10	46.65	0.18	-	-	-	0.05	-	0.19	-	-	97.07	88.64						0	335	1524	0	0
13	150318-03-mi-ol4b		39.19	-	-	11.33	0.08	46.48	0.19	-	-	-	0.01	-	0.21	-	-	97.50	87.97						0	89	1627	0	0
11	150318-03-mi-px1-1		67.00	2.47	10.53	3.97	0.23	1.12	5.36	1.84	2.41	-	0.00	-	-	0.20	0.02	95.15	33.34	46.35	28.83	53.54	15.49	30.97	0	0	0	2010	84
12	150318-03-mi-px2-1		65.76	0.80	13.38	5.76	0.09	1.26	4.72	2.08	1.82	-	0.04	-	-	0.21	0.03	95.94	28.00	44.34	35.33	43.05	15.94	41.01	0	294	0	2090	132
Average	150318-03-mi-px3-1	melt inclusion	64.71	0.74	15.28	3.57	0.13	1.08	4.67	2.00	2.25	-	0.00	-	-	0.19	0.00	94.62	35.06	42.58	32.96	52.15	16.78	31.07	0	0	0	1885	14
Average	150318-03-mi-px3-2		69.43	1.08	10.44	5.28	0.08	0.97	3.59	1.46	3.57	-	0.00	-	-	0.24	0.28	96.41	24.70	34.23	25.23	39.58	14.92	45.50	0	31	0	2365	1110
17	150318-03-mi-px4-1		68.10	0.63	12.85	3.82	0.10	0.58	1.81	1.81	3.36	-	0.00	-	-	0.28	0.03	93.38	21.37	19.94	36.10	32.32	14.46	53.21	0	0	0	2830	108
18	150318-03-mi-px4-2		66.70	0.74	13.39	4.08	0.05	1.23	3.59	2.08	2.85	-	0.01	-	-	0.20	0.45	95.37	35.03	33.40	35.03	42.27	20.22	37.51	0	82	0	2010	1780
28	150318-03-gm1		57.78	1.36	14.49	11.11	0.22	3.50	6.66	2.11	1.38	-	0.00	-	-	0.13	-	98.75	35.99	54.93	31.55	32.95	24.13	42.92	0	0	0	1320	0
29	150318-03-gm2		56.12	0.64	15.67	8.24	0.20	6.17	9.80	1.72	0.73	-	0.00	-	-	0.05	-	99.32	57.17	71.16	22.54	39.49	34.59	25.92	0	0	0	500	0
30	150318-03-gm3		58.56	0.92	17.17	7.37	0.14	3.49	8.37	2.30	1.00	-	0.02	-	-	0.10	-	99.45	45.78	60.98	30.33	44.11	25.58	30.30	0	144	0	990	0
31	150318-03-gm4		58.64	1.24	14.89	9.30	0.22	3.33	7.42	2.10	1.25	-	0.00	-	-	0.12	-	98.51	38.98	58.38	29.88	38.41	24.01	37.58	0	0	0	1190	0
32	150318-03-gm5		56.43	0.81	16.75	8.18	0.15	4.25	8.68	2.26	0.96	-	0.02	-	-	0.07	-	98.55	48.07	62.44	29.35	41.39	28.17	30.44	0	109	0	680	0
33	150318-03-gm6	groundmass (gm)	57.46	1.25	13.53	10.33	0.19	4.07	7.83	1.71	1.34	-	0.01	-	-	0.10	-	97.81	41.27	62.59	24.68	36.31	26.28	37.40	0	89	0	1010	0
34	150318-03-gm7		57.17	1.00	14.76	10.03	0.16	4.88	8.61	1.99	1.06	-	0.00	-	-	0.06	-	99.71	46.48	63.91	26.76	37.05	29.26	33.69	0	0	0	620	0
35	150318-03-gm8		59.50	0.82	15.46	7.26	0.15	4.12	8.61	2.00	1.18	-	0.00	-	-	0.07	-	99.16	50.32	63.16	26.58	43.02	28.67	28.30	0	0	0	670	0
	150319-01 (Ng Tephra)																											
13	150319-01-e-pl1		47.64	0.00	34.31	0.37	-	0.09	17.63	1.27	0.04	-	-	0.00	-	-	-	101.35		88.29	11.47				0	0	0	0	0
14	150319-01-e-pl2		47.86	0.00	34.19	0.43	-	0.10	17.61	1.36	0.03	-	-	0.00	-	-	-	101.57		87.63	12.20				0	0	0	0	0
15	150319-01-e-pl3		48.33	0.00	34.05	0.38	-	0.11	17.21	1.41	0.07	-	-	0.00	-	-	-	101.56		86.72	12.85				0	0	0	0	0
16	150319-01-e-pl4		47.40	0.00	34.39	0.39	-	0.10	17.56	1.30	0.04	-	-	0.00	-	-	-	101.17		87.97	11.82				0	0	0	0	0
17	150319-01-e-pl5-mic	plagioclase	51.02	0.00	31.94	0.56	-	0.15	15.13	3.01	0.10	-	-	0.00	-	-	-	101.89		73.11	26.30				0	0	0	0	0
18	150319-01-e-pl6-mic		50.61	0.00	32.30	0.51	-	0.14	15.11	2.88	0.09	-	-	0.00	-	-	-	101.64		73.99	25.47				0	0	0	0	0
19	150319-01-e-pl7-mic		48.41	0.00	34.02	0.56	-	0.08	17.25	1.42	0.03	-	-	0.00	-	-	-	101.76		86.89	12.94				0	0	0	0	0
20	150319-01-e-pl8-mic		54.31	0.02	29.46	0.69	-	0.20	12.46	3.82	0.21	-	-	0.01	-	-	-	101.18		63.48	35.26				85	0	0	0	0
21	150319-01-e-pl9-mic		50.47	0.00	32.24	0.46	-	0.16	15.33	2.69	0.09	-	-	0.00	-	-	-	101.43		75.56	23.94				0	0	0	0	0

5	150319-01-e-cpx1		52.18	0.32	0.86	7.76	0.20	17.31	20.79	0.09	0.00	-	0.12	-	-	-	-	99.63	79.90			40.82	47.29	11.89	0	814	0	0	0
6	150319-01-e-cpx2-c		52.02	0.53	0.57	12.05	0.28	15.01	19.67	0.10	0.00	-	0.00	-	-	-	-	100.22	68.95			39.37	41.80	18.82	0	0	0	0	0
7	150319-01-e-cpx2-i		52.63	0.26	0.95	5.96	0.14	17.88	21.10	0.12	0.01	-	0.35	-	-	-	-	99.38	84.24			41.68	49.14	9.19	0	2361	0	0	0
8	150319-01-e-cpx2-r		52.68	0.32	0.74	7.72	0.17	17.02	21.02	0.12	0.00	-	0.33	-	-	-	-	100.12	79.72			41.44	46.68	11.88	0	2224	0	0	0
9	150319-01-e-cpx3		52.73	0.37	0.67	8.33	0.22	17.34	20.01	0.11	0.00	-	0.26	-	-	-	-	100.03	78.77			39.51	47.65	12.84	0	1752	0	0	0
10	150319-01-e-cpx4		52.10	0.39	0.80	7.80	0.20	17.30	20.52	0.09	0.02	-	0.23	-	-	-	-	99.44	79.82			40.49	47.50	12.01	0	1539	0	0	0
37	150319-01-E-MI-PX1		53.63	0.16	1.76	5.25	0.16	19.12	17.92	0.05	-	-	0.11	-	0.02	-	-	98.18	86.65			36.85	54.71	8.43	0	773	173	0	0
4	150319-01-e-mi-px2		52.19	0.52	2.05	10.18	0.28	15.05	22.76	-	-	-	0.00	-	-	-	-	103.04	72.50			44.07	40.55	15.38	0	21	0	0	0
39	150319-01-E-MI-PX4		50.81	0.48	2.95	8.44	0.27	15.95	17.67	0.05	-	-	0.11	-	0.00	-	-	96.74	77.11			38.04	47.78	14.19	0	780	0	0	0
38	150319-01-E-MI-PX5		52.77	0.46	2.04	11.79	0.48	14.95	18.49	0.06	-	-	0.00	-	0.02	-	-	101.04	69.34			38.13	42.90	18.97	0	0	157	0	0
40	150319-01-E-MI-PX6		52.02	0.33	2.71	6.70	0.18	16.64	20.01	0.03	-	-	0.34	-	0.03	-	-	98.98	81.58			41.35	47.84	10.81	0	2313	196	0	0
10	150319-01-i-cpx1	pyroxene	53.11	0.38	2.67	7.66	0.26	16.83	20.26	0.24	0.00	-	0.09	-	-	-	-	101.49	79.66			40.79	47.17	12.04	0	595	0	0	0
11	150319-01-i-cpx2-c		52.37	0.38	2.68	8.68	0.24	15.76	20.60	0.24	0.00	-	0.09	-	-	-	-	101.05	76.40			41.77	44.48	13.74	0	602	0	0	0
12	150319-01-i-cpx2-r		52.78	0.34	2.72	7.32	0.20	16.99	20.16	0.23	0.00	-	0.24	-	-	-	-	100.96	80.54			40.72	47.74	11.53	0	1669	0	0	0
13	150319-01-i-cpx3		52.49	0.40	3.06	7.44	0.21	16.89	20.31	0.24	0.00	-	0.29	-	-	-	-	101.32	80.18			40.93	47.36	11.71	0	1977	0	0	0
3	150319-01-e-opx1		54.09	-	-	13.68	0.30	28.67	1.67	-	-	-	0.13	-	0.00	-	-	98.54	78.89			3.19	76.37	20.44	0	917	24	0	0
4	150319-01-e-opx2		53.84	-	-	13.02	0.30	28.88	1.72	-	-	-	0.19	-	0.03	-	-	97.97	79.82			3.29	77.19	19.52	0	1286	204	0	0
5	150319-01-e-opx3		54.12	-	-	14.10	0.31	28.16	1.67	-	-	-	0.08	-	0.03	-	-	98.46	78.07			3.21	75.56	21.23	0	527	196	0	0
6	150319-01-e-opx4		54.58	-	-	13.72	0.32	29.06	1.79	-	-	-	0.08	-	0.06	-	-	99.62	79.06			3.38	76.39	20.23	0	575	503	0	0
11	150319-01-e-opx1		54.73	0.15	0.56	14.20	0.25	29.58	1.66	0.00	0.00	-	0.12	-	-	-	-	101.26	78.78			3.09	76.35	20.56	0	828	0	0	0
12	150319-01-e-opx2		55.20	0.14	0.43	14.22	0.32	29.50	1.71	0.00	0.00	-	0.10	-	-	-	-	101.61	78.71			3.17	76.22	20.61	0	705	0	0	0
13	150319-01-e-opx3		54.36	0.18	0.54	14.47	0.34	29.45	1.66	0.00	0.00	-	0.09	-	-	-	-	101.07	78.40			3.07	75.99	20.94	0	582	0	0	0
14	150319-01-e-opx4		54.90	0.12	0.55	14.02	0.34	29.78	1.74	0.00	0.01	-	0.19	-	-	-	-	101.64	79.12			3.21	76.58	20.21	0	1286	0	0	0
41	150319-01-E-MI-PX7		54.93	0.13	1.37	13.25	0.28	28.51	1.64	0.00	-	-	0.08	-	0.07	-	-	100.25	79.32			3.17	76.81	20.02	0	534	519	0	0
8	150319-01-i-opx1		54.50	0.17	1.83	13.81	0.26	28.04	1.96	-	-	-	0.10	-	-	-	-	100.67	78.35			3.78	75.39	20.83	0	698	0	0	0
15	150319-01-e-ol5	ol	38.67	0.00	0.02	23.31	0.39	40.88	0.17	0.00	0.01	-	0.02	-	-	-	-	103.47	75.77						0	157	0	0	0
15	150319-01-e-gm1		60.04	1.28	14.13	9.27	0.14	3.18	5.95	2.02	1.88	-	0.03	-	-	0.15	-	98.07	37.91	50.22	30.85	33.79	25.10	41.11	0	233	0	1450	0
16	150319-01-e-gm2	groundmass	61.01	1.15	14.61	8.10	0.15	2.88	5.79	2.33	2.39	-	0.00	-	-	0.16	-	98.57	38.76	45.07	32.83	35.93	24.83	39.24	0	0	0	1590	0
17	150319-01-e-gm3		59.35	1.07	14.45	8.52	0.15	2.79	5.78	2.22	2.07	-	0.00	-	-	0.13	-	96.53	36.83	47.14	32.74	35.47	23.77	40.76	0	0	0	1310	0
18	150319-01-e-gm4		60.24	1.10	14.84	8.26	0.16	3.00	6.19	2.01	1.81	-	0.00	-	-	0.11	-	97.71	39.26	51.63	30.37	36.82	24.80	38.38	0	0	0	1120	0

19	150319-01-e-gm5		59.10	1.17	14.13	9.40	0.16	3.38	6.61	1.87	1.70	-	0.00	-	-	0.13	-	97.66	39.06	54.98	28.16	35.44	25.22	39.34	0	27	0	1320	0
20	150319-01-e-gm6		59.81	1.16	14.50	8.19	0.15	3.02	6.17	2.31	1.94	-	0.00	-	-	0.11	-	97.37	39.61	48.75	33.00	36.82	25.03	38.15	0	7	0	1090	0
21	150319-01-e-gm7		59.83	1.14	14.62	8.82	0.18	3.16	6.48	2.08	1.83	-	0.02	-	-	0.12	-	98.27	39.02	52.15	30.35	36.46	24.79	38.75	0	103	0	1220	0
22	150319-01-e-gm8		61.48	1.03	14.55	7.15	0.12	2.67	5.48	2.25	2.33	-	0.01	-	-	0.08	-	97.14	39.92	44.41	33.07	37.08	25.12	37.80	0	41	0	830	0
23	150319-01-e-gm9		58.91	1.14	14.61	8.63	0.15	2.95	6.56	2.01	1.82	-	0.00	-	-	0.12	-	96.90	37.85	53.06	29.43	37.71	23.58	38.71	0	0	0	1210	0
24	150319-01-e-gm10		60.02	1.13	14.88	8.35	0.17	3.06	6.51	2.02	1.77	-	0.02	-	-	0.12	-	98.06	39.52	52.99	29.81	37.67	24.63	37.70	0	144	0	1200	0
25	150319-01-e-gm11		58.45	1.15	14.59	8.41	0.17	3.07	6.46	1.88	1.84	-	0.02	-	-	0.12	-	96.17	39.41	53.65	28.21	37.35	24.69	37.96	0	151	0	1240	0
26	150319-01-e-gm12		59.42	1.10	14.87	8.73	0.12	2.99	6.75	1.89	1.63	-	0.01	-	-	0.12	-	97.63	37.90	55.73	28.29	38.08	23.47	38.45	0	41	0	1150	0
27	150319-01-e-gm13		60.79	1.13	15.12	7.91	0.17	3.15	6.41	1.91	1.92	-	0.02	-	-	0.12	-	98.64	41.53	52.77	28.44	37.76	25.85	36.39	0	109	0	1170	0
97	150319-01-e-mi-px1-1a		58.30	0.58	15.46	4.85	0.42	2.75	5.26	2.84	1.22	0.04	0.00	-	-	0.07	0.42	92.21	50.29	44.45	43.33	40.85	29.75	29.41	0	0	0	680	1672
98	150319-01-e-mi-px1-1b		56.65	0.59	15.48	3.90	0.09	2.53	4.94	2.78	0.21	0.07	0.00	-	-	0.08	0.44	87.76	53.67	48.33	49.25	42.90	30.64	26.46	0	0	0	830	1756
16	150319-01-e-mi-px2-1		59.74	0.43	11.99	4.88	0.12	7.39	11.40	1.91	1.64	-	0.05	-	-	0.10	0.08	99.71	72.97	67.83	20.56	44.72	40.34	14.94	0	328	0	1020	328
17	150319-01-e-mi-px2-1		61.34	0.45	14.08	4.61	0.07	5.32	9.41	0.73	1.97	-	0.05	-	-	0.15	0.08	98.20	67.30	72.00	10.10	46.11	36.27	17.62	0	308	0	1510	304
91	150319-01-e-mi-px4-2		56.98	1.21	14.09	8.10	0.17	1.46	4.83	3.66	2.03	0.14	0.00	-	-	0.23	0.11	93.03	24.35	34.82	47.74	36.65	15.42	47.93	0	21	0	2320	428
93	150319-01-e-mi-px5-2	melt inclusion (MI)	55.77	0.43	22.35	2.28	0.03	0.16	8.20	3.50	12.63	0.00	0.00	-	-	0.07	0.03	105.44	11.39	27.74	21.41	80.36	2.24	17.40	0	0	0	660	120
94	150319-01-e-mi-px5-3		55.36	1.32	15.82	7.50	0.12	0.59	4.55	3.17	0.00	0.07	0.04	-	-	0.26	0.34	89.14	12.21	44.24	55.76	40.59	7.26	52.15	0	239	0	2590	1364
95	150319-01-e-mi-px5-4		49.08	0.05	28.88	1.39	0.01	0.69	14.41	2.87	0.05	0.00	0.01	-	-	0.00	0.00	97.44	47.08	73.29	26.39	87.54	5.87	6.60	0	96	0	0	4
96	150319-01-e-mi-px5-5		55.21	1.63	14.70	6.50	0.18	2.34	6.85	3.12	1.16	0.01	0.00	-	-	0.25	0.97	92.92	39.14	49.32	40.72	45.10	21.49	33.41	0	0	0	2460	3888
88	150319-01-e-mi-px6-1		57.22	0.88	18.69	5.96	0.10	1.30	5.14	3.48	1.47	0.02	0.01	-	-	0.26	0.31	94.83	27.96	38.95	47.77	44.31	15.57	40.12	0	41	0	2560	1236
89	150319-01-e-mi-px6-2		57.63	0.86	19.76	3.99	0.06	0.92	5.56	3.57	1.51	0.04	0.04	-	-	0.27	0.34	94.56	29.14	40.24	46.73	55.81	12.88	31.31	0	274	0	2730	1360
90	150319-01-e-mi-px6-3		57.43	0.87	18.67	5.43	0.15	1.07	5.37	3.57	1.48	0.02	0.01	-	-	0.26	0.29	94.60	25.97	39.53	47.54	48.39	13.40	38.21	0	62	0	2640	1160
92	150319-01-e-mi-px7-1		58.10	1.02	16.76	6.85	0.11	1.01	5.49	3.30	1.63	0.00	0.05	-	-	0.27	0.28	94.86	20.81	40.92	44.56	44.84	11.48	43.68	0	335	0	2690	1104
22	150319-01-i-gm1		59.42	1.11	14.80	8.16	0.13	2.71	6.77	3.46	2.06	-	0.00	-	-	0.13	0.00	98.75	37.20	43.70	40.44	40.04	22.30	37.66	0	0	0	1260	0
23	150319-01-i-gm2	groundmass	59.65	1.00	15.72	8.26	0.13	3.70	6.70	3.13	1.47	-	0.01	-	-	0.17	0.07	100.00	44.43	47.45	40.14	36.60	28.17	35.23	0	82	0	1680	272
24	150319-01-i-gm3		58.33	0.90	16.70	7.92	0.15	3.69	7.53	3.18	1.35	-	0.01	-	-	0.15	0.11	100.02	45.37	50.58	38.60	39.95	27.24	32.81	0	82	0	1530	424
25	150319-01-i-gm4		57.95	0.89	16.95	6.73	0.12	3.21	7.06	3.69	1.44	-	0.00	-	-	0.12	0.08	98.24	45.96	45.68	43.21	42.07	26.63	31.30	0	0	0	1230	328
26	150319-01-i-gm5		59.32	1.13	14.63	6.56	0.14	3.18	6.45	3.21	1.83	-	0.00	-	-	0.16	0.02	96.64	46.37	44.71	40.18	40.33	27.67	32.00	0	0	0	1600	88
17	150319-01-i-mi-cpx2-1		55.12	0.93	16.65	6.32	0.14	1.32	5.59	3.12	1.40	-	0.04	-	-	0.21	0.25	91.05	27.16	43.36	43.72	45.24	14.87	39.88	0	274	0	2110	1016
18	150319-01-i-mi-cpx2-2	MI	57.68	0.91	17.46	7.50	0.13	2.13	5.82	3.54	1.43	-	0.00	-	-	0.21	0.27	97.04	33.64	41.75	46.00	39.74	20.27	39.99	0	0	0	2100	1092
19	150319-01-i-mi-px-3		58.82	0.82	19.35	4.94	0.09	1.76	6.01	3.38	1.28	-	0.02	-	-	0.22	0.39	97.04	38.87	44.02	44.79	48.78	19.91	31.31	0	103	0	2190	1576

	150319-02 (Ng 1975)																								
3	150319-02-d-pl1		52.28	0.00	29.83	0.40	-	0.08	13.14	3.75	0.19	-	-	0.00	-	-	-	99.67	65.21	33.67		0	0	0	0	0
4	150319-02-d-pl2		49.84	0.00	31.73	0.46	-	0.09	14.97	2.72	0.11	-	-	0.00	-	-	-	99.91	74.75	24.60		0	0	0	0	0
5	150319-02-d-pl3		51.20	0.00	30.84	0.57	-	0.09	14.11	3.12	0.17	-	-	0.00	-	-	-	100.09	70.71	28.27		0	0	0	0	0
6	150319-02-d-pl4		45.34	0.00	34.88	0.30	-	0.07	18.52	0.83	0.03	-	-	0.00	-	-	-	99.97	92.37	7.47		0	0	0	0	0
7	150319-02-d-pl5-c		47.35	0.00	33.60	0.46	-	0.06	17.07	1.40	0.07	-	-	0.00	-	-	-	100.02	86.73	12.86		0	0	0	0	0
8	150319-02-d-pl5-i		49.14	0.00	32.22	0.41	-	0.11	15.74	2.45	0.09	-	-	0.00	-	-	-	100.15	77.66	21.83		0	0	0	0	0
9	150319-02-d-pl5-r		51.15	0.01	30.81	0.51	-	0.13	14.29	3.17	0.14	-	-	0.00	-	-	-	100.20	70.78	28.42		0	0	0	0	0
10	150319-02-d-pl6mic		51.59	0.00	30.23	0.60	-	0.15	13.91	3.27	0.17	-	-	0.00	-	-	-	99.92	69.44	29.55		0	0	0	0	0
13	150319-02-d-pl9mic		52.92	0.02	28.95	0.79	-	0.17	12.53	3.92	0.24	-	-	0.00	-	-	-	99.53	62.93	35.63		0	0	0	0	0
3	150319-02-b2-pl1-c		46.49	0.00	34.31	0.34	-	0.06	18.20	0.99	0.02	-	-	0.00	-	-	-	100.40	90.98	8.92		0	0	0	0	0
4	150319-02-b2-pl2-c		47.17	0.00	34.12	0.36	-	0.03	17.51	1.18	0.03	-	-	0.00	-	-	-	100.41	88.97	10.87		0	0	0	0	0
5	150319-02-b2-pl2-r		52.71	0.00	28.75	0.54	-	0.10	12.44	3.71	0.17	-	-	0.00	-	-	-	98.42	64.28	34.70		0	0	0	0	0
6	150319-02-b2-pl1-r		50.62	0.00	31.97	0.38	-	0.13	15.18	2.84	0.07	-	-	0.00	-	-	-	101.17	74.43	25.18		0	0	0	0	0
7	150319-02-b2-pl3	plagioclase	47.66	0.00	34.06	0.35	-	0.05	17.40	1.31	0.04	-	-	0.00	-	-	-	100.86	87.80	11.99		0	0	0	0	0
8	150319-02-b2-pl4-mic		52.86	0.00	29.89	0.69	-	0.11	13.02	3.78	0.17	-	-	0.00	-	-	-	100.50	64.88	34.12		0	0	0	0	0
9	150319-02-b2-pl5-mic		54.64	0.00	29.12	0.56	-	0.08	11.92	4.42	0.22	-	-	0.00	-	-	-	100.96	59.04	39.65		0	0	0	0	0
10	150319-02-b2-pl6-mic		55.24	0.03	28.36	0.66	-	0.11	11.39	4.57	0.21	-	-	0.00	-	-	-	100.57	57.23	41.51		0	0	0	0	0
11	150319-02-b2-pl7-mic		55.03	0.02	28.60	0.62	-	0.10	11.43	4.51	0.24	-	-	0.00	-	-	-	100.55	57.50	41.08		0	0	0	0	0
12	150319-02-a2-pl1-c		46.56	0.00	32.91	0.25	-	0.01	16.59	1.42	0.05	-	-	0.00	-	-	-	97.78	86.33	13.36		0	0	0	0	0
13	150319-02-a2-pl1-r		52.58	0.00	30.61	0.58	-	0.08	13.81	3.62	0.16	-	-	0.00	-	-	-	101.44	67.17	31.88		0	0	0	0	0
14	150319-02-a2-pl2		53.32	0.00	30.47	0.29	-	0.04	12.92	3.91	0.15	-	-	0.00	-	-	-	101.09	64.07	35.06		0	0	0	0	0
15	150319-02-a2-pl3		46.24	0.00	35.16	0.39	-	0.08	18.39	0.90	0.01	-	-	0.00	-	-	-	101.17	91.81	8.12		0	0	0	0	0
16	150319-02-a2-pl4-mic		51.18	0.00	31.47	0.64	-	0.11	14.81	3.03	0.09	-	-	0.00	-	-	-	101.33	72.63	26.87		0	0	0	0	0
17	150319-02-a2-pl5-mic		50.48	0.00	32.11	0.56	-	0.10	15.19	2.86	0.07	-	-	0.00	-	-	-	101.38	74.28	25.29		0	0	0	0	0
18	150319-02-a2-pl6-mic		47.76	0.00	33.96	0.54	-	0.07	17.21	1.35	0.06	-	-	0.00	-	-	-	100.94	87.26	12.40		0	0	0	0	0
19	150319-02-a1-pl1		48.77	0.00	32.92	0.33	-	0.09	16.44	1.64	0.05	-	-	0.00	-	-	-	100.24	84.41	15.27		0	0	0	0	0
20	150319-02-a1-pl2-c		47.65	0.00	34.07	0.30	-	0.06	17.37	1.29	0.05	-	-	0.00	-	-	-	100.79	87.88	11.85		0	0	0	0	0
21	150319-02-a1-pl2-i		49.65	0.01	32.67	0.36	-	0.07	16.02	2.45	0.06	-	-	0.00	-	-	-	101.27	78.08	21.57		0	0	0	0	0
22	150319-02-a1-pl2-r		54.30	0.00	29.33	0.62	-	0.09	12.19	4.27	0.22	-	-	0.00	-	-	-	101.02	60.37	38.31		0	0	0	0	0

23	150319-02-a1-pl3		56.17	0.01	28.18	0.52	-	0.08	10.77	4.92	0.28	-	-	0.00	-	-	-	100.93		53.84	44.51				0	0	0	0	0
24	150319-02-a1-pl4-i		46.78	0.00	34.79	0.38	-	0.09	18.33	1.04	0.01	-	-	0.00	-	-	-	101.43		90.61	9.31				0	0	0	0	0
25	150319-02-a1-pl4-r		54.04	0.00	29.52	0.50	-	0.08	12.42	4.19	0.21	-	-	0.00	-	-	-	100.96		61.34	37.43				0	0	0	0	0
26	150319-02-a1-pl5-mic		56.09	0.01	27.98	0.52	-	0.09	10.93	4.80	0.27	-	-	0.00	-	-	-	100.68		54.80	43.60				0	0	0	0	0
27	150319-02-a1-pl6-mic		50.47	0.00	31.83	0.49	-	0.08	15.10	2.89	0.10	-	-	0.00	-	-	-	100.97		73.80	25.60				0	0	0	0	0
28	150319-02-a1-pl7-mic		56.40	0.01	27.71	0.57	-	0.11	10.55	4.93	0.27	-	-	0.00	-	-	-	100.55		53.27	45.10				0	0	0	0	0
29	150319-02-a1-pl8-mic		55.08	0.01	28.52	0.72	-	0.09	11.52	4.56	0.27	-	-	0.00	-	-	-	100.75		57.33	41.07				0	0	0	0	0
30	150319-02-a1-pl9-mic		49.84	0.00	32.04	0.53	-	0.08	15.17	2.82	0.10	-	-	0.00	-	-	-	100.57		74.39	25.03				0	0	0	0	0
5	150319-02-a2-cpx1		51.62	0.56	0.70	11.67	0.28	16.27	18.92	0.12	0.01	-	0.09	-	-	-	-	100.24	71.32			37.35	44.68	17.97	0	588	0	0	0
6	150319-02-a2-cpx2		51.71	0.64	0.54	13.22	0.36	15.57	19.27	0.08	0.00	-	0.01	-	-	-	-	101.40	67.74			37.60	42.27	20.13	0	82	0	0	0
7	150319-02-a2-cpx3		51.71	0.58	0.65	13.53	0.35	15.80	18.44	0.17	0.01	-	0.00	-	-	-	-	101.24	67.55			36.17	43.12	20.72	0	0	0	0	0
45	150319-02-A2-MI-PX3		52.12	0.26	3.52	5.67	0.24	16.90	20.46	0.03	-	-	0.81	-	0.03	-	-	100.04	84.17			42.27	48.59	9.14	0	5569	212	0	0
43	150319-02-A2-MI-PX4		48.20	0.45	3.04	7.66	0.24	15.40	17.06	0.07	-	-	0.15	-	0.02	-	-	92.29	78.20			38.37	48.19	13.44	0	1013	181	0	0
44	150319-02-A2-MI-PX4b		50.26	0.44	4.36	6.98	0.16	15.89	19.37	0.06	-	-	0.42	-	0.00	-	-	97.93	80.23			41.29	47.11	11.61	0	2894	0	0	0
8	150319-02-a1-cpx1-c		53.53	0.30	0.44	19.78	0.42	25.57	1.80	0.00	0.01	-	0.14	-	-	-	-	102.00	69.74			3.40	67.37	29.23	0	972	0	0	0
9	150319-02-a1-cpx1-i		51.60	0.39	0.91	8.02	0.22	17.43	20.65	0.13	0.00	-	0.37	-	-	-	-	99.71	79.49			40.37	47.40	12.23	0	2511	0	0	0
10	150319-02-a1-cpx1-r		52.18	0.50	0.67	12.44	0.30	15.96	18.60	0.12	0.00	-	0.08	-	-	-	-	100.84	69.57			36.82	43.95	19.22	0	547	0	0	0
11	150319-02-b2-cpx1		51.45	0.61	0.53	12.62	0.35	16.10	18.60	0.13	0.00	-	0.12	-	-	-	-	100.51	69.46			36.57	44.06	19.37	0	801	0	0	0
12	150319-02-b2-cpx2	pyroxene	52.66	0.30	1.01	8.59	0.21	18.55	17.57	0.12	0.01	-	0.19	-	-	-	-	99.20	79.37			35.08	51.53	13.39	0	1273	0	0	0
13	150319-02-b2-cpx3		50.05	0.53	1.25	9.14	0.29	17.29	18.15	0.13	0.01	-	0.37	-	-	-	-	97.21	77.12			36.79	48.75	14.46	0	2545	0	0	0
3	150319-02-b2-mi-px1		52.46	0.28	1.16	22.41	0.52	22.26	1.98	-	-	-	0.02	-	-	-	-	101.08	63.91			3.92	61.40	34.67	0	130	0	0	0
14	150319-02-d-cpx1-c		51.27	0.51	0.59	11.71	0.33	16.14	18.29	0.08	0.00	-	0.06	-	-	-	-	98.96	71.07			36.66	45.02	18.33	0	376	0	0	0
15	150319-02-d-cpx1-r		50.84	0.68	0.55	14.25	0.39	14.57	18.27	0.14	0.00	-	0.04	-	-	-	-	99.73	64.58			36.78	40.83	22.40	0	253	0	0	0
16	150319-02-d-cpx2-c		51.50	0.44	1.03	9.54	0.20	16.80	20.23	0.12	0.00	-	0.17	-	-	-	-	100.01	75.85			39.62	45.79	14.58	0	1149	0	0	0
17	150319-02-d-cpx2-r		52.10	0.28	0.79	7.16	0.24	18.21	20.41	0.08	0.00	-	0.24	-	-	-	-	99.51	81.94			39.76	49.37	10.88	0	1622	0	0	0
3	150319-02-d-opx1		53.81	0.05	3.49	12.82	0.16	27.88	2.13	-	-	-	0.05	-	-	-	-	100.39	79.50			4.17	76.18	19.64	0	363	0	0	0
4	150319-02-d-opx2		53.15	0.14	1.39	20.23	0.21	23.74	2.12	-	-	-	0.00	-	-	-	-	100.97	67.66			4.15	64.85	30.99	0	27	0	0	0
5	150319-02-d-opx3		52.83	0.10	1.95	20.75	0.21	22.86	2.19	-	-	-	0.04	-	-	-	-	100.93	66.26			4.36	63.37	32.26	0	253	0	0	0
6	150319-02-d-opx4		52.63	0.12	1.94	20.54	0.22	22.65	2.36	-	-	-	0.05	-	-	-	-	100.50	66.28			4.72	63.15	32.13	0	356	0	0	0
7	150319-02-b2-opx1		52.99	0.10	1.20	21.39	0.24	22.56	2.47	-	-	-	0.02	-	-	-	-	100.97	65.28			4.88	62.09	33.02	0	130	0	0	0

8	150319-02-b2-opx2-c		51.77	0.11	1.41	24.51	0.32	19.93	2.36	-	-	-	0.00	-	-	-	-	100.41	59.18		4.80	56.34	38.86	0	21	0	0	0
9	150319-02-b2-opx2-r		53.89	0.09	1.05	18.06	0.22	24.83	2.24	-	-	-	0.01	-	-	-	-	100.40	71.03		4.40	67.90	27.70	0	96	0	0	0
10	150319-02-a2-opx1		53.00	0.12	1.23	21.62	0.16	22.41	2.40	-	-	-	0.01	-	-	-	-	100.94	64.89		4.76	61.80	33.43	0	34	0	0	0
11	150319-02-a2-opx2		52.12	0.15	1.66	22.62	0.22	21.37	2.45	-	-	-	0.00	-	-	-	-	100.59	62.75		4.91	59.67	35.42	0	0	0	0	0
46	150319-02-A2-MI-PX2		52.15	0.18	1.02	24.03	0.58	21.16	1.61	0.02	-	-	0.04	-	0.02	-	-	100.81	61.09		3.23	59.12	37.65	0	294	157	0	0
12	150319-02-a1-opx1		52.32	0.12	1.68	22.92	0.28	21.79	2.04	-	-	-	0.00	-	-	-	-	101.16	62.89		4.06	60.34	35.61	0	0	0	0	0
13	150319-02-a1-opx2		52.12	0.11	2.10	21.95	0.23	22.24	2.30	-	-	-	0.03	-	-	-	-	101.08	64.36		4.56	61.43	34.02	0	205	0	0	0
14	150319-02-a1-opx3		52.37	0.10	1.74	23.59	0.26	21.37	2.01	-	-	-	0.00	-	-	-	-	101.44	61.77		4.01	59.29	36.70	0	0	0	0	0
32	150319-02-A1-MI-PX1a		51.93	0.21	1.35	16.33	0.40	24.26	1.68	0.01	-	-	0.04	-	0.00	-	-	96.21	72.58		3.49	70.05	26.46	0	246	0	0	0
33	150319-02-A1-MI-PX1b		52.11	0.09	0.92	15.50	0.31	24.67	1.60	0.01	-	-	0.03	-	0.00	-	-	95.24	73.94		3.33	71.48	25.19	0	219	0	0	0
30	150319-02-A1-MI-PX2		53.66	0.20	0.80	19.37	0.42	24.12	1.90	0.00	-	-	0.05	-	0.00	-	-	100.53	68.94		3.75	66.36	29.89	0	308	0	0	0
31	150319-02-A1-MI-PX4		52.37	0.19	0.78	17.75	0.31	23.85	1.79	0.00	-	-	0.04	-	0.00	-	-	97.07	70.54		3.66	67.96	28.38	0	281	0	0	0
3	150319-02-a1-ox1		0.10	14.34	2.56	74.99	0.18	1.92	-	-	-	-	0.15	-	-	-	-	94.25						0	1040	0	0	0
4	150319-02-a1-ox2		0.10	14.31	2.55	75.61	0.16	1.91	-	-	-	-	0.12	-	-	-	-	94.77						0	842	0	0	0
5	150319-02-a1-ox3		0.12	13.97	2.56	75.02	0.18	1.99	-	-	-	-	0.14	-	-	-	-	93.98						0	972	0	0	0
6	150319-02-a1-ox4		0.11	10.93	3.05	75.85	0.17	1.64	-	-	-	-	0.18	-	-	-	-	91.93						0	1259	0	0	0
7	150319-02-a1-ox5		0.12	11.60	2.88	76.86	0.17	1.62	-	-	-	-	0.11	-	-	-	-	93.36						0	746	0	0	0
8	150319-02-a1-ox6		0.10	12.27	2.71	78.04	0.12	1.53	-	-	-	-	0.18	-	-	-	-	94.96						0	1211	0	0	0
9	150319-02-a1-ox7		0.10	16.20	2.47	71.51	0.16	2.01	-	-	-	-	0.13	-	-	-	-	92.57						0	917	0	0	0
10	150319-02-a1-ox8		0.07	14.88	2.52	75.26	0.17	2.02	-	-	-	-	0.08	-	-	-	-	95.00						0	520	0	0	0
11	150319-02-a1-ox9	opaque	0.09	14.91	2.52	74.80	0.17	1.91	-	-	-	-	0.07	-	-	-	-	94.46						0	479	0	0	0
12	150319-02-a2-ox1		0.07	14.82	2.67	74.07	0.23	2.32	-	-	-	-	0.14	-	-	-	-	94.33						0	978	0	0	0
13	150319-02-a2-ox2		0.16	13.69	3.01	73.02	0.17	2.71	-	-	-	-	0.21	-	-	-	-	92.96						0	1457	0	0	0
14	150319-02-a2-ox3		0.07	9.79	3.90	75.72	0.14	3.11	-	-	-	-	0.15	-	-	-	-	92.88						0	1040	0	0	0
15	150319-02-a2-ox4		0.08	14.02	2.81	74.98	0.19	2.42	-	-	-	-	0.13	-	-	-	-	94.63						0	869	0	0	0
16	150319-02-b2-ox1		0.08	10.77	3.48	74.47	0.10	3.23	-	-	-	-	0.09	-	-	-	-	92.23						0	595	0	0	0
17	150319-02-b2-ox2		0.08	13.61	2.89	72.69	0.18	2.34	-	-	-	-	0.16	-	-	-	-	91.94						0	1061	0	0	0
18	150319-02-b2-ox3		0.10	14.55	2.61	74.16	0.15	2.36	-	-	-	-	0.08	-	-	-	-	94.00						0	527	0	0	0
19	150319-02-b2-ox4		0.10	9.21	4.15	74.95	0.16	3.27	-	-	-	-	0.33	-	-	-	-	92.16						0	2231	0	0	0
20	150319-02-b2-ox5		0.13	14.39	2.70	70.04	0.18	2.36	-	-	-	-	0.10	-	-	-	-	89.90						0	671	0	0	0

21	150319-02-d-ox1		0.07	11.17	4.38	68.86	0.15	2.96	-	-	-	-	5.92	-	-	-	-	93.51								0	40505	0	0	0
22	150319-02-d-ox2		0.17	10.42	4.91	68.35	0.15	3.05	-	-	-	-	6.24	-	-	-	-	93.28								0	42667	0	0	0
23	150319-02-d-ox3		0.14	13.74	3.18	73.62	0.14	2.41	-	-	-	-	0.18	-	-	-	-	93.40								0	1218	0	0	0
36	150319-02-A1-MI-OL1		38.71	0.00	0.01	18.51	0.32	40.87	0.03	0.00	-	-	0.05	-	0.07	-	-	98.56	79.74							0	369	519	0	0
35	150319-02-A1-MI-OL2		38.67	0.00	0.05	18.01	0.23	41.41	0.05	0.01	-	-	0.03	-	0.12	-	-	98.57	80.39							0	233	927	0	0
34	150319-02-A1-MI-OL3		37.60	0.00	0.00	16.55	0.00	41.23	0.03	0.00	-	-	0.02	-	0.00	-	-	95.43	81.62							0	116	0	0	0
29	150319-02-A1-MI-OL7		38.82	0.00	0.01	18.31	0.25	41.14	0.03	0.01	-	-	0.00	-	0.05	-	-	98.61	80.02							0	0	393	0	0
3	150319-02-a2-mi-ol1		38.71	0.01	-	20.36	0.29	40.80	0.14	-	-	-	-	-	0.03	-	-	100.33	78.13							0	0	251	0	0
14	150319-02-a2-mi-h-ol1		36.12	-	-	26.40	0.21	33.62	0.15	-	-	-	0.02	-	0.08	-	-	96.59	69.42							0	103	652	0	0
15	150319-02-a2-mi-h-ol2		37.92	-	-	19.59	0.17	40.13	0.13	-	-	-	0.01	-	0.09	-	-	98.03	78.51							0	75	715	0	0
16	150319-02-a2-mi-h-ol3	olivine	38.36	-	-	19.67	0.20	39.25	0.13	-	-	-	0.01	-	0.04	-	-	97.66	78.06							0	34	346	0	0
17	150319-02-a2-mi-h-ol4		37.52	-	-	20.15	0.19	38.86	0.15	-	-	-	0.02	-	0.10	-	-	97.00	77.47							0	123	802	0	0
4	150319-02-b2-mi-ol1		38.31	0.02	-	21.45	0.32	41.33	0.13	-	-	-	-	-	0.03	-	-	101.58	77.46							0	0	267	0	0
5	150319-02-b2-mi-ol2		37.96	0.00	-	20.54	0.30	41.52	0.12	-	-	-	-	-	0.08	-	-	100.53	78.28							0	0	644	0	0
6	150319-02-b2-mi-ol4		36.82	0.00	-	30.48	0.45	33.14	0.15	-	-	-	-	-	0.06	-	-	101.10	65.97							0	0	495	0	0
42	150319-02-B2-MI-OL3		37.84	0.00	0.00	19.10	0.29	40.20	0.04	0.01	-	-	0.01	-	0.04	-	-	97.52	78.96							0	41	322	0	0
3	150319-02-d-ol1		37.99	-	-	25.47	0.37	37.35	0.13	-	-	-	0.00	-	0.07	-	-	101.39	72.33							0	27	581	0	0
4	150319-02-d-ol2		37.74	-	-	24.12	0.36	38.44	0.12	-	-	-	0.02	-	0.10	-	-	100.90	73.97							0	123	809	0	0
5	150319-02-d-ol3		37.57	-	-	24.46	0.37	37.56	0.12	-	-	-	0.00	-	0.08	-	-	100.16	73.25							0	0	637	0	0
6	150319-02-d-opx4	px	52.23	-	-	21.32	0.53	22.42	1.98	-	-	-	0.02	-	0.00	-	-	98.51	65.21			3.98	62.62	33.40	0	116	0	0	0
7	150319-02-d-opx5		52.27	-	-	21.07	0.49	22.96	1.81	-	-	-	0.04	-	0.00	-	-	98.63	66.03			3.61	63.64	32.75	0	274	0	0	0
5	150319-02-a1-gm1		65.99	0.92	13.00	6.67	0.10	1.08	3.36	2.36	3.09	-	0.03	-	-	0.12	-	96.70	22.33	29.70	37.82	33.41	14.87	51.72	0	178	0	1220	0
6	150319-02-a1-gm2		64.46	0.85	12.82	6.98	0.14	1.04	3.29	2.53	3.13	-	0.01	-	-	0.16	-	95.40	20.96	28.38	39.51	32.30	14.19	53.51	0	55	0	1620	0
7	150319-02-a1-gm3		65.55	0.86	12.79	6.78	0.11	0.29	3.49	0.68	3.10	-	0.00	-	-	0.16	-	93.80	6.97	41.51	14.54	38.01	4.32	57.66	0	0	0	1590	0
8	150319-02-a1-gm4		64.47	0.84	12.80	6.98	0.09	1.13	3.46	2.45	3.04	-	0.00	-	-	0.14	-	95.39	22.35	30.06	38.48	33.05	14.96	51.99	0	0	0	1390	0
9	150319-02-a1-gm5		64.62	0.83	12.76	6.93	0.11	1.04	3.31	2.36	3.04	-	0.00	-	-	0.14	-	95.15	21.14	29.57	38.07	32.56	14.26	53.18	0	0	0	1400	0
10	150319-02-a1-gm6	groundmass	65.50	0.79	12.91	6.76	0.10	1.05	3.51	2.55	3.20	-	0.04	-	-	0.17	-	96.57	21.65	29.41	38.63	34.23	14.24	51.53	0	287	0	1730	0
11	150319-02-a1-gm7		65.82	0.80	12.80	6.89	0.10	1.06	3.41	2.65	3.17	-	0.01	-	-	0.17	-	96.88	21.47	28.46	40.03	33.25	14.33	52.42	0	41	0	1670	0
12	150319-02-a1-gm8		65.94	0.85	13.04	6.68	0.11	1.06	3.36	2.56	3.12	-	0.00	-	-	0.16	-	96.87	22.11	28.68	39.60	33.42	14.72	51.86	0	0	0	1580	0
13	150319-02-a1-gm9		65.96	0.88	12.71	6.60	0.13	1.08	3.36	2.70	3.11	-	0.00	-	-	0.16	-	96.69	22.55	28.10	40.88	33.58	14.98	51.45	0	0	0	1580	0

14	150319-02-a1-gm10		66.26	0.84	13.00	6.40	0.13	0.96	3.16	2.52	3.15	-	0.00	-	-	0.11	-	96.54	21.07	27.55	39.77	33.29	14.06	52.65	0	0	0	1110	0
86	150319-02-a1-mi-px1-1a		56.99	0.84	15.38	5.99	0.13	2.15	5.48	3.27	1.45	0.11	0.00	-	-	0.11	0.19	92.09	39.05	41.82	45.05	41.70	22.77	35.54	0	0	0	1090	760
87	150319-02-a1-mi-px1-1b		57.80	0.88	15.38	6.30	0.15	2.18	5.64	3.39	1.66	0.07	0.00	-	-	0.13	0.18	93.75	38.18	41.01	44.61	41.51	22.34	36.16	0	0	0	1320	716
83	150319-02-a1-mi-px1-2		57.53	0.86	14.74	5.96	0.12	1.24	4.84	3.35	1.79	0.14	0.00	-	-	0.13	0.12	90.82	26.99	37.12	46.52	43.19	15.33	41.48	0	0	0	1260	460
84	150319-02-a1-mi-px1-3a		61.36	0.97	12.47	5.05	0.00	0.91	3.42	3.47	2.55	0.11	0.00	-	-	0.21	0.10	90.62	24.31	26.84	49.33	39.62	14.68	45.70	0	7	0	2090	384
85	150319-02-a1-mi-px1-3b		48.56	0.02	28.33	0.94	0.06	0.07	11.60	3.36	0.18	0.00	0.05	-	-	0.01	0.01	93.19	11.91	64.82	34.01	93.33	0.80	5.88	0	363	0	100	56
77	150319-02-a1-mi-px2-1		64.96	1.05	15.26	5.70	0.09	0.93	5.05	3.44	2.60	0.31	0.00	-	-	0.22	0.09	99.71	22.48	35.14	43.34	46.78	11.97	41.25	0	0	0	2230	372
78	150319-02-a1-mi-px2-2		64.00	0.81	15.28	5.70	0.06	1.17	4.89	3.81	1.99	0.10	0.00	-	-	0.17	0.12	98.10	26.76	34.56	48.73	44.61	14.83	40.57	0	0	0	1650	484
79	150319-02-a1-mi-px2-3	melt inclusion	60.96	0.85	12.79	8.27	0.19	5.22	3.40	3.35	2.59	0.10	0.00	-	-	0.22	0.05	97.98	52.94	27.08	48.32	19.85	42.44	37.72	0	0	0	2170	200
80	150319-02-a1-mi-px4-1a		64.59	1.02	13.60	6.18	0.05	1.02	4.03	3.50	2.88	0.28	0.01	-	-	0.22	0.10	97.47	22.66	29.19	45.96	39.21	13.77	47.01	0	48	0	2190	388
81	150319-02-a1-mi-px4-1b		52.04	0.05	29.76	1.03	0.00	0.07	12.68	3.65	0.21	0.00	0.00	-	-	0.01	0.00	99.49	10.63	64.92	33.80	93.35	0.71	5.94	0	0	0	50	0
82	150319-02-a1-mi-px4-2		61.96	0.84	15.47	5.63	0.03	0.94	4.33	3.76	2.06	0.18	0.03	-	-	0.17	0.18	95.56	22.95	31.90	50.06	43.16	13.05	43.80	0	171	0	1710	712
75	150319-02-a1-mi-ol3-1		49.43	0.86	18.65	5.41	0.07	1.60	10.62	3.20	0.56	0.00	0.00	-	-	0.17	0.13	90.70	34.54	62.22	33.88	62.20	13.06	24.74	0	0	0	1700	528
76	150319-02-a1-mi-ol3-1b		41.83	0.39	10.17	12.10	0.20	22.38	4.15	1.32	0.26	0.00	0.04	-	-	0.08	0.07	92.98	76.73	60.56	34.90	9.27	69.61	21.11	0	260	0	800	268
74	150319-02-a1-mi-ol5-1		58.00	0.52	19.45	6.76	0.12	1.67	6.08	5.04	1.15	0.12	0.02	-	-	0.30	0.09	99.32	30.63	36.68	55.03	44.41	17.03	38.57	0	151	0	2950	348
71	150319-02-a1-mi-ol7-1b1		52.68	0.90	20.39	6.30	0.10	3.26	11.55	2.96	0.68	0.00	0.02	-	-	0.16	0.13	99.14	47.98	65.20	30.25	54.99	21.59	23.41	0	103	0	1620	524
72	150319-02-a1-mi-ol7-1b2		53.14	0.88	20.75	6.44	0.16	3.19	11.62	3.24	0.63	0.04	0.00	-	-	0.18	0.15	100.40	46.85	63.79	32.13	55.13	21.02	23.85	0	0	0	1800	588
73	150319-02-a1-mi-ol7-1b3		53.08	0.96	20.75	6.25	0.03	3.34	11.65	2.89	0.62	0.05	0.00	-	-	0.17	0.14	99.93	48.82	66.09	29.71	55.00	21.97	23.03	0	0	0	1710	568
15	150319-02-a2-gm1		64.36	1.16	14.13	6.67	0.11	1.45	4.63	2.62	2.15	-	0.00	-	-	0.08	-	97.35	27.98	38.83	39.71	39.05	17.05	43.90	0	0	0	780	0
16	150319-02-a2-gm2		63.48	1.19	13.02	7.69	0.12	1.45	3.82	2.33	3.03	-	0.02	-	-	0.09	-	96.23	25.15	32.82	36.25	32.30	17.02	50.68	0	109	0	930	0
17	150319-02-a2-gm3		66.78	1.05	13.39	6.29	0.17	1.21	3.47	2.34	3.20	-	0.00	-	-	0.07	-	97.96	25.57	30.13	36.76	34.44	16.77	48.80	0	0	0	730	0
18	150319-02-a2-gm4		60.16	1.19	14.51	8.66	0.15	2.33	5.71	2.57	1.67	-	0.03	-	-	0.10	-	97.08	32.40	46.27	37.60	36.36	20.62	43.03	0	233	0	950	0
19	150319-02-a2-gm5	groundmass	58.12	1.03	15.55	8.01	0.17	3.08	6.66	2.57	1.50	-	0.00	-	-	0.06	-	96.73	40.70	50.86	35.49	38.72	24.94	36.34	0	0	0	620	0
20	150319-02-a2-gm6		61.08	1.16	14.85	8.48	0.16	2.25	5.66	2.55	1.86	-	0.01	-	-	0.10	-	98.15	32.11	45.32	36.96	36.76	20.31	42.94	0	41	0	990	0
21	150319-02-a2-gm7		61.58	1.16	15.28	7.61	0.14	1.95	5.64	2.55	1.85	-	0.00	-	-	0.08	-	97.83	31.36	45.29	37.05	39.45	18.99	41.56	0	21	0	830	0
22	150319-02-a2-gm8		59.89	1.29	14.89	7.86	0.09	1.60	5.35	2.72	2.11	-	0.00	-	-	0.12	-	95.91	26.63	41.88	38.49	39.02	16.24	44.74	0	0	0	1160	0
23	150319-02-a2-gm9		59.47	1.00	16.67	7.17	0.15	1.16	6.08	2.93	1.60	-	0.00	-	-	0.07	-	96.31	22.38	45.73	39.92	45.76	12.14	42.10	0	0	0	730	0
24	150319-02-a2-gm10		62.08	1.17	14.10	8.50	0.15	1.90	4.95	2.70	1.73	-	0.00	-	-	0.07	-	97.34	28.54	41.63	41.06	34.77	18.62	46.61	0	0	0	700	0
25	150319-02-a2-gm11		61.55	1.22	13.62	8.48	0.16	1.96	4.11	2.26	3.02	-	0.00	-	-	0.10	-	96.47	29.17	34.81	34.66	30.52	20.27	49.21	0	0	0	980	0

10 5	150319-02-a2-mi-px3-1a		61.63	0.69	17.40	4.82	0.03	1.36	4.29	3.88	2.63	0.38	0.00	-	-	0.22	0.08	97.40	33.52	29.69	48.64	43.12	19.07	37.81	0	0	0	2170	316
10 6	150319-02-a2-mi-px3-1b		61.67	0.73	17.53	5.24	0.06	1.91	4.59	3.01	2.13	0.41	0.01	-	-	0.20	0.08	97.57	39.38	36.54	43.31	40.47	23.45	36.09	0	82	0	1990	332
10 7	150319-02-a2-mi-px3-2		57.77	0.34	18.66	4.21	0.09	2.73	6.67	3.99	2.36	0.15	0.06	-	-	0.25	0.07	97.34	53.67	39.95	43.21	48.49	27.65	23.87	0	411	0	2450	284
10 8	150319-02-a2-mi-px3-3		50.25	0.09	25.84	2.55	0.09	2.07	15.46	2.33	0.12	0.00	0.09	-	-	0.01	0.01	98.93	59.04	77.96	21.30	76.06	14.14	9.81	0	629	0	120	44
10 2	150319-02-a2-mi-px4-1		57.75	0.78	16.48	7.76	0.08	0.81	4.32	3.11	1.30	0.07	0.02	-	-	0.14	0.39	93.01	15.67	37.60	48.90	37.55	9.79	52.67	0	130	0	1400	1572
10 3	150319-02-a2-mi-px4-2		64.85	1.22	13.61	5.06	0.05	0.81	3.03	3.07	2.77	0.21	0.00	-	-	0.23	0.08	94.99	22.18	25.48	46.77	37.36	13.89	48.75	0	0	0	2330	324
10 4	150319-02-a2-mi-px4-3		58.74	0.66	17.82	3.70	0.03	0.89	4.83	3.35	1.12	0.08	0.01	-	-	0.18	0.36	91.78	29.90	39.53	49.56	53.95	13.77	32.28	0	89	0	1780	1452
13	150319-02-a2-mi-ol1-1		50.27	0.93	19.48	5.47	0.12	1.63	10.60	2.82	0.59	-	0.00	-	-	0.15	0.33	92.39	34.74	64.59	31.13	61.85	13.25	24.90	0	0	0	1520	1308
14	150319-02-a2-mi-ol1-1		50.02	0.92	19.64	5.71	0.07	1.87	10.77	2.81	0.62	-	0.02	-	-	0.15	0.25	92.83	36.81	64.95	30.61	60.42	14.57	25.01	0	103	0	1540	988
15	150319-02-a2-mi-ol1-1		50.06	0.90	19.83	5.35	0.09	1.69	11.40	3.01	0.64	-	0.01	-	-	0.13	0.33	93.45	36.02	64.75	30.92	63.62	13.10	23.28	0	62	0	1320	1308
Average	150319-02-a2-mi-h-ol2-1		47.83	0.78	16.97	8.35	0.14	7.83	9.97	2.56	0.44	-	0.01	-	-	0.14	0.28	95.30	62.57	65.90	30.61	36.42	39.78	23.80	0	48	0	1415	1130
23	150319-02-a2-mi-h-ol2-2		46.83	0.66	15.64	9.16	0.18	11.88	8.50	2.64	0.44	-	0.06	-	-	0.13	0.26	96.39	69.80	61.56	34.64	26.41	51.37	22.22	0	397	0	1310	1036
Average	150319-02-a2-mi-h-ol3-1		49.68	0.80	16.18	9.69	0.16	6.64	8.95	2.36	0.62	-	0.01	-	-	0.13	0.39	95.62	55.00	64.10	30.59	34.73	35.90	29.37	0	92	0	1335	1560
26	150319-02-a2-mi-h-ol3-2		46.77	0.58	12.52	12.13	0.13	15.54	6.43	1.57	0.51	-	0.00	-	-	0.10	0.29	96.57	69.55	65.12	28.79	17.13	57.63	25.24	0	21	0	1020	1172
27	150319-02-a2-mi-h-ol4-1a	melt inclusion	49.07	0.80	17.02	8.13	0.13	6.87	10.09	2.67	0.55	-	0.03	-	-	0.15	0.16	95.68	60.09	64.75	31.02	38.82	36.76	24.42		212		1450	648
28	150319-02-a2-mi-h-ol4-1b		46.56	0.77	16.43	7.74	0.07	6.61	9.50	2.47	0.48	-	0.02	-	-	0.40	0.20	91.23	60.37	65.32	30.78	38.41	37.18	24.41		109		3980	788
29	150319-02-a2-mi-h-ol4-2		48.10	0.83	17.75	9.14	0.14	6.27	9.92	2.79	0.48	-	0.03	-	-	0.16	0.23	95.83	55.00	63.86	32.46	38.47	33.84	27.69	0	185	0	1600	924
26	150319-02-b2-gm1		60.20	1.19	14.25	8.19	0.17	1.90	5.08	2.69	1.97	-	0.02	-	-	0.10	-	95.74	29.24	41.31	39.60	35.96	18.73	45.31	0	109	0	950	0
28	150319-02-b2-gm3		62.79	1.16	13.42	7.87	0.12	1.68	4.48	2.08	3.26	-	0.01	-	-	0.10	-	96.98	27.55	36.94	31.06	34.57	18.02	47.40	0	68	0	980	0
29	150319-02-b2-gm4		59.17	1.17	14.20	9.15	0.14	2.77	5.64	2.44	1.91	-	0.07	-	-	0.09	-	96.74	35.03	45.74	35.80	33.91	23.15	42.94	0	458	0	850	0
30	150319-02-b2-gm5		60.76	1.25	14.54	9.01	0.15	2.34	5.44	2.33	1.93	-	0.01	-	-	0.10	-	97.85	31.66	45.49	35.26	34.59	20.71	44.70	0	62	0	1020	0
31	150319-02-b2-gm6	groundmass	62.56	1.20	13.82	7.82	0.13	1.64	4.79	2.76	1.91	-	0.00	-	-	0.09	-	96.71	27.23	39.76	41.40	36.37	17.33	46.30	0	0	0	890	0
33	150319-02-b2-gm8		63.14	1.14	14.32	6.90	0.11	1.14	4.16	2.65	2.33	-	0.00	-	-	0.07	-	95.96	22.70	35.47	40.86	37.41	14.21	48.38	0	21	0	720	0
34	150319-02-b2-gm9		59.67	1.22	14.69	8.15	0.16	1.51	5.31	2.51	1.98	-	0.00	-	-	0.10	-	95.28	24.77	43.47	37.24	38.56	15.22	46.22	0	21	0	950	0
35	150319-02-b2-gm10		60.31	1.06	15.40	7.42	0.14	2.24	5.96	2.44	1.97	-	0.00	-	-	0.08	-	97.02	34.96	46.83	34.70	40.11	20.94	38.95	0	0	0	750	0
5	150319-02-b2-mi-px1-1		65.58	0.87	14.16	5.91	0.14	0.91	3.87	3.82	3.02	-	0.00	-	-	0.23	0.06	98.51	21.51	26.93	48.08	39.70	12.97	47.33	0	27	0	2300	244
6	150319-02-b2-mi-px1-1		65.13	0.86	14.21	5.95	0.08	1.01	4.06	2.87	2.91	-	0.00	-	-	0.24	0.09	97.34	23.25	31.95	40.82	40.15	13.91	45.94	0	21	0	2400	364
7	150319-02-b2-mi-px1-2		61.76	0.79	12.75	9.45	0.20	4.72	3.95	3.00	2.24	-	0.00	-	-	0.20	0.11	99.13	47.08	32.81	45.02	22.08	36.69	41.23	0	7	0	2020	444
8	150319-02-b2-mi-px1-2		64.40	1.22	15.01	5.94	0.14	0.72	4.82	2.75	2.66	-	0.03	-	-	0.25	0.14	98.03	17.83	37.19	38.37	46.06	9.62	44.32	0	192	0	2530	552

10	150319-02-b2-mi-ol2-1		60.01	0.84	18.00	4.82	0.04	2.06	7.18	3.71	1.40	-	0.00	-	-	0.32	0.07	98.36	43.19	46.16	43.13	52.00	20.73	27.27	0	0	0	3200	280
99	150319-02-b2-mi-ol3-1a		51.32	0.81	19.14	7.20	0.08	3.13	10.05	2.63	0.65	0.00	0.01	-	-	0.15	0.51	95.67	43.65	64.50	30.56	50.19	21.74	28.07	0	41	0	1460	2028
100	150319-02-b2-mi-ol3-1b		52.05	0.88	19.22	7.30	0.14	1.57	10.69	2.58	0.63	0.01	0.00	-	-	0.16	0.50	95.71	27.75	66.38	29.00	57.56	11.78	30.66	0	7	0	1550	1980
101	150319-02-b2-mi-ol3-3		53.74	0.94	18.79	6.83	0.08	1.13	9.42	3.36	1.01	0.04	0.00	-	-	0.16	0.48	95.99	22.79	56.37	36.43	57.70	9.64	32.66	0	0	0	1620	1916
36	150319-02-d-gm1		61.30	1.32	13.69	8.66	0.16	1.46	5.05	2.65	2.59	-	0.01	-	-	0.08	-	96.97	23.15	39.00	37.13	36.45	14.71	48.84	0	82	0	790	0
37	150319-02-d-gm2		60.12	1.49	12.66	10.76	0.20	2.25	5.72	2.13	2.33	-	0.00	-	-	0.08	-	97.73	27.14	46.32	31.22	33.15	18.14	48.70	0	0	0	780	0
38	150319-02-d-gm3		60.92	1.53	12.31	10.98	0.17	2.16	5.17	2.29	2.28	-	0.01	-	-	0.08	-	97.91	25.96	42.97	34.45	30.88	17.94	51.17	0	89	0	830	0
39	150319-02-d-gm4		60.81	1.69	12.63	8.75	0.15	1.25	4.55	2.32	2.56	-	0.00	-	-	0.13	-	94.85	20.33	38.57	35.56	34.67	13.28	52.05	0	0	0	1320	0
40	150319-02-d-gm5	groundmass	63.14	1.50	13.40	8.35	0.14	1.38	5.16	2.51	2.53	-	0.01	-	-	0.10	-	98.21	22.70	40.59	35.72	37.96	14.08	47.96	0	82	0	960	0
41	150319-02-d-gm6		62.18	1.54	13.11	8.97	0.15	1.88	5.23	2.34	2.28	-	0.00	-	-	0.09	-	97.76	27.20	42.96	34.79	35.23	17.62	47.15	0	0	0	910	0
42	150319-02-d-gm7		59.27	1.09	17.50	6.82	0.13	1.29	6.51	2.80	1.72	-	0.00	-	-	0.07	-	97.18	25.24	47.81	37.16	47.77	13.18	39.04	0	0	0	730	0
43	150319-02-d-gm8		61.21	1.14	16.61	6.47	0.11	1.05	6.04	2.69	2.00	-	0.00	-	-	0.08	-	97.40	22.41	45.46	36.64	48.14	11.62	40.24	0	14	0	750	0
44	150319-02-d-gm9		61.46	1.42	12.82	9.67	0.17	1.94	5.30	2.19	2.36	-	0.00	-	-	0.09	-	97.42	26.36	43.89	32.80	34.07	17.38	48.55	0	0	0	910	0
45	150319-02-d-gm10		62.88	1.40	14.12	9.16	0.13	1.40	4.92	2.32	2.33	-	0.00	-	-	0.08	-	98.75	21.46	41.32	35.34	35.08	13.93	50.99	0	21	0	800	0
	150321-02 (Te Rato)																											
3	150321-02-c-pl1-mic (in host)		51.58	0.00	30.75	0.76	-	0.19	14.19	3.34	0.11	-	-	0.00	-	-	-	100.92		69.68	29.67				0	0	0	0	0
4	150321-02-c-pl2-mic (in host)	pl	52.87	0.01	29.57	0.80	-	0.20	12.85	3.80	0.15	-	-	0.02	-	-	-	100.27		64.59	34.53				186	0	0	0	0
5	150321-02-c-pl3-mic (in host)		53.51	0.00	28.95	0.82	-	0.35	12.69	3.78	0.17	-	-	0.00	-	-	-	100.27		64.28	34.69				0	0	0	0	0
3	150321-02-c-opx1	px	50.57	-	-	28.96	0.93	17.72	0.39	-	-	-	0.00	-	0.00	-	-	98.56	52.17			0.82	51.74	47.44	0	0	0	0	0
24	150321-02-c-opx1		51.67	0.09	0.26	30.24	1.06	18.16	0.38	0.00	0.00	-	0.00	-	-	-	-	101.87	51.71			0.78	51.31	47.91	0	0	0	0	0
22	150321-02-c-hbl1		43.85	1.59	12.38	14.83	0.47	13.28	10.86	0.85	0.40	-	0.00	-	-	-	-	98.51	61.48						0	0	0	0	0
23	150321-02-c-hbl2	hornblende	44.37	1.54	12.01	14.46	0.47	13.82	10.65	0.83	0.36	-	0.00	-	-	-	-	98.51	63.02						0	0	0	0	0
25	150321-02-c-hbl3		43.46	1.64	12.92	13.40	0.16	14.94	10.60	0.92	0.29	-	0.00	-	-	-	-	98.33	66.54						0	0	0	0	0
3	150321-02-c-ox1		0.35	4.29	4.49	79.05	0.13	2.39	-	-	-	-	0.02	-	-	-	-	90.72							0	103	0	0	0
4	150321-02-c-ox2	opaque	0.15	5.31	4.42	77.91	0.14	2.51	-	-	-	-	0.02	-	-	-	-	90.45							0	116	0	0	0
7	150321-02-c-ox5		0.25	5.86	4.48	77.30	0.16	2.39	-	-	-	-	0.03	-	-	-	-	90.46							0	219	0	0	0
5	150321-02-c-gm1 (in host)		61.02	0.53	19.28	5.12	0.13	1.62	6.59	2.48	1.52	-	0.00	-	-	0.10	-	98.39		51.15	34.80				0	0	0	1010	0
8	150321-02-c-gm4	gm	56.99	0.54	18.08	5.59	0.10	3.50	7.21	1.94	1.13	-	0.00	-	-	0.10	-	95.17		59.79	29.03				0	0	0	950	0

9	150321-02-c-gm5		57.72	0.70	17.69	8.04	0.13	2.76	6.19	2.30	1.38	-	0.03	-	-	0.07	-	97.00		51.64	34.69				0	192	0	720	0
10	150321-02-c-gm6		59.84	0.58	18.15	5.30	0.10	1.88	6.61	2.43	1.56	-	0.00	-	-	0.11	-	96.57		51.37	34.16				0	0	0	1080	0
	150320-01a (Te Rato)																											
3	150320-01a-a-pl1 (in host)		53.36	0.00	30.18	0.52	-	0.07	12.96	3.98	0.14	-	-	0.00	-	-	-	101.19		63.79	35.42				0	0	0	0	0
4	150320-01a-a-pl2 (in host)		51.53	0.00	31.34	0.56	-	0.15	14.43	3.15	0.11	-	-	0.00	-	-	-	101.26		71.25	28.12				0	0	0	0	0
5	150320-01a-a-pl3 (in host)		51.94	0.00	30.99	0.45	-	0.10	14.07	3.54	0.11	-	-	0.00	-	-	-	101.22		68.27	31.12				0	0	0	0	0
6	150320-01a-a-pl4 (in host)		56.94	0.00	28.33	0.43	-	0.02	9.98	5.35	0.20	-	-	0.02	-	-	-	101.26		50.16	48.65				144	0	0	0	0
7	150320-01a-a-pl5 (in host)	plagioclase	55.92	0.00	28.90	0.47	-	0.05	10.92	4.97	0.18	-	-	0.00	-	-	-	101.40		54.24	44.72				0	0	0	0	0
8	150320-01a-a-pl6 (in lense)		52.73	0.00	30.71	0.52	-	0.14	13.57	3.73	0.13	-	-	0.00	-	-	-	101.53		66.31	32.95				0	0	0	0	0
9	150320-01a-a-pl7 (in lense)		51.86	0.01	30.33	0.50	-	0.34	13.87	3.46	0.10	-	-	0.00	-	-	-	100.46		68.51	30.89				0	0	0	0	0
10	150320-01a-a-pl8 (in lense)		52.35	0.00	30.64	0.47	-	0.11	13.51	3.63	0.11	-	-	0.00	-	-	-	100.83		66.81	32.52				0	0	0	0	0
11	150320-01a-a-pl9 (in lense)		51.46	0.01	31.50	0.49	-	0.13	14.38	3.29	0.09	-	-	0.00	-	-	-	101.36		70.35	29.14				0	0	0	0	0
12	150320-01a-a-pl10 (in lense)		52.17	0.00	30.98	0.57	-	0.15	13.88	3.42	0.13	-	-	0.00	-	-	-	101.30		68.65	30.57				0	0	0	0	0
18	150320-01a-a-opx1		54.31	0.24	0.67	20.23	0.49	25.82	1.09	0.04	0.00	-	0.01	-	-	-	-	102.91	69.47			2.07	68.03	29.90	0	82	0	0	0
17	150320-01a-a-opx2	px	52.38	0.29	1.14	16.62	0.34	27.00	1.62	0.00	0.02	-	0.00	-	-	-	-	99.41	74.33			3.11	72.02	24.87	0	0	0	0	0
16	150320-01a-a-cpx1		51.11	0.43	1.53	7.78	0.19	16.21	20.83	0.13	0.00	-	0.13	-	-	-	-	98.34	78.80			42.12	45.61	12.27	0	896	0	0	0
19	150320-01a-a-cpx3		50.73	0.52	1.24	8.84	0.24	15.61	21.19	0.15	0.02	-	0.21	-	-	-	-	98.74	75.90			42.54	43.61	13.85	0	1403	0	0	0
3	150320-01a-a-ox1 (in host)		1.21	6.06	3.85	78.23	0.19	2.84	-	-	-	-	0.06	-	-	-	-	92.44							0	390	0	0	0
4	150320-01a-a-ox2 (in host)		0.09	5.74	5.69	76.28	0.17	3.36	-	-	-	-	0.13	-	-	-	-	91.45							0	883	0	0	0
5	150320-01a-a-ox3 (in host)	opaque	0.09	5.58	5.09	77.19	0.13	3.07	-	-	-	-	0.03	-	-	-	-	91.18							0	226	0	0	0
7	150320-01a-a-ox5 (in lense)		0.12	5.87	3.95	78.05	0.13	2.47	-	-	-	-	0.04	-	-	-	-	90.64							0	287	0	0	0
10	150320-01a-a-ox8 (in lense)		0.08	5.83	4.19	77.97	0.14	2.47	-	-	-	-	0.03	-	-	-	-	90.71							0	212	0	0	0
5	150320-01a-a-gm1 (in host)		66.60	0.47	17.34	3.34	0.09	0.54	5.25	2.43	2.09	-	0.00	-	-	0.12	-	98.27	22.47	43.27	36.18	60.94	8.77	30.28	0	0	0	1220	0
7	150320-01a-a-gm3 (in host)		64.43	0.45	17.36	3.81	0.06	1.33	5.60	2.59	1.83	-	0.00	-	-	0.10	-	97.56	38.33	44.92	37.61	53.74	17.73	28.53	0	0	0	1030	0
8	150320-01a-a-gm4 (in host)		63.62	0.63	15.62	6.26	0.15	3.00	5.24	2.36	1.85	-	0.00	-	-	0.12	-	98.84	46.03	44.73	36.43	36.63	29.17	34.20	0	0	0	1190	0
9	150320-01a-a-gm5 (in host)		63.61	0.47	18.87	3.43	0.07	0.96	6.16	2.71	1.76	-	0.00	-	-	0.10	-	98.14	33.39	46.80	37.28	60.53	13.18	26.29	0	0	0	950	0
10	150320-01a-a-gm6 (in lense)	groundmass	64.37	0.52	17.28	4.19	0.11	1.43	5.59	2.52	1.78	-	0.02	-	-	0.10	-	97.92	37.86	45.57	37.18	51.51	18.36	30.14	0	157	0	1040	0
11	150320-01a-a-gm7 (in lense)		67.06	0.62	14.35	4.58	0.13	1.13	3.72	2.33	2.56	-	0.02	-	-	0.17	-	96.67	30.60	33.89	38.32	41.97	17.76	40.27	0	123	0	1700	0
12	150320-01a-a-gm8 (in lense)		66.49	0.39	14.11	4.28	0.18	2.46	3.29	2.12	2.29	-	0.02	-	-	0.14	-	95.76	50.64	33.37	38.97	32.73	34.07	33.21	0	123	0	1400	0
13	150320-01a-a-gm9 (in lense)		66.61	0.48	16.89	3.45	0.09	0.78	4.80	2.55	2.18	-	0.00	-	-	0.11	-	97.94	28.83	40.00	38.42	55.96	12.69	31.35	0	0	0	1100	0

14	150320-01a-a-gm10 (inlense)		67.92	0.60	13.30	5.59	0.15	2.13	3.39	1.75	2.56	-	0.00	-	-	0.15	-	97.53	40.47	35.35	32.92	31.64	27.66	40.70	0	0	0	1450	0
	150320-01e (Wharepu)																											
9	150320-01e-b-pl1-mic (in host)		51.12	0.02	31.15	0.66	-	0.19	14.75	3.12	0.09	-	-	0.01	-	-	-	101.10		71.96	27.52				110	0	0	0	0
11	150320-01e-b-pl3-mic (in host)		51.95	0.01	30.50	0.76	-	0.17	13.96	3.16	0.11	-	-	0.00	-	-	-	100.63		70.48	28.88				0	0	0	0	0
12	150320-01e-b-pl4-mic (in host)		53.11	0.00	29.86	0.74	-	0.18	13.09	3.83	0.11	-	-	0.00	-	-	-	100.92		64.96	34.39				0	0	0	0	0
13	150320-01e-b-pl5-mic (in lense)		52.13	0.02	30.64	0.77	-	0.21	14.00	3.09	0.11	-	-	0.00	-	-	-	100.97		70.98	28.33				0	0	0	0	0
18	150320-01e-b-pl9-mic (in lense)		50.21	0.07	31.03	1.17	0.03	0.16	14.61	3.00	0.18	-	-	-	-	-	-	100.46		72.13	26.82				0	0	0	0	0
19	150320-01e-b-pl10-mic (in lense)	plagioclase	51.06	0.41	28.67	3.58	0.05	0.48	13.49	2.73	0.54	-	-	-	-	-	-	101.01		70.75	25.89				0	0	0	0	0
20	150320-01e-b-pl11-mic (in lense)		50.70	0.06	30.24	1.38	0.00	0.21	14.26	2.99	0.22	-	-	-	-	-	-	100.06		71.53	27.15				0	0	0	0	0
22	150320-01e-b-pl13-mic (in lense)		50.73	0.11	30.42	1.37	0.03	0.26	14.31	3.01	0.22	-	-	-	-	-	-	100.46		71.52	27.20				0	0	0	0	0
17	150320-01e-d-pl1-mic (in host)		53.50	0.04	28.57	1.13	-	0.35	13.08	3.56	0.22	-	-	0.00	-	-	-	100.44		66.13	32.58				0	0	0	0	0
19	150320-01e-d-pl3-mic (in host)		53.74	0.06	28.58	1.08	-	0.33	12.80	3.67	0.25	-	-	0.00	-	-	-	100.51		64.90	33.62				0	0	0	0	0
23	150320-01e-d-pl7-mic (in host)		51.77	0.00	30.58	0.76	-	0.21	14.33	3.20	0.11	-	-	0.00	-	-	-	100.96		70.74	28.61				0	0	0	0	0
9	150320-01E-A-mi-OL3		39.88	0.00	0.01	17.69	0.32	43.67	0.04	0.00	-	-	0.01	-	0.08	-	-	101.69	81.49						0	48	644	0	0
10	150320-01E-A-mi-OL5a		39.89	0.00	0.01	15.99	0.20	45.29	0.04	0.00	-	-	0.02	-	0.07	-	-	101.50	83.47						0	109	519	0	0
11	150320-01E-A--mi-OL5b		39.52	0.00	0.00	15.70	0.21	44.97	0.04	0.00	-	-	0.04	-	0.11	-	-	100.57	83.63						0	267	825	0	0
3	150320-01e-a-mi-h-ol1		38.74	-	-	14.42	0.15	42.82	0.12	-	-	-	0.03	-	0.12	-	-	96.39	84.11										
4	150320-01e-a-mi-h-ol1b		38.42	-	-	14.11	0.12	42.14	0.15	-	-	-	0.01	-	0.09	-	-	95.02	84.19										
3	150320-01e-a-mi-h-ol2	olivine	38.19	-	-	17.78	0.16	41.22	0.12	-	-	-	0.03	-	0.03	-	-	97.54	80.52						0	233	228	0	0
4	150320-01e-a-mi-h-ol3		38.21	-	-	16.80	0.12	42.53	0.12	-	-	-	0.00	-	0.06	-	-	97.85	81.86						0	21	495	0	0
5	150320-01e-a-mi-h-ol4		38.73	-	-	15.90	0.13	42.58	0.10	-	-	-	0.02	-	0.06	-	-	97.52	82.68						0	137	464	0	0
4	150320-01e-b-ol1		38.29	-	-	22.02	0.31	39.79	0.16	-	-	-	0.01	-	0.04	-	-	100.63	76.31						0	96	306	0	0
5	150320-01e-b-ol2		38.06	-	-	22.52	0.31	39.24	0.17	-	-	-	0.00	-	0.00	-	-	100.31	75.65						0	0	0	0	0
8	150320-01e-d-ol1		38.50	-	-	19.65	0.27	41.51	0.15	-	-	-	0.03	-	0.07	-	-	100.18	79.02						0	185	542	0	0

9	150320-01e-d-ol2		38.54	-	-	19.43	0.29	41.30	0.17	-	-	-	0.02	-	0.05	-	-	99.80	79.12						0	103	416	0	0
10	150320-01e-d-ol3		38.34	-	-	20.62	0.30	40.75	0.16	-	-	-	0.04	-	0.04	-	-	100.23	77.89						0	239	283	0	0
10	150320-01e-d30mic-ol1		39.71	0.00	-	17.27	0.27	43.79	0.13	-	-	-	-	-	0.04	-	-	101.20	81.89						0	0	314	0	0
6	150320-01e-m-mi-ol1a		38.02	-	-	18.59	0.12	40.52	0.10	-	-	-	0.02	-	0.05	-	-	97.42	79.53						0	109	409	0	0
8	150320-01e-m-mi-ol2		38.25	-	-	16.56	0.13	41.03	0.11	-	-	-	0.00	-	0.05	-	-	96.13	81.54						0	0	416	0	0
9	150320-01e-m-mi-ol3		37.85	-	-	18.69	0.15	39.98	0.12	-	-	-	0.01	-	0.05	-	-	96.84	79.23						0	68	377	0	0
7	150320-01E-A-mi-PX7a		52.17	0.40	1.96	10.69	0.32	14.67	19.73	0.07	-	-	0.01	-	0.00	-	-	100.02	70.99	40.70	42.09	17.20	0	62	0	0	0
8	150320-01E-A-mi-PX7b		51.07	0.45	3.96	7.95	0.18	16.23	19.98	0.05	-	-	0.10	-	0.06	-	-	100.03	78.45	40.97	46.31	12.72	0	650	440	0	0
9	150320-01e-a-mi-px12a		52.21	0.51	2.65	9.18	0.24	15.15	19.97	0.29	0.01	-	0.03	-	-	-	-	100.24	74.64	41.42	43.72	14.86	0	185	0	0	0
10	150320-01e-a-mi-px12b		46.95	0.46	3.68	8.98	0.21	14.03	20.73	0.27	0.01	-	0.03	-	-	-	-	95.35	73.59	43.85	41.32	14.83	0	171	0	0	0
7	150320-01e-m-mi-px1		52.12	0.19	2.31	17.27	0.31	24.82	1.46	0.00	0.00	-	0.06	-	-	-	-	98.54	71.92	2.96	69.80	27.25	0	438	0	0	0
7	150320-01e-m-mi-px2		52.17	0.25	2.19	5.75	0.16	16.58	20.87	0.15	0.00	-	0.07	-	-	-	-	98.19	83.72	43.09	47.64	9.27	0	479	0	0	0
11	150320-01e-m-mi-px3		52.86	0.23	2.45	5.88	0.16	17.52	21.05	0.17	0.01	-	0.26	-	-	-	-	100.58	84.17	42.09	48.74	9.17	0	1772	0	0	0
8	150320-01e-m-mi-px4		50.59	0.56	2.79	10.98	0.27	14.04	19.53	0.37	0.01	-	0.04	-	-	-	-	99.17	69.52	41.01	41.01	17.98	0	239	0	0	0
6	150320-01e-m-mi-px5a		51.29	-	-	5.80	0.09	16.56	21.29	-	-	-	0.44	-	0.00	-	-	95.47	83.57	43.56	47.17	9.27	0	2983	24	0	0
7	150320-01e-m-mi-px5b		50.14	-	-	6.24	0.12	16.01	21.24	-	-	-	0.43	-	0.01	-	-	94.18	82.07	43.89	46.05	10.06	0	2922	94	0	0
16	150320-01e-b-cpx1	pyroxene	53.08	0.15	0.58	5.42	0.12	17.92	21.97	0.11	0.00	-	0.52	-	-	-	-	99.87	85.49	42.96	48.76	8.28	0	3531	0	0	0
19	150320-01e-b-cpx2		53.96	0.09	0.44	4.38	0.12	18.45	22.34	0.10	0.01	-	0.66	-	-	-	-	100.55	88.24	43.43	49.92	6.65	0	4488	0	0	0
20	150320-01e-b-cpx3		53.70	0.11	0.58	4.44	0.13	18.41	22.01	0.13	0.02	-	0.76	-	-	-	-	100.28	88.07	43.08	50.13	6.79	0	5221	0	0	0
12	150320-01e-d-cpx1		51.75	0.40	1.07	7.81	0.20	16.47	21.52	0.16	0.00	-	0.27	-	-	-	-	99.67	79.00	42.58	45.36	12.06	0	1875	0	0	0
13	150320-01e-d-cpx2		51.17	0.64	0.94	11.37	0.24	14.73	19.94	0.17	0.01	-	0.23	-	-	-	-	99.43	69.79	40.44	41.57	17.99	0	1560	0	0	0
14	150320-01e-d-cpx3		52.03	0.30	0.95	9.27	0.25	16.89	19.67	0.11	0.01	-	0.00	-	-	-	-	99.47	76.47	39.02	46.63	14.35	0	0	0	0	0
15	150320-01e-d-cpx4		51.62	0.42	1.01	8.09	0.24	16.53	21.45	0.17	0.00	-	0.27	-	-	-	-	99.80	78.46	42.26	45.31	12.43	0	1875	0	0	0
14	150320-01e-d30mic-cpx1		51.71	0.37	3.32	7.78	0.13	16.10	21.00	0.26	0.01	-	0.07	-	-	-	-	100.75	78.68	42.44	45.28	12.27	0	452	0	0	0
17	150320-01e-b-opx1		52.95	0.15	0.30	23.01	0.49	23.91	0.93	0.04	0.00	-	0.00	-	-	-	-	101.78	64.94	1.79	63.77	34.43	0	0	0	0	0
18	150320-01e-b-opx2		52.95	0.28	0.42	21.44	0.43	23.70	1.59	0.02	0.00	-	0.08	-	-	-	-	100.90	66.34	3.11	64.28	32.62	0	527	0	0	0
21	150320-01e-b-opx3		53.41	0.18	0.68	18.28	0.44	26.50	1.53	0.02	0.00	-	0.03	-	-	-	-	101.08	72.10	2.91	70.00	27.09	0	205	0	0	0
6	150320-01e-b-opx3		52.10	-	-	21.81	0.53	22.57	1.55	-	-	-	0.07	-	0.00	-	-	98.62	64.85	3.10	62.84	34.06	0	445	0	0	0
7	150320-01e-b-opx4		51.85	-	-	20.24	0.40	22.98	1.57	-	-	-	0.12	-	0.08	-	-	97.24	66.93	3.19	64.80	32.01	0	807	589	0	0

62	150320-01e-a-mi-px6-2		58.81	0.90	16.51	6.02	0.10	1.17	5.66	3.04	2.19	0.04	0.00	-	-	0.20	0.22	94.85	25.78	41.07	40.00	47.21	13.61	39.18	0	0	0	1980	868
63	150320-01e-a-mi-px7-1a		57.89	0.84	14.79	7.80	0.18	2.19	5.72	2.90	1.28	0.04	0.00	-	-	0.22	0.24	94.08	33.40	45.80	41.99	38.47	20.55	40.98	0	0	0	2150	960
64	150320-01e-a-mi-px7-1b		58.33	0.85	14.90	7.74	0.13	2.21	5.68	2.28	1.25	0.10	0.00	-	-	0.19	0.21	93.86	33.70	50.24	36.59	38.39	20.77	40.85	0	0	0	1910	848
65	150320-01e-a-mi-px7-2		60.75	0.78	15.69	5.30	0.08	1.49	4.73	2.97	2.18	0.10	0.00	-	-	0.20	0.22	94.47	33.33	37.23	42.35	43.27	18.91	37.82	0	0	0	1970	876
66	150320-01e-a-mi-px7-3		62.77	0.81	16.01	5.79	0.15	0.97	4.50	3.21	1.59	0.07	0.00	-	-	0.25	0.42	96.53	22.94	36.87	47.57	43.42	12.98	43.60	0	0	0	2510	1664
average	150320-01e-a-mi-px12-1		62.35	0.79	15.70	5.20	0.09	1.96	5.25	1.54	1.93	-	0.00	-	-	0.14	0.08	95.01	40.18	50.79	27.00	43.61	22.66	33.73	0	0	0	1370	338
56	150320-01e-a-mi-ol5-1a		50.17	0.68	15.01	7.73	0.20	3.16	11.20	1.76	0.52	0.00	0.03	-	-	0.22	0.57	91.25	42.16	74.67	21.22	51.77	20.33	27.90	0	226	0	2160	2280
57	150320-01e-a-mi-ol5-1b		50.17	0.67	14.78	7.77	0.22	3.16	11.02	1.97	0.56	0.01	0.03	-	-	0.22	0.57	91.14	42.01	72.23	23.39	51.32	20.45	28.23	0	171	0	2220	2264
58	150320-01e-a-mi-ol5-2a		50.12	0.67	15.47	7.16	0.07	2.49	11.27	1.95	0.54	0.00	0.00	-	-	0.23	0.57	90.54	38.23	72.96	22.89	55.47	17.02	27.51	0	21	0	2270	2288
59	150320-01e-a-mi-ol5-2b		50.34	0.69	15.54	7.19	0.10	2.35	11.49	2.05	0.54	0.00	0.03	-	-	0.21	0.59	91.11	36.83	72.50	23.46	56.40	16.06	27.55	0	205	0	2130	2340
60	150320-01e-a-mi-ol5-3a		51.66	0.73	16.12	6.73	0.12	2.21	11.06	2.20	0.58	0.00	0.03	-	-	0.24	0.60	92.29	36.93	70.30	25.30	57.03	15.87	27.10	0	192	0	2400	2408
61	150320-01e-a-mi-ol5-3b	melt inclusion	51.58	0.75	16.20	6.67	0.09	1.68	11.15	2.18	0.56	0.00	0.04	-	-	0.24	0.57	91.70	30.93	70.76	25.00	59.64	12.48	27.87	0	246	0	2430	2280
average	150320-01e-a-mi-h-ol1-1		48.69	0.65	14.09	8.26	0.16	4.56	9.41	0.49	0.33	-	0.04	-	-	0.19	0.53	87.40	49.62	87.93	8.35	42.37	28.60	29.03	0	255	0	1850	2105
11	150320-01e-b-gm1 (in lense)		59.76	0.39	22.51	5.27	0.08	1.93	2.68	3.06	3.22	-	0.00	-	-	0.05	-	98.94	39.42	22.22	45.93	28.25	28.28	43.46	0	0	0	500	0
13	150320-01e-b-gm3 (in lense)		54.40	1.03	15.24	10.26	0.23	5.52	8.34	1.71	1.05	-	0.01	-	-	0.10	-	97.89	48.95	65.75	24.35	34.69	31.97	33.34	0	62	0	980	0
14	150320-01e-b-gm4 (in lense)		54.23	0.82	15.72	9.47	0.22	7.18	9.09	1.67	0.80	-	0.01	-	-	0.08	-	99.28	57.49	69.61	23.08	34.34	37.75	27.91	0	82	0	820	0
15	150320-01e-b-gm5 (in lense)		55.10	0.80	19.11	7.67	0.10	2.18	8.48	2.22	1.08	-	0.01	-	-	0.12	-	96.87	33.66	61.54	29.15	48.44	17.36	34.21	0	82	0	1220	0
17	150320-01e-b-gm7 (in host)		55.50	0.73	17.78	8.19	0.18	3.38	8.34	2.19	1.12	-	0.00	-	-	0.13	-	97.53	42.41	61.20	29.03	42.91	24.21	32.88	0	0	0	1270	0
18	150320-01e-b-gm8 (in host)		56.40	0.93	15.16	9.69	0.15	4.92	7.57	1.68	1.19	-	0.00	-	-	0.14	-	97.82	47.51	62.99	25.26	34.45	31.14	34.40	0	0	0	1360	0
19	150320-01e-b-gm9 (in host)		56.32	0.80	18.24	6.90	0.12	2.09	8.06	2.25	1.23	-	0.00	-	-	0.12	-	96.12	35.11	59.29	29.96	49.28	17.81	32.91	0	0	0	1180	0
20	150320-01e-b-gm10 (in host)		56.07	0.82	16.74	8.56	0.16	4.03	8.45	1.93	1.05	-	0.00	-	-	0.12	-	97.94	45.62	64.07	26.43	40.74	27.04	32.23	0	0	0	1220	0
19	150320-01e-b-gm11 (in lense)	groundmass	56.30	0.74	18.09	8.39	0.42	3.92	5.26	3.14	2.06	0.02	0.00	-	-	0.12	0.00	98.47	45.42	39.27	42.40	30.49	31.58	37.94	0	0	0	1220	8
20	150320-01e-b-gm12 (in lense)		54.87	1.25	20.06	9.11	0.60	2.56	4.65	2.80	2.42	0.00	0.00	-	-	0.10	0.01	98.43	33.36	36.92	40.20	30.36	23.24	46.41	0	0	0	1030	52
21	150320-01e-b-gm13 (in lense)		63.09	1.94	13.68	10.08	0.98	2.64	1.63	1.77	2.61	0.00	0.00	-	-	0.02	0.02	98.44	31.84	20.49	40.42	12.35	27.90	59.74	0	0	0	190	64
22	150320-01e-b-gm14 (in lense)		80.94	5.38	3.83	2.42	0.23	0.34	3.21	0.72	1.30	0.00	0.01	-	-	0.02	0.02	98.41	20.08	53.09	21.37	57.63	8.51	33.86	0	96	0	160	84
23	150320-01e-b-gm15 (in lense)		56.47	0.84	17.34	9.24	0.28	3.94	6.96	2.46	1.39	0.02	0.01	-	-	0.14	0.01	99.10	43.15	53.30	34.04	35.42	27.86	36.71	0	41	0	1410	52
21	150320-01e-d-gm1 (in host)		54.61	1.07	14.36	10.26	0.17	5.34	8.33	1.52	1.33	-	0.01	-	-	0.13	-	97.12	48.10	65.80	21.71	35.04	31.24	33.72	0	48	0	1320	0

22	150320-01e-d-gm2 (in host)		54.14	1.01	16.21	10.33	0.20	5.16	8.58	1.75	0.96	-	0.02	-	-	0.08	-	98.43	47.11	66.54	24.60	36.01	30.15	33.84	0	109	0	830	0
23	150320-01e-d-gm3 (in host)		53.50	0.86	15.98	8.62	0.15	4.88	7.44	1.73	1.01	-	0.01	-	-	0.17	-	94.36	50.24	63.16	26.59	35.47	32.42	32.11	0	68	0	1730	0
24	150320-01e-d-gm4 (in host)		53.98	0.90	16.06	9.39	0.21	5.77	8.21	1.81	0.89	-	0.00	-	-	0.08	-	97.29	52.27	65.44	26.13	34.85	34.05	31.10	0	0	0	830	0
27	150320-01e-d-gm7 (in lense)		53.82	0.72	19.00	7.81	0.15	2.58	7.85	2.23	1.22	-	0.00	-	-	0.14	-	95.53	37.04	58.86	30.27	44.78	20.45	34.76	0	21	0	1420	0
average	150320-01e-m-mi-px5-1		52.42	0.68	18.77	8.63	0.11	3.21	7.38	2.12	0.59	-	0.00	-	-	0.18	0.28	94.39	39.89	61.96	32.12	39.71	24.05	36.24	0	14	0	1840	1120
7	150320-01e-m-mi-px5-2		53.23	0.43	19.48	6.06	0.15	2.46	6.95	1.78	0.29	-	0.00	-	-	0.17	0.39	91.38	42.00	66.14	30.55	46.04	22.67	31.30	0	0	0	1720	1564
Average	150320-01e-m-mi-ol1-1	MI	50.17	0.76	16.49	6.91	0.12	3.07	9.58	1.18	0.69	-	0.01	-	-	0.22	0.49	89.70	44.21	76.41	16.99	49.77	22.21	28.02	0	75	0	2185	1962
7	150320-01e-m-mi-ol2-1		50.45	0.81	16.69	7.15	0.12	2.32	10.09	0.97	0.60	-	0.00	-	-	0.24	0.50	89.95	36.69	80.35	13.95	53.38	17.10	29.51	0	0	0	2410	1996
8	150320-01e-m-mi-ol3-1		51.67	0.79	17.03	6.10	0.09	1.84	9.22	0.96	0.80	-	0.02	-	-	0.19	0.52	89.22	34.90	77.40	14.65	55.75	15.44	28.81	0	103	0	1940	2068
	150317-01 (Te Maari LF)																												
5	150317-01-pl1		55.19	0.00	29.42	0.54	-	0.05	11.41	4.75	0.23	-	-	0.00	-	-	-	101.59		56.28	42.38				0	0	0	0	0
6	150317-01-pl2		54.81	0.02	29.77	0.61	-	0.05	11.98	4.74	0.21	-	-	0.00	-	-	-	102.18		57.57	41.24				0	0	0	0	0
7	150317-01-pl3		55.34	0.01	29.12	0.51	-	0.05	11.45	4.95	0.23	-	-	0.00	-	-	-	101.66		55.33	43.33				0	0	0	0	0
8	150317-01-pl4-c		55.34	0.01	29.31	0.46	-	0.05	11.72	4.78	0.24	-	-	0.00	-	-	-	101.88		56.77	41.87				0	0	0	0	0
9	150317-01-pl4-i	plagioclase	55.41	0.01	29.34	0.55	-	0.06	11.43	4.63	0.23	-	-	0.00	-	-	-	101.67		56.89	41.73				0	0	0	0	0
10	150317-01-pl4-r		54.05	0.02	30.08	0.51	-	0.05	12.21	4.45	0.19	-	-	0.00	-	-	-	101.55		59.59	39.29				0	0	0	0	0
11	150317-01-pl5		54.56	0.02	30.16	0.53	-	0.04	12.30	4.52	0.22	-	-	0.00	-	-	-	102.35		59.33	39.42				0	0	0	0	0
12	150317-01-pl6		54.51	0.00	30.26	0.54	-	0.06	12.47	4.39	0.22	-	-	0.00	-	-	-	102.46		60.30	38.42				0	0	0	0	0
13	150317-01-pl7-c		55.00	0.00	29.45	0.54	-	0.04	11.60	4.89	0.21	-	-	0.00	-	-	-	101.73		56.04	42.74				0	0	0	0	0
14	150317-01-pl7-r		50.54	0.02	32.38	0.70	-	0.14	15.43	2.69	0.11	-	-	0.00	-	-	-	102.01		75.55	23.82				0	0	0	0	0
15	150317-01-pl8		51.92	0.01	31.60	0.65	-	0.05	14.17	3.47	0.14	-	-	0.00	-	-	-	102.01		68.74	30.47				0	0	0	0	0
5	150317-01-cpx1		52.21	0.50	1.79	11.05	0.36	14.58	20.19	0.29	0.00	-	0.01	-	-	-	-	100.97	70.17			41.13	41.31	17.56	0	75	0	0	0
6	150317-01-cpx2		52.33	0.46	2.27	9.85	0.27	15.30	20.05	0.25	0.00	-	0.03	-	-	-	-	100.81	73.46			40.89	43.42	15.69	0	205	0	0	0
7	150317-01-cpx3		52.43	0.39	1.46	11.09	0.34	14.50	20.57	0.28	0.01	-	0.02	-	-	-	-	101.09	69.99			41.63	40.85	17.51	0	151	0	0	0
8	150317-01-cpx4		52.25	0.49	1.82	10.75	0.33	14.55	20.58	0.31	0.00	-	0.01	-	-	-	-	101.09	70.71			41.82	41.14	17.04	0	68	0	0	0
9	150317-01-cpx5	pyroxene	52.17	0.37	3.94	5.75	0.18	16.59	22.09	0.22	0.00	-	0.42	-	-	-	-	101.74	83.73			44.49	46.48	9.03	0	2860	0	0	0
3	150317-01-opx1		52.92	0.26	1.08	22.95	0.57	22.37	1.52	-	-	-	0.00	-	-	-	-	101.67	63.48			3.01	61.56	35.42	0	0	0	0	0
4	150317-01-opx2		53.16	0.21	0.75	23.56	0.60	22.68	1.48	-	-	-	0.02	-	-	-	-	102.45	63.19			2.87	61.37	35.76	0	123	0	0	0
5	150317-01-opx3		52.29	0.26	2.38	21.64	0.50	23.09	1.28	-	-	-	0.02	-	-	-	-	101.45	65.54			2.55	63.87	33.58	0	137	0	0	0
6	150317-01-opx4		52.74	0.20	0.72	21.74	0.56	21.63	1.43	-	-	-	0.00	-	-	-	-	99.02	63.95			2.96	62.06	34.99	0	0	0	0	0

7	150317-01-opx5		53.10	0.18	0.66	23.35	0.62	22.25	1.48	-	-	-	0.00	-	-	-	-	101.65	62.95			2.92	61.11	35.97	0	0	0	0	0
9	150317-01-opx6		52.81	0.20	0.96	20.61	0.62	24.30	1.54	-	-	-	0.00	-	-	-	-	101.04	67.77			2.99	65.74	31.27	0	0	0	0	0
3	150317-01-ol1		40.68	0.01	-	9.35	0.16	50.20	0.16	-	-	-	-	-	0.38	-	-	100.94	90.54						0	0	2955	0	0
4	150317-01-ol2-c		40.84	0.03	-	9.34	0.14	50.54	0.18	-	-	-	-	-	0.38	-	-	101.45	90.60						0	0	2970	0	0
5	150317-01-ol2-r	olivine	40.18	0.03	-	14.50	0.25	46.20	0.19	-	-	-	-	-	0.16	-	-	101.51	85.03						0	0	1242	0	0
6	150317-01-ol3		41.17	0.00	-	9.06	0.16	50.71	0.16	-	-	-	-	-	0.35	-	-	101.62	90.89						0	0	2735	0	0
7	150317-01-ol4		40.21	0.00	-	11.99	0.18	47.99	0.19	-	-	-	-	-	0.27	-	-	100.83	87.71						0	0	2114	0	0
8	150317-01-ol5-c		40.72	0.00	-	11.56	0.16	48.69	0.18	-	-	-	-	-	0.23	-	-	101.54	88.25						0	0	1807	0	0
5	150317-01-il1		0.00	31.24	0.14	60.27	0.33	2.30	-	-	-	-	0.03	-	-	-	-	94.32							0	192	0	0	0
6	150317-01-il2		0.02	53.08	0.51	37.29	0.23	3.67	-	-	-	-	0.03	-	-	-	-	94.81							0	171	0	0	0
7	150317-01-il3		0.01	52.40	0.58	37.53	0.13	3.56	-	-	-	-	0.04	-	-	-	-	94.26							0	246	0	0	0
8	150317-01-il4		0.04	52.60	1.27	37.18	0.19	3.44	-	-	-	-	0.01	-	-	-	-	94.72							0	41	0	0	0
9	150317-01-ox1		0.00	42.44	0.20	48.07	0.82	5.13	-	-	-	-	0.00	-	-	-	-	96.66							0	7	0	0	0
10	150317-01-ox2		0.04	34.73	0.16	56.05	0.36	2.92	-	-	-	-	0.02	-	-	-	-	94.28							0	144	0	0	0
11	150317-01-mt3		0.07	13.38	3.18	74.18	0.34	2.41	-	-	-	-	0.17	-	-	-	-	93.72							0	1156	0	0	0
12	150317-01-mt4		0.12	5.52	4.34	80.33	0.38	2.76	-	-	-	-	0.12	-	-	-	-	93.57							0	828	0	0	0
13	150317-01-mt5		0.08	18.97	1.87	69.30	0.34	2.49	-	-	-	-	0.10	-	-	-	-	93.15							0	698	0	0	0
14	150317-01-mt6		0.08	5.90	3.55	81.94	0.53	2.21	-	-	-	-	0.17	-	-	-	-	94.39							0	1177	0	0	0
15	150317-01-mt7	opaque	0.09	7.30	2.94	80.50	0.44	2.45	-	-	-	-	0.16	-	-	-	-	93.87							0	1102	0	0	0
16	150317-01-ox5		0.00	26.25	0.61	65.25	0.20	1.61	-	-	-	-	0.11	-	-	-	-	94.03							0	766	0	0	0
17	150317-01-ox6		0.09	26.33	0.63	63.96	0.26	1.82	-	-	-	-	0.14	-	-	-	-	93.22							0	931	0	0	0
18	150317-01-il7		0.12	9.70	3.05	77.64	0.35	2.46	-	-	-	-	0.20	-	-	-	-	93.51							0	1389	0	0	0
19	150317-01-il8		0.08	4.80	3.16	81.69	0.53	2.81	-	-	-	-	0.12	-	-	-	-	93.18							0	807	0	0	0
20	150317-01-il9		0.08	5.49	2.98	81.30	0.44	3.01	-	-	-	-	0.12	-	-	-	-	93.41							0	794	0	0	0
21	150317-01-mt8		0.30	3.18	3.45	77.72	0.48	2.50	-	-	-	-	0.13	-	-	-	-	87.76							0	917	0	0	0
22	150317-01-mt9		0.11	6.19	3.09	81.31	0.61	3.31	-	-	-	-	0.11	-	-	-	-	94.73							0	739	0	0	0
23	150317-01-mt10		0.09	7.01	2.57	80.47	0.55	2.89	-	-	-	-	0.14	-	-	-	-	93.72							0	965	0	0	0
24	150317-01-mt11		0.08	7.20	3.25	79.43	0.42	2.41	-	-	-	-	0.15	-	-	-	-	92.93							0	1019	0	0	0
7	150317-01-gm1		64.68	0.98	17.31	5.25	0.05	0.77	5.51	3.61	2.29	-	0.00	-	-	0.11	0.01	100.57	20.80	37.33	44.22	51.60	10.07	38.33	0	0	0	1060	52
8	150317-01-gm2		61.17	0.67	21.16	3.62	0.00	0.71	7.85	3.60	1.80	-	0.00	-	-	0.07	0.01	100.67	25.95	47.54	39.49	67.26	8.49	24.24	0	0	0	660	52
9	150317-01-gm3	groundmass	62.16	0.79	18.23	5.20	0.09	1.56	7.07	3.43	1.78	-	0.00	-	-	0.10	0.00	100.39	34.80	45.92	40.33	53.18	16.29	30.52	0	0	0	970	12
10	150317-01-gm4		65.50	0.98	15.67	5.96	0.07	1.25	4.29	3.78	2.67	-	0.00	-	-	0.10	0.00	100.28	27.19	29.97	47.82	40.16	16.27	43.57	0	0	0	1030	12

11	150317-01-gm5		64.26	0.85	16.42	5.53	0.16	1.37	5.76	3.36	2.34	-	0.03	-	-	0.11	0.00	100.18	30.55	39.39	41.59	48.09	15.86	36.05	0	171	0	1100	0
12	150317-01-gm6		59.04	0.52	22.66	3.44	0.08	0.74	9.04	3.42	1.43	-	0.00	-	-	0.05	0.04	100.44	27.80	53.41	36.55	70.87	8.10	21.03	0	0	0	500	144
13	150317-01-gm7		69.00	1.10	14.16	5.02	0.00	0.53	3.39	3.36	3.25	-	0.00	-	-	0.15	0.01	99.97	15.84	25.44	45.57	42.14	9.16	48.70	0	0	0	1540	52
14	150317-01-gm8		63.31	0.81	18.48	4.74	0.03	0.83	6.61	3.64	1.91	-	0.02	-	-	0.10	0.01	100.48	23.67	42.69	42.62	57.66	10.02	32.32	0	123	0	960	44
15	150317-01-gm9		61.81	0.65	20.84	3.97	0.04	0.57	7.89	3.87	1.70	-	0.02	-	-	0.06	0.01	101.43	20.30	46.64	41.37	66.98	6.70	26.32	0	151	0	640	40
16	150317-01-gm10		66.29	0.97	16.33	4.74	0.01	0.55	4.84	3.56	2.83	-	0.02	-	-	0.13	0.00	100.25	17.04	33.03	44.01	52.04	8.17	39.78	0	109	0	1260	0
5	150317-01-mi-opx5-1	MI	66.87	1.70	13.29	7.78	0.19	0.73	3.76	3.53	2.15	-	0.00	-	-	0.19	0.03	100.16	14.29	29.61	50.25	34.69	9.33	55.98	0	0	0	1870	124
3	160727-01 (Te Maari LF) 160727-01-c-pl1		52.32	0.02	30.25	0.55	0.03	0.05	13.14	3.65	0.24	-	-	-	-	-	-	100.24		65.57	32.99				0	0	0	0	0
4	160727-01-c-pl2c		47.14	0.01	33.97	0.58	0.00	0.05	17.02	1.79	0.10	-	-	-	-	-	-	100.65		83.54	15.90				0	0	0	0	0
5	160727-01-c-pl2r		52.90	0.02	29.74	0.61	0.02	0.04	12.62	4.18	0.28	-	-	-	-	-	-	100.42		61.52	36.83				0	0	0	0	0
6	160727-01-c-pl3c		52.13	0.03	30.29	0.61	0.00	0.04	13.04	3.68	0.28	-	-	-	-	-	-	100.11		65.12	33.22				0	0	0	0	0
7	160727-01-c-pl4c		51.31	0.04	30.93	0.51	0.01	0.05	13.75	3.47	0.22	-	-	-	-	-	-	100.29		67.76	30.94				0	0	0	0	0
8	160727-01-c-pl4r		49.49	0.01	32.02	0.75	0.00	0.15	15.11	2.63	0.18	-	-	-	-	-	-	100.32		75.23	23.70				0	0	0	0	0
9	160727-01-c-pl5	plagioclase	54.37	0.02	28.81	0.56	0.01	0.06	11.46	4.67	0.37	-	-	-	-	-	-	100.33		56.29	41.54				0	0	0	0	0
10	160727-01-c-pl6mic		53.25	0.03	29.78	0.57	0.03	0.06	12.52	4.15	0.32	-	-	-	-	-	-	100.70		61.31	36.82				0	0	0	0	0
11	160727-01-c-pl7mic		54.36	0.01	29.14	0.53	0.02	0.04	11.62	4.39	0.36	-	-	-	-	-	-	100.47		58.11	39.76				0	0	0	0	0
12	160727-01-c-pl8mic		52.78	0.02	30.19	0.73	0.00	0.04	12.87	3.84	0.32	-	-	-	-	-	-	100.79		63.76	34.38				0	0	0	0	0
13	160727-01-c-pl9mic		53.29	0.04	29.69	0.54	0.00	0.04	12.27	4.33	0.32	-	-	-	-	-	-	100.52		59.88	38.26				0	0	0	0	0
14	160727-01-c-pl10mic		52.28	0.00	30.56	0.51	0.00	0.05	13.26	3.54	0.27	-	-	-	-	-	-	100.48		66.34	32.03				0	0	0	0	0
15	160727-01-c-pl11c		53.57	0.06	29.39	0.56	0.00	0.04	11.93	4.41	0.39	-	-	-	-	-	-	100.35		58.59	39.16				0	0	0	0	0
16	160727-01-c-pl11r		52.46	0.01	29.57	0.56	0.00	0.05	12.49	3.85	0.34	-	-	-	-	-	-	99.32		62.90	35.07				0	0	0	0	0
17	160727-01-c-pl12		53.12	0.04	29.56	0.55	0.01	0.05	12.23	4.21	0.34	-	-	-	-	-	-	100.12		60.36	37.64				0	0	0	0	0
16	160727-01-c-px4		52.17	0.45	2.68	8.96	0.28	14.84	20.67	0.07	-	-	0.13	-	0.00	-	-	100.25	74.72			42.78	42.75	14.47	0	896	0	0	0
17	160727-01-c-px5		52.65	0.42	1.82	9.86	0.31	15.11	20.66	0.07	-	-	0.00	-	0.00	-	-	100.89	73.19			41.83	42.57	15.59	0	0	0	0	0
19	160727-01-c-px6r		51.64	0.63	4.51	6.66	0.20	16.45	20.46	0.05	-	-	0.34	-	0.02	-	-	100.95	81.50			42.15	47.15	10.70	0	2306	173	0	0
21	160727-01-c-px8mic	pyroxene	52.48	0.37	1.55	10.56	0.43	14.77	20.64	0.07	-	-	0.01	-	0.00	-	-	100.87	71.38			41.76	41.57	16.67	0	55	0	0	0
24	160727-01-c-px10r		51.32	0.59	4.25	7.93	0.29	17.15	19.18	0.04	-	-	0.18	-	0.03	-	-	100.95	79.40			38.96	48.47	12.57	0	1259	244	0	0
17	160727-01-C-MI-PX1		52.36	0.38	1.72	9.60	0.30	14.92	20.13	0.07	-	-	0.00	-	0.02	-	-	99.50	73.47			41.60	42.91	15.49	0	0	157	0	0
23	160727-01-C-MI-PX2		52.73	0.31	1.37	10.18	0.27	14.50	20.47	0.05	-	-	0.01	-	0.00	-	-	99.87	71.75			42.12	41.53	16.35	0	55	0	0	0

18	160727-01-C-MI-PX6		52.33	0.31	0.87	10.92	0.32	14.25	20.09	0.06	-	-	0.05	-	0.00	-	-	99.21	69.94		41.48	40.93	17.60	0	335	0	0	0
26	160727-01-C-MI-PX7		52.32	0.45	1.72	9.65	0.29	14.75	20.07	0.05	-	-	0.00	-	0.04	-	-	99.33	73.15		41.71	42.64	15.65	0	0	283	0	0
27	160727-01-C-MI-PX11		52.71	0.33	1.39	9.76	0.28	14.76	20.38	0.07	-	-	0.00	-	0.00	-	-	99.68	72.95		42.00	42.31	15.69	0	0	0	0	0
21	160727-01-C-MI-PX13		52.21	0.43	2.11	9.23	0.30	15.11	20.15	0.08	-	-	0.04	-	0.01	-	-	99.66	74.48		41.64	43.47	14.89	0	239	39	0	0
20	160727-01-C-MI-PX14b		53.04	0.23	2.40	4.50	0.19	17.06	21.83	0.04	-	-	0.51	-	0.00	-	-	99.81	87.11		44.48	48.37	7.16	0	3496	0	0	0
19	160727-01-C-MI-PX14a		51.64	0.50	2.99	7.79	0.15	15.30	20.60	0.08	-	-	0.10	-	0.00	-	-	99.14	77.77		42.94	44.38	12.68	0	650	0	0	0
28	160727-01-C-MI-PX15		52.53	0.25	0.68	10.59	0.38	14.19	20.38	0.06	-	-	0.00	-	0.01	-	-	99.07	70.49		42.12	40.80	17.08	0	7	55	0	0
22	160727-01-C-MI-PX17		53.01	0.24	0.81	10.65	0.23	14.14	20.36	0.07	-	-	0.00	-	0.00	-	-	99.52	70.30		42.10	40.70	17.20	0	0	0	0	0
24	160727-01-C-MI-PX18		51.99	0.41	1.93	10.75	0.38	14.18	19.81	0.08	-	-	0.02	-	0.00	-	-	99.54	70.17		41.33	41.17	17.50	0	144	0	0	0
13	160727-01-c-px1		52.91	0.23	0.52	23.25	0.58	22.29	0.34	0.00	-	-	0.00	-	0.00	-	-	100.12	63.09		0.68	62.66	36.66	0	7	0	0	0
14	160727-01-c-px2		53.39	0.20	0.57	21.77	0.67	22.48	1.47	0.00	-	-	0.02	-	0.00	-	-	100.56	64.80		2.95	62.89	34.17	0	103	0	0	0
15	160727-01-c-px3		53.21	0.20	0.70	22.24	0.59	22.40	0.45	0.10	-	-	0.00	-	0.02	-	-	99.90	64.23		0.91	63.64	35.44	0	0	181	0	0
18	160727-01-c-px6c		52.09	0.19	0.57	22.08	0.55	21.89	2.15	0.16	-	-	0.01	-	0.00	-	-	99.69	63.87		4.32	61.11	34.57	0	55	0	0	0
20	160727-01-c-px7mic		52.50	0.21	0.88	22.82	0.63	21.47	1.63	0.00	-	-	0.09	-	0.00	-	-	100.22	62.65		3.30	60.58	36.12	0	636	0	0	0
22	160727-01-c-px9mic		53.40	0.20	0.42	22.81	0.60	22.70	0.36	0.01	-	-	0.00	-	0.02	-	-	100.52	63.96		0.72	63.50	35.78	0	0	157	0	0
23	160727-01-c-px10c		53.18	0.17	0.48	22.93	0.59	22.41	0.39	0.00	-	-	0.00	-	0.01	-	-	100.16	63.54		0.78	63.04	36.18	0	0	39	0	0
25	160727-01-c-px11		53.30	0.23	0.76	21.26	0.66	23.71	0.38	0.00	-	-	0.00	-	0.00	-	-	100.29	66.53		0.76	66.03	33.22	0	0	0	0	0
26	160727-01-c-px12mic		53.14	0.21	0.62	22.60	0.73	21.71	0.45	0.08	-	-	0.03	-	0.04	-	-	99.60	63.13		0.93	62.55	36.52	0	185	306	0	0
27	160727-01-c-px13mic		52.24	0.19	0.63	22.21	0.63	21.79	1.66	0.00	-	-	0.00	-	0.00	-	-	99.36	63.63		3.37	61.48	35.15	0	0	0	0	0
25	160727-01-C-MI-PX10		53.49	0.20	0.47	22.26	0.64	22.45	1.48	0.00	-	-	0.00	-	0.01	-	-	101.00	64.26		2.96	62.36	34.68	0	0	86	0	0
7	160727-01-c-ol1		40.40	0.01	0.14	13.90	0.17	44.35	0.06	0.09	-	-	0.06	-	0.20	-	-	99.38	85.05					0	438	1579	0	0
8	160727-01-c-ol2		39.66	0.00	0.02	12.90	0.19	47.14	0.07	0.00	-	-	0.03	-	0.19	-	-	100.20	86.69					0	226	1509	0	0
9	160727-01-c-ol3		39.93	0.00	0.00	12.73	0.21	47.10	0.06	0.08	-	-	0.04	-	0.22	-	-	100.38	86.83					0	301	1752	0	0
10	160727-01-c-ol4r		41.19	0.00	0.10	19.86	0.28	42.77	0.06	0.02	-	-	0.00	-	0.15	-	-	104.43	79.34					0	0	1194	0	0
11	160727-01-c-ol4c	olivine	40.04	0.01	0.01	11.67	0.14	47.71	0.07	0.00	-	-	0.01	-	0.25	-	-	99.89	87.94					0	48	1925	0	0
12	160727-01-c-ol5		40.92	0.00	0.03	10.42	0.19	52.84	0.08	0.00	-	-	0.03	-	0.25	-	-	104.75	90.04					0	205	1925	0	0
15	160727-01-C-MI-OL1		40.67	0.00	0.00	10.81	0.15	47.97	0.05	0.00	-	-	0.02	-	0.29	-	-	99.95	88.78					0	116	2295	0	0
16	160727-01-C-MI-OL4		40.50	0.00	0.02	10.28	0.12	48.30	0.05	0.00	-	-	0.07	-	0.35	-	-	99.68	89.33					0	452	2719	0	0
13	160727-01-C-MI-OL6		40.90	0.00	0.03	8.74	0.20	49.83	0.06	0.00	-	-	0.07	-	0.29	-	-	100.12	91.04					0	486	2271	0	0
12	160727-01-C-MI-OL7		40.76	0.00	0.02	10.36	0.13	48.18	0.04	0.00	-	-	0.05	-	0.32	-	-	99.86	89.24					0	335	2522	0	0

14	160727-01-C-MI-OL8		40.87	0.00	0.01	9.26	0.14	48.90	0.04	0.00	-	-	0.05	-	0.34	-	-	99.61	90.40		0	328	2664	0	0
18	160727-01-c-mi-h-ol1		38.12	-	-	7.54	0.11	46.69	0.17	-	-	-	0.02	-	0.24	-	-	92.88	91.70		0	157	1870	0	0
19	160727-01-c-mi-h-ol2		39.47	-	-	10.40	0.10	47.62	0.19	-	-	-	0.02	-	0.20	-	-	98.01	89.08		0	164	1587	0	0
5	160727-01-c-mi-h-ol4		39.90	-	-	8.76	0.09	48.38	0.16	-	-	-	0.05	-	0.39	-	-	97.73	90.78		0	322	3080	0	0
24	160727-01-c-mi-h-ol7		39.76	-	-	8.63	0.10	49.24	0.15	-	-	-	0.07	-	0.36	-	-	98.31	91.05		0	445	2845	0	0
25	160727-01-c-mi-h-ol8		39.08	-	-	11.42	0.11	45.87	0.20	-	-	-	0.03	-	0.18	-	-	96.89	87.74		0	233	1430	0	0
26	160727-01-c-mi-h-ol9		39.52	-	-	9.03	0.07	48.45	0.16	-	-	-	0.08	-	0.33	-	-	97.64	90.54		0	575	2593	0	0
8	160727-01-c-ox2b		0.04	27.47	0.62	62.73	0.12	1.60	-	-	-	-	0.10	-	-	-	-	92.68			0	684	0	0	0
12	160727-01-c-ox3b		0.07	30.71	0.53	60.50	0.24	1.84	-	-	-	-	0.10	-	-	-	-	93.98			0	684	0	0	0
14	160727-01-c-ox3d		0.01	44.09	0.30	48.08	0.31	3.70	-	-	-	-	0.02	-	-	-	-	96.51			0	157	0	0	0
15	160727-01-c-ox3e		0.00	40.89	0.40	50.51	0.34	3.24	-	-	-	-	0.01	-	-	-	-	95.40			0	75	0	0	0
18	160727-01-c-ox5b		0.07	22.88	0.79	66.13	0.21	1.59	-	-	-	-	0.19	-	-	-	-	91.87			0	1321	0	0	0
22	160727-01-c-ox7b		0.06	26.35	0.63	63.96	0.19	1.60	-	-	-	-	0.15	-	-	-	-	92.95			0	1033	0	0	0
23	160727-01-c-ox7c		0.01	25.07	0.73	63.94	0.23	1.45	-	-	-	-	0.12	-	-	-	-	91.55			0	835	0	0	0
25	160727-01-c-ox8b		0.03	30.40	0.45	60.72	0.18	1.43	-	-	-	-	0.08	-	-	-	-	93.29			0	575	0	0	0
26	160727-01-c-ox8c		0.02	34.59	0.35	57.53	0.25	1.98	-	-	-	-	0.09	-	-	-	-	94.81			0	616	0	0	0
5	160727-01-c-ox1a		0.07	9.30	2.98	78.48	0.30	1.78	-	-	-	-	0.16	-	-	-	-	93.05			0	1074	0	0	0
6	160727-01-c-ox1b	opaque	0.08	16.49	2.66	73.23	0.30	1.84	-	-	-	-	0.14	-	-	-	-	94.73			0	951	0	0	0
7	160727-01-c-ox2a		0.04	9.35	2.82	78.13	0.34	2.12	-	-	-	-	0.13	-	-	-	-	92.93			0	896	0	0	0
9	160727-01-c-ox1c		0.05	9.10	3.07	79.20	0.31	1.69	-	-	-	-	0.13	-	-	-	-	93.55			0	889	0	0	0
10	160727-01-c-ox1d		0.03	10.60	2.75	77.94	0.36	1.84	-	-	-	-	0.17	-	-	-	-	93.69			0	1143	0	0	0
11	160727-01-c-ox3a		0.02	10.51	2.62	77.90	0.25	2.07	-	-	-	-	0.11	-	-	-	-	93.48			0	773	0	0	0
13	160727-01-c-ox3c		0.10	10.41	2.80	77.81	0.35	2.26	-	-	-	-	0.12	-	-	-	-	93.85			0	828	0	0	0
16	160727-01-c-ox4		0.05	12.84	2.19	76.62	0.34	1.69	-	-	-	-	0.11	-	-	-	-	93.84			0	766	0	0	0
17	160727-01-c-ox5a		0.04	4.99	3.71	80.46	0.52	2.53	-	-	-	-	0.12	-	-	-	-	92.37			0	807	0	0	0
19	160727-01-c-ox6a		0.05	7.82	2.93	79.87	0.47	1.96	-	-	-	-	0.16	-	-	-	-	93.25			0	1095	0	0	0
20	160727-01-c-ox6b		0.06	6.49	3.32	80.59	0.41	1.72	-	-	-	-	0.14	-	-	-	-	92.73			0	965	0	0	0
21	160727-01-c-ox7a		0.05	6.97	3.01	79.37	0.50	1.88	-	-	-	-	0.16	-	-	-	-	91.94			0	1081	0	0	0
24	160727-01-c-ox8a		0.01	11.64	2.25	78.04	0.43	1.77	-	-	-	-	0.14	-	-	-	-	94.28			0	951	0	0	0

24	160727-01-c-gm1	groundmass	64.89	0.94	16.81	4.99	0.11	0.50	5.77	3.50	2.32	0.06	0.02	-	-	0.16	0.00	100.06	15.16	38.85	42.58	55.70	6.71	37.58	0	144	0	1580	0
25	160727-01-c-gm2		63.37	0.77	17.13	5.17	0.11	1.33	5.90	3.83	2.27	0.00	0.02	-	-	0.11	0.01	100.02	31.42	37.99	44.63	50.07	15.69	34.24	0	130	0	1080	28
26	160727-01-c-gm3		66.58	1.03	15.92	4.12	0.02	0.39	4.51	3.71	2.69	0.05	0.00	-	-	0.16	0.02	99.20	14.39	31.26	46.55	54.58	6.54	38.89	0	0	0	1600	96
27	160727-01-c-gm4		64.97	0.82	16.47	4.24	0.00	0.69	5.43	3.69	2.46	0.11	0.00	-	-	0.11	0.00	98.99	22.56	36.11	44.41	55.99	9.93	34.08	0	0	0	1120	0
28	160727-01-c-gm5		60.86	0.66	19.37	5.10	0.13	0.98	7.32	3.51	1.76	0.02	0.00	-	-	0.09	0.00	99.78	25.46	46.46	40.25	57.82	10.74	31.44	0	0	0	900	0
29	160727-01-c-gm6		62.79	0.73	18.36	3.86	0.07	0.73	6.21	4.04	2.33	0.05	0.00	-	-	0.08	0.00	99.25	25.25	38.10	44.90	60.60	9.95	29.45	0	0	0	800	0
30	160727-01-c-gm7		67.36	1.17	12.84	6.12	0.12	1.14	3.52	3.46	3.15	0.11	0.00	-	-	0.15	0.03	99.16	24.92	26.02	46.25	35.60	16.05	48.35	0	0	0	1470	100
31	160727-01-c-gm8		65.50	1.02	15.62	4.95	0.12	0.58	4.91	3.48	2.73	0.09	0.00	-	-	0.19	0.04	99.22	17.37	33.97	43.57	51.19	8.48	40.33	0	0	0	1920	144
32	160727-01-c-gm9		66.54	1.02	16.21	3.96	0.05	0.48	4.77	3.61	2.67	0.06	0.00	-	-	0.13	0.04	99.53	17.83	32.93	45.13	55.88	7.87	36.26	0	21	0	1270	164
33	160727-01-c-gm10		62.46	0.66	20.39	3.32	0.04	0.36	7.32	3.65	1.82	0.00	0.00	-	-	0.08	0.01	100.12	16.27	45.49	41.03	70.29	4.83	24.88	0	0	0	840	36
34	160727-01-c-gm11		66.26	0.96	15.50	4.58	0.10	0.92	4.24	3.72	2.83	0.08	0.00	-	-	0.11	0.02	99.30	26.45	29.57	46.97	46.61	14.12	39.27	0	0	0	1120	68
35	160727-01-c-gm12		61.82	0.63	19.93	3.56	0.09	0.55	7.48	3.50	1.89	0.00	0.03	-	-	0.09	0.02	99.59	21.64	46.54	39.43	67.85	6.96	25.19	0	192	0	850	72
10	160727-01-c-mi-px1-1	melt inclusion	74.38	1.71	13.93	1.93	0.06	0.35	2.16	3.54	2.92	0.00	0.00	-	-	0.27	0.02	101.28	24.30	17.95	53.17	52.02	11.66	36.32	0	0	0	2700	96
8	160727-01-c-mi-px1-2		71.52	0.51	14.54	1.71	0.00	0.20	1.79	3.84	3.32	0.00	0.01	-	-	0.27	0.05	97.77	17.45	14.06	54.77	52.46	8.30	39.25	0	62	0	2710	184
9	160727-01-c-mi-px1-3		55.79	0.00	29.18	0.69	0.01	0.04	11.49	4.61	0.28	0.00	0.00	-	-	0.00	0.01	102.10	8.53	56.97	41.37	95.14	0.41	4.44	0	0	0	10	48
11	160727-01-c-mi-px1-4		53.09	0.00	30.35	0.70	0.04	0.04	13.08	3.84	0.19	0.00	0.02	-	-	0.00	0.01	101.35	9.09	64.60	34.28	95.64	0.40	3.97	0	123	0	10	56
42	160727-01-c-mi-px2-1a		70.74	0.48	14.06	1.98	0.06	0.32	2.31	3.97	3.07	0.10	0.00	-	-	0.27	0.03	97.38	22.17	17.57	54.62	53.81	10.24	35.95	0	0	0	2720	136
43	160727-01-c-mi-px2-1b		71.59	0.50	14.33	2.10	0.00	0.33	2.33	2.30	3.06	0.12	0.00	-	-	0.27	0.00	96.93	21.68	23.03	41.00	52.71	10.25	37.04	0	0	0	2670	0
12	160727-01-c-mi-px6-1		72.14	1.06	13.45	1.17	0.05	0.19	1.97	3.58	2.89	0.02	0.00	-	-	0.18	0.02	96.72	22.18	16.58	54.47	62.68	8.28	29.04	0	0	0	1820	92
13	160727-01-c-mi-px6-2		73.51	0.47	13.28	1.29	0.07	0.09	1.52	3.25	3.31	0.00	0.00	-	-	0.24	0.02	97.04	10.59	13.36	51.87	57.29	4.53	38.19	0	0	0	2380	88
14	160727-01-c-mi-px6-3		73.91	0.44	12.99	1.57	0.07	0.09	1.58	3.18	3.31	0.00	0.00	-	-	0.25	0.02	97.40	9.17	13.99	51.10	53.88	4.23	41.89	0	0	0	2460	92
15	160727-01-c-mi-px6-4		70.28	1.71	14.69	2.09	0.17	0.35	3.17	3.70	2.50	0.15	0.00	-	-	0.28	0.01	99.10	22.72	24.66	52.14	59.97	9.09	30.93	0	0	0	2790	48
16	160727-01-c-mi-px6-5		73.68	0.47	13.09	1.47	0.11	0.09	1.53	3.22	3.29	0.00	0.00	-	-	0.22	0.02	97.18	10.13	13.53	51.71	54.41	4.62	40.97	0	0	0	2180	64
17	160727-01-c-mi-px6-6		71.66	0.50	15.01	1.30	0.07	0.13	2.17	3.68	2.66	0.00	0.01	-	-	0.29	0.01	97.50	15.35	18.08	55.55	64.43	5.46	30.11	0	75	0	2910	24
30	160727-01-c-mi-px7-1		72.12	0.53	13.95	1.85	0.06	0.35	1.78	3.54	3.25	0.00	0.00	-	-	0.27	0.03	97.72	25.40	14.80	53.15	47.91	13.23	38.86	0	0	0	2700	104
31	160727-01-c-mi-px7-2		54.85	0.04	29.66	0.68	0.03	0.05	12.09	4.10	0.20	0.00	0.01	-	-	0.01	0.00	101.72	12.28	61.28	37.55	95.27	0.58	4.15	0	75	0	50	8
32	160727-01-c-mi-px9-1		53.70	0.01	30.13	1.12	0.05	0.04	12.39	3.83	0.21	0.00	0.00	-	-	0.00	0.01	101.51	5.97	63.30	35.40	93.00	0.42	6.58	0	14	0	30	48
37	160727-01-c-mi-px10-1		50.45	0.02	30.32	1.65	0.00	0.35	14.20	2.87	0.11	0.00	0.00	-	-	0.00	0.01	99.98	27.61	72.73	26.58	88.87	3.07	8.06	0	0	0	0	56
28	160727-01-c-mi-px12-1		74.19	0.50	14.15	1.29	0.01	0.09	1.92	3.55	3.09	0.00	0.00	-	-	0.25	0.02	99.06	11.27	15.93	53.50	62.76	4.20	33.05	0	0	0	2490	92
29	160727-01-c-mi-px12-2		74.32	0.48	13.88	1.28	0.01	0.17	1.61	3.11	3.37	0.00	0.01	-	-	0.24	0.04	98.50	18.69	14.34	49.95	56.76	8.08	35.16	0	41	0	2390	148

24	160727-01-c-mi-px13-1		69.80	0.97	15.01	1.62	0.08	0.36	2.11	4.46	2.91	0.00	0.01	-	-	0.28	0.05	97.66	28.36	15.48	59.14	54.45	12.92	32.63	0	41	0	2840	216
25	160727-01-c-mi-px13-1b		70.52	1.04	15.09	1.69	0.12	0.38	2.15	2.36	3.06	0.04	0.01	-	-	0.32	0.08	96.86	28.51	21.36	42.42	53.76	13.19	33.06	0	62	0	3170	324
26	160727-01-c-mi-px13-2		70.50	1.67	13.94	2.89	0.10	0.28	2.61	3.93	3.02	0.00	0.00	-	-	0.29	0.02	99.26	14.89	19.60	53.44	49.58	7.51	42.91	0	0	0	2900	72
27	160727-01-c-mi-px13-2b		71.34	1.69	14.22	2.90	0.10	0.28	2.56	2.35	3.21	0.00	0.02	-	-	0.31	0.04	99.01	14.73	24.13	39.94	49.12	7.49	43.39	0	130	0	3100	140
5	160727-01-c-mi-px14-1		66.59	0.24	17.60	1.27	0.00	0.21	3.07	4.15	2.73	0.03	0.00	-	-	0.48	0.05	96.42	22.77	22.21	54.27	70.54	6.71	22.75	0	0	0	4790	200
6	160727-01-c-mi-px14-2		64.52	0.77	19.21	0.89	0.04	0.30	3.86	5.22	1.81	0.00	0.00	-	-	0.36	0.36	97.33	37.17	24.97	61.10	77.74	8.27	13.99	0	0	0	3640	1432
7	160727-01-c-mi-px14-2b		65.07	0.64	18.46	0.84	0.00	0.31	3.52	4.90	1.84	0.00	0.00	-	-	0.38	0.30	96.25	39.49	24.16	60.83	76.39	9.33	14.29	0	0	0	3760	1208
44	160727-01-c-mi-px15-1a		74.26	0.37	13.58	1.64	0.00	0.10	1.88	3.38	3.29	0.00	0.00	-	-	0.26	0.02	98.79	9.96	15.81	51.37	56.93	4.29	38.78	0	0	0	2570	80
45	160727-01-c-mi-px15-1b		74.71	0.39	13.59	1.76	0.04	0.15	1.94	3.63	3.33	0.07	0.02	-	-	0.27	0.00	99.90	13.16	15.56	52.66	55.01	5.92	39.06	0	164	0	2660	0
46	160727-01-c-mi-px15-2		67.51	0.95	17.39	2.98	0.00	0.04	2.79	5.80	3.17	0.22	0.03	-	-	0.27	0.02	101.16	2.45	16.36	61.54	53.97	1.13	44.90	0	205	0	2700	80
47	160727-01-c-mi-px15-3		53.78	0.01	30.10	0.70	0.05	0.04	12.66	3.74	0.24	0.00	0.00	-	-	0.01	0.00	101.33	8.99	64.22	34.32	95.45	0.41	4.14	0	0	0	50	0
18	160727-01-c-mi-px17-1		74.31	0.42	12.29	2.02	0.06	0.16	1.31	2.68	4.51	0.00	0.00	-	-	0.31	0.00	98.08	12.43	11.37	42.02	42.08	7.20	50.72	0	0	0	3140	4
22	160727-01-c-mi-px17-2		72.59	1.75	13.83	2.70	0.08	0.51	2.75	3.12	3.04	0.22	0.00	-	-	0.24	0.06	100.89	25.29	22.88	46.96	49.34	12.81	37.85	0	0	0	2440	244
19	160727-01-c-mi-px17-3		75.78	0.41	13.07	1.59	0.03	0.07	1.42	2.74	4.82	0.00	0.02	-	-	0.33	0.00	100.27	7.20	11.71	40.90	51.54	3.49	44.97	0	157	0	3270	0
20	160727-01-c-mi-px17-4		72.51	0.41	13.16	4.95	0.04	0.37	2.31	3.36	3.62	0.00	0.00	-	-	0.24	0.34	101.31	11.84	18.17	47.84	34.46	7.76	57.78	0	0	0	2440	1356
21	160727-01-c-mi-px17-5		72.25	0.81	14.80	1.18	0.05	0.22	1.90	3.30	3.77	0.00	0.01	-	-	0.29	0.01	98.59	24.73	15.38	48.32	60.77	9.70	29.53	0	75	0	2940	20
23	160727-01-c-mi-px17-6		68.35	1.03	14.06	6.60	0.09	0.48	3.14	3.03	3.22	0.22	0.00	-	-	0.29	0.07	100.58	11.37	25.23	44.02	35.08	7.38	57.54	0	0	0	2890	288
38	160727-01-c-mi-px18-1a		71.93	0.65	14.13	1.66	0.04	0.19	1.97	4.02	2.98	0.04	0.02	-	-	0.23	0.02	97.87	16.82	15.41	56.83	55.89	7.42	36.69	0	130	0	2290	92
39	160727-01-c-mi-px18-1b		72.05	0.64	14.11	1.68	0.03	0.19	2.08	3.92	3.08	0.00	0.00	-	-	0.24	0.03	98.02	16.71	16.19	55.25	56.90	7.20	35.90	0	21	0	2350	116
40	160727-01-c-mi-px18-2		71.34	0.44	15.72	1.78	0.08	0.26	2.57	4.04	2.93	0.00	0.00	-	-	0.27	0.06	99.47	20.58	19.20	54.69	59.52	8.33	32.15	0	21	0	2690	236
41	160727-01-c-mi-px18-3		54.35	0.00	29.82	0.61	0.02	0.05	12.12	4.17	0.20	0.00	0.00	-	-	0.00	0.00	101.33	12.39	60.90	37.89	95.74	0.53	3.73	0	0	0	0	0
54	160727-01-c-mi-ol1-1a		61.57	0.23	21.35	1.57	0.10	1.28	4.28	4.37	1.35	0.09	0.00	-	-	0.53	0.22	96.93	59.19	31.02	57.36	58.81	24.38	16.81	0	0	0	5290	872
55	160727-01-c-mi-ol1-1b		54.00	0.46	19.56	4.78	0.09	5.66	6.39	3.21	1.11	0.11	0.00	-	-	0.32	0.19	95.88	67.84	47.24	42.96	35.48	43.77	20.75	0	21	0	3220	760
48	160727-01-c-mi-ol6-1a		42.57	0.93	16.35	7.64	0.07	16.37	10.99	2.12	0.28	0.01	0.00	-	-	0.12	0.04	97.49	79.26	72.48	25.33	27.65	57.34	15.01	0	7	0	1150	144
49	160727-01-c-mi-ol6-1b		43.15	1.00	15.05	7.88	0.10	14.51	15.26	1.66	0.20	0.00	0.00	-	-	0.07	0.07	98.94	76.64	82.50	16.22	36.68	48.53	14.79	0	0	0	670	284
51	160727-01-c-mi-ol7-1a		59.06	0.53	22.16	1.32	0.12	0.26	5.73	3.84	1.36	0.14	0.01	-	-	0.46	0.58	95.55	26.20	40.09	48.61	80.38	5.14	14.48	0	41	0	4560	2300
52	160727-01-c-mi-ol7-1b		45.52	1.40	16.43	8.13	0.05	7.23	17.63	1.25	0.36	0.01	0.04	-	-	0.08	0.10	98.23	61.32	86.73	11.16	51.79	29.56	18.65	0	274	0	790	388
53	160727-01-c-mi-ol7-2		43.67	1.62	16.94	8.10	0.15	9.00	18.80	1.22	0.27	0.10	0.00	-	-	0.12	0.11	100.11	66.45	88.13	10.37	49.94	33.27	16.80	0	0	0	1230	444
50	160727-01-c-mi-ol8-2		58.60	0.20	23.03	1.63	0.02	0.72	4.52	4.14	1.50	0.11	0.00	-	-	0.47	0.34	95.28	43.98	32.78	54.26	66.53	14.72	18.75	0	0	0	4720	1352

36	160727-01-c-mi-ol-1		51.35	0.43	19.08	9.90	0.07	0.78	5.33	3.83	1.20	0.07	0.00	-	-	0.27	12.76	105.05	12.32	38.94	50.66	37.68	7.68	54.64	0	0	0	2720	51028
37	160727-01-c-mi-ol-2		58.94	0.48	21.57	2.77	0.09	0.89	5.47	4.40	1.56	0.11	0.00	-	-	0.32	0.87	97.47	36.45	35.77	52.04	61.65	13.98	24.37	0	0	0	3160	3460
38	160727-01-c-mi-ol-3a		59.09	0.48	22.14	2.92	0.12	0.76	5.82	4.38	1.67	0.08	0.00	-	-	0.29	0.33	98.07	31.73	37.02	50.37	63.57	11.56	24.87	0	21	0	2910	1304
39	160727-01-c-mi-ol-3b		59.70	0.53	22.70	2.87	0.05	0.81	5.75	2.85	1.66	0.04	0.00	-	-	0.30	0.38	97.63	33.37	44.63	40.01	63.09	12.32	24.59	0	0	0	3010	1504
Average	160727-01-c-mi-h-ol1-1		44.10	0.67	13.16	5.79	0.12	12.52	11.55	1.63	0.41	-	0.15	-	-	0.19	0.48	90.73	79.41	77.05	19.70	34.50	52.02	13.49	0	999	0	1910	1900
Average	160727-01-c-mi-h-ol2-1		45.45	0.68	14.37	7.39	0.10	12.03	12.66	1.94	0.44	-	0.05	-	-	0.17	0.53	95.76	74.37	75.84	21.00	35.99	47.61	16.40	0	311	0	1735	2106
34	160727-01-c-mi-h-ol3-1		41.35	0.61	13.29	4.56	0.11	16.48	10.60	1.78	0.47	-	0.05	-	-	0.20	0.60	90.05	86.56	73.72	22.37	28.57	61.83	9.60	0	308	0	2040	2412
35	160727-01-c-mi-h-ol4-1a		45.86	0.76	15.00	5.93	0.10	10.11	12.67	2.17	0.53	-	0.04	-	-	0.20	0.60	93.93	75.26	73.51	22.81	40.40	44.85	14.74	0	294	0	2000	2404
36	160727-01-c-mi-h-ol5-1		41.67	0.67	13.12	5.62	0.08	11.53	11.36	1.80	0.37	-	0.14	-	-	0.19	0.58	87.07	78.54	75.48	21.59	35.75	50.46	13.79	0	944	0	1850	2312
Average	160727-01-c-mi-h-ol7-1		47.40	0.78	14.53	8.45	0.08	12.19	9.99	1.96	0.54	-	0.02	-	-	0.14	0.13	96.16	72.00	70.44	25.06	29.78	50.56	19.66	0	103	0	1410	510
39	160727-01-c-mi-h-ol8-1		46.75	0.70	14.51	8.05	0.09	9.58	11.42	1.84	0.60	-	0.02	-	-	0.16	0.53	94.20	67.97	73.83	21.57	36.80	42.96	20.24	0	103	0	1630	2132
Average	160727-01-c-mi-h-ol9-1		46.32	0.66	13.63	7.87	0.15	11.74	10.81	1.87	0.49	-	0.05	-	-	0.15	0.46	94.16	72.67	73.10	22.93	32.48	49.07	18.45	0	308	0	1495	1840
	150318-01 (North Crater LF)																											
3	150318-01-pl1r		50.91	0.01	30.61	0.73	0.00	0.09	13.99	3.20	0.19	-	-	-	-	-	-	99.73		69.94	28.94				0	0	0	0	0
4	150318-01-pl1c		48.95	0.05	32.34	0.71	0.00	0.07	15.38	2.61	0.14	-	-	-	-	-	-	100.25		75.92	23.28				0	0	0	0	0
5	150318-01-pl2		56.62	0.02	27.09	0.29	0.00	0.01	9.55	5.41	0.58	-	-	-	-	-	-	99.57		47.67	48.90				0	0	0	0	0
6	150318-01-pl3		49.83	0.03	31.44	0.73	0.00	0.07	14.78	2.86	0.20	-	-	-	-	-	-	99.94		73.19	25.62				0	0	0	0	0
7	150318-01-pl4	plagioclase	46.81	0.00	33.88	0.71	0.01	0.07	17.06	1.65	0.07	-	-	-	-	-	-	100.25		84.77	14.84				0	0	0	0	0
8	150318-01-pl5		49.65	0.04	31.78	0.59	0.01	0.04	14.85	2.80	0.19	-	-	-	-	-	-	99.96		73.77	25.13				0	0	0	0	0
9	150318-01-pl6mic		55.93	0.05	27.17	0.64	0.00	0.08	10.17	4.89	0.50	-	-	-	-	-	-	99.43		51.84	45.14				0	0	0	0	0
10	150318-01-pl7mic		49.56	0.04	31.73	0.92	0.00	0.09	15.22	2.74	0.18	-	-	-	-	-	-	100.49		74.63	24.30				0	0	0	0	0
11	150318-01-pl8mic		51.63	0.10	30.40	0.89	0.04	0.13	14.29	2.91	0.23	-	-	-	-	-	-	100.62		72.06	26.56				0	0	0	0	0
12	150318-01-pl9mic		49.41	0.04	32.06	0.83	0.00	0.07	15.26	2.46	0.17	-	-	-	-	-	-	100.31		76.59	22.38				0	0	0	0	0
13	150318-01-pl10mic		69.86	1.39	13.42	5.03	0.08	0.73	2.73	1.51	6.20	-	-	-	-	-	-	100.94		21.24	21.31				0	0	0	0	0
7	150318-01-cpx1		43.05	0.21	3.00	5.47	0.15	15.46	19.01	0.29	-	-	0.46	-	0.03	-	-	87.14	83.44			42.44	48.03	9.53	0	3161	212	0	0
9	150318-01-cpx2	pyroxene	51.97	0.45	1.68	11.95	0.29	14.47	19.44	0.08	-	-	0.01	-	0.04	-	-	100.36	68.34			39.75	41.17	19.07	0	48	283	0	0
10	150318-01-cpx3		51.66	0.53	2.16	11.27	0.32	14.28	19.82	0.05	-	-	0.00	-	0.00	-	-	100.08	69.31			40.87	40.98	18.15	0	0	0	0	0
16	150318-01-cpx4 (opx)		53.29	0.23	0.97	19.64	0.47	24.18	2.05	0.04	-	-	0.01	-	0.00	-	-	100.87	68.70			4.01	65.95	30.04	0	55	0	0	0

17	150318-01-cpx5r		53.78	0.19	2.13	5.22	0.14	18.63	20.20	0.03	-	-	0.44	-	0.00	-	-	100.77	86.43			40.25	51.65	8.11	0	3038	0	0	0
18	150318-01-cpx5c		52.14	0.48	1.77	11.37	0.31	14.63	19.41	0.07	-	-	0.04	-	0.01	-	-	100.24	69.65			39.91	41.85	18.24	0	294	110	0	0
8	150318-01-opx1		54.13	0.20	0.95	16.81	0.38	26.00	2.37	0.00	-	-	0.05	-	0.03	-	-	100.94	73.39			4.58	70.03	25.40	0	363	251	0	0
11	150318-01-opx2c		53.90	0.29	0.61	19.04	0.59	24.92	1.60	0.00	-	-	0.02	-	0.02	-	-	101.00	70.00			3.13	67.81	29.06	0	103	181	0	0
12	150318-01-opx3r (cpx)		51.94	0.53	2.30	9.09	0.21	15.71	20.08	0.05	-	-	0.09	-	0.03	-	-	100.03	75.50			40.96	44.57	14.46	0	595	212	0	0
13	150318-01-opx3c		52.87	0.24	0.75	17.55	0.51	25.59	1.56	0.01	-	-	0.00	-	0.00	-	-	99.08	72.22			3.07	70.00	26.93	0	14	0	0	0
14	150318-01-opx4		52.44	0.34	0.68	20.27	0.51	23.73	1.76	0.02	-	-	0.03	-	0.04	-	-	99.81	67.61			3.48	65.25	31.26	0	171	299	0	0
15	150318-01-opx5		53.45	0.27	0.94	19.21	0.39	24.19	1.95	0.16	-	-	0.01	-	0.03	-	-	100.60	69.18			3.86	66.51	29.63	0	82	212	0	0
6	150318-01-ox1b		0.04	46.67	0.30	42.70	0.38	5.44	-	-	-	-	0.05	-	-	-	-	95.58							0	308	0	0	0
8	150318-01-ox2b		0.00	42.36	0.43	47.39	0.33	4.77	-	-	-	-	0.10	-	-	-	-	95.36							0	677	0	0	0
5	150318-01-ox1a		0.06	15.58	2.17	71.32	0.40	3.32	-	-	-	-	0.34	-	-	-	-	93.18							0	2313	0	0	0
7	150318-01-ox2a		0.06	13.75	3.28	71.53	0.39	3.71	-	-	-	-	0.48	-	-	-	-	93.19							0	3264	0	0	0
9	150318-01-ox2c	opaque	0.09	13.23	3.50	71.88	0.31	3.76	-	-	-	-	0.41	-	-	-	-	93.18							0	2798	0	0	0
10	150318-01-ox2d		0.08	15.53	3.15	70.49	0.32	3.64	-	-	-	-	0.38	-	-	-	-	93.58							0	2614	0	0	0
11	150318-01-ox3a		0.03	13.93	3.37	72.11	0.31	3.51	-	-	-	-	0.33	-	-	-	-	93.58							0	2244	0	0	0
12	150318-01-ox3b		0.05	13.53	3.40	71.67	0.36	3.74	-	-	-	-	0.38	-	-	-	-	93.14							0	2614	0	0	0
13	150318-01-ox4a		0.03	13.74	3.35	71.49	0.28	3.61	-	-	-	-	0.36	-	-	-	-	92.88							0	2470	0	0	0
14	150318-01-ox4b		0.07	13.14	3.47	71.49	0.28	3.81	-	-	-	-	0.31	-	-	-	-	92.56							0	2094	0	0	0
5	150318-01-mi-px2-1a	MI	52.36	0.03	29.88	0.63	0.09	0.05	12.82	3.77	0.29	0.00	0.00	-	-	0.00	0.01	99.91	11.31	64.17	34.12	95.86	0.47	3.67	0	0	0	0	40
6	150318-01-mi-px2-1b		52.18	0.02	29.71	0.65	0.00	0.05	13.22	3.30	0.27	0.00	0.01	-	-	0.00	0.01	99.43	11.62	67.70	30.63	95.83	0.48	3.68	0	41	0	30	32
7	150318-01-gm1		65.16	0.83	15.14	5.84	0.09	1.31	4.51	3.80	1.65	0.07	0.02	-	-	0.15	0.04	98.61	28.60	33.79	51.49	41.39	16.76	41.84	0	151	0	1450	176
8	150318-01-gm2		62.76	0.90	15.59	6.51	0.02	2.11	5.40	3.61	1.52	0.04	0.00	-	-	0.13	0.04	98.62	36.66	39.31	47.54	40.21	21.92	37.87	0	0	0	1300	140
9	150318-01-gm3		63.83	0.96	15.25	6.84	0.12	2.10	4.47	3.87	1.70	0.07	0.00	-	-	0.15	0.02	99.36	35.37	33.13	51.84	35.13	22.94	41.93	0	0	0	1450	76
10	150318-01-gm4		63.24	0.88	15.45	5.76	0.11	1.52	5.97	3.85	1.38	0.05	0.02	-	-	0.12	0.02	98.36	31.95	40.95	47.80	47.48	16.78	35.74	0	103	0	1200	64
11	150318-01-gm5		63.29	0.95	15.26	6.51	0.19	2.06	4.58	3.65	2.31	0.05	0.00	-	-	0.14	0.03	99.01	36.08	32.89	47.41	36.57	22.88	40.55	0	0	0	1360	108
12	150318-01-gm6	groundmass	63.55	0.93	15.46	5.96	0.05	1.41	5.90	3.44	1.84	0.07	0.01	-	-	0.12	0.04	98.77	29.70	41.22	43.50	47.16	15.69	37.15	0	41	0	1180	160
13	150318-01-gm7		62.71	0.90	15.67	6.67	0.09	2.23	4.90	3.27	2.53	0.04	0.00	-	-	0.15	0.06	99.21	37.40	35.39	42.81	37.06	23.54	39.40	0	0	0	1510	248
14	150318-01-gm8		60.96	0.92	15.69	5.93	0.11	2.26	4.94	2.21	4.66	0.08	0.01	-	-	0.14	0.05	97.95	40.39	34.11	27.57	38.86	24.70	36.45	0	89	0	1430	188
15	150318-01-gm9		62.34	0.90	15.81	6.18	0.11	2.27	6.06	3.22	1.60	0.07	0.00	-	-	0.13	0.07	98.75	39.55	43.99	42.23	43.17	22.48	34.35	0	0	0	1260	284
16	150318-01-gm10		62.33	0.99	15.74	6.66	0.20	2.17	5.02	3.45	2.10	0.07	0.00	-	-	0.13	0.07	98.91	36.73	36.46	45.39	37.92	22.80	39.27	0	0	0	1270	260

17	150318-01-gm11	61.25	0.88	15.38	6.70	0.09	2.32	4.98	2.39	4.14	0.09	0.01	-	-	0.18	0.06	98.48	38.19	35.00	30.35	37.05	24.04	38.91	0	82	0	1770	248
18	150318-01-gm12	62.71	0.93	15.86	6.12	0.10	1.99	4.99	2.69	3.29	0.05	0.00	-	-	0.13	0.06	98.91	36.66	36.22	35.33	39.84	22.06	38.11	0	0	0	1340	224

Electron microprobe analysis were done using a JEOL JXA-8230 Electron Probe Micro-Analyzer (EPMA) at the School of Geography, Environment and Earth Sciences, Victoria University of Wellington.

Not analysed (-)

Text in red are possible erroneous values

Standards analysed as unknown for the analyses are listed in Appendix Table 8

Mg#=molar(Mg/(Mg+Fe))*100

%An=molar(Ca/(Ca+Na+K))*100

%Ab=molar(Na/(Ca+Na+K))*100

Wo=molar(Ca/(Ca+Mg+Fetotal))*100

En=molar(Mg/(Ca+Mg+Fetotal))*100

Fs=molar(Fetotal/(Ca+Mg+Fetotal))*100

Appendix Table 8. Statistics for all standards analysed as unknown, and comparison to reference values. Compiled from several analysis sessions.

	SiO_2	TiO_2	Al_2O_3	FeO	MnO	MgO	CaO	Na_2O	K_2O	P_2O_5	SrO	Cr_2O_3	NiO	F	Cl	SO_3	Total	Comment
									Plagioclase									
N	38	38	38	38	16	38	38	38	38		22						38	
Mean	51.46	0.03	30.92	0.37	0.01	0.13	13.65	3.49	0.14		0.001						100.19	
Median	51.40	0.03	30.97	0.43	0.01	0.14	13.69	3.46	0.12								100.29	
SD	0.4	0.02	0.2	0.1	0.01	0.01	0.2	0.1	0.04		0.01						0.5	
Reference Value	51.25	0.05	30.91	0.46	0.01	0.14	13.64	3.45	0.18								100.09	Plagioclase, NMNH 11590
Relative Uncertainty (%)	0.7	48	0.6	23	99	9	1	4	22									
									Orthopyroxene									
N	64	64	64	64	64	64	64	48	8			64	40				64	
Mean	54.68	0.08	0.81	15.05	0.49	27.41	0.99	0.004	0.002			0.67	0.005				100.19	
Median	54.48	0.08	0.69	15.08	0.50	27.25	1.21					0.71					99.96	
SD	0.6	0.02	0.2	0.3	0.07	0.6	0.5	0.01	0.003			0.1	0.01				1.0	
Reference Value	54.09	0.16	1.23	15.22	0.49	26.79	1.52	<0.05	<0.05			0.75					99.50	Hypersthene, USNM 746
Relative Uncertainty (%)	1	12	16	2	15	2	34					16						
									Olivine									
N	68	48	36	68	68	68	68	36				56	68				68	
Mean	39.37	0.002	0.003	16.84	0.30	44.13	0.01	0.003				0.02	0.01				100.68	
Median	39.27			16.86	0.32	43.92						0.02					100.40	
SD	0.4	0.003	0.004	0.3	0.06	0.7	0.01	0.01				0.01	0.01				1	
Reference Value	38.95			16.62	0.30	43.58						0.02					99.47	Olivine, USNM 2566
Relative Uncertainty (%)	1			2	20	2						65						
									Basaltic Glass									
N	49	49	49	49	49	49	49	49	49	21		49		12	49	37	49	
Mean	50.68	4.00	12.33	13.26	0.19	5.05	9.16	2.31	0.84	0.31		0.01			0.02	0.03	98.02	
Median	50.82	4.00	12.32	13.30	0.19	5.06	9.19	2.46	0.84	0.31		0.01			0.02	0.03	98.32	

SD	0.4	0.05	0.1	0.2	0.04	0.09	0.2	0.4	0.03	0.03	0.02		0.004	0.01	1	
Reference Value	50.94	4.06	12.49	13.30	0.15	5.08	9.30	2.66	0.82						98.80	Glass, Basalt NMNH 113498-1 (A-99)
Relative Uncertainty (%)	0.7	1	1	2	28	2	2	14	4							
								Rhyolitic Glass								
N	49	49	49	49	49	49	49	49	49	21	49	12	49	37	49	
Mean	76.87	0.07	12.14	1.10	0.03	0.02	0.44	3.04	4.92		0.01	0.06	0.10	0.01	98.72	
Median	76.98	0.07	12.18	1.11	0.02	0.02	0.43	3.42	4.94			0.06	0.11	0.01	99.07	
SD	0.6	0.01	0.2	0.07	0.02	0.01	0.02	0.7	0.1		0.01	0.02	0.02	0.01	1	
Reference Value	76.71	0.12	12.06	1.23	0.03	<0.10	0.50	3.75	4.89						99.29	Glass, Rhyolite NMNH 72854 VG-568
Relative Uncertainty (%)	0.8	10	1	6	80		3	17	2							
								Magnetite								
N	26	26	26	26	26	26					26				26	
Mean	0.02	0.09	0.03	91.09	0.06	0.09					0.22				91.59	
Median	0.03	0.08	0.03	91.03	0.06	0.08					0.24				91.58	
SD	0.02	0.03	0.01	0.5	0.03	0.01					0.07				0.6	
Reference Value		0.16		90.95	<0.01	0.05					0.25				91.41	Magnetite, NMNH 114887
Relative Uncertainty (%)		21		0.6		23					27					
								Ilmenite								
N	26	26	26	26	26	26					26				26	
Mean	0.01	45.41	0.01	45.75	4.42	0.31					0.01				95.93	
Median	0.002	45.45	0.01	45.57	4.51	0.31					0.01				96.25	
SD	0.01	0.7	0.01	0.8	0.5	0.02					0.01				0.8	
Reference Value		45.70		46.54	4.77	0.31									97.32	Ilmenite, NMNH 96189
Relative Uncertainty (%)		2		2	11	7										
									Clinopyroxene - Augite							
N	67	67	67	67	67	67	67	67	27		67	40			67	
Mean	50.83	0.80	8.75	6.45	0.14	16.82	15.80	0.55	0.01		0.15	0.04			100.32	

Median	50.79	0.79	8.73	6.45	0.13	16.75	15.84	0.31	0.004		0.15	0.04	100.41	
SD	0.4	0.04	0.1	0.2	0.03	0.3	0.3	0.4	0.01		0.03	0.02	0.6	
Reference Value	50.73	0.74	8.73	6.34	0.13	16.65	15.82	1.27					100.41	Kakanui augite, NMNH 122142
Relative Uncertainty (%)	0.8	5	2	3	23	2	2	30						
								Clinopyroxene - Diopside						
N	18	18	18	18	18	18	18	18	18		18		18	
Mean	55.98	0.01	0.02	0.07	0.02	19.29	25.96	0.01	0.004		0.01		101.37	
Median	56.06		0.01	0.06	0.01	19.23	26.03	0.01					101.44	
SD	0.4	0.02	0.02	0.03	0.02	0.4	0.3	0.01	0.01		0.02		0.9	
Reference Value	55.81		0.11	0.24	0.04	18.30	25.63	0.34					99.53	Diopside, NMNH 117733
Relative Uncertainty (%)	0.7		21	11	48	2	1	3						

Standards analyzed as unknown for all the microprobe analysis sessions.

Reference values are from http://mineralsciences.si.edu/facilities/standards/datasheets.htm

Appendix Table 9. Microprobe analytical conditions.

Plagioclase

15 kV, 12 nA, 1 micron

Oxide	Channel	Crystal	Peak/Bkg (seconds)	Standard
CaO	1	PETL	30/15	Plagioclase NMNH 115900
TiO2	1	PETL	30/15	TiO2 synthetic
Na2O	2	TAP	30/15	Plagioclase NMNH 115900
MgO	2	TAP	30/15	MgO synthetic
SiO2	3	TAP	30/15	Plagioclase NMNH 115900
Al2O3	3	TAP	30/15	Plagioclase NMNH 115900
FeO	4	LIF	30/15	FeO synthetic
K2O	4	PETJ	30/15	Orthoclase Or-1A
SrO	5	PETL	60/30	Strontianite NMNH R 10065

Clinopyroxene (original analyses)

15 kV, 12 nA, 1 micron

CaO	1	PETL	30/15	Kakanui Augite
TiO2	1	PETL	30/15	TiO2 synthetic
Na2O	2	TAP	30/15	Plagioclase NMNH 115900
MgO	2	TAP	30/15	Kakanui Augite
SiO2	3	TAP	30/15	Kakanui Augite
Al2O3	3	TAP	30/15	Kakanui Augite
FeO	4	LIF	30/15	Kakanui Augite
K2O	4	PETJ	30/15	Orthoclase Or-1A
MnO	5	LIFL	30/15	MnO synthetic
Cr2O3	5	LIFL	30/15	Cr2O3 synthetic

Orthopyroxene

15 kV, 12 nA, 1 micron

CaO	1	PETL	30/15	Hypersthene USNM 746
TiO2	1	PETL	30/15	TiO2 synthetic
MgO	2	TAP	30/15	Hypersthene USNM 746
SiO2	3	TAP	30/15	Hypersthene USNM 746
Al2O3	3	TAP	30/15	Hypersthene USNM 746
FeO	4	LIF	30/15	Hypersthene USNM 746
MnO	5	LIFL	30/15	MnO synthetic
Cr2O3	5	LIFL	30/15	Cr2O3 synthetic

Oxides

15 kV, 12 nA, 1 micron

TiO2	1	PETL	30/15	Ilmenite NMNH 96189

Appendix Table 9 continued

MgO	2	TAP	30/15	MgO synthetic
SiO2	3	TAP	30/15	Plagioclase NMNH 115900
Al2O3	3	TAP	30/15	Plagioclase NMNH 115900
FeO	4	LIF	30/15	Magnetite NMNH 96189
MnO	5	LIFL	30/15	MnO synthetic
Cr2O3	5	LIFL	30/15	Cr2O3 synthetic
Olivine				
15 kV, 12 nA, 1 micron				
CaO	1	PETL	30/15	Wollastonite synthetic
MnO	1	LIFL	30/15	MnO synthetic
MgO	2	TAP	30/15	Springwater Olivine
SiO2	3	TAP	30/15	Springwater Olivine
FeO	4	LIF	30/15	Springwater Olivine
Cr2O3	5	LIFL	30/15	Cr2O3 synthetic
NiO	5	LIFL	30/15	NiO synthetic
Glass				
15 kV, 8 nA, 10 micron				
CaO	1	PETL	30/15	VG-A99
TiO2	1	PETL	30/15	TiO2 synthetic
FeO	1	LIFL	30/15	VG-A99
K2O	1	LIFL	30/15	VGA-568
Na2O	2	TAP	15/10 (no peak search)	VGA-568
MgO	2	TAP	30/15	VG-A99
F	2	LDE1	60/30	Fluorite
SiO2	3	TAP	30/15	VGA-568
Al2O3	3	TAP	30/15	VGA-568
MnO	5	LIFL	30/15	MnO synthetic
Cr2O3	5	LIFL	30/15	Cr2O3 synthetic
Cl	5	LIFL	60/30	Scapolite 63-1805

Appendix Table 10. List of FTIR measurements, sample spectra measurements and corresponding concentrations.

					Sample spectra measurements								Concentrations			
					Transmission				Reflection							
		SiO_2	Density	thickness	H_2Ot	H_2Omol	CO_3^-		RI				H_2Ot	H_2Omol	OH^-	CO_2
Sample	Comp.	wt.%	g/cm³	µm	3535 cm^{-1}	1630 cm^{-1}	1515 cm^{-1}	1430 cm^{-1}	n	m	v1	v2		wt.%		ppm
150319-02-a1-mi-px1-1	Andesite	57	2.6633	36	0.240	0.0750			1.56	5	2380	1936	0.72	0.33	0.39	
150319-02-a1-mi-px1-2	Andesite	58	2.6346	37	0.281	0.0770			1.56	5	2094	1659	0.84	0.34	0.50	
150319-02-a1-mi-px1-3	Andesite	61	2.5732	53	0.164	0.0710			1.54	4	1585	1338	0.35	0.23	0.13	
150319-02-a1-mi-px2-1	Andesite	65	2.6029	26	0.086	0.0470			1.53	8	2920	1898	0.37	0.30	0.07	
150319-02-a1-mi-px4-1	Andesite	65	2.5967	34	0.187	0.0600			1.53	5	2677	2198	0.61	0.29	0.32	
150319-02-a1-mi-ol1-1	Basalt	52	2.7879	68	0.242				1.58	6	2141	1863	0.36	0.00	0.36	
150319-02-a1-mi-ol3-1	Basalt	49	2.7625	87	0.120				1.59	5	1659	1477	0.14	0.00	0.14	
150319-02-a1-mi-ol6-01	Basalt	52	2.7879	18	0.111	0.0260			1.58	4	2839	2121	0.65	0.34	0.31	
150319-02-a1-mi-ol6-02	Basalt	52	2.7879	18	0.129	0.0160			1.58	4	2854	2160	0.73	0.20	0.52	
150319-02-a1-mi-ol7-01a	Basalt	53	2.7963	24	0.142	0.0190			1.58	4	2935	2411	0.60	0.18	0.42	
150319-02-a1-mi-ol7-01b	Basalt	53	2.7963	26	0.110	0.0160			1.58	4	2225	1743	0.43	0.14	0.29	
150319-02-a2-mi-ol1-1	Basalt	50	2.7674	56	0.965	0.2380			1.59	8	1763	1311	1.79	0.99	0.80	
150319-02-a2-mi-ol2-01	Basalt	52	2.7709	35	0.333	0.0820			1.58	6	2927	2384	0.99	0.55	0.44	
150319-02-a2-mi-ol2-02	Basalt	52	2.7709	36	0.498	0.1750	0.045	0.01	1.58	3	2206	1940	1.44	1.14	0.30	339
150319-02-a2-mi-h-ol2-1a	Basalt	48	2.9095	34	0.383	0.045	0.023	0.04	1.60	4	2981	2615	1.10	0.29	0.81	355
150319-02-a2-mi-h-ol2-1b	Basalt	48	2.9095	33	0.487	0.060	0.022		1.60	4	2781	2407	1.43	0.40	1.03	133
150319-02-a2-mi-h-ol2-2a	Basalt	47	2.9729	34	0.212				1.60	4	2391	2025	0.60	0.00	0.60	
150319-02-a2-mi-h-ol2-2b	Basalt	47	2.9729	35	0.153				1.60	5	2638	2198	0.41	0.00	0.41	
150319-02-a2-mi-h-ol3-1	Basalt	50	2.8864	20	0.269	0.057			1.59	4	2839	2202	1.35	0.64	0.71	
150319-02-a2-mi-h-ol3-2	Basalt	47	3.0523	20	0.168				1.60	4	2850	2218	0.80	0.00	0.80	
150319-02-a2-mi-h-ol4-1	Basalt	48	2.8833	12	0.122	0.035			1.60	4	3062	2017	1.01	0.65	0.36	
150319-02-a2-mi-h-ol4-2	Basalt	48	2.9009	12	0.083				1.60	3	2958	2179	0.68	0.00	0.68	
150319-02-b2-mi-ol2-1	Andesite	60	2.6547	45	0.218				1.55	4	2268	1979	0.53	0.00	0.53	
150319-02-b2-mi-ol3-1	Basalt	52	2.7872	45	0.350	0.2090		0.06	1.58	5	1666	1319	0.79	1.06	-0.27	269
150319-02-b2-mi-ol3-2	Basalt	52	2.7872	40	0.326	0.1050			1.58	5	2160	1763	0.84	0.61	0.23	
150319-02-b2-mi-ol3-3	Basalt	54	2.7416	38	0.296	0.1030			1.58	5	2198	1778	0.82	0.64	0.18	
150319-02-a2-mi-px1-01	Andesite	61	2.6201	25	0.148	0.0400			1.54	4	2785	2256	0.67	0.27	0.40	

150319-02-a2-mi-px3-01	Andesite	62	2.6099	46	0.167	0.0550			1.54	4	1647	1365	0.40	0.20	0.21	
150319-02-a2-mi-px4-01	Andesite	58	2.654	45	0.303	0.1610	0.036		1.56	3	2634	2422	0.73	0.57	0.16	175
150319-02-b2-mi-px1-1	Andesite	65	2.5867	20	0.211	0.0630			1.53	5	2322	1485	1.21	0.53	0.68	
150319-02-b2-mi-px1-2	Andesite	63	2.6539	20	0.128	0.0960			1.54	6	2839	1840	0.72	0.79	-0.08	
150319-02-b2-mi-px2-1	Andesite	61	2.6201	15	0.258				1.54	4	3444	2561	1.95	0.00	1.95	
150319-02-b2-mi-px2-2	Andesite	61	2.6201	14	0.170	0.0360			1.54	5	3020	1902	1.30	0.41	0.89	
150319-01-e-mi-px1-1	Andesite	58	2.6303	55	0.267	0.0860	0.053		1.56	6	2777	2426	0.54	0.26	0.28	215
150319-01-e-mi-px4-01	Andesite	57	2.6878	31	0.238				1.56	5	2819	2295	0.84	0.00	0.84	
150319-01-e-mi-px4-02	Andesite	57	2.6878	33	0.280	0.0870			1.56	5	2495	2009	0.92	0.42	0.50	
150319-01-e-mi-px5-01	Basalt	55	2.7096	20	0.254	0.1150			1.57	3	2245	1778	1.31	1.33	-0.02	
150319-01-e-mi-px6-01	Andesite	57	2.6542	51	0.523	0.2670			1.56	5	2777	2465	1.12	0.84	0.27	
150319-01-e-mi-px8-01	Andesite	55	2.6705	45	0.552	0.2780			1.56	3	1959	1747	1.33	0.99	0.34	
150318-03-mi-px1-1	Rhyolite	67	2.5634	24	0.115	0.019			1.52	4	2951	2395	0.38	0.10	0.28	
150318-03-mi-px3-1	Rhyolite	66	2.5481	23	0.29	0.086			1.52	4	2677	2106	0.99	0.48	0.51	
150318-03-mi-px4-1	Rhyolite	68	2.4894	20	0.222	0.075			1.52	4	2792	2125	0.90	0.50	0.40	
150318-03-mi-px4-2	Rhyolite	67	2.5343	20	0.127	0.024			1.52	4	2777	2129	0.49	0.15	0.34	
150320-01e-a-mi-ol1-01	Basalt	51	2.7872	16	0.439	0.1940			1.59	5	2638	1659	2.80	2.78	0.02	
150320-01e-a-mi-ol2-01	Basalt	51	2.7872	34	0.442	0.1350			1.59	4	2395	2025	1.33	0.92	0.42	
150320-01e-a-mi-ol4-01	Basalt	51	2.7872	36	1.730	0.7010			1.59	5	2110	1674	4.92	5.46	-0.54	
150320-01e-a-mi-ol5-01	Basalt	50	2.8138	45	1.597	0.7970	0.025	0.02	1.59	4	2800	2519	3.63	4.08	-0.45	219
150320-01e-a-mi-ol5-02	Basalt	50	2.7962	48	1.143	0.6010	0.025	0.03	1.59	5	2237	1909	2.44	2.88	-0.45	219
150320-01e-a-mi-ol5-03	Basalt	52	2.7693	46	1.177	0.6360	0.026	0.02	1.58	4	2168	1894	2.63	3.20	-0.57	193
150320-01e-a-mi-ol6-01	Basalt	51	2.7872	54	0.532	0.2370			1.59	4	2029	1797	1.00	1.00	0.00	
150320-01e-a-mi-ol7-01	Basalt	51	2.7872	22	1.035	0.4530	0.012	0.01	1.59	4	3035	2465	4.81	4.73	0.07	229
150320-01e-m-mi-ol1-1a	Basalt	50	2.7772	34	1.568	0.713	0.039	0.06	1.59	5	2924	2461	4.75	4.86	-0.11	629
150320-01e-m-mi-ol1-1b	Basalt	50	2.7772	27	1.278	0.537	0.035	0.04	1.59	4	2769	2306	4.84	4.58	0.26	568
150320-01e-m-mi-ol1-1c	Basalt	50	2.7772	20	0.841	0.465	0.026	0.02	1.59	4	2754	2133	4.28	5.32	-1.04	470
150320-01e-m-mi-ol1-1c2	Basalt	50	2.7772	21	1.115	0.571			1.59	5	2893	2129	5.58	6.43	-0.85	
150320-01e-m-mi-ol1-1d1	Basalt	50	2.7772	13	0.869	0.352	0.013	0.01	1.59	4	2723	1782	6.70	6.10	0.59	364
150320-01e-m-mi-ol1-1d2	Basalt	50	2.7772	15	0.815	0.306			1.59	4	2831	1967	5.76	4.87	0.89	
150320-01e-m-mi-ol2-1	Basalt	50	2.7747	21	0.819	0.346		0.01	1.59	4	2742	2133	4.09	3.89	0.20	133
150320-01e-m-mi-ol3-1	Basalt	52	2.7273	15	0.296	0.112			1.58	4	2897	2071	2.03	1.72	0.30	
150320-01e-a-mi-h-ol1-1a	Basalt	49	2.8249	26	0.477	0.208			1.60	5	3005	2399	1.86	1.83	0.04	
150320-01e-a-mi-h-ol1-3	Basalt	49	2.8249	28	0.442	0.117			1.60	3	2241	1909	1.58	0.94	0.64	
150320-01e-a-mi-h-ol3-1a	Basalt	49	2.8249	33	0.107				1.60	3	2168	1882	0.33	0.00	0.33	

150320-01e-a-mi-h-ol3-1b	Basalt	49	2.8249	33	0.296	0.086			1.60	4	2264	1886	0.90	0.59	0.31	
150320-01E-a-px2-1	Andesite	59	2.6532	32	0.529	0.2420			1.55	7	2303	1608	1.78	1.20	0.58	
150320-01E-a-px6-1	Andesite	59	2.646	24	0.269	0.1170			1.55	4	2488	1948	1.24	0.80	0.44	
150320-01E-a-px7-1	Andesite	58	2.6836	65	0.561	0.3480			1.56	5	2133	1886	0.93	0.85	0.08	
150320-01e-a-mi-px8-01	Andesite	59	2.6532	32	0.925	0.3640	0.023	0.02	1.55	4	2326	1917	3.21	1.86	1.35	316
150320-01e-a-mi-px10-01	Andesite	59	2.6532	36	0.510				1.55	4	1959	1597	1.57	0.00	1.57	
150320-01e-a-mi-px12-1a	Andesite	62	2.6049	31	0.747	0.280			1.70	3	2939	2657	2.66	1.47	1.19	
150320-01e-a-mi-px12-1b	Andesite	62	2.6049	30	0.604	0.212			1.70	3	2295	1998	2.27	1.17	1.09	
150320-01e-m-mi-px5-1a	Basalt	52	2.7755	16	0.475	0.192			1.58	3	3039	2449	3.05	2.77	0.28	
150320-01e-m-mi-px5-1b	Basalt	52	2.7755	16	0.486	0.169			1.58	3	3020	2438	3.07	2.41	0.67	
150320-01e-m-mi-px5-2	Basalt	53	2.699	21	0.511	0.158			1.58	4	2765	2156	2.60	1.81	0.79	
160727-01-c-mi-ol2-01	Andesite	60	2.5781	74	0.206				1.55	4	2202	2029	0.31	0.00	0.31	
160727-01-c-mi-ol3-01	Andesite	60	2.5781	46	0.251	0.1080			1.55	4	2287	2009	0.61	0.39	0.22	
160727-01-c-mi-ol6-01	Andesite	60	2.5781	53	0.582	0.5280		0.04	1.55	5	2183	1878	1.24	1.66	-0.42	159
160727-01-c-mi-ol7-01	Andesite	59	2.5636	51	0.741	0.3000			1.55	4	2198	1948	1.63	0.98	0.66	
160727-01-c-mi-ol8-01	Andesite	59	2.5633	65	0.367	0.1840			1.55	4	2098	1901	0.64	0.47	0.17	
160727-01-c-mi-ol10-01	Andesite	60	2.5781	39	0.119				1.55	6	2303	1809	0.34	0.00	0.34	
160727-01-c-mi-h-ol1-1	Basalt	44	2.9804	37	0.524	0.060			1.62	5	2457	2040	1.35	0.35	1.00	
160727-01-c-mi-h-ol2-1a	Basalt	45	3.0051	20	0.246				1.61	4	3074	2461	1.16	0.00	1.16	
160727-01-c-mi-h-ol2-1b	Basalt	45	3.0051	21	0.217				1.61	4	2754	2160	0.99	0.00	0.99	
160727-01-c-mi-h-ol2-1c	Basalt	45	3.0051	20	0.27				1.61	4	2785	2156	1.30	0.00	1.30	
160727-01-c-mi-h-ol3-1	Basalt	41	3.0366	31	0.356				1.63	5	2904	2403	1.09	0.00	1.09	
160727-01-c-mi-h-ol4-1a	Basalt	46	2.9472	34	0.763				1.61	5	3035	2573	2.20	0.00	2.20	
160727-01-c-mi-h-ol4-1b	Basalt	46	2.9472	33	0.694				1.61	4	3032	2657	2.02	0.00	2.02	
160727-01-c-mi-h-ol4-1c	Basalt	46	2.9472	34	0.793	0.068	0.04	0.04	1.61	5	2858	2399	2.27	0.44	1.83	470
160727-01-c-mi-h-ol5-1	Basalt	42	2.9866	30	0.434				1.63	3	2804	2499	1.37	0.00	1.37	
160727-01-c-mi-h-ol6-1a	Basalt	45	2.9796	30	0.661				1.61	5	2557	2033	2.14	0.00	2.14	
160727-01-c-mi-h-ol6-1b	Basalt	45	2.9796	30	0.471				1.61	5	2345	1832	1.49	0.00	1.49	
160727-01-c-mi-h-ol6-1c	Basalt	45	2.9796	31	0.159				1.61	4	2295	1890	0.50	0.00	0.50	
160727-01-c-mi-h-ol7-1a	Basalt	47	2.9757	46	0.26				1.60	6	2735	2326	0.55	0.00	0.55	
160727-01-c-mi-h-ol7-1b	Basalt	47	2.9757	45	0.258				1.60	6	2870	2453	0.55	0.00	0.55	
160727-01-c-mi-h-ol7-1c	Basalt	47	2.9757	44	0.286				1.60	4	2954	2673	0.62	0.00	0.62	
160727-01-c-mi-h-ol9-1a	Basalt	46	2.9768	22	0.449	0.031	0.022	0.02	1.61	4	2573	2013	1.94	0.30	1.64	337
160727-01-c-mi-h-ol9-1b	Basalt	46	2.9768	22	0.416	0.021	0.014	0.02	1.61	4	2819	2256	1.81	0.21	1.60	286
160727-01-c-mi-px1-1	Rhyolite	74	2.4711	52	0.171	0.0500			1.49	6	2387	1998	0.27	0.13	0.14	

160727-01-c-mi-px1-2	Rhyolite	72	2.4576	51	0.570	0.3040	0.018		1.50	7	3074	2619	0.90	0.79	0.12	84
160727-01-c-mi-px2-1	Rhyolite	71	2.4689	30	0.793	0.3800			1.50	7	2584	1809	2.14	1.68	0.46	
160727-01-c-mi-px3-1	Rhyolite	70	2.4849	17	0.182	0.0820		0.01	1.51	3	2661	2083	0.85	0.63	0.22	178
160727-01-c-mi-px6-1	Rhyolite	72	2.4475	114	1.072	0.6060			1.50	7	2974	2769	0.77	0.71	0.06	
160727-01-c-mi-px7-1	Rhyolite	72	2.4555	28	0.433	0.2270			1.50	5	2472	1882	1.25	1.07	0.18	
160727-01-c-mi-px11-01	Rhyolite	70	2.4849	18	0.449	0.2370			1.51	4	2630	1882	2.04	1.76	0.28	
160727-01-c-mi-px13-01	Rhyolite	70	2.4715	35	0.484	0.2290			1.51	4	1971	1593	1.11	0.86	0.25	
160727-01-c-mi-px13-02	Rhyolite	71	2.4997	36	0.205	0.0340			1.50	3	2279	2006	0.45	0.12	0.33	
160727-01-c-mi-px15-01	Rhyolite	74	2.4397	27	0.277	0.0840			1.49	6	2704	1959	0.84	0.42	0.42	
160727-01-c-mi-px17-01	Rhyolite	74	2.4371	49	0.637	0.3260			1.49	5	2291	1952	1.06	0.88	0.17	
160727-01-c-mi-px17-02	Rhyolite	73	2.4962	45	0.302	0.1800			1.50	4	2256	1959	0.54	0.52	0.01	
160727-01-c-mi-px18-01	Rhyolite	72	2.4574	38	0.953	0.4870			1.50	5	3059	2615	2.06	1.72	0.34	
160727-01-c-mi-px18-02	Rhyolite	71	2.4728	36	0.559	0.2140			1.50	4	2862	2495	1.24	0.78	0.46	

	ϵ		
	1630cm^{-1}	3535cm^{-1}	1515cm^{-1}/1430cm^{-1}
Basalt	28	63	375
Andesite	42	62	375
Rhyolite	55	90	375

Extinction Coefficient values (ϵ) are from Dixon et al., 1988 and Dixon et al., 1995 for basalt; Mandeville et al., 2002 for andesite; Hauri et al., 2002 and Newman et al., 1986 for rhyolite; Fine and Stolper, 1985 for the 1515cm^{-1} and 1430cm^{-1} wavenumbers.

Text in red are samples without microprobe analysis for major elements, proxy compositions were used to derive density values.

Duplicate measurements are included in the list. Table 4-1 in the thesis show average values or selected values for the duplicate measurements

Analysis were done at the Institute of Agriculture and Environment, Massey University

Appendix Table 11. Rhyolite MELTS and DCompress input parameters.

Rhyolite MELTS

	Section 3			**Section 4**				**Section 5**		
	Wharepu		Te Maari	Ngauruhoe 1975		Wharepu		Wharepu		Red Crater
	150320-01E-b (calculated, less quartz)	150320-01E-b (calculated, less quartz)	160727-01c-mi-h-ol1-1	150319-02-a2-mi-h-ol2-1	150319-02-a2	150320-01E-b (calculated, less quartz)	150320-01D-c	150320-01D-c	150320-01D-c	150318-03
SiO_2	52.99	52.99	44.10	47.83	56.24	52.99	48.07	48.07	48.07	52.95
TiO_2	0.81	0.81	0.67	0.78	0.80	0.81	0.72	0.72	0.72	0.74
Al_2O_3	18.40	18.40	13.16	16.97	17.70	18.40	16.63	16.63	16.63	15.38
FeO	7.52	7.52	3.70	7.35	6.79	7.52	7.00	7.00	5.49	6.50
Fe_2O_3	1.37	1.37	2.35	1.12	1.12	1.37	3.12	3.12	3.50	2.37
MnO	0.15	0.15	0.12	0.14	0.15	0.15	0.14	0.14	0.14	0.17
MgO	5.64	5.64	12.52	7.83	4.32	5.64	7.51	7.51	7.51	7.74
CaO	8.93	8.93	11.55	9.97	7.85	8.93	9.47	9.47	9.47	10.26
Na_2O	2.49	2.49	1.63	2.56	3.00	2.49	1.61	1.61	1.61	2.37
K_2O	0.74	0.74	0.41	0.44	1.05	0.74	0.14	0.14	0.14	0.60
P_2O_5	0.12	0.12	0.15			0.12	0.04	0.04	0.04	0.12
H_2O	1.00	1.00	1.35	1.95	0.50	6.70	0.50	0.50	0.50	0.50
T initial (°C)	1300	1150	1357.03*	1212.62*	1000	1300	1300	1300	1300	1300
T final (°C)	1140	1135	1017.03	1002.62	1150	900	1000	1000	1000	1000
ΔT	10	1	20	10	10	10	20	20	20	20
P initial (bar)	8000	8000	1000	4000	4000	5000	10000	10000	1000	10000
P final (bar)	8000	500	1000	4000	4000	5000	10000	10000	1000	10000
ΔP	0	500	0	0	0	0	0	0	0	0
condition	equilibrium	equilibrium	fractional	equilibrium	equilibrium	equilibrium	fractional	equilibrium garnet suppressed	fractional	equilibrium

Dcompress

	Basalt 1	Basalt 2	Basalt 3	Rhyolite 1
P initial (bar)	3000	3000	3000	3000
P final (bar)	100	100	100	100
T (°C)	1300	1300	1300	1110
ΔNNO	1.4	1.4	1.4	1.4
H2O (wt. %)	2.27	2.27	5.3	2.27
CO2 (ppm)	2500	1176	1100	1125
wt. % gas	1	1	1	1
magma type	basalt	basalt	Basalt	rhyolite
system	C-S-O-H-Fe	C-S-O-H-Fe	C-S-O-H-Fe	C-S-O-H-Fe
behavior	open	open	open	open

* Temperature at liquidus

Appendix Table 12. Olivine and orthopyroxene hosted melt inclusion compositions calculated to equilibrium.

	Olivine correction														
	SiO_2	TiO_2	Al_2O_3	Fe_2O_3	FeO	MnO	MgO	CaO	Na_2O	K_2O	H_2O	Totals	Host Mg#	Fe^{2+}/Fe^{3+}	FeO*
Wharepu															
150320-01e-a-mi-ol5-2b	50.34	0.69	15.54	8.08		0.10	2.35	11.49	2.05	0.54	2.40	93.58	83.47	6.10	7.20
	53.51	**0.70**	**15.71**	**1.13**	**6.21**	**0.12**	**5.90**	**11.68**	**2.07**	**0.55**	**2.43**	**100.00**			
150320-01e-a-mi-ol5-3a	51.66	0.73	16.12	7.56		0.12	2.21	11.06	2.20	0.58	2.63	94.87	83.47	6.10	6.73
	54.15	**0.73**	**16.14**	**1.05**	**5.76**	**0.14**	**5.48**	**11.13**	**2.20**	**0.58**	**2.63**	**100.00**			
150320-01e-m-mi-ol1-1	50.17	0.76	16.49	7.77		0.12	3.07	9.58	1.18	0.69	6.70	96.54	79.53	6.10	6.92
	52.10	**0.77**	**16.76**	**1.10**	**6.02**	**0.14**	**4.65**	**9.76**	**1.20**	**0.71**	**6.81**	**100.00**			
150320-01e-m-mi-ol2-1	50.45	0.81	16.69	8.03		0.12	2.32	10.09	0.97	0.60	4.09	94.18	81.54	6.10	7.15
	53.44	**0.83**	**16.96**	**1.11**	**6.11**	**0.15**	**5.37**	**10.30**	**0.98**	**0.61**	**4.16**	**100.00**			
150320-01e-m-mi-ol3-1	51.67	0.79	17.03	6.86		0.09	1.84	9.22	0.96	0.80	2.03	91.28	79.23	6.10	6.11
	56.62	**0.84**	**18.19**	**0.96**	**5.28**	**0.11**	**4.07**	**9.87**	**1.03**	**0.85**	**2.17**	**100.00**			
Ngauruhoe 1975															
150319-02-a1-mi-ol3-1	49.43	0.86	18.65	6.08		0.07	1.60	10.62	3.20	0.56	0.14	91.21	81.62	7.30	5.41
	54.16	**0.92**	**19.86**	**0.74**	**4.86**	**0.09**	**3.89**	**11.34**	**3.41**	**0.60**	**0.15**	**100.00**			
150319-02-a1-mi-ol7-1b	52.97	0.91	20.63	7.11		0.10	3.26	11.61	3.03	0.64	0.51	100.77	80.02	7.30	6.33
	52.72	**0.90**	**20.29**	**0.84**	**5.54**	**0.10**	**4.04**	**11.42**	**2.98**	**0.63**	**0.50**	**99.97***			
150319-02-a2-mi-ol1-1	50.11	0.92	19.65	6.19		0.10	1.73	10.92	2.88	0.62	1.79	94.90	78.13	7.30	5.51
	52.93	**0.95**	**20.38**	**0.74**	**4.85**	**0.11**	**3.22**	**11.34**	**2.99**	**0.64**	**1.86**	**100.00**			
150319-02-b2-mi-ol2-1	60.01	0.84	18.00	5.42		0.04	2.06	7.18	3.71	1.40	0.53	99.17	78.28	7.30	4.82
	60.64	**0.84**	**18.06**	**0.65**	**4.25**	**0.04**	**2.67**	**7.21**	**3.72**	**1.40**	**0.53**	**100.00**			
150319-02-b2-mi-ol3-1	51.69	0.85	19.18	8.15		0.11	2.35	10.37	2.61	0.64	0.79	96.72	78.96	7.30	7.25
	53.48	**0.85**	**19.29**	**0.97**	**6.34**	**0.13**	**4.43**	**10.45**	**2.62**	**0.64**	**0.80**	**100.00**			
150319-02-b2-mi-ol3-3	53.74	0.94	18.79	7.68		0.08	1.13	9.42	3.36	1.01	0.82	96.97	78.96	7.30	6.84
	55.10	**0.93**	**18.49**	**0.91**	**5.98**	**0.10**	**4.06**	**9.30**	**3.31**	**0.99**	**0.81**	**99.96***			
150319-02-a2-mi-h-ol2-1	47.83	0.78	16.97	9.38		0.14	7.83	9.97	2.56	0.44	1.27	97.18	78.51	7.30	8.35

	50.50	**0.88**	**19.16**	**1.12**	**7.33**	**0.09**	**4.85**	**11.25**	**2.89**	**0.50**	**1.43**	**100.00**			
150319-02-a2-mi-h-ol2-2	46.83	0.66	15.64	10.29		0.18	11.88	8.50	2.64	0.44	0.51	97.58	78.51	7.30	9.16
	50.11	**0.82**	**19.48**	**1.23**	**8.06**	**0.02**	**5.21**	**10.60**	**3.29**	**0.55**	**0.64**	**100.00**			
150319-02-a2-mi-h-ol3-1	49.68	0.80	16.18	10.89		0.16	6.64	8.95	2.36	0.62	1.35	97.63	78.06	7.30	9.69
	51.89	**0.86**	**17.37**	**1.30**	**8.52**	**0.15**	**5.66**	**9.60**	**2.53**	**0.67**	**1.45**	**100.00**			
150319-02-a2-mi-h-ol3-2	46.77	0.58	12.52	13.63		0.13	15.54	6.43	1.57	0.51	0.80	98.47	78.06	7.30	12.13
	50.54	**0.77**	**16.73**	**1.62**	**10.67**	**0.00**	**7.18**	**8.65**	**2.10**	**0.68**	**1.07**	**100.00**			
150319-02-a2-mi-h-ol4-1a	49.07	0.80	17.02	9.14		0.13	6.87	10.09	2.67	0.55	1.01	97.36	77.47	7.30	8.13
	51.59	**0.89**	**18.85**	**1.09**	**7.15**	**0.08**	**4.49**	**11.18**	**2.96**	**0.61**	**1.12**	**100.00**			
150319-02-a2-mi-h-ol4-2	48.10	0.83	17.75	10.27		0.14	6.27	9.92	2.79	0.48	0.68	97.22	77.47	7.30	9.14
	50.45	**0.90**	**19.26**	**1.22**	**8.03**	**0.11**	**4.99**	**10.76**	**3.02**	**0.52**	**0.74**	**100.00**			
												* removed P_2O_5			
Te Maari 1500AD															
160727-01c-mi-h-ol1-1	44.10	0.67	13.16	6.50		0.12	12.52	11.55	1.63	0.41	1.35	92.02	91.70	1.70	5.79
	49.57	**0.88**	**17.10**	**2.38**	**3.64**	**0.10**	**7.03**	**14.89**	**2.12**	**0.53**	**1.75**	100.00			
160727-01c-mi-h-ol2-1	45.45	0.68	14.37	8.30		0.10	12.03	12.66	1.94	0.44	1.15	97.11	89.08	1.70	7.39
	48.13	**0.81**	**17.31**	**3.04**	**4.65**	**0.05**	**6.64**	**15.11**	**2.33**	**0.53**	**1.39**	100.00			
160727-01c-mi-h-ol3-1	41.35	0.61	13.29	5.12		0.11	16.48	10.60	1.78	0.47	1.09	90.89	89.08	1.70	4.56
	47.60	**0.97**	**21.08**	**1.87**	**2.87**	**0.00**	**4.06**	**16.26**	**2.82**	**0.75**	**1.73**	100.00			
160727-01c-mi-h-ol4-1c	45.86	0.76	15.00	6.66		0.10	10.11	12.67	2.17	0.53	2.27	96.14	89.50	1.70	5.93
	48.85	**0.90**	**17.71**	**2.44**	**3.73**	**0.07**	**5.58**	**14.86**	**2.57**	**0.63**	**2.68**	100.00			
160727-01c-mi-h-ol5-1	41.67	0.67	13.12	6.31		0.08	11.53	11.36	1.80	0.37	1.37	88.27	89.08	1.70	5.62
	49.04	**0.94**	**18.40**	**2.31**	**3.53**	**0.01**	**5.10**	**15.73**	**2.52**	**0.52**	**1.92**	100.00			
160727-01c-mi-h-ol7-1	47.40	0.78	14.53	9.49		0.08	12.19	9.99	1.96	0.54	0.57	97.52	91.05	1.70	8.45
	49.69	**0.87**	**16.30**	**3.48**	**5.32**	**0.07**	**9.69**	**11.15**	**2.20**	**0.60**	**0.64**	100.00			
160727-01c-mi-h-ol9-1	46.32	0.66	13.63	8.84		0.15	11.74	10.81	1.87	0.49	1.87	96.38	90.54	1.70	7.87
	49.26	0.76	15.80	3.24	4.95	0.14	8.49	12.46	2.17	0.57	2.17	100.00			

*text in red have more than 20% increase in H_2O

*Fe elemental ratio based on MELTS input (see Appendix Table 11), model used for Petrolog is Danyushevsky 2001

Orthopyroxene correction

Ngauruhoe 1975	SiO_2	TiO_2	Al_2O_3	FeO*	MnO	MgO	CaO	Na_2O	K_2O	P_2O_5	H_2O	Total
150319-02-a1-mi-px1-1a	56.99	0.84	15.38	5.99	0.13	2.15	5.48	3.27	1.45		0.72	92.09
2.5%	**56.86**	**0.82**	**15.03**	**6.25**	**0.14**	**2.70**	**5.39**	**3.19**	**1.41**			
150319-02-a1-mi-px1-2	57.53	0.86	14.74	5.96	0.12	1.24	4.84	3.35	1.79	0.14	0.72	90.82
7.0%	**57.14**	**0.81**	**13.80**	**6.69**	**0.14**	**2.85**	**4.62**	**3.12**	**1.66**			
150319-02-a1-mi-px2-1	64.96	1.05	15.26	5.70	0.09	0.93	5.05	3.44	2.60	0.31	0.37	99.71
6.0%	**64.28**	**1.00**	**14.39**	**6.52**	**0.11**	**2.32**	**4.86**	**3.23**	**2.44**			
150319-02-a1-mi-px2-2	64.00	0.81	15.28	5.70	0.06	1.17	4.89	3.81	1.99	0.1	0.37	98.1
4.8%	**63.50**	**0.78**	**14.58**	**6.35**	**0.08**	**2.27**	**4.75**	**3.63**	**1.89**			
150319-02-a1-mi-px2-3	60.96	0.85	12.79	8.27	0.19	5.22	3.40	3.35	2.59	0.1	0.37	97.98
-13.0%	**62.05**	**0.95**	**14.58**	**6.61**	**0.16**	**2.40**	**3.62**	**3.85**	**2.98**			
150319-02-a1-mi-px4-2	61.96	0.84	15.47	5.63	0.03	0.94	4.33	3.76	2.06	0.18	0.72	95.56
4.5%	**61.32**	**0.80**	**14.49**	**6.45**	**0.05**	**2.47**	**4.16**	**3.51**	**1.92**			

Appendix Table 13. List of copyright permissions.

File name	Scanned item
DRC 16Arpa.pdf	DRC 16 form
RightsLink Printable License.pdf	Copyright permission from Springer

MASSEY UNIVERSITY
GRADUATE RESEARCH SCHOOL

STATEMENT OF CONTRIBUTION TO DOCTORAL THESIS CONTAINING PUBLICATIONS

(To appear at the end of each thesis chapter/section/appendix submitted as an article/paper or collected as an appendix at the end of the thesis)

We, the candidate and the candidate's Principal Supervisor, certify that all co-authors have consented to their work being included in the thesis and they have accepted the candidate's contribution as indicated below in the *Statement of Originality*.

Name of Candidate: Maria Carmencita B. Arpa

Name/Title of Principal Supervisor: Georg Zellmer

Name of Published Research Output and full reference:

Arpa MC, Zellmer GF, Christenson B, Lube G, Shellnutt G. Variable magma reservoir depths for Tongariro Volcanic Complex eruptive deposits from 10,000 years to present. 2017. Bulletin of Volcanology, 79:56.

In which Chapter is the Published Work: 3

Please indicate either:

- The percentage of the Published Work that was contributed by the candidate:

  and / or

- Describe the contribution that the candidate has made to the Published Work:

  The paper draft was written by the candidate, it was sent to co-authors and was reviewed by 3 co-authors (supervisors). The paper was revised based on their reviews. The candidate submitted the draft to the Journal and revised it based on journal reviewers' comments.

Maria Carmencita Arpa — Digitally signed by Maria Carmencita Arpa Date: 2017.11.20 10:30:40 +08'00'

Candidate's Signature — 20 Nov. 2017 — Date

Georg F. Zellmer — Digitally signed by Georg F. Zellmer Date: 2017.11.22 17:54:41 +13'00'

Principal Supervisor's signature — 22/11/2017 — Date

SPRINGER LICENSE
TERMS AND CONDITIONS

Nov 29, 2017

This Agreement between Ms. Maria Carmencita Arpa ("You") and Springer ("Springer") consists of your license details and the terms and conditions provided by Springer and Copyright Clearance Center.

License Number	4230981141499
License date	Nov 16, 2017
Licensed Content Publisher	Springer
Licensed Content Publication	Bulletin of Volcanology
Licensed Content Title	Variable magma reservoir depths for Tongariro Volcanic Complex eruptive deposits from 10,000 years to present
Licensed Content Author	Maria Carmencita Arpa, Georg F. Zellmer, Bruce Christenson et al
Licensed Content Date	Jan 1, 2017
Licensed Content Volume	79
Licensed Content Issue	7
Type of Use	Thesis/Dissertation
Portion	Full text
Number of copies	1
Author of this Springer article	Yes and you are the sole author of the new work
Order reference number	
Title of your thesis / dissertation	Magma generation, storage and ascent below Tongariro Volcanic Complex, Southern Taupo Volcanic Zone
Expected completion date	Nov 2017
Estimated size(pages)	200
Requestor Location	Ms. Maria Carmencita Arpa 125 Eastville Ave Eastville Filinvest East Antipolo City, Rizal 1870 Philippines Attn: Ms. Maria Carmencita Arpa
Billing Type	Invoice
Billing Address	Ms. Maria Carmencita Arpa 125 Eastville Ave Eastville Filinvest East Antipolo City, Philippines 1870 Attn: Ms. Maria Carmencita Arpa
Total	0.00 USD
Terms and Conditions	

Introduction
The publisher for this copyrighted material is Springer. By clicking "accept" in connection

with completing this licensing transaction, you agree that the following terms and conditions apply to this transaction (along with the Billing and Payment terms and conditions established by Copyright Clearance Center, Inc. ("CCC"), at the time that you opened your Rightslink account and that are available at any time at http://myaccount.copyright.com).

Limited License

With reference to your request to reuse material on which Springer controls the copyright, permission is granted for the use indicated in your enquiry under the following conditions:

- Licenses are for one-time use only with a maximum distribution equal to the number stated in your request.
- Springer material represents original material which does not carry references to other sources. If the material in question appears with a credit to another source, this permission is not valid and authorization has to be obtained from the original copyright holder.
- This permission
• is non-exclusive
• is only valid if no personal rights, trademarks, or competitive products are infringed.
• explicitly excludes the right for derivatives.
- Springer does not supply original artwork or content.
- According to the format which you have selected, the following conditions apply accordingly:
• **Print and Electronic:** This License include use in electronic form provided it is password protected, on intranet, or CD-Rom/DVD or E-book/E-journal. It may not be republished in electronic open access.
• **Print:** This License excludes use in electronic form.
• **Electronic:** This License only pertains to use in electronic form provided it is password protected, on intranet, or CD-Rom/DVD or E-book/E-journal. It may not be republished in electronic open access.

For any electronic use not mentioned, please contact Springer at permissions.springer@spi-global.com.

- Although Springer controls the copyright to the material and is entitled to negotiate on rights, this license is only valid subject to courtesy information to the author (address is given in the article/chapter).
- If you are an STM Signatory or your work will be published by an STM Signatory and you are requesting to reuse figures/tables/illustrations or single text extracts, permission is granted according to STM Permissions Guidelines: http://www.stm-assoc.org/permissions-guidelines/

For any electronic use not mentioned in the Guidelines, please contact Springer at permissions.springer@spi-global.com. If you request to reuse more content than stipulated in the STM Permissions Guidelines, you will be charged a permission fee for the excess content.

Permission is valid upon payment of the fee as indicated in the licensing process. If permission is granted free of charge on this occasion, that does not prejudice any rights we might have to charge for reproduction of our copyrighted material in the future.

-If your request is for reuse in a Thesis, permission is granted free of charge under the following conditions:

This license is valid for one-time use only for the purpose of defending your thesis and with a maximum of 100 extra copies in paper. If the thesis is going to be published, permission needs to be reobtained.

- includes use in an electronic form, provided it is an author-created version of the thesis on his/her own website and his/her university's repository, including UMI (according to the definition on the Sherpa website: http://www.sherpa.ac.uk/romeo/);
- is subject to courtesy information to the co-author or corresponding author.

Geographic Rights: Scope

Licenses may be exercised anywhere in the world.

Altering/Modifying Material: Not Permitted

Figures, tables, and illustrations may be altered minimally to serve your work. You may not alter or modify text in any manner. Abbreviations, additions, deletions and/or any other alterations shall be made only with prior written authorization of the author(s).

Reservation of Rights

Springer reserves all rights not specifically granted in the combination of (i) the license details provided by you and accepted in the course of this licensing transaction and (ii) these terms and conditions and (iii) CCC's Billing and Payment terms and conditions.

License Contingent on Payment

While you may exercise the rights licensed immediately upon issuance of the license at the end of the licensing process for the transaction, provided that you have disclosed complete and accurate details of your proposed use, no license is finally effective unless and until full payment is received from you (either by Springer or by CCC) as provided in CCC's Billing and Payment terms and conditions. If full payment is not received by the date due, then any license preliminarily granted shall be deemed automatically revoked and shall be void as if never granted. Further, in the event that you breach any of these terms and conditions or any of CCC's Billing and Payment terms and conditions, the license is automatically revoked and shall be void as if never granted. Use of materials as described in a revoked license, as well as any use of the materials beyond the scope of an unrevoked license, may constitute copyright infringement and Springer reserves the right to take any and all action to protect its copyright in the materials.

Copyright Notice: Disclaimer

You must include the following copyright and permission notice in connection with any reproduction of the licensed material:

"Springer book/journal title, chapter/article title, volume, year of publication, page, name(s) of author(s), (original copyright notice as given in the publication in which the material was originally published) "With permission of Springer"

In case of use of a graph or illustration, the caption of the graph or illustration must be included, as it is indicated in the original publication.

Warranties: None

Springer makes no representations or warranties with respect to the licensed material and adopts on its own behalf the limitations and disclaimers established by CCC on its behalf in its Billing and Payment terms and conditions for this licensing transaction.

Indemnity

You hereby indemnify and agree to hold harmless Springer and CCC, and their respective officers, directors, employees and agents, from and against any and all claims arising out of your use of the licensed material other than as specifically authorized pursuant to this license.

No Transfer of License

This license is personal to you and may not be sublicensed, assigned, or transferred by you without Springer's written permission.

No Amendment Except in Writing

This license may not be amended except in a writing signed by both parties (or, in the case of Springer, by CCC on Springer's behalf).

Objection to Contrary Terms

Springer hereby objects to any terms contained in any purchase order, acknowledgment, check endorsement or other writing prepared by you, which terms are inconsistent with these terms and conditions or CCC's Billing and Payment terms and conditions. These terms and conditions, together with CCC's Billing and Payment terms and conditions (which are incorporated herein), comprise the entire agreement between you and Springer (and CCC) concerning this licensing transaction. In the event of any conflict between your obligations established by these terms and conditions and those established by CCC's Billing and Payment terms and conditions, these terms and conditions shall control.

Jurisdiction
All disputes that may arise in connection with this present License, or the breach thereof, shall be settled exclusively by arbitration, to be held in the Federal Republic of Germany, in accordance with German law.

Other conditions:
V 12AUG2015

Questions? customercare@copyright.com or +1-855-239-3415 (toll free in the US) or +1-978-646-2777.

Fumaroles on Upper Te Maari Crater

References

Aiuppa, A., Federico, C., Giudice, G., Giuffrida, G., Guida, R., Gurrieri, S., Liuzzo, M., Moretti, R. & Papale, P. 2009. The 2007 eruption of Stromboli Volcano: insights from real-time measurement of the volcanic gas plume CO_2/SO_2 ratio. *Journal of Volcanology and Geothermal Research,* 182**,** 221-230.

Allard, P. 1997. Endogenous magma degassing and storage at Mount Etna. *Geophysical Research Letters,* 24**,** 2219-2222.

Andersen, D., Lindsley, D. & Davidson, P. 1993. QUILF: A pascal program to assess equilibria among Fe-Mg-Mn-Ti oxides, pyroxenes, olivine, and quartz. *Computers & Geosciences,* 19**,** 1333-1350.

Annen, C., Blundy, J. D. & Sparks, R. S. J. 2006. The genesis of intermediate and silicic magmas in deep crustal hot zones. *Journal of Petrology,* 47**,** 505-539.

Arpa, M. C., Zellmer, G. F., Christenson, B., Lube, G. & Shellnutt, G. 2017. Variable magma reservoir depths for Tongariro Volcanic Complex eruptive deposits from 10,000 years to present. *Bulletin of Volcanology,* 79.

Arpa, M. C. B., Bornas, M. a. V., Abigania, M. I. T., Solidum, R. U., Listanco, E. L., Ozawa, A. & Tagami, T. 2006. Characterization of lava flow and pyroclasts from the February to March 2000 eruption of Mayon Volcano, Philippines. *Journal of the Geological Society of the Philippines,* 61.

Asimow, P. D. & Ghiorso, M. S. 1998. Algorithmic modifications extending MELTS to calculate subsolidus phase relations. *American Mineralogist,* 83**,** 1127-1131.

Asmerom, Y., Dufrane, S. A., Mukasa, S. B., Cheng, H. & Edwards, R. L. 2005. Time scale of magma differentiation in arcs from protactinium-radium isotopic data. *Geology,* 33**,** 633-636.

Auer, A., Martin, C. E., Palin, J. M., White, J. D. L., Nakagawa, M. & Stirling, C. 2015. The evolution of hydrous magmas in the Tongariro Volcanic Centre: the 10 ka Pahoka-Mangamate eruptions. *New Zealand Journal of Geology & Geophysics,* 58**,** 364-384.

Bachmann, O. & Bergantz, G. W. 2003. Rejuvenation of the Fish Canyon magma body: A window into the evolution of large-volume silicic magma systems. *Geology,* 31**,** 789-792.

Basher, R. 2005. *Physical volcanology and future volcanic risk from Te Maari Craters, Tongariro.* M.S., University of Waikato.

Beanland, S. & Haines, J. 1998. The kinematics of active deformation in the North Island, New Zealand, determined from geological strain rates. *New Zealand Journal of Geology and Geophysics* 41**,** 311-323.

Beckett, F. M., Burton, M., Mader, H. M., Phillips, J. C., Polacci, M., Rust, A. C. & Witham, F. 2014. Conduit convection driving persistent degassing at basaltic volcanoes. *Journal of Volcanology and Geothermal Research,* 283**,** 19-35.

Behn, M. D., Kelemen, P. B., Hirth, G., Hacker, B. R. & Massonne, H.-J. 2011. Diapirs as the source of the sediment signature in arc lavas. *Nature Geoscience,* 4**,** 641-646.

Belkin, H. E., De Vivo, B., Torok, K. & Webster, J. D. 1998. Pre-eruptive volatile content, melt-inclusion chemistry, and microthermometry of interplinian Vesuvius lavas (pre-A.D. 1631). *Journal of Volcanology and Geothermal Research,* 82**,** 79-95.

Bergantz, G. W., Schleicher, J. M. & Burgisser, A. 2015. Open-system dynamics and mixing in magma mushes. *Nature Geoscience,* 8.

Bibby, H. M., Caldwell, T. G., Davey, F. J. & Webb, T. H. 1995. Geophysical evidence on the structure of the Taupo Volcanic Zone and its hydrothermal circulation. *Journal of Volcanology and Geothermal Research,* 68**,** 29-58.

Bindeman, I. 2008. Oxygen Isotopes in Mantle and Crustal Magmas as Revealed by Single Crystal Analysis. *Reviews in Mineralogy & Geochemistry,* 69**,** 445-478.

Blatter, D. L. & Carmichael, I. S. E. 1998. Hornblende peridotite xenoliths from central Mexico reveal the highly oxidized nature of subarc upper mantle. *Geology,* 26**,** 1035-1038.

Blattner, P. & Reid, F. 1982. The origin of lavas and ignimbrites of the Taupo Volcanic Zone, New Zealand, in the light of oxygen isotope data. *Geochimica et Cosmochimica Acta,* 46**,** 1417-1429.

Blundy, J. & Cashman, K. 2005. Rapid decompression-driven crystallization recorded by melt inclusions from Mount St. Helens volcano. *Geology,* 33**,** 793-796. Available: DOI doi: 10.1130/G21668.1.

Brenguier, F., Shapiro, N. M., Campillo, M., Nercessian, A. & Ferrazzini, V. 2007. 3-D surface wave tomography of the Piton de la Fournaise volcano using seismic noise correlations. *Geophysical Research Letters*. Available: DOI doi.10.1029/2006GL028586.

Burgisser, A., Alletti, M. & Scaillet, B. 2015. Simulating the behavior of volatiles belonging to the C-O-H-S system in silicate melts under magmatic conditions with the software D-Compress. *Computers & Geosciences,* 79**,** 1-14.

Burnham, C. W. 1994. Development of the Burnham Model for Prediction of H_2O Solubilities in Magmas. *In:* Carroll, M. R. & Holloway, J. R. (eds.) *Volatiles in Magmas.* Virginia: Mineralogical Society of America.

Carmichael, I. S. E. & Ghiorso, M. S. 1986. Oxidation-reduction relations in basic magma: a case for homogenous equilibria. *Earth and Planetary Science Letters,* 78**,** 200-210.

Carroll, M. R. & Webster, J. D. 1994. Solubilities of Sulfur, Noble Gases, Nitrogen, Chlorine, and Fluorine in Magmas. *In:* Carroll, M. R. & Holloway, J. R. (eds.) *Volatiles in Magmas.* Virginia: Mineralogical Society of America.

Castillo, P. R. & Newhall, C. G. 2004. Geochemical Constraints on Possible Subduction Components in Lavas of Mayon and Taal Volcanoes, Southern Luzon, Philippines. *Journal of Petrology,* 45**,** 1089-1108.

Charlier, B. L. A., Wilson, C. J. N., Lowenstern, J. B., Blake, S., Van Calsteren, P. W. & Davidson, J. P. 2005. Magma Generation at a Large, Hyperactive Silicic Volcano (Taupo, New Zealand) Revealed by U-Th and U-Pb Systematics in Zircons. *Journal of Petrology,* 46**,** 3-32.

Christenson, B. W. 2000. Geochemistry of fluids associated with the 1995-1996 eruption of Mt. Ruapehu, New Zealand: signatures and processes in the magmatic-hydrothermal system. *Journal of Volcanology and Geothermal Research,* 97**,** 1-30.

Christenson, B. W., Britten, K., Mazot, A. & Fitzgerald, J. The 2012 Eruption of Te Mari, New Zealand: Characteristics of a shallow magmatic degassing event. American Geophysical Union, Fall Meeting 2013 San Francisco, USA.

Christenson, B. W., Reyes, A. G., Young, R., Moebis, A., Sherburn, S., Cole-Baker, J. & Britten, K. 2010. Cyclic processes and factors leading to phreatic eruption events: Insights from the 25 September 2007 eruption through Ruapehu Crater Lake, New Zealand. *Journal of Volcanology and Geothermal Research,* 191**,** 15-32.

Cole, J. W. 1978. Andesites of the Tongariro Volcanic Centre, North Island, New Zealand. *Journal of Volcanology and Geothermal Research,* 3**,** 121-153.

Cole, J. W. 1981. Genesis of lavas of the Taupo Volcanic Zone, North Island, New Zealand. *Journal of Volcanology and Geothermal Research,* 10**,** 317-337.

Cole, J. W., Graham, I. J., Hackett, W. R. & Houghton, B. F. 1986. Volcanology and petrology of the Quaternary composite volcanoes of Tongariro Volcanic Centre, Taupo Volcanic Zone. *Royal Society of New Zealand Bulletin,* 23**,** 224-250.

Cole, J. W., Thordarson, T. & Burt, R. M. 2000. Magma origin and evolution of White Island (Whakaari) Volcano, Bay of Plenty, New Zealand. *Journal of Petrology,* 41**,** 867-895.

Conway, C. E. 2016. *Studies on the Glaciovolcanic and Magmatic Evolution of Ruapehu Volcano, New Zealand.* Doctor of Philosophy in Geology, Victoria University of Wellington.

Couch, S., Sparks, R. S. J. & Carroll, M. R. 2003. The Kinetics of Degassing-Induced Crystallization at Soufriere Hills Volcano, Montserrat. *Journal of Petrology,* 44**,** 1477-1502.

Danyushevsky, L. V., Della-Pasqua, F. N. & Sokolov, S. 2000. Re-equilibration of melt inclusions trapped by magnesian olivine phenocrysts from subduction-related magmas: petrological implications. *Contributions to Mineralogy and Petrology,* 138**,** 68 - 83.

Darby, D. J., Hodgkinson, K. M. & Blick, G. H. 2000. Geodetic measurement of deformation in the Taupo Volcanic Zone, New Zealand: The north Taupo network revisited. *New Zealand Journal of Geology and Geophysics,* 43**,** 157-170.

Deering, C. D., Bachmann, O., Dufek, J. & Gravley, D. M. 2011. Rift-related transition from andesite to rhyolite volcanism in the Toupo volcanic Zone 9New Zealand) controlled by crystal-melt dynamics in mush zones with variable mineral assemblages. *Journal of Petrology,* 52**,** 2243-2263.

Dixon, J. E., Stolper, E. & Delaney, J. R. 1988. Infrared spectroscopic measurements of CO_2 and H_2O in Juan de Fuca Ridge basaltic glasses. *Earth and Planetary Science Letters,* 90**,** 87-104.

Dixon, J. E., Stolper, E. & Holloway, J. R. 1995. An Experimental Study of Water and Carbon Dioxide Solubilities in Mid-Ocean Ridge Basaltic Liquids. Part I: Calibration and Solubility Models. *Journal of Petrology,* 36**,** 1607-1631.

Donoghue, S. L., Neall, V. E. & Palmer, A. S. 1995. Stratigraphy and chronology of late Quaternary andesitic tephra deposits, Tongariro Volcanic Centre, New Zealand. *Journal of the Royal Society of New Zealand,* 25**,** 115-206.

Donoghue, S. L., Stewart, R. B. & Palmer, A. S. 1991. Morphology and chemistry of olivine phenocrysts of Mangamate Tephra, Tongariro Volcanic Centre, New Zealand. *Journal of the Royal Society of New Zealand,* 21**,** 225-236.

Edmonds, M., Aiuppa, A., Humphreys, M., Moretti, R., Giudice, G., Martin, R. S., Herd, R. A. & Christopher, T. 2010. Excess volatiles supplied by mingling of mafic magma at an andesite arc volcano. *Geochemistry Geophysics Geosystems,* 11**,** 1-16.

Edmonds, M., Sides, I. R., Swanson, D. A., Werner, C., Martin, R. S., Mather, T. A., Herd, R. A., Jones, R. L., Mead, M. I., Sawyer, G., Roberts, T. J., Sutton, A. J. & Elias, T. 2013. Magma storage, transport and degassing during the 2008-10 summit eruption at Kilauea Volcano, Hawaii. *Geochimica et Cosmochimica Acta,* 123**,** 284-301.

Fairbanks, R. G. 2005. *Radiocarbon age to calendar age conversion* [Online]. Available: http://radiocarbon.ldeo.columbia.edu/research/radcarbcal.htm 2015].

Ferguson, D. J., Gonnermann, H. M., Ruprecht, P., Plank, T., Hauri, E. H., Houghton, B. F. & Swanson, D. A. 2016. Magma decompression rates during explosive eruptions of Kilauea volcano, Hawaii, recorded by melt embayments. *Bulletin of Volcanology,* 78**,** 1-12.

Fine, G. & Stolper, E. 1985. Dissolved carbon dioxide in basaltic glasses: concentrations and speciation. *Earth and Planetary Science Letters,* 76**,** 263-278.

Fischer, T. P. 2008. Fluxes of volatiles (H_2O, CO_2, N_2, Cl, F. *Geochemical Journal,* 42**,** 21-38.

Forster, H., Oles, D., Knittel, U., Defant, M. J. & Torres, R. C. 1990. The Macolod Corridor: A rift crossing the Philippine island arc. *Tectonophysics,* 183**,** 265-271.

Gaetani, G. A., O'leary, J. A., Shimizu, N., Bucholz, C. E. & Newville, M. 2012. Rapid reequilibration of H_2O and oxygen fugacity in olivine-hosted melt inclusions. *Geology,* 40**,** 915-918.

Gaillard, F., Scaillet, B., Pichavant, M. & Iacono-Marziano, G. 2015. The redox geodynamics linking basalts and their mantle sources through space and time. *Chemical Geology,* 418**,** 217-233. Available: DOI doi:10.1016/j.chemgeo.2015.07.030.

Gale, A., Dalton, C. A., Langmuir, C. H., Su, Y. & Schilling, J.-G. 2013. The Mean Composition of Ocean Ridge Basalts. *Geochemistry Geophysics Geosystems,* 14**,** 489-518.

Gamble, J. A., Price, R. C., Smith, I. E. M., Mcintosh, W. C. & Dunbar, N. W. 2003. $^{40}Ar/^{39}Ar$ geochronology of magmatic activity, magma flux and hazards at Ruapehu volcano, Taupo Volcanic Zone, New Zealand. *Journal of Volcanology and Geothermal Research,* 120**,** 271-287.

Gamble, J. A., Smith, I. E. M., Graham, I. J., Kokelaar, B. P., Cole, J. W., Houghton, B. F. & Wilson, C. J. N. 1990. The Petrology, Phase Relations and Tectonic Setting of Basalts from the Taupo Volcanic Zone, New Zealand and Kermadec Island Arc- Havre Trough, SW Pacific. *Journal of Volcanology and Geothermal Research,* 43**,** 253-270.

Gamble, J. A., Wood, C. P., Price, R. C., Smith, I. E. M., Stewart, R. B. & Waight, T. 1999. A fifty year perspective of magmatic evolution on Ruapehu Volcano, New Zealand: verification of open system behaviour in an arc volcano. *Earth and Planetary Science Letters,* 170**,** 301-314.

Gerlach, T. M. 1986. Exsolution of H_2O, CO_2, and S During Eruptive Episodes at Kilauea Volcano, Hawaii. *Journal of Geophysical Research,* 91**,** 12,177-12,185.

Gerlach, T. M., Westrich, H. R. & Symonds, R. B. 1996. Preeruption Vapor in Magma of the Climactic Mount Pinatubo Eruption: Source of the Giant Stratospheric Sulfur Dioxide Cloud. *In:* Newhall, C. G. & Punongbayan, R. S. (eds.) *Fire and Mud: Eruptions and Lahars of Mount Pinatubo, Philippines.* University of Washington Press.

Ghiorso, M. S. & Evans, B. W. 2008. Thermodynamics of Rhombohedral Oxide Solid Solutions and a Revision of the Fe-Ti Two-oxide Geothermometer and Oxygen-barometer. *American Journal of Science,* 308**,** 957-1039.

Ghiorso, M. S. & Sack, R. O. 1995. Chemical Mass Transfer in Magmatic Processes. IV. A Revised and Internally Consistent Thermodynamic Model for the Interpolation and Extrapolation of Liquid-Solid Magmatic Systems at Elevated Temperatures and Pressures. *Contributions to Mineralogy and Petrology,* 119**,** 197-212.

Giggenbach, W. F. 1987. Redox processes governing the chemistry of fumarolic gas discharges from White Island, New Zealand. *Applied Geochemistry,* 2**,** 143-161. Available: DOI 10. 1016/0883-2927(87)90030-8.

Giggenbach, W. F. 1996. Chemical Composition of Volcanic Gases. *In:* Scarpa, R. & Tilling, R. I. (eds.) *Monitoring and Mitigation of Volcano Hazards.* Berlin Heidelberg: Springer-Verlag.

Gomez-Vasconcelos, M. G., Villamor, P., Cronin, S., Procter, J., Palmer, A., Townsend, D. & Leonard, G. 2017. Crustal extension in the Tongariro graben, New Zealand: Insights into volcano-tectonic interactions and active deformation in a young continental rift. *GSA Bulletin,* 129**,** 1085-1099.

Gonnermann, H. M. & Manga, M. 2003. Explosive volcanism may not be an inevitable consequence of magma fragmentation. *Nature,* 426.

Graham, I. J. 1985. *Petrochemical and Sr Isotopic Studies of Lavas and Xenoliths from Tongariro Volcanic Centre - Implications for Crustal Contamination of Calc-Alkaline Magmas.* Doctor of Philisophy, Victoria University of Wellington.

Graham, I. J., Cole, J. W., Briggs, R. M., Gamble, J. A. & Smith, I. E. M. 1995. Petrology and petrogenesis of volcanic rocks from the Taupo Volcanic Zone: a review. *Journal of Volcanology and Geothermal Research,* 68**,** 59-87.

Gregg, D. R. 1960. The Geolgy of Tongariro Subdivision. *In:* Research, N. Z. D. O. S. a. I. (ed.). New Zealand: New Zealand Geological Survey.

Greve, A., Turner, G. M., Conway, C. E., Townsend, D. B., Gamble, J. A. & Leonard, G. S. 2016. Paleomagnetic refinement of the eruption ages of Holocene lava flows, and implications for the eruptive history of the Tongariro Volcanic Centre, New Zealand. *Geophysical Journal International,* 207**,** 702-718.

Grove, T. L., Chatterjee, N., Parman, S. W. & Medard, E. 2006. The influence of H_2O on mantle wedge melting. *Earth and Planetary Science Letters,* 249**,** 74-89.

Grove, T. L., Elkins-Tanton, L. T., Parman, S. W., Chatterjee, N., Muntener, O. & Gaetani, G. A. 2003. Fractional crystallization and mantle-melting controls on calc-alkaline differentiation trends. *Contributions to Mineralogy and Petrology,* 145**,** 515-533.

Gualda, G. a. R., Ghiorso, M. S., Lemons, R. V. & Carley, T. L. 2012. Rhyolite-MELTS: a Modified Calibration of MELTS Optimized for Silica-rich, Fluid-bearing Magmatic Systems. *Journal of Petrology,* 0**,** 1-16. Available: DOI doi:10.1093/petrology/erg080.

Hackett, W. R. 1985. *Geology and Petrology of Ruapehu Volcano and Related Vents.* Ph.D, Victoria University of Wellington.

Hamilton, W. B. 1988. Plate tectonics and island arcs. *Geological Society of America Bulletin,* 100**,** 1503-1527.

Harlow, D. H., Power, J. A., Laguerta, E. P., Ambubuyog, G., White, R. A. & Hoblitt, R. P. 1996. Precursory seismicity and forecasting of the June 15, 1991, eruption of Mount Pinatubo. *In:* Newhall, C. G. & Punongbayan, R. S. (eds.) *Fire and Mud: Eruptions and Lahars of Mount Pinatubo, Philippines.* Seattle and London: University of Washington Press.

Harmon, R. S. & Hoefs, J. 1995. Oxygen isotope heterogeneity of the mantle deduced from global ^{18}O systematics of basalts from different geotectonic settings. *Contributions to Mineralogy and Petrology,* 120**,** 95-114.

Harris, C. & Ashwal, L. D. 2002. The origin of low $d^{18}O$ granites and related rocks from the Seychelles. *Contributions to Mineralogy and Petrology,* 143**,** 366-376.

Harris, C. & Erlank, A. J. 1992. The production of large-volume, low-$\delta^{18}O$ rhyolites during the rifting of Africa and Antarctica: The Lebombo Monocline, southern Africa. *Geochimica et Cosmochimica Acta,* 56**,** 3561-3570.

Harrison, A. & White, R. S. 2006. Lithospheric structure of an active backarc basin: the Taupo Volcanic Zone, New Zealand. *Geophysical Journal International* 167**,** 968-990.

Hartley, M. E., Neave, D. A., Maclennan, J., Edmonds, M. & Thordarson, T. 2015. Diffusive over-hydration of olivine-hosted melt inclusions. *Earth and Planetary Science Letters,* 425**,** 168-178.

Hartley, M. E., Shorttle, O., Maclennan, J., Moussallam, Y. & Edmonds, M. 2017. Olivine-hosted melt inclusions as an archive of redox heterogeneity in magmatic systems. *Earth and Planetary Science Letters*. Available: DOI 10.1016/j.epsl.2017.09.029.

Hauri, E. H., Wang, J., Dixon, J. E., King, P. L., Mandeville, C. & Newman, S. 2002. SIMS analysis of volatiles in silicate glasses 1. Calibration, matrix effects and comparisons with FTIR. *Chemical Geology,* 183**,** 99-114.

Hildreth, W. 2004. Volcanological perspectives on Long Valley, Mammoth Mountain, and Mono Craters: several contiguous but discrete systems. *Journal of Volcanology and Geothermal Research,* 136**,** 169-198.

Hildreth, W. & Moorbath, S. 1988. Crustal contributions to arc magmatism in the Andes of Central Chile. *Contributions to Mineralogy and Petrology,* 98**,** 455-489.

Hill, D. P. & Prejean, S. 2005. Magmatic unrest beneath Mammoth Mountain, California. *Journal of Volcanology and Geothermal Research,* 146**,** 257-283.

Hill, G. J., Bibby, H. M., Ogawa, Y., Wallin, E. L., Bennie, S. L., Caldwell, T. G., Keys, H., Bertrand, E. A. & Heise, W. 2015. Structure of the Tongariro Volcanic system: Insights from magnetotelluric imaging. *Earth and Planetary Science Letters,* 432**,** 115-125.

Hobden, B. J. 1997. *Modelling magmatic trends in time and space: eruptive and magmatic history of Tongariro Volcanic Complex, New Zealand.* PhD, University of Canterbury.

Hobden, B. J., Houghton, B. F., Davidson, J. P. & Weaver, S. D. 1999. Small and short-lived magma batches at composite volcanoes: time windows at Tongariro volcano, New Zealand. *Journal of the Geological Society, London,* 156**,** 865-868.

Hobden, B. J., Houghton, B. F. & Nairn, I. A. 2002. Growth of a young, frequently active composite cone: Ngauruhoe Volcano, New Zealand. *Bulletin of Volcanology,* 64**,** 392-409.

Hochstein, M. P. Steaming ground at Red Crater and in the Te Mari Craters, Mt. Tongariro Geothermal System (New Zealand). 7th NZ Geothermal Workshop, 1985 New Zealand.

Holloway, J. R. & Blank, J. G. 1994. Application of Experimental Results to C-O-H Species in Natural Melts. *In:* Carroll, M. R. & Holloway, J. R. (eds.) *Volatiles in Magmas.* Virginia: Mineralogical Society of America.

Hudgins, T. R., Mukasa, S. B., Simon, A. C., Moore, G. & Barifaijo, E. 2015. Melt inclusion evidence for CO_2-rich melts beneath the western branch of the East African Rift: implications for long-term storage of volatiles in the deep lithospheric mantle. *Contributions to Mineralogy and Petrology,* 169.

Hutchison, C. S. 1973. *Laboratory Handbook of Petrographic Techniques,* New York, Wiley.

Ito, E., White, W. M. & Gopel, C. 1987. The O, Sr, Nd and Pb isotope geochemistry of MORB. *Chemical Geology,* 62**,** 157-176.

James, M. R., Lane, S. J. & Chouet, B. A. 2006. Gas slug ascent through changes in conduit diameter: Laboratory insights into volcano-seismic source process in low-viscosity magmas. *Journal of Geophysical Research,* 111.

Johnson, G. W., Ehrlich, R. & Full, W. 2002. Principal Components Analysis and Receptor models in environmental forensics. *In:* Murphy & Morrison (eds.) *An Introduction to Environmental Forensics.* San Diego: Academic Press.

Kamenetsky, V. S., Crawford, A. J., Eggins, S. & Muhe, R. 1997. Phenocryst and melt inclusion chemistry of near-axis seamounts, Valu Fa Ridge, Lau Basin: insight into mantle wedge melting and the addition of subduction components. *Earth and Planetary Science Letters,* 151**,** 205-223.

Karig, D. E. 1974. Evolution of Arc Systems in the Western Pacific. *Annual Review of Earth and Planetary Sciences,* 2**,** 51-75.

Karlstrom, L., Dufek, J. & Manga, M. 2010. Magma chamber stability in arc and continental crust. *Journal of Volcanology and Geothermal Research,* 190**,** 249-270.

Kazahaya, K., Shinohara, H. & Saito, G. 1994. Excessive degassing of Izu-Oshima Volcano: magma convection in a conduit. *Bulletin of Volcanology,* 56**,** 207-216.

Kazahaya, K., Shinohara, H. & Saito, G. 2002. Degassing process of Satsuma-Iwojima volcano, Japan: Supply of volatile components from a deep magma chamber. *Earth Planets Space,* 54**,** 327-335.

Kent, A. J. R., Peate, D. W., Newman, S., Stolper, E. M. & Pearce, J. A. 2002. Chlorine in submarine glasses from the Lau Basin: seawater contamination and constraints on the composition of slab-derived fluids. *Earth and Planetary Science Letters,* 202**,** 361-377.

Kress, V. C. & Carmichael, I. S. E. 1991. The compressibility of silicate liquids containing Fe_2O_3 and the effect of composition, temperature, oxygen fugacity and pressure on their redox states. *Contributions to Mineralogy and Petrology,* 108**,** 82-92.

Langmuir, C. H., Vocke, J., R. D., Hanson, G. N. & Hart, S. R. 1978. A General Mixing Equations with Applications to Icelandic Basalts. *Earth and Planetary Science Letters,* 37**,** 380-392.

Lassiter, J. C., Hauri, E. H., Nikogosian, I. K. & Barsczus, H. G. 2002. Chlorine-potassium variations in melt inclusions from Raivavae and Rapa, Austral Islands: constraints on chlorine recycling in the mantle and evidence for brine-induced melting of oceanic crust. *Earth and Planetary Science Letters,* 202**,** 525-540.

Lecointre, J. A., Neall, V. E., Wallace, R. C., Elliot, M. B. & Sparks, R. 2004. Late Quaternary evolution of the Rotoaira Basin, northern Tongariro ring plain, New Zealand. *New Zealand Journal of Geology & Geophysics,* 47**,** 549-565.

Lifshin, E. & Gauvin, R. 2001. Minimizing Errors in Electron Microprobe Analysis. *Microscopy and Microanalysis,* 7**,** 168-177.

Lindsley, D. H. 1983. Pyroxene thermometry. *American Mineralogist,* 68**,** 477-493.

Lloyd, A. S., Ruprecht, P., Hauri, E. H., Rose, W., Gonnermann, H. M. & Plank, T. 2014. NanoSIMS results from olivine-hosted melt embayments: Magma ascent rate during explosive basaltic eruptions. *Journal of Volcanology and Geothermal Research,* 283**,** 1-18.

Lowe, D. J., Shane, P. a. R., Alloway, B. V. & Newnham, R. M. 2008. Fingerprints and age models for widespread New Zealand tephra marker beds erupted since 30,000 years ago: a framework for NZ-INTIMATE. *Quaternary Science Reviews,* 27**,** 95-126.

Lube, G., Cronin, S. J., Platz, T., Freundt, A., Procter, J. N., Henderson, C. & Sheridan, M. F. 2007. Flow and deposition of pyroclastic granular flows: A type example from the 1975 Ngauruhoe eruption, New Zealand. *Journal of Volcanology and Geothermal Research,* 161**,** 165-186.

Mandeville, C. W., Webster, J. D., Rutherford, M. J., Taylor, B. E., Timbal, A. & Faure, K. 2002. Determination of molar absorptivities for infrared absorption bands of H2O in andesitic glasses. *American Mineralogist,* 87**,** 813-821.

Mangan, M., Mastin, L. & Sisson, T. 2004. Gas evolution in eruptive conduits: combining insights from high temperature and pressure decompression experiments with steady-state flow modeling. *Journal of Volcanology and Geothermal Research,* 129**,** 23-36.

Mangan, M. & Sisson, T. 2000. Delayed, disequilibrium degassing in rhyolite magma: decompression experiments and implications for explosive volcanism. *Earth and Planetary Science Letters,* 183**,** 441-455.

Mathews, W. H. 1967. A contribution to the geology of the Mount Tongariro massif, North Island, New Zealand. *New Zealand Journal of Geology and Geophysics,* 10**,** 1027-1038.

Mcmillan, P. F. 1994. Water Solubility and Speciation Models. *In:* Carroll, M. R. & Holloway, J. R. (eds.) *Volatiles in Magmas.* Virginia: Mineralogical Society of America.

Metrich, N. & Wallace, P. J. 2008. Volatile Abundances in Basaltic Magmas and Their Degassing Paths Tracked by Melt Inclusions. *Reviews in Mineralogy & Geochemistry,* 69**,** 363-402.

Michael, P. J. 1988. The concentration, behaviour and storage of H_2O in the suboceanic upper mantle: implications for mantle metasomatism. *Geochimica et Cosmochimica Acta,* 52**,** 555-566.

Miklius, A., Flower, M. F. J., Huijsmans, J. P. P., Mukasa, S. B. & Castillo, P. 1991. Geochemistry of lavas from Taal Volcano, Southwestern Luzon, Philippines: Evidence for Multiple Magma Supply Systems and Mantle Source Heterogeneity. *Journal of Petrology,* 32**,** 593-627.

Moebis, A. 2010. *Understanding the Holocene explosive eruption record of the Tongariro Volcanic Centre, New Zealand.* PhD, Massey University.

Moebis, A., Cronin, S. J., Neall, V. E. & Smith, I. E. 2011. Unravelling a complex volcanic history from fine-grained, intricate Holocene ash sequences at the Tongariro Volcanic Centre, New Zealand. *Quaternary International,* 246**,** 352-363.

Moretti, R., Arienzo, I., Civetta, L., Orsi, G. & Papale, P. 2013. Multiple magma degassing sources at an explosive volcano. *Earth and Planetary Science Letters,* 367**,** 95-104.

Moriguti, T. & Nakamura, E. 1998. Across-arc variation of Li isotopes in lavas and implications for crust/mantle recycling at subduction zones. *Earth and Planetary Science Letters,* 163**,** 167-174.

Mukasa, S. B., Flower, M. F. J. & Miklius, A. 1994. The Nd-, Sr- and Pb-isotopic character of lavas from Taal, Laguna de Bay and Arayat volcanoes, southwest Luzon, Philippines: implications for arc magma petrogenesis. *Tectonophysics,* 235**,** 205-221.

Mysen, B. O. & Boettcher, A. L. 1975. Melting of a Hydrous Mantle: I. Phase Relations of Natural Peridotite at High Pressures and Temperatures with Controlled Activities of Water, Carbon Dioxide, and Hydrogen. *Journal of Petrology,* 16**,** 520-548.

Nairn, I. A., Kobayashi, T. & Nakagawa, M. 1998. The ~10 ka multiple vent pyroclastic eruption sequence at Tongariro Volcanic Centre, Taupo Volcanic Zone, New Zealand: Part 1. Eruptive processes during regional extension. *Journal of Volcanology and Geothermal Research,* 86**,** 19-44.

Nairn, I. A. & Self, S. 1978. Explosive eruptions and pyroclastic avalanches from Ngauruhoe in February 1975. *Journal of Volcanology and Geothermal Research,* 3**,** 39-60.

Nakagawa, M., Nairn, I. A. & Kobayashi, T. 1998. The ~10 ka multiple vent pyroclastic eruption sequence at Tongariro Volcanic Centre, Taupo Volcanic Zone, New Zealand Part 2. Petrological insights into magma storage and transport during regional extension. *Journal of Volcanology and Geothermal Research,* 86**,** 45-65.

Newman, S. & Lowenstern, J. B. 2002. VOLATILECALC: a silicate melt-H_2O-CO_2 solution model written in Visual Basic for excel. *Computers & Geosciences,* 28**,** 597-604.

Newman, S., Stolper, E. M. & Epstein, S. 1986. Measurement of water in rhyolitic glasses: Calibration of an infrared spectroscopic technique. *American Mineralogist,* 71**,** 1527-1541.

Oles, D., Knittel, U., Forster, H., Torres, R., Wolfe, J. & Bellon, H. 1995. Basaltic volcanism associated with extensional tectonics in the southern part of the Luzon Island Arc, the Philippines: Part I. Tectonic setting and volcanological evolution. . *In:* Institute of Mineralogy, R. A., Germany and Philippine Institute of Volcanology and Seismology, Philippines (ed.). unpublished report.

Parks, M. M., Biggs, J., England, P., Mather, T. A., Nomikou, P., Palamartchouk, K., Papanikolaou, X., Paradissis, D., Parsons, B., Pyle, D. M., Raptakis, C. & Zacharis, V. 2012. Evolution of Santorini Volcano dominated by episodic and rapid fluxes of melt from depth. *Nature Geoscience,* 5. Available: DOI doi:10.1038/NGEO1562.

Patane, D., Barberi, G., Cocina, O., De Gori, P. & Chiarabba, C. 2006. Time-Resolved Seismic Tomography Detects Magma Intrusions at Mount Etna. *Science,* 313.

Paulatto, M., Annen, C., Henstock, T. J., Kiddle, E., Minshull, T. A., Sparks, R. S. J. & Voight, B. 2012. Magma chamber properties from integrated seismic tomography and thermal modeling at Montserrat. *Geochemistry Geophysics Geosystems,* 13. Available: DOI doi:10.1029/2011GC003892.

Peacock, S. M. 1990. Fluid Processes in Subduction Zones. *Science,* 248**,** 329-337.

Petrelli, M., Poli, G., Perugini, D. & Peccerillo, A. 2005. Petrograph: a New Software to Visualize, Model, and Present Geochemical Data in Igneous Petrology. *Geochemistry Geophysics Geosystems,* 6. Available: DOI doi:10.1029/2005GC000932.

Plank, T., Kelley, K. A., Zimmer, M. M., Hauri, E. H. & Wallace, P. J. 2013. Why do mafic arc magmas contain ~4 wt% water on average? *Earth and Planetary Science Letters,* 364**,** 168 - 179.

Plank, T. & Langmuir, C. H. 1998. The chemical composition of subducting sediment and its consequences for the crust and mantle. *Chemical Geology,* 145**,** 325-394.

Price, R. C., A., G. J., Smith, I. E. M., Stewart, R. B., Eggins, S. & Wright, I. C. 2005. An integrated model for the temporal evolution of andesites and rhyolites and crustal development in New Zealand's North Island. *Journal of Volcanology and Geothermal Research,* 140**,** 1-24.

Price, R. C., Smith, I., Cronin, S., Gamble, J., Hobden, B., Turner, M. & Stewart, R. 2013. *A field guide to the volcanic geology of North Island, New Zealand*.

Price, R. C., Turner, S., Cook, C., Hobden, B., Smith, I. E. M., Gamble, J. A., Handley, H., Maas, R. & Mobis, A. 2010. Crustal and mantle influences and U-Th-Ra disequilibrium in andesitic lavas of Ngauruhoe volcano, New Zealand. *Chemical Geology,* 277**,** 355-373.

Putirka, K. D. 2008. Thermometers and Barometers for Volcanic Systems. *Reviews in Mineralogy & Geochemistry,* 69**,** 61-120.

Reyners, M., Eberhart-Phillips, D., Stewart, G. & Nishimura, Y. 2006. Imaging subduction from the trench to 300 km depth beneath the central North Island, New Zealand, with Vp and Vp/Vs. *Geophysical Journal International,* 165**,** 565-583.

Rhodes, J. M., Dungan, M. A., Blanchard, D. P. & Long, P. E. 1979. Magma Mixing at Mid-Ocean Ridges: Evidence From Basalts Drilled Near 22°N on the Mid-Atlantic Ridge. *Tectonophysics,* 55**,** 35-61.

Rowe, M. C., Kent, A. J. R. & Nielsen, R. L. 2009. Subduction Influence on Oxygen Fugacity and Trace and Volatile Elements in Basalts Across the Cascade Volcanic Arc. *Journal of Petrology,* 50**,** 61-91.

Rowland, J. V. & Sibson, R. H. 2001. Extensional fault kinematics within the Taupo Volcanic Zone, New Zealand: soft-linked segmentation of a continental rift system. *New Zealand Journal of Geology and Geophysics,* 44**,** 271-283.

Rudnick, R. L. & Goldstein, S. L. 1990. The Pb isotopic compositions of lower crustal xenoliths and the evolution of lower crustal Pb. *Earth and Planetary Science Letters,* 98**,** 192-207.

Rüpke, L. H., Morgan, J. P., Hort, M. & Connolly, J. a. D. 2002. Are the regional variations in Central American arc lavas due to differing basaltic versus peridotitic slab sources of fluids? *Geological Society of America Bulletin,* 30**,** 1035-1038.

Ryan, J. G., Morris, J., Tera, F., Leeman, W. P. & Tsvetkov, A. 1995. Cross-arc geochemical variations in the Kurile Arc as a function of slab depth. *Science,* 270**,** 625-627.

Scaillet, B., Pichavant, M. & Cioni, R. 2008. Upward migration of Vesuvius magma chamber over the past 20,000 years. *Nature,* 455. Available: DOI doi:10.1038/nature07232.

Schmincke, H. U. 2004. *Volcanism,* Berlin Heidelberg, Springer-Verlag.

Shane, P., Doyle, L. R. & Nairn, I. A. 2008. Heterogeneous andesite-dacite ejecta in 26-16.6 ka pyroclastic deposits of Tongariro Volcano, New Zealand: the product of multiple magma-mixing events. *Bulletin of Volcanology,* 70**,** 517-536.

Shane, P., Maas, R. & Lindsay, J. 2017. History of Red Crater volcano, Tongariro Volcanic Centre (New Zealand): Abrupt shift in magmatism following recharge and contrasting evolution between neighboring volcanoes. *Journal of Volcanology and Geothermal Research,* 340**,** 1-15.

Sisson, T. W. & Grove, T. L. 1993. Experimental investigations of the role of H_2O in calc-alkaline differentiation and subduction zone magmatism. *Contributions to Mineralogy and Petrology,* 113**,** 143-166.

Smith, I. E. M. & Price, R. C. 2006. The Tonga-Kermadec arc and Havre-Lau back-arc system: Their role in the development of tectonic and magmatic models for the western Pacific. *Journal of Volcanology and Geothermal Research,* 156**,** 315-331.

Smith, I. E. M., Worthington, T. J., Stewart, R. B., Price, R. C. & Gamble, J. A. 2003. Felsic volcanism in the Kermadec arc, SW Pacific: crustal recycling in an oceanic setting. *In:* Later, R. D. & Leat, P. T. (eds.) *Intra-Oceanic Subduction Systems: Tectonic and Magmatic Processes.* Geological Society, London, Special Publications.

Staudacher, T. & Allègre, C. J. 1988. Recycling of oceanic crust and sediments: the noble gas subduction barrier. *Earth and Planetary Science Letters,* 89**,** 173-183.

Stern, T., Stratford, W., Seward, A., Henderson, M., Savage, M., Smith, E., Benson, A., Greve, S. & Salmon, M. 2010. Crust-mantle structure of the central North Island, New Zealand based on seismological observations. *Journal of Volcanology and Geothermal Research,* 190**,** 58-74.

Stern, T. A. 1985. A back-arc basin formed within continental lithosphere: the central volcanic region of New Zealand. *Tectonophysics,* 112**,** 385-409.

Stern, T. A. & Davey, F. J. 1987. A seismic investigation of the crustal and upper mantle structure within the Central Volcanic Region of New Zealand. *New Zealand Journal of Geology and Geophysics* 30**,** 217-231.

Stern, T. A., Stratford, W. R. & Salmon, M. L. 2006. Subduction evolution and mantle dynamics at a continental margin: central North Island, New Zealand. *Reviews of Geophysics* 44. Available: DOI 4010.1029/2005 RG000171.

Stevens, N. F. 2002. Emplacement of the large andesite lava flow in the Oturere Stream valley, Tongariro Volcano, from airborne interferometric radar. *New Zealand Journal of Geology & Geophysics,* 45**,** 387-394.

Stevenson, D. S. & Blake, S. 1998. Modelling the dynamics and thermodynamics of volcanic degassing. *Bulletin of Volcanology,* 60**,** 307-317.

Stolper, E. 1982. The speciation of water in silicate melts. *Geochimica et Cosmochimica Acta,* 46**,** 2609-2620.

Stolper, E., Fine, G., Johnson, T. & Newman, S. 1987. Solubility of carbon dioxide in albitic melt. *American Mineralogist,* 72**,** 1071-1085.

Stratford, W. R. & Stern, T. A. 2006. Crust and upper mantle structure of a continental backarc: central North Island, New Zealand. *Geophysics Journal International,* 166**,** 469-484.

Straub, S. M., Gomez-Tuena, A., Stuart, F. M., Zellmer, G. F., Cai, Y. & Espinasa-Perena, R. 2011. Formation of hybrid arc andesites beneath thick continental crust. *Earth and Planetary Science Letters,* 303**,** 337-347.

Takeuchi, S. 2011. Preeruptive magma viscosity: An important measure of maagma eruptibility. *Journal of Geophysical Research,* 116. Available: DOI doi:10.1029/2011JB008243.

Taran, Y. A., Hedenquist, J. W., Korzhinsky, M. A., Tkachenko, S. I. & Shmulovich, K. I. 1995. Geochemistry of magmatic gases from Kudryavy volcano, Iturup, Kuril Islands. *Geochimica et Cosmochimica Acta,* 59**,** 1749-1761.

Tatsumi, Y. 1989. Migration of fluid phases and genesis of basalt magmas in subduction zones. *Journal of Geophysical Research,* 94**,** 4697-4707.

Taylor, H. P. & Sheppard, S. M. F. 1986. Igneous rocks: I. Processes of isotopic fractionation and isotope systematics. *In:* Valley, J. W., Taylor, H. P. & O'neil, J. R. (eds.) *Stable Isotopes in High Temperature Geological Processes.* Washington: Mineralogical Society of America.

Till, C. B., Grove, T. L. & Withers, A. C. 2012. The beginnings of hydrous mantle wedge melting. *Contributions to Mineralogy and Petrology,* 163**,** 669-688.

Topping, W. W. 1973. Tephrostratigraphy and chronology of late quaternary eruptives from the Tongariro Volcanic Centre, New Zealand. *New Zealand Journal of Geology & Geophysics,* 16**,** 397-423.

Topping, W. W. 1974. *Some aspects of quaternary history of Tongariro Volcanic Centre.* PhD, Victoria University.

Vogel, T. A., Flood, T. P., Patino, L. C., Wilmot, M. S., Maximo, R. P. R., Arpa, C. B., Arcilla, C. A. & Stimac, J. A. 2006. Geochemistry of silicic magmas in the Macolod Corridor, SW Luzon, Philippines: evidence of distinct, mantle-derived, crustal sources for silicic magmas. *Contributions to Mineralogy and Petrology,* 151**,** 267-281.

Wallace, P. J., Dufek, J., Anderson, A. T. & Zhang, Y. 2003. Cooling rates of Plinian-fall and pyroclastic-flow deposits in the Bishop Tuff: inferences from water speciation in quartz-hosted glass inclusions. *Bulletin of Volcanology,* 65**,** 105-123. Available: DOI 10.1007/s00445-002-0247-9.

Walther, J. V. & Orville, P. M. 1982. Volatile Production and Transport in Regional Metamorphism. *Contributions to Mineralogy and Petrology,* 79**,** 252-257.

White, R. A. 1996. Precursory Deep Long-Period Earthquakes at Mount Pinatubo: Spatio-Temporal Link to a Basalt Trigger. *In:* Newhall, C. G. & Punongbayan, R. S. (eds.) *Fire and Mud: Eruptions and Lahars of Mount Pinatubo, Philippines.* Seattle and London: University of Washington Press.

White, W. M. 2013. *Geochemistry*, Wiley-Blackwell.

Winter, J. 2001. *An Introduction to Igneous and Metamorphic Petrology*, Prentice Hall.

Wolff, J. A., Grandy, J. S. & Larson, P. B. 2000. Interaction of mantle-derived magma with island crust? Trace element and oxygen isotope data from the Diego Hernandez Formation, Las Cañadas, Tenerife. *Journal of Volcanology and Geothermal Research,* 103**,** 343-366.

Www.Gns.Cri.Nz. *About Tongariro* [Online]. GNS Science. Available: http://www.gns.cri.nz/Home/Learning/Science-Topics/Volcanoes/New-Zealand-Volcanoes/Tongariro/About-Tongariro 2015].

Www.Gns.Cri.Nz. *Ngauruhoe* [Online]. GNS Science. Available: http://www.gns.cri.nz/Home/Learning/Science-Topics/Volcanoes/New-Zealand-Volcanoes/Ngauruhoe 2015].

Www.Volcano.Si.Edu. *Smithsonian Institution Global Volcanism Program: Tongariro* [Online]. Available: http://volcano.si.edu/volcano.cfm?vn=241080 2015].

Yogodzinski, G. M. & Kelemen, P. B. 1998. Slab melting in the Aleutians: implications of an ion probe study of clinopyroxene in primitive adakite and basalt. *Earth and Planetary Science Letters,* 158**,** 53-65.

Zellmer, G. F., Sakamoto, N., Iizuka, Y., Miyoshi, M., Tamura, Y., Hsieh, H.-H. & Yurimoto, H. 2013. Crystal uptake into aphyric arc melts: insights from two-pyroxene pseudo-decompression paths, plagioclase hygrometry, and measurement of hydrogen in olivines from mafic volcanics of SW Japan. *In:* Gomez-Tuena, A., Straub, S. M. & Zellmer, G. F. (eds.) *Orogenic Andesites and Crustal Growth.* Geological Society of London.

Zhang, Y., Stolper, E. M. & Ihinger, P. D. 1995. Kinetics of the reaction $H_2O + O = 2OH$ in rhyolitic and albitic glasses: Preliminary results. *American Mineralogist,* 80**,** 593 - 612.

Zindler, A. & Hart, S. 1986. Chemical Geodynamics. *Annual Review of Earth and Planetary Sciences,* 14**,** 493-571.

Zlotnicki, J., Sasai, Y., Toutain, J. P., Villacorte, E. U., Bernard, A., Sabit, J. P., Gordon Jr., J. M., Corpuz, E. G., Harada, M., Punongbayan, J. T., Hase, H. & Nagao, T. 2008. Combined electromagnetic, geochemical and thermal surveys of Taal volcano (Philippines) during the period 2005-2006. *Bulletin of Volcanology*. Available: DOI DOI 10.1007/s00445-008-0205-2.